Feldspar dissolution during the weathering of granite under tropical conditions

Zainuddin Mdyusoff

Thesis submitted in fulfilment of
the requirements for the degree of
Doctor of Philosophy

School of Geosciences
University of Edinburgh

2008

Abstract

Tropical areas with extreme climates are host to extreme weathering processes and the weathered materials are normally left in situ with the absence of large scale denudation processes such as glaciations. This research tries to understand the behaviour of feldspar minerals in the extremely thick weathered soil profiles. The study location chosen is Malaysia, about 3°N of the equator which experience a hot and humid climate all year round with mean daily temperatures ranging from 22 to 32°C. The annual rainfall averages from 200 cm to 250 cm. The thick layer of weathered soil creates slope failures and landslides, especially on cut slopes at the road sides. Much of Malaysia is composed of granite. Samples ranging from unweathered granite to surface soils from newly exposed cut slopes and drill-holes were analysed using Quantitative X-ray Powder Diffraction (QXRPD), X-ray Fluorescence spectrometry (XRF), Inductively-coupled plasma mass spectrometry (ICP-MS), Scanning Electron Microscopy (SEM) and Optical microscopy. Samples were also sent to commercial laboratories for the determination of geotechnical engineering index and strength properties. The analyses have brought about a categorization of the weathering profiles into 4 'zones': top soil, saprolite, weathering boundary and unweathered granite zones. The reactions within the active weathering boundary zone dictate the formation of secondary minerals. The findings in each different zone have enlightened the understanding of the development of secondary minerals especially clays in a deep weathering profile. The study also confirms and furthers understanding of the way chemical weathering occurs on the K-feldspar grains and is followed by the mechanical collapse of the grains leading to the reduction in the geotechnical strength of the material. The major element mobility study did not show any relation to the degree of weathering within the saprolite. Trace element study did not give conclusive results. However, a rare earth element (REE) study shows that the mobility of REE depends on the degree of weathering. The presence of clay minerals and feldspar grains are related to the geotechnical engineering properties, especially the strength properties which are responsible to the stability of slopes.

Contents

Acknowledgement

I would like to express my thanks firstly, to the Government of Malaysia for funding this research, and particularly to my supervisors, Prof. Dr Ian Parsons and Dr Bryne Ngwenya from the Department of Geology and Geophysics for many helpful discussions during the course of this study and the support they gave me throughout. Also to Dr Steve Hillier from The Macaulay Institute, Aberdeen, and Dr Valerie Olive from Scottish Universities Environmental Research Centre, East Kilbride for the fruitful discussions.

I wish to express my gratitude and appreciation to the wide and varied group of fellow PhD students, Postdocs (especially those in the Old Attic) and the department's academic and administrative staffs that have become my friends over the years.

Last and definitely not least, to my wife (*Maswati Saal*), our two daughters (*ZulaikhaMaisarah* and *SufiNuraisyah*) and our families.

Dedicated to our late fathers, my late mother and my late sister:

Hj Mohamad Yusoff Abdul Razak (-10 Dec 1990)
Hj Saal Kasbon (-28 Jan 2007)
Hjh Aminah Mohamad (-16 Nov 2006)
Hjh Hasnah Mohamad Yusoff (-14 Jan 1978)

List of figures

List of tables

1. INTRODUCTION

Malaysia, comprising Peninsular Malaysia and East Malaysia is located in Asia at about 3°N of the equator and experience a hot and humid climate all year round with temperatures ranging from 22 to 32°C. The annual rainfall averages from 200cm to 250cm with extremities during the annual southwest (April to October) and northeast monsoons (October to February). With the development of the country, roads and highways are constructed to connect the urban and rural areas, and increase in the housing development on hilly areas due to the increasing needs of accommodation. Slope failure and landslides are becoming more frequent of late, including a worst collapse of a 12 storey high rise building in 1993 with 48 casualties. Public discussions ensued and comments from local experts to members of parliament ranges from the failure of exposed geological weaknesses to the weathering parameters, soil erosion, designed slopes were not done as it should be, exceptionally high rain fall during the particular period and uncontrolled denudation of the surrounding areas .

Granitic rocks occupy about 50% of the exposed landmass of peninsular Malaysia. Weathered material in excess of 30m thick is common and in areas of massive granitic rocks, weathering produces rounded core boulders, with diameter more than 20cm (British Standard Institution, 1990a), of unweathered rock that maybe "floating" in a thick layer of otherwise completely weathered material (Gobbett and Hutchison, 1972) These boulders create difficulties in the drilling activities for site investigation as it is difficult to tell whether the drill has hit solid 'bedrock' or a boulder. The thick residual soils and the presence of boulders are some of the main problems faced by civil engineers in designing the cut slopes especially for highways and foundations for high rise buildings. Feldspars being the most abundant mineral in almost all crustal igneous rock and the subsolidus phase transformation and exsolution microstructure are more complex and informative then any other mineral group (Brown and Parsons, 1994) prompted the writer to study in detail on the weathering of feldspars under tropical conditions.

1.1 Key aims and rationale

This study will focus on the weathering mechanisms in calc-alkaline granites under the hot and humid conditions of Peninsular Malaysia. The extremely thick soil and weathered soil profiles prompted questions like whether this layer is getting thicker or have they reached equilibrium whereby the weathering of fresh layer has halted because solutes can no longer get into the surface or weather the advancement of the weathering is as fast as the erosion process and what is controlling the rate of processes in the interface zones between solid rock and weathered materials. In previous studies on feldspars from temperate areas, feldspar microtextures seem to exert a strong control on the reaction rates (e.g. Lee, Waldron and Parsons, 1995b; Lee, Hodson and Parsons, 1998; Waldron, Lee and Parsons, 1998). It would be interesting to know whether this also applies to the feldspars in tropical areas.

1.2 Research aim and approach

The main research aim is to examine the properties and conditions of feldspar grains at different weathering depth in the tropical area, Malaysia. This will help to characterise the evolution of the grain surfaces at different depth in weathering profile. To do this, very recently exposed cut slopes and drillhole samples were taken and analysed. The surface texture of the grains will be studied under SEM. The study also involves bulk chemical analyses and X-ray diffraction work to establish the change in bulk feldspar content and development of clays in the profiles. XRF and ICP-MS will also be used to study the major elements, trace elements and REE bulk composition to study the mobility of the elements.

1.3 Structure of thesis

This study is structured in a way so as to lead the reader through a logical progression of evidence and interpretation under different chapters, of the dissolution of feldspars in a thick weathering profile. In Chapter 2, the selected literatures are reviewed. The

subtopics are the chemical reactions of feldspars (especially K feldspars), structure and nomenclature of feldspars and the dissolution of feldspars.

Chapter 3 presents the geological background of the studied area and the sampling procedures.

Chapter 4 examines the detail mineralogy and geochemistry of the samples taken. The results of analyses provide the basis for categorising the profiles into different zone and these zones correspond to different scale of weathering activity. The mineralogy and chemistry of each zone are presented separately, from the unweathered granite to the most weathered zones, to lead the reader on the dissolution process of feldspar grains. A discussion will be at the end of the chapter to provide the interpretation of the analyses results.

Chapter 5 looks into the mobility of the major, trace and rare earth elements with regards to the weathering activity.

Chapter 6 relates the findings of this study with the basic cut slope designs practiced by geotechnical engineers. The chapter will start with a review of the basics of the slope stability calculations. The parameters used in the design of slopes will than be discussed in terms of the dissolution of feldspar grains.

The conclusions of this study are presented in Chapter 7.

2. LITERATURE REVIEW

Introduction

The first section of this chapter will review the literature and discuss general aspects of the weathering of granite under tropical conditions. It will touch briefly on the reactions of mineral components of granite especially K-feldspar and the formation of clays. The reasons why feldspar is particularly important in this study are also explained. Then there will be a review of literature on the feldspars, their properties and behaviour, and their occurrence in igneous rocks. The final section will discuss the dissolution mechanism of feldspars.

2.1 Chemistry of weathering of granite in tropical areas

2.1.1 Chemical reactions of K-feldspars and formation of clays

Weathering can be defined as the effect of weather on rocks in situ, whereby the disintegration and decomposition of rocks and minerals by natural processes occurs. The process can be physical and /or chemical. Chemical and mechanical weathering often go hand in hand. In this study, hydrolysis, a form of chemical weathering involving the action of acidic water on rock forming minerals, especially K-feldspars has been studied. It involves the detachment and attachment of atoms at the mineral surface (White, 1995). This process, acting on aluminosilicate bearing rock under sub-tropical or tropical rainfall conditions mainly produces kaolinite, amorphous Al $(OH)_3$ and gibbsite. These transformations are related to the removal of alkali and alkaline-earth metals, and silica and lead to mechanical disintegration of the rocks.

Pedro (1997) noted that hydrolytic weathering always results in at least some loss of silica and alkalis from the initial rock, whereas Al and Fe are retained in-situ forming secondary Al phyllosilicates and Al hydroxides. Three prime scenarios involved are:

1. Total hydrolysis: complete loss of silica and alkalis, inducing formation of gibbsite, Al $(OH)_3$.

2. If hydrolysis is less pervasive, silica loss is partial but loss of alkalis is complete. Kaolin-type phyllosilicates are formed.
3. If hydrolysis is weak, with incomplete loss of silica and alkalis, phyllosilicates of smectite type (beidellite) are formed.

In some very slightly weathered formations, small amounts of gibbsite are formed as a secondary mineral. These observations have led to two approaches in studying weathering. The first is the degree of weathering measured as the amount of weatherable primary minerals that have actually disappeared. In massive weathering, chemical decomposition affects all weatherable materials and they are replaced by large amounts of secondary minerals (gibbsite, kaolinite or smectite). During progressive weathering, differential leaching of primary minerals occurs and the resulting intermediate material tends to contain a large amount of coarse grains. The second approach is based on geochemical changes as recorded in the soil profile (Boulet et al, 1997) categorised soil profiles into two groups. The first is soil covers that are in dynamic equilibrium, which have developed in conditions stable enough to keep the sequence of transformation from parent rock to soil surface constant. Secondly, soil covers that are in chemical disequilibrium. This is the transformation phase where the rock/soil will transform to another soil type which tends towards a dynamic equilibrium.

The weathering of granites in tropical areas can result in residual soils or saprolites as thick as 30m. Residual soil or saprolite is defined as a deposit of disintegrating rocks that is found in its original place. Granites are composed of quartz, K-feldspar, plagioclase, sometimes muscovite, mafic minerals like biotite and hornblende, opaque oxide minerals, and also important accessory minerals such as zircon and titanite. During chemical weathering, the minerals present are altered and gradually decomposed to substances that are stable at low temperatures. Theoretically, the dissolution of aluminosilicates such as K-feldspars can occur congruently whereby all the initial minerals go into solution (Equation 2.1).

$$KAlSi_3O_{8\,(s)} + 4H^+_{(aq)} + 4H_2O_{(l)} \Rightarrow Al_{(aq)} + K^+_{(aq)} + 3H_4SiO_{4\,(aq)} \qquad \text{(Equation 2.1)}$$

However, the Al^{3+} is normally retained in secondary (clay) minerals making the reaction an incongruent dissolution (Equation 2.2).

$$\underset{\text{(K-feldspar)}}{2KAlSi_3O_{8\,(S)}} + \underset{\text{(carbonic acid)}}{2(H_2HCO_3)_{(aq)} + H_2O_{(l)}} \Rightarrow \underset{\text{(kaolinite)}}{Al_2Si_2O_5(OH)_{4\,(s)}} + \underset{\text{(potassium Ions)}}{2K^+_{(aq)}} + \underset{\text{(bicarbonate ions)}}{2HCO_3^-{}_{(aq)}} + \underset{\text{(silica)}}{4SiO_{2\,(s)}}$$

(Equation 2.2)

H^+ ions in solution are provided by carbonic acid, which ionizes to H^+ and HCO_3^-. K-feldspars in the granite will react with the H^+ ions to produce kaolinite and the SiO_2 produced in this reaction forms stable quartz grains. The potassium and bicarbonate ions will either combine to form potassium bicarbonate or be taken up by plants as nutrients. If potassium is not lost, illite is likely to form rather than kaolinite (Deer et al., 1992). Some silicic acid is also formed as a product of reactions between SiO_2 and water (Equation 2.3) and also from the reaction between kaolinite and water (Equation 2.4).

$$SiO_{2\,(s)} + 2H_2O_{(l)} \Rightarrow H_4SiO_{4\,(aq)} \qquad \text{(Equation 2.3)}$$

$$\underset{\text{(kaolinite)}}{Al_2Si_2O_5(OH)_{4\,(s)}} + 5\,H_2O_{(l)} \Rightarrow \underset{\text{(gibbsite)}}{2Al(OH)_{3\,(s)}} + \underset{\text{(silicic acid)}}{2H_4SiO_{4\,(aq)}} \qquad \text{(Equation 2.4)}$$

Gibbsite or an equivalent amorphous phase is produced in this reaction. The chemical formulae of the principle minerals involved in this research is given in Table 2.1. At low pH, Al^{3+} is the dominant species and as the pH increases, the solubility of gibbsite decreases (Equation 2.5). However, as pH increases, the other hydroxyl complexes are formed and the solubility of gibbsite depends on their behaviour. A summary of the reactions discussed above is given in Figure 2.1a.

$$\underset{\text{gibbsite}}{Al(OH)_{3\,(s)}} + 3H^+_{(aq)} \Rightarrow Al^{3+}_{(aq)} + 3H_2O_{(l)} \qquad \text{(Equation 2.5)}$$

Mineral	Chemical formula
Alkali feldspar	$(K,Na)[AlSi_3O_8]$
Biotite	$KFe_3AlSi_3O_{10}(OH)_2$
Boehmite	γ-AlO(OH)
Chlorite	$(Mg,Fe^{2+},Fe^{3+},Mn,Al)_{12}[(Si,Al)_8O_{20}](OH)_{16}$
Diaspore	α-AlO(OH)
Gibbsite	$Al(OH)_3$
Halloysite	$Al_4[Si_4O_{10}](OH)_8$
Hematite	α-Fe_2O_3
Hornlende	$Ca_2(Mg,Fe)_4AlSi_7AlO_{22}(OH)_2$
Kaolinite	$Al_4[Si_4O_{10}](OH)_8$
K-feldspar	$KAlSi_3O_8$
Muscovite	$K_2Al_4[Si_6Al_2O_{20}](OH, F)_4$
Plagioclase	$Na[AlSi_3O_8]$-$Ca[Al_2Si_2O_8]$
Quartz	SiO_2
Titanite	$CaTi[SiO_4](O,OH,F)$
Zircon	$Zr[SiO_4]$

Table 2.1: Chemical formulae of principle minerals discussed in this research (Deer, Howie and Zusmann, 1992).

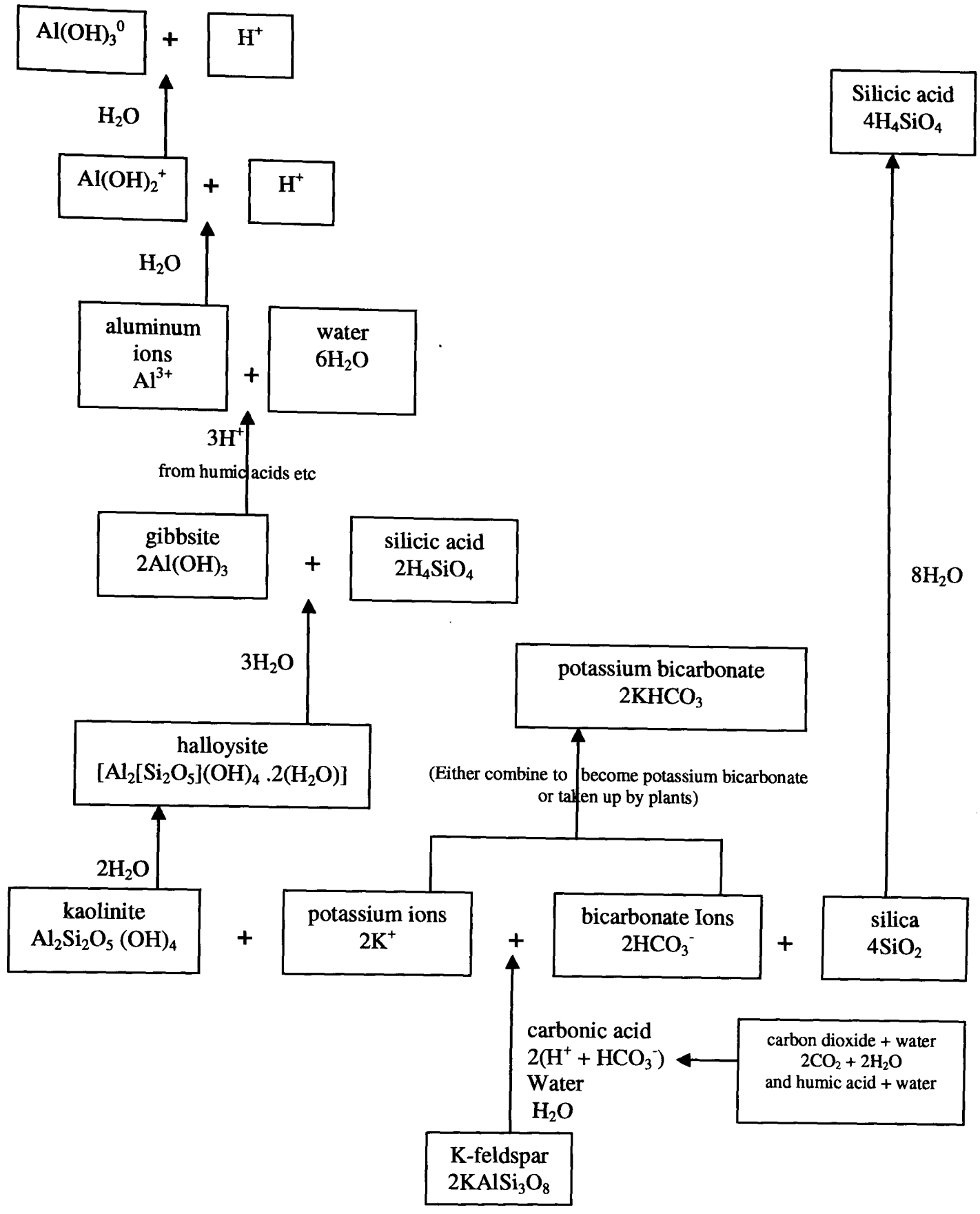

Figure 2.1a: Summary of the dissolution of K-feldspar, based on the theoretical consideration of equilibrium between K-feldspar and aqueous solution, compiled and modified from Wilson, (1975); Schwartz at al, (1995); and Drever, (1997)

Several other probable reactions were not discussed in the summary mentioned above and are shown in equations 2.6 to 2.8 and summarised in Figures 2.1b and c.

$$3KAlSi_3O_{8\,(S)} + 2H^+_{\,(aq)} + 12H_2O \Rightarrow KAl_3Si_3O_{10}(OH)_{2\,(s)} + 2K^+_{(aq)} + 6H_4SiO_{4\,(s)} \quad \text{(Equation 2.6)}$$

(K-feldspar) (muscovite)

$$KAl_3Si_3O_{10}(OH)_{2\,(s)} + H^+_{\,(aq)} + 9H_2O_{\,(l)} \Rightarrow 3Al(OH)_{3\,(s)} + K^+_{(aq)} + 3H_4SiO_{2\,(s)} \quad \text{(Equation 2.7)}$$

(muscovite) (gibbsite)

$$KAlSi_3O_{8\,(S)} + 8H_2O_{\,(l)} \Rightarrow Al(OH)_{3\,(s)} + K^+_{\,(aq)} + OH^-_{(aq)}\, 3H_4SiO_{2\,(s)} \quad \text{(Equation 2.8)}$$

(K-feldspar) (gibbsite)

(b)

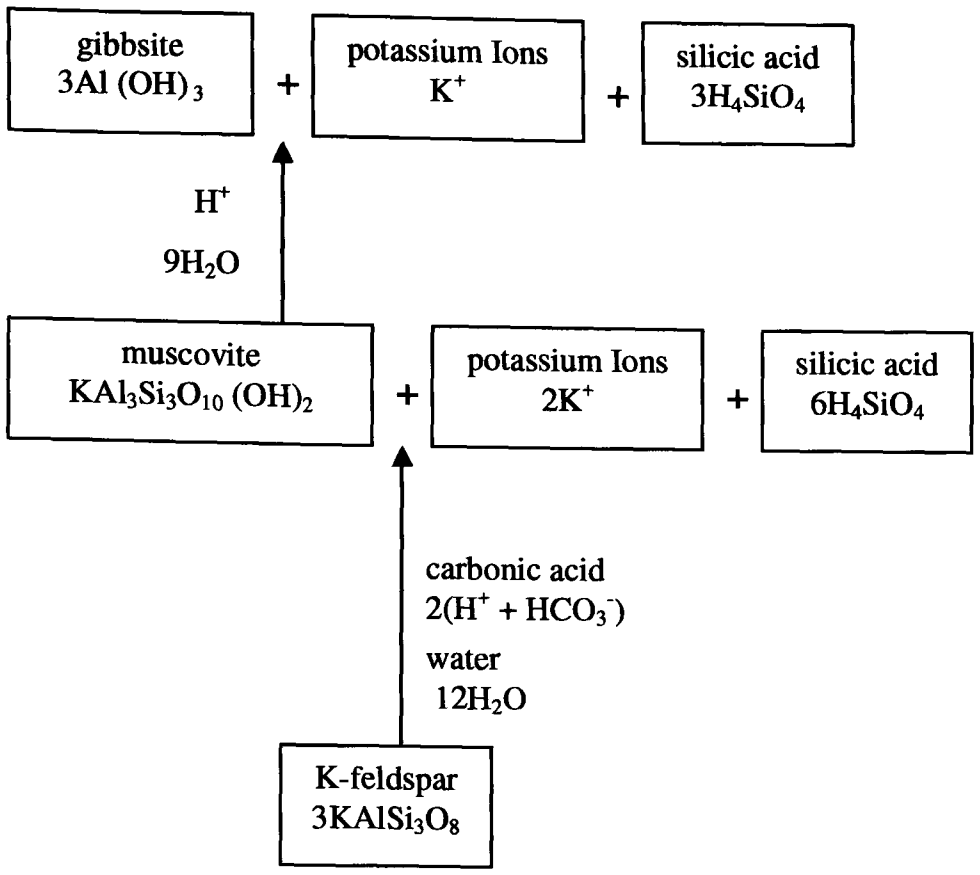

(c)

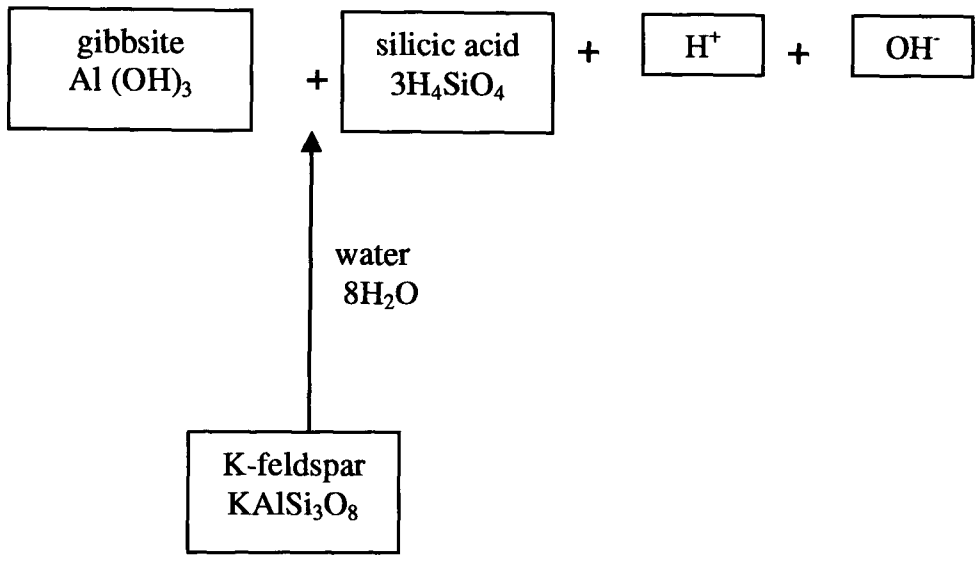

Figure 2.1b and c: Summary of the possible reactions for the dissolution of K-feldspar (Drever, 1997).

In general, at any particular silica activity, the most stable aluminum hydroxide or silicate will be the one with the lowest equilibrium dissolved aluminium concentration (Drever, 1997). The least soluble phase is the most stable as equilibrium is a state of minimum free energy. The stability relationship among some of the minerals in the system K_2O-Al_2O_3-SiO_2-H_2O system at 25°C of the equations 2.1 to 2.8 above can be represented by plotting activity of the ions a, in terms of log (a_{K+}/a_{H+}) and log a_{H4SiO4}) (Figure 2.2). The kaolinite field for example, represents solution composition in which kaolinite is the most stable of the minerals considered. These activities occur in the solution which is in contact with these minerals.

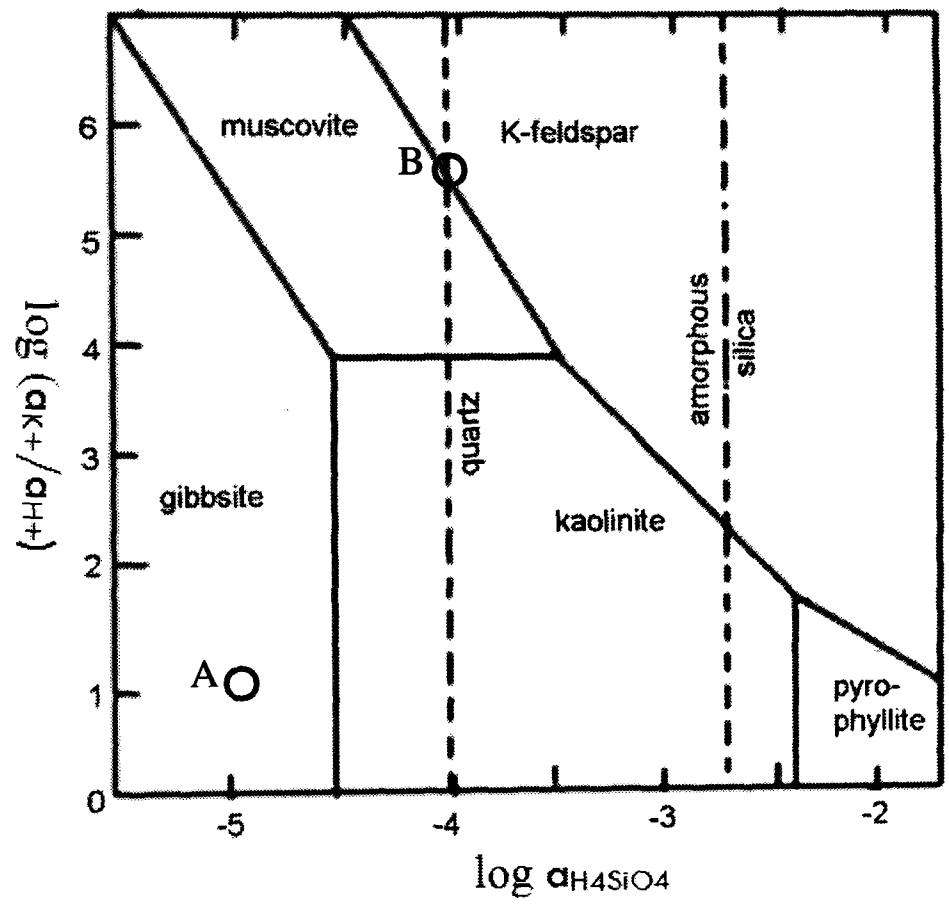

Figure 2.2: Stability relationship among minerals in the K_2O-Al_2O_3-SiO_2-H_2O system at 25°C (Drever, 1997). Acid rain would be expected to plot close to A and fluid in equilibrium with the minerals in a muscovite granite would lie close to B. It will be shown later that the mineralogical zonation in the profiles in the top down: gibbsite, gibbsite + kaolinite, ultimately to granite correspond to the expected evolutionary path of a down-ward percolating fluid, consistent with the stability relationships.

Quartz is the most resistant to weathering in granite and its hardness and absence of cleavage helps deter the attacks from weathering agents. Quartz grains are present even in the most weathered samples in the present study. K-feldspar and plagioclase however, show observable depletion as weathering progresses and because of their considerable abundance in the fresh rock, their dissolution in the weathering of granite under tropical conditions is crucial, understandably the weathering of K-feldspar was one of the main objectives of this project.

2.2 Feldspars

2.2.1 Structure and nomenclature

Feldspars are framework silicates having a general formula MT_4O_8. Al and Si occupy the T sites while the M sites are occupied by Na^+, K^+ and Ca^{2+} with minor amounts of Rb^+, Sr^{2+} or Ba^{2+}. The basic building unit of the framework is a four-membered ring of Si-O or Al-O tetrahedra. Each tetrahedron is centered by a silicon or aluminium atom collectively denoted as T atoms (Smith and Brown, 1988; Deer et al, 1992; Putnis, 1992). For monovalent M (Na and K), one of the T atoms is Al while for divalent M (Ca and Ba), two T atoms are Al, giving end members having the chemical formula: orthoclase ($KAlSi_3O_8$), albite ($NaAlSi_3O_8$) and anorthite ($CaAl_2Si_2O_8$). The members of the feldspar group of minerals are the most abundant constituents of crustal igneous rocks.

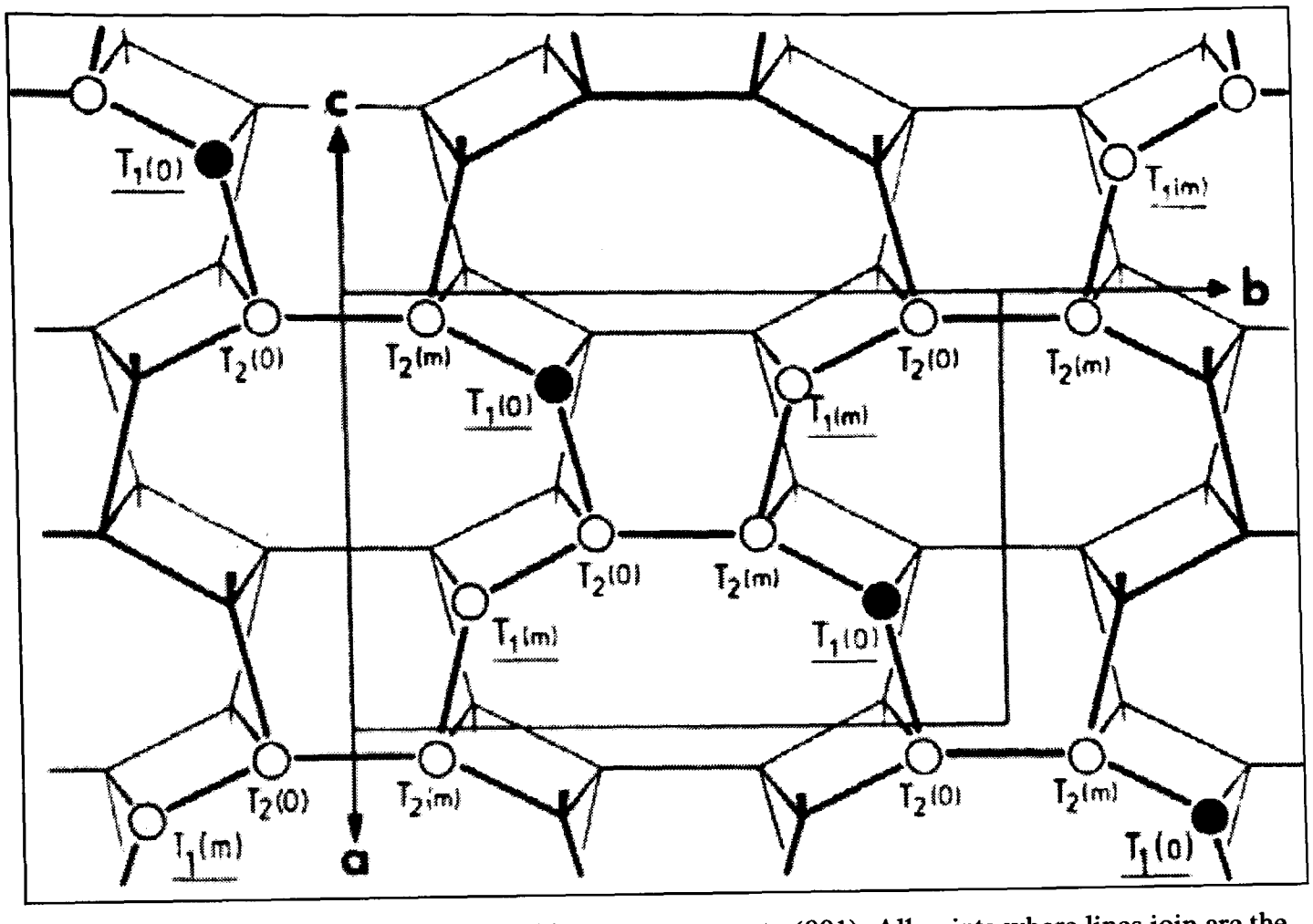

Figure 2.3. Idealized projection of the feldspar structure onto (001). All points where lines join are the centers of Si-O or Al-O tetrahedral (T-sites). The structure is idealized, with monoclinic symmetry. In a fully disordered structure, Al_3^+ (solid circles) and Si_4^+ (open circles) would be distributed randomly on T sites (the oxygen ions are not shown). However, the structure showed is fully ordered, with all Al_3^+ on a site called T1(0), forming a chain in the [110] direction. The equivalent [1$\bar{1}$0] chain contains no Al, and the mirror symmetry is lost. In a real structure, ordering would be accompanied by relative twisting of the tetrahedra, and the unit cell would be triclinic. (Ribbe, 1983)

To understand the order-disorder structure of feldspar, figure 2.3 is referred. Every point where lines join is the centre of a Si-O or Al-O tetrahedron. In alkali feldspars, the Si:Al ratio is 3:1. At high T, the Si and Al ions are arranged randomly (are disordered) over four equivalent tetrahedral sites labelled by convention $T_1(0)$, $T_1(m)$, $T_2(0)$ and $T_2(m)$. (Parsons and Lee, 2005). High sanidine is almost fully disordered, but orders during slow cooling to produce partially ordered low sanidine by diffusion of Al from T_2 to T_1 sites. Further ordering leads to development of triclinic polymorph microcline, usually easily recognised in thin section by its "tartan" twinning. The monoclinic symmetry is

broken and the structure becomes triclinic because Al diffuses into $T_1(0)$ sites (shown by black atoms in Figure 2.3). Although the structure is drawn with monoclinic symmetry, in reality this ordered framework would give rise to a triclinic cell by slight relative twisting of the tetrahedra. The monoclinic-triclinic symmetry change in albite-rich alkali feldspars does not involve diffusion of framework ions, but is caused by tilting of Si-Al-O tetrahedral. It is called "shearing" or "displacive" phase-transition and is instantaneous and unquenchable. In sanidine, the symmetry changes leading to microcline is an order-disorder transformation, which is relatively slow. Because high albite is triclinic at the onset of ordering, diffusion of Al into $T_1(0)$ from T_2 and $T_1(m)$ sites starts at high temperature *T* and takes place by a one-step process. In albite, the symmetry change from monoclinic to triclinic occurs by shearing whether it is ordered or not. In K-feldspar (sanidine) it occurs only by ordering Therefore, it is fast in albite and slow in K-feldspar.

The degree of order depends on temperature of crystallization and thermal history. In situations where exsolution (see section on exsolution) has not led to significant phase separation an alternative nomenclature based on disordered and ordered feldspars was proposed by Smith and Brown, (1988). In the dry An-Ab-Or system at low pressure, based on their symmetry, three fields of disordered disordered feldspars are shown (Figure 2.4a). They are monoclinic on growth and at room temperature (M), triclinic on growth and at room temperature (T) and monoclinic on growth and triclinic at room temperature (M→T). The stippled zone represents where the Or-rich feldspars can crystallize with monoclinic symmetry, at very high *T* only, close to, or above crystallization temperatures of most magmas at or near the surface of the earth. The proposed nomenclature for disordered ternary feldspars is given in figure 2.4b). High-temperature feldspars will change through Al,Si ordering when there is sufficient time during the cooling process or following fluid-feldspar reactions. The proposed nomenclature for ordered ternary feldspars is given in figure 2.5. The phase transition in Si-Al ordering is slow and disordered crystals often persist metastably at low temperature.

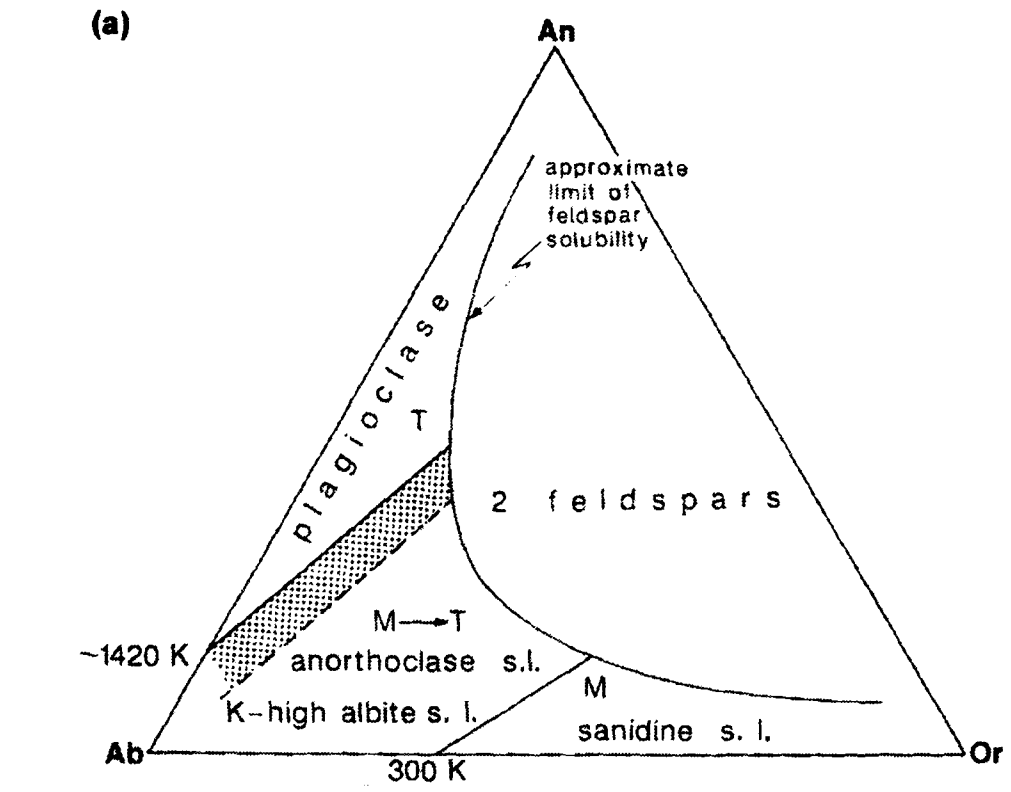

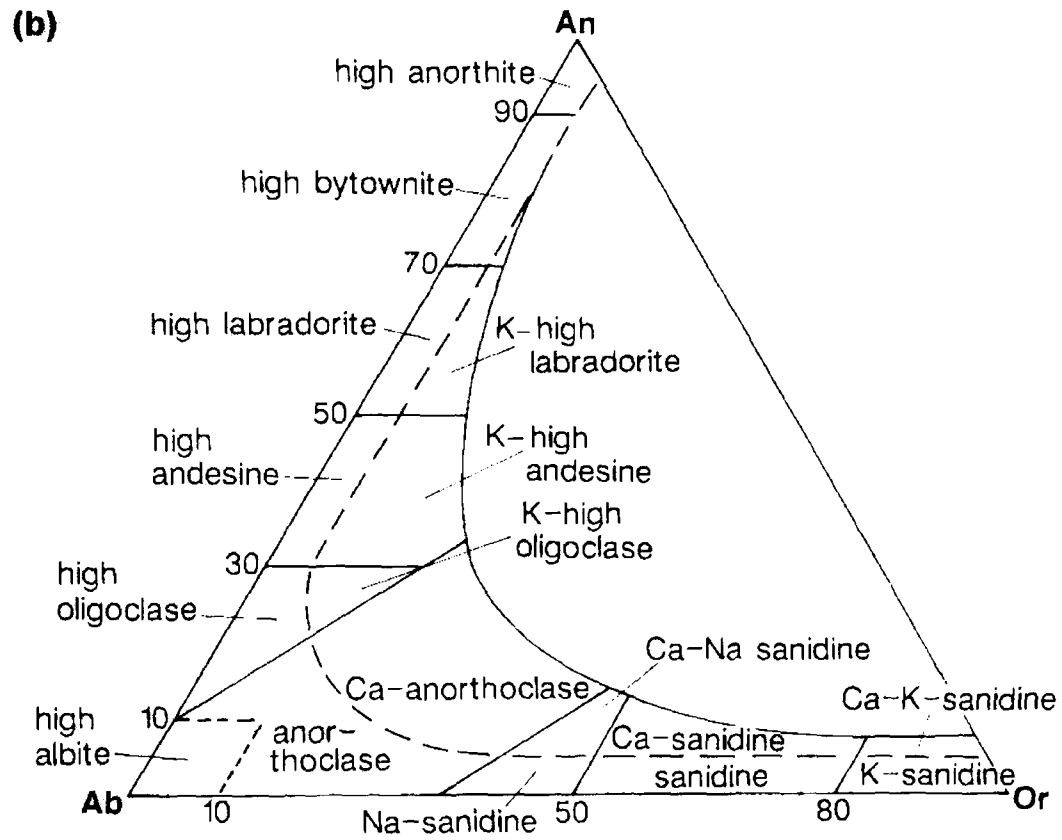

Figure 2.4. **(a)** Approximate limit of feldspar solubility at low pressure showing nomenclature of disordered feldspars. **(b)** Proposed nomenclature for disordered ternary feldspars. (Smith and Brown, 1988)

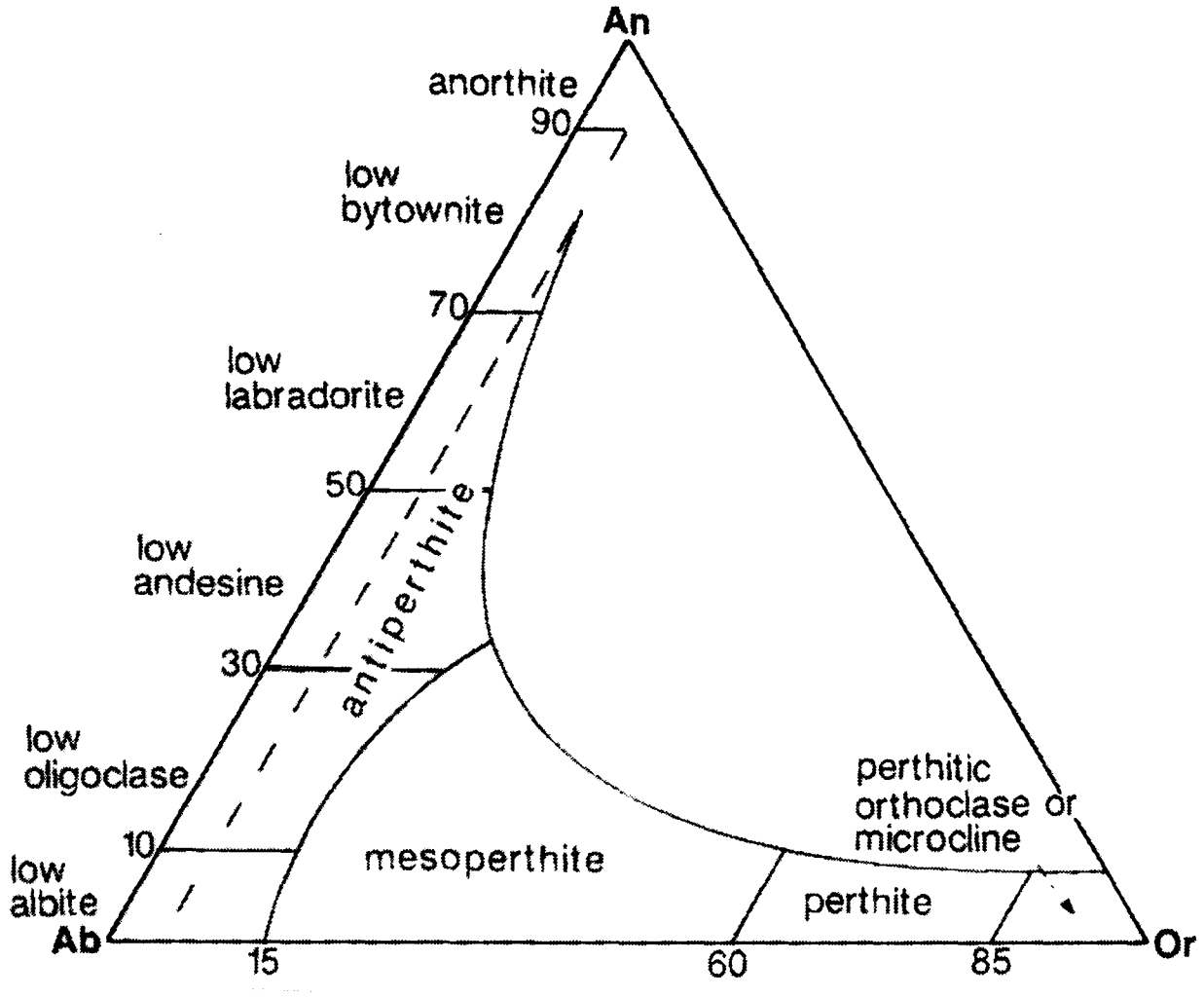

Figure 2.5. The proposed nomenclature for ordered ternary feldspars. (Smith and Brown, 1988).

2.2.2 Phase Equilbria and behaviour

The phase diagram of binary alkali feldspar (Ab-Or) was originally presented as given in Figure 2.6 which shows phase relationship in hypersolvus rocks in which the liquidus was determined by finding the temperature at which the last crystals disappeared and the solidus was when the first liquid appeared (Brown and Tuttle, 1950). The solvus on Bowen and Tuttles diagram was a reconnaissance. A revised solvus was determined at 0.1GPa by Smith and Parsons (1974) (Figure 2.7) and at > 1.0GPa by Goldsmith and Newton (1974).

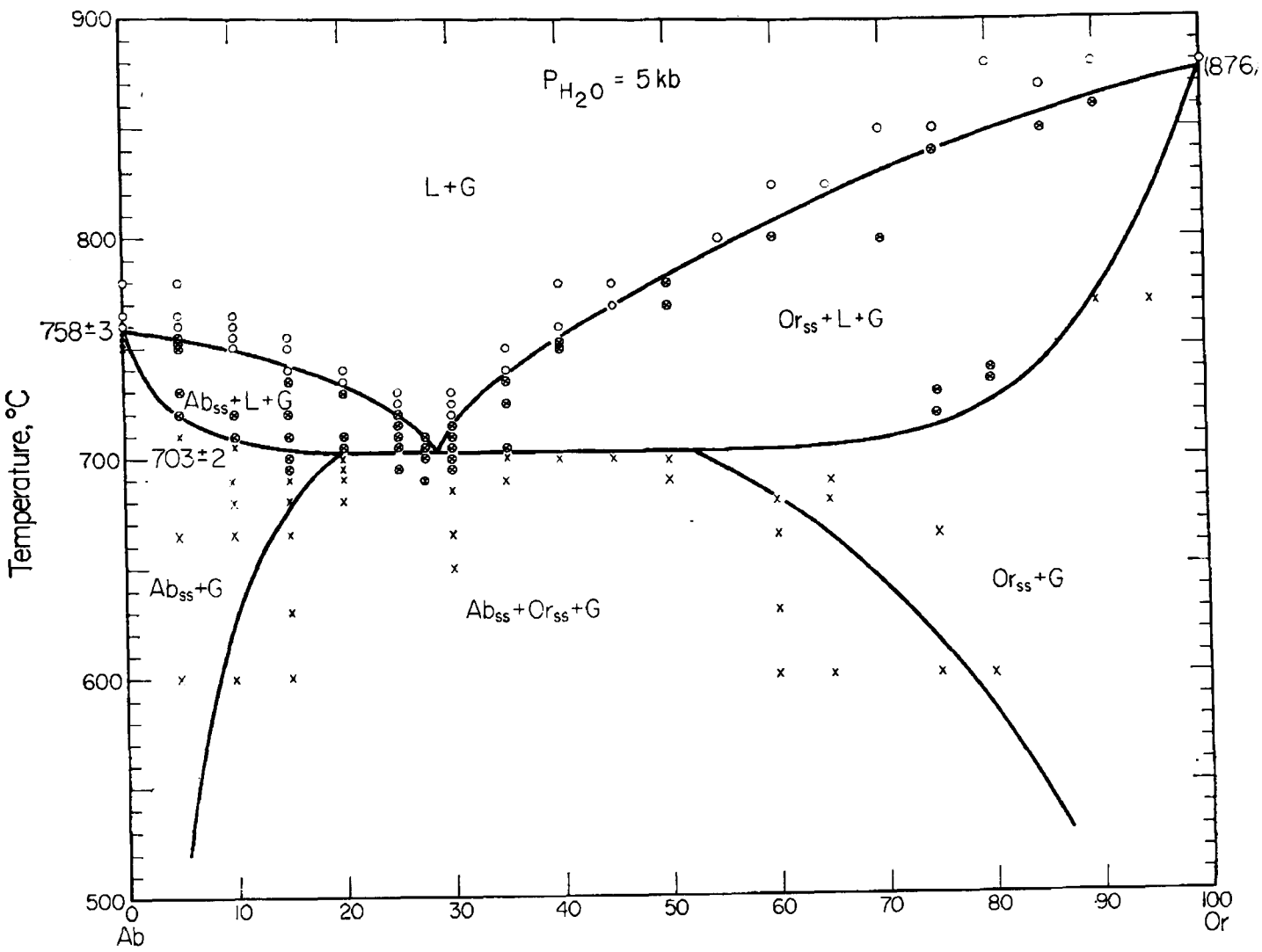

Figure 2.6. Equilibrium diagrams of the system AB-Or-H_2O at 5 kb, projected from H_2O onto the anhydrous join. Ab=albite, Or=K feldspar, SS = solid solution, L=liquid, G=gas. (Morse, 1970). The system is anorthite-free. Adding anorthite has the effect of making the solvus wider.

At low temperature, a mechanical mixture of low albite and microcline is thermodynamically stable mixture for intermediate composition as in (Na, K)$AlSi_3O_8$ (Brown and Parsons, 1989). At higher temperature above the solvus, growth produces albite-sanidine solid solutions (Figure 2.7a).

Subsolidus relationships in plagioclase are complex (Figure 2.7b) but because of charge linkage between (Ca + Al) and (Na + Si), which enormously shows diffusions, they are almost always sub-optical in scale (Smith and Brown, 1988).

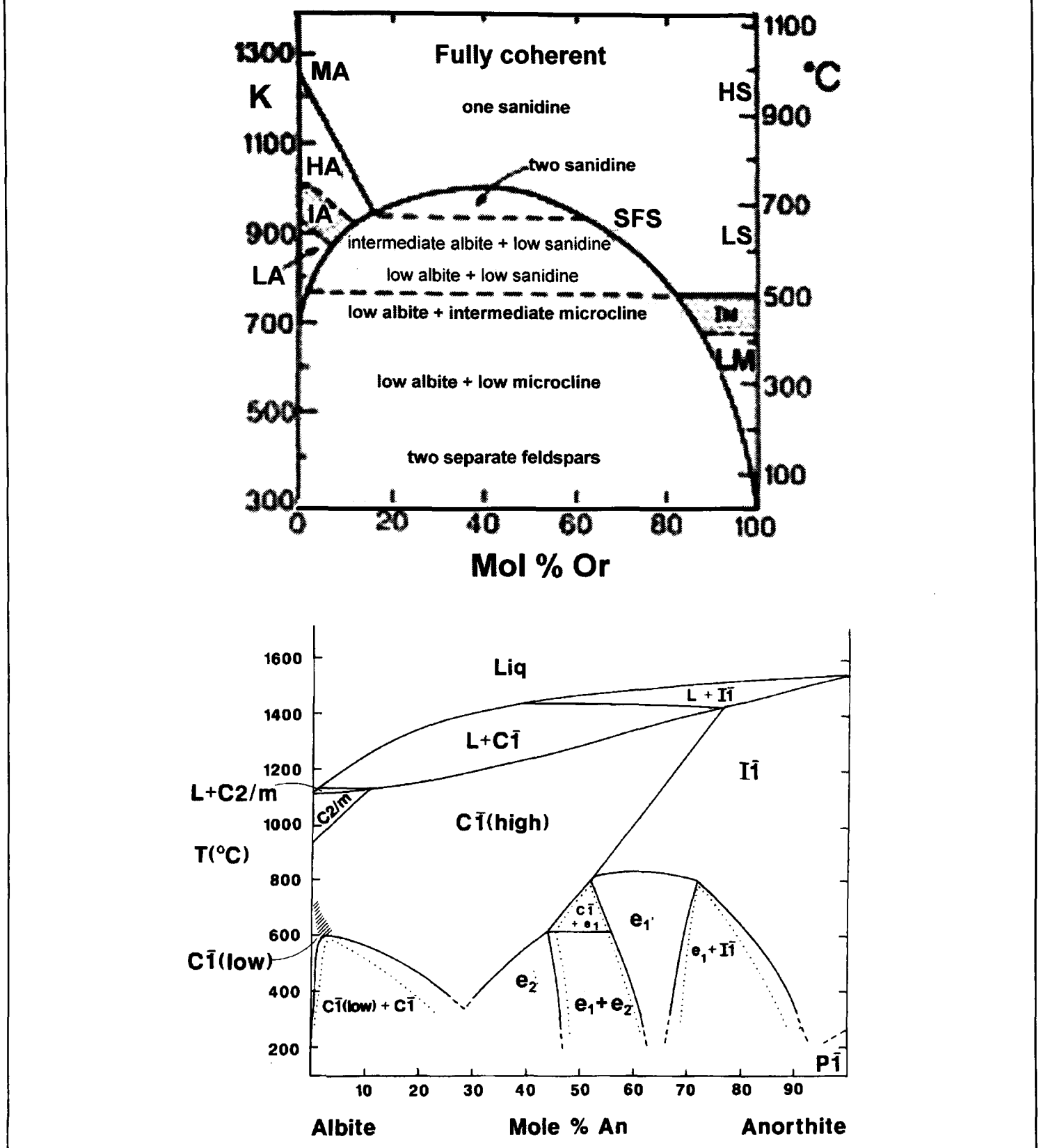

Figure 2.7. **(a)** Phase diagram for An-free alkali feldspar under complete incoherent equilibrium at low pressure. Note that this diagram is estimated for feldspars with an equilibrium degree of Si, Al order (Brown and Parsons, 1989). **(b)**: proposed equilibrium phase diagram for plagioclase at low pressure The topology is based on experimental data for some of the order/disorder transition, including the conclusion that e_1 structure has an equilibrium field stability (Carpenter, 1994)

2.2.3 Shearing

In a very rapid cooling situation, the crystals cool too fast to either exsolve or order. However, when an albite-rich alkali feldspar passes the shearing transformation line, the crystal structure changes from monoclinic to triclinic by shearing of the monoclinic cell. This is a non-quenchable process and this phase transition also leads to cross-hatched twinning which disappears reversibly on heating. The shearing phase transition from monoclinic albite to triclinic anorthoclase is instantaneous, compared to the slow, diffusive situation in the ordering-disordering process.

2.2.4 Exsolution

At temperatures above the solvus curves Na and Ca ions can mix freely to give a stable solid solution. As the temperature decreases, the solid solution becomes unstable and the alkali cations will diffuse through the Si, Al-O framework or the feldspar will recrystallize to form an intergrowth of two phases with compositions defined by the solvus . In alkali feldspars, such intergrowths are generically called perthite. Perthite senso stricto should be used for crystals with Or-rich bulk compositions, Ab-rich bulk compositions are called antiperthites, and feldspars with roughly equal proportions are called mesoperthites. In hypersolvus plutonic rocks, mesoperthitic intergrowths are formed following slow cooling whilst in subsolvus rocks, as in the case of Malaysian calc-alkaline granites, separate plagioclase and K-feldspar phases grow initially on the strain-free solvus, subsequently forming in principle, antiperthites and perthites respectively. Because the solvus is asymmetrical, and much steeper at the Ab-rich side, antiperthites are usually extremely fine scale, or not present at all in granitic feldspars. Mesoperthites are intergrowths wherein there is no obvious host as both phases are present in about equal proportions. In perthites, K-feldspars form the host and albite as the minor phase while antiperthites are vice-versa. During the diffusion of Na and K atoms to form lamellar regions, the aluminosilicate framework may remain unbroken giving 'coherent' intergrowths. The framework flexes to accommodate the difference in cell dimensions which introduces coherency strain (Smith and Brown, 1988).

2.2.5 Feldspars in Igneous rocks

Development of feldspars in igneous rocks occurs in 3 stages (Parsons, 1984). The first stage is the magmatic stage where crystals grow from melt. In this stage, nucleation and growth of feldspar with high Si, Al disorder occurs. Both growth and partial dissolution are involved in situations where crystals are in contact with different liquids during magma mixing. Preservation of zoning in plagioclase is a result of Ca-Al and (Na, K)-Si coupling and very slow Si, Al diffusion. Low water content of the liquid leads to hypersolvus crystallization, high P_{H2O} leads to simultaneous 'subsolvus' growth of plagioclase and alkali feldspar. The second stage is the subsolidus or post-magmatic transformation stage where coherent exsolution and development of regular 'strained controlled' cryptoperthite or microperthite occurs. Intracrystalline changes may occur during the subsolidus transformation stage, involving phase-transformation and exsolution microtextures. During this stage, the shape and orientation of the intergrowths is controlled by the minimization of coherency strain. The third stage is the development of deuteric or hydrothermal alteration. Deuteric alteration produces negligible changes in the bulk composition, whereas hydrothermal alteration may produce drastic changes, to the extent of a complete replacement of feldspar by other minerals. It is during this stage that feldspar fluid interactions occur and give rise to irregular, coarse patch and vein perthites, which are largely incoherent, and the associated development of turbidity caused by micropores (Walker, Lee and Parsons, 1995).

2.3 Dissolution of feldspars

2.3.1 Mineral dissolution

In chemical weathering below the soil surface under natural conditions, water operates as a reactant and transporting agent of dissolved and particulate components from land to catchment areas. Weathering of minerals starts with the exposure of the fresh mineral surfaces to weathering agents. To study the mechanism of dissolution of mineral surfaces, one approach is to consider the mass transfer of reactants and products in the

solid phase (the so called 'transport controlled mechanism') and the other is to consider the reactions controlled by surface processes and the related detachment of reactants (the 'surface-controlled mechanism') (Berner,1978; Stumm and Morgan,1996; Drever,1997).

Transport-controlled mechanism

In the transport-controlled mechanism, the concentration of solute adjacent to the mineral surface reflects the solubility equilibrium whereby the concentration decreases towards equilibrium with the bulk of the solution away from the mineral surfaces (Figure 2.8a and b). The dissolution rate of this mechanism can be calculated (equation 2.21a) and is faster when compared to the observed rate (Drever, 1997).

$$r = dC/dt = k_p t^{1/2} \ (Ms^{-1}) \qquad \text{(Equation 2.21a)}$$

and by integration, concentration can be calculated:

$$C = C_0 + 2\, k_p t^{1/2} \qquad \text{(Equation 2.21b)}$$

Where

r = dissolution rate (Ms^{-1})

C = concentration (M)

t = time (s)

k_p = reaction rate constant

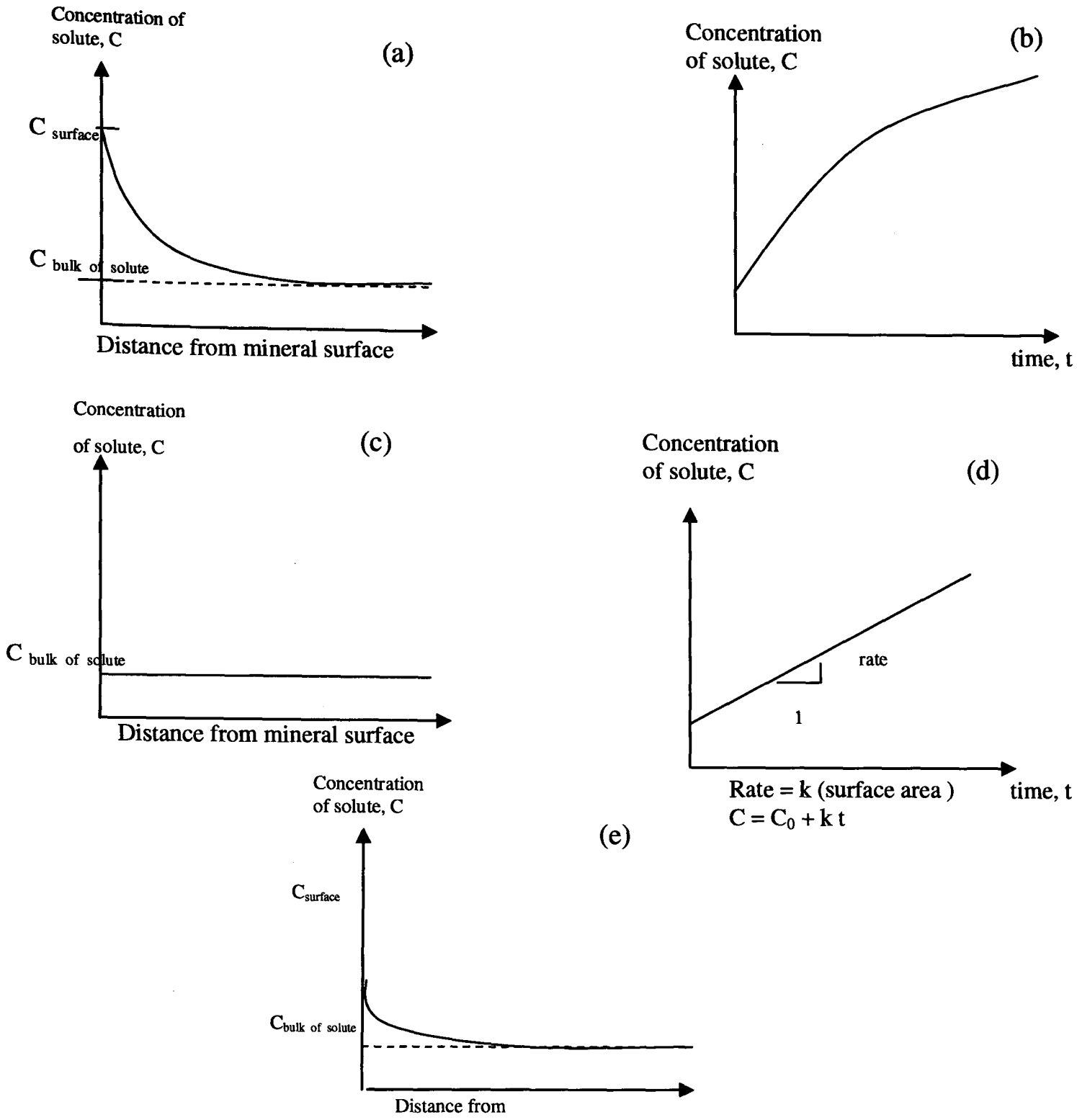

Figure 2.8.(a) Transport (or diffusion) controlled mechanism with high concentration gradient near the surface of the mineral (b) Concentration in terms of time for transport controlled reaction showing that the after a period of time, the increment of the solute concentration starts to level out. (c) surface controlled mechanism showing a constant concentration at any distance from the mineral surface (d) Concentration in terms of time for surface controlled reaction showing that the rate is not affected by flow velocities (e) Mixed control, where both transport (or diffusion) and surface reactions control the dissolution mechanism. The concentration gradient is not as steep as the pure transport controlled mechanism (Berner, 1978; Stumm and Morgan, 1996; Drever, 1997).

Surface-controlled mechanism

In the surface-controlled dissolution mechanism, the dissolution processes are so slow that the concentration of solutes adjacent to the surface is the same (but not necessarily in equilibrium as the dissolution process is still ongoing) as that within the bulk solution (equations 2.22a and b). Due to this there is no concentration gradient between the solute adjacent to the surface and the bulk solutions (Figures 2.8c and d). However, both transport and surface-controlled mechanism of dissolution may occur together and this is shown in Figure 2.8e, with the concentration gradient not as steep as the transport-controlled reaction.

$$r = dC/dt = kA\ (Ms^{-1}) \qquad \text{(Equation 2.22a)}$$

and by integration, concentration can be calculated:

$$C = C_0 + kt \qquad \text{(Equation 2.22b)}$$

Where

r = dissolution rate (Ms^{-1})

C = concentration (M)

t = time (s)

k = reaction rate constant

A = surface area (m^2)

Surface nucleation model

This model was originally proposed for growth but works equally well for dissolution (Figure 2.9). This model takes the basic thermodynamic approach by considering: (i) when a unit is removed from the crystal into an undersaturated solution, the energy released is $\Delta\mu = \mu_{liquid} - \mu_{solid}$, where $\Delta\mu$ is the change in chemical potential, which is related to the solution composition by $\Delta\mu = kT\ \ln(Q/K)$ where k is Boltmann's constant,

Q is the activity product and K is the equilibrium constant, and (ii) Silicate surfaces in aqueous solution have a positive surface free energy (σ), indicating the creation of surface area is thermodynamically unfavourable, and the energy required to increase the surface area by A equals $A\sigma$ (Blum, 1984). For feldspars, σ is estimated to be 500 ergs/cm^2 (Lasaga, 1986). This free energy will change for the formation of either a cluster on the surface by precipitation of atoms or a pit by the dissolution of atoms and a new surface area will be created.

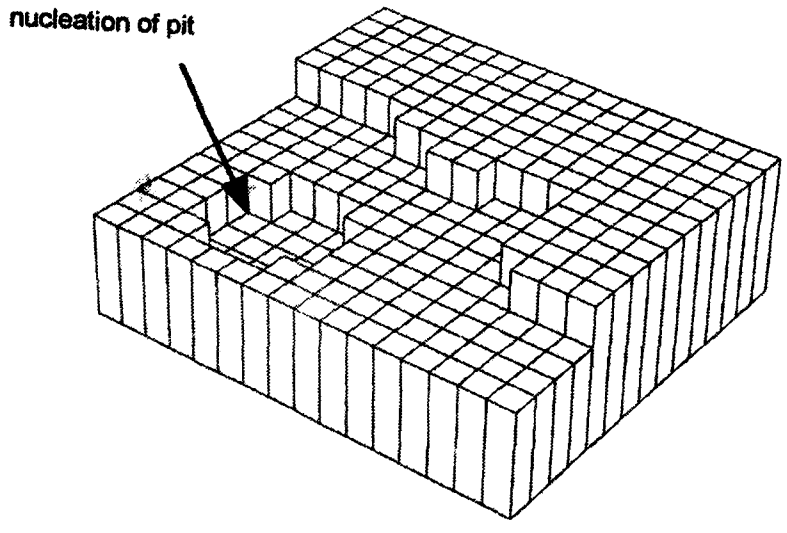

Figure 2.9. Schematic diagram of the surface nucleation model (Blum, 1994).

In an ideal crystal structure every unit cell is identical and with a specified shape, size, cell content and atomic arrangements (Putnis, 1992). However, in a real mineral there are always defects in these perfect arrangements. All crystals at temperature above absolute zero contain some point defects which are generally vacant atomic sites or impurity atoms. There might also be line defects or dislocations, where one part of the crystal is translated relative to the adjacent part due to stresses beyond its plastic limit. These dislocations are of two types: simple edge and screw dislocations, sometimes occurring in combination of several types of dislocations (Fig. 2.10). The dislocation can provide a surface topography for the dissolution processes (Fig. 2.10 f –k). and with high free energy because of unsatisfied bonds and local strain

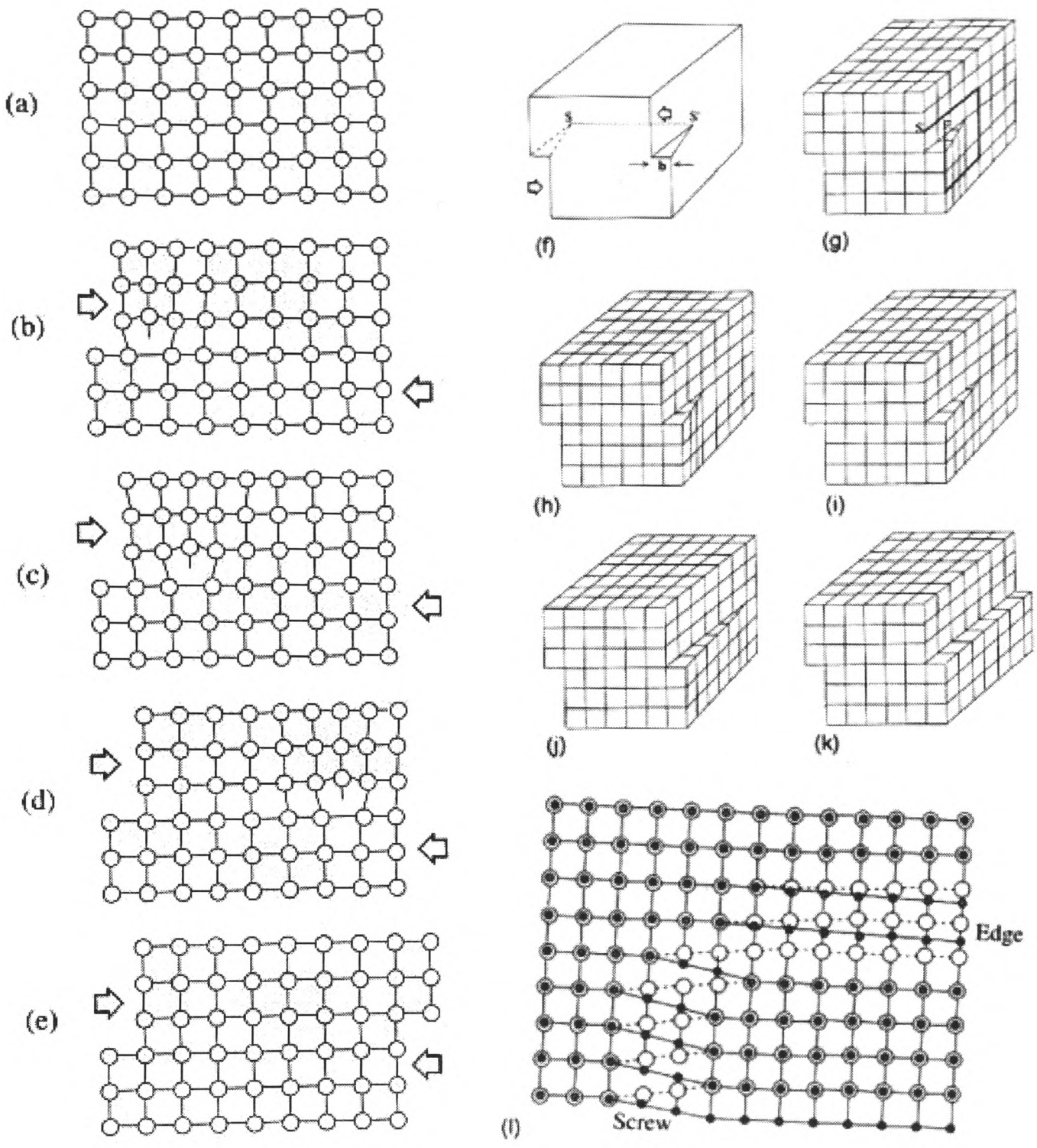

Figure 2.10. (a) to (e): Successive steps in the migration of a single dislocation during deformation. The arrows show the direction of the applied stress. (f) to (k): Screw dislocations. As the dislocation moves out of the crystal, slip steps are left on the surface. (l): Part of a dislocation loop in which an edge dislocation becomes a screw dislocation as the dislocation line turns through 90° (Putnis, 1992).

Dislocations can represent reactive sites and dissolution at these sites produces an intricate network of interconnected sub- μm microtubes which penetrate into the structure. (Figure 2.11)

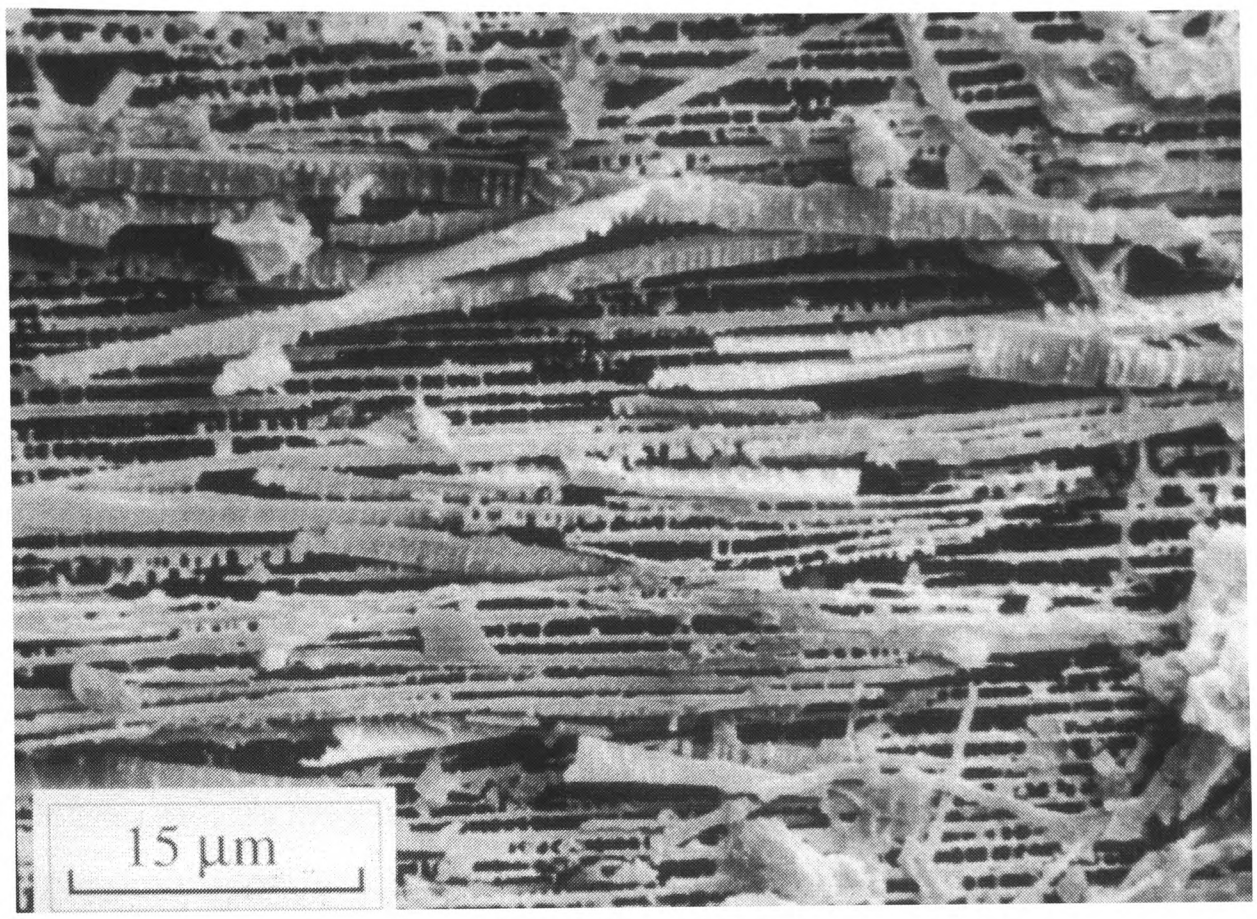

Figure 2.11. Entirely naturally weathered K-feldspar grains. The grain was etched by very acidic natural soil water. Almost all albite has dissolved leaving slots with wafers of dissolved orthoclase standing between them. You can still see signs of the tubes that formed down the dislocations (like Figure 2.18a). They get bigger as the albite dissolves (Figure 2.17). K feldspar grains are from Shap granite, North Cumbria, UK (Lee and Parsons, 1997)

The kinetics of mineral dissolution are controlled by many factors: mineral composition, pH, temperature, surface area, defect types and the solution composition including organic acids.

pH dependence

The pH dependence of the dissolution kinetics for far from equilibrium condition of most silicate minerals can be schematically represented as in figures 2.12a and b (Blum, 1994; Drever, 1994). In the acid region, the dissolution rate decreases with increasing

pH to a transition point whereby the rate is generally independent of pH. Above this transition pH, or in the alkaline region, the rate increases with increasing pH. The surface protonation of O and OH lattice sites accelerates the dissolution with decreasing pH (Helgeson et al, 1984; Stumm and Morgan, 1996). The protonation causes slow detachment of Al from the crystal which is coupled by the subsequent detachment of $Si(OH)_4$ species. At high pH, detachment of Si controls the overall silicate dissolution rates and at low pH, detachment of structure forming oxides other than silicon controls dissolution rates of multi-oxide silicates (Brady and Walther, 1989).

(a)

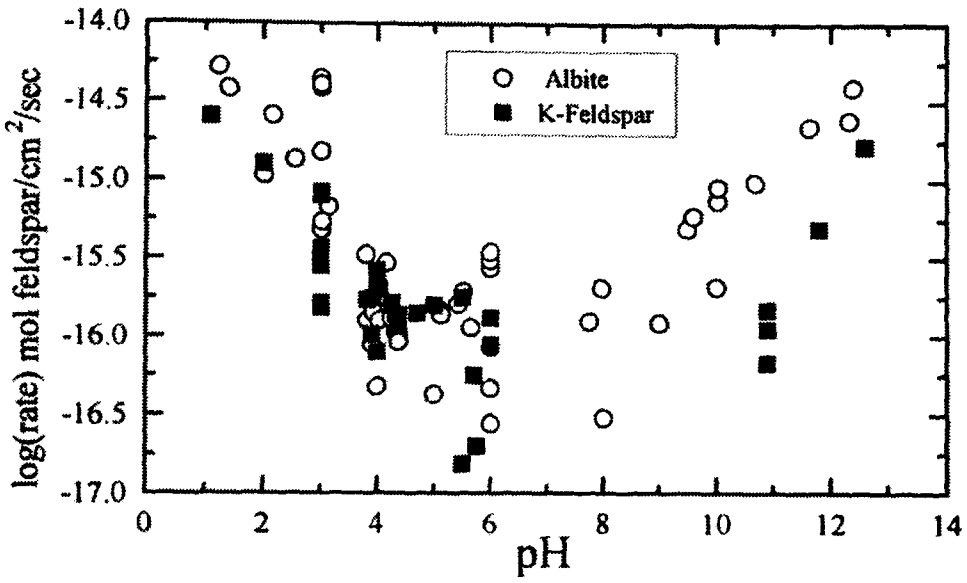

(b)

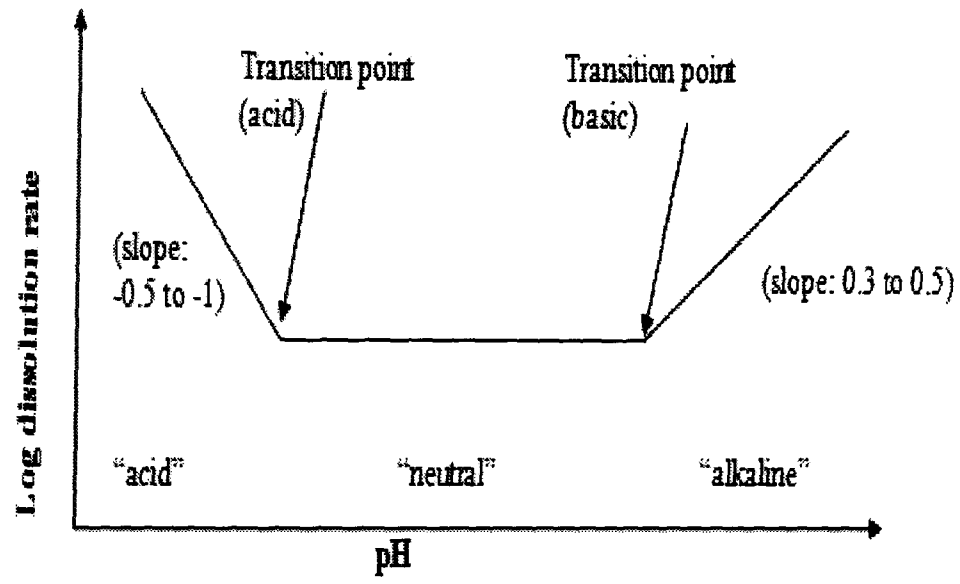

Figure 2.12: (a) Comparison of albite and K-feldspar dissolution rates as a function of pH (Blum, 1994). The data used were compiled from several publications (b) Schematic relationship between pH and dissolution rate for silicate minerals (Drever, 1994).

Temperature dependence

Generally, reaction rates increase with increasing temperature (Langmuir, 1997). The relation between reaction rates, R and T can be related to the Arrhenius expression (Equation 2.23)

$$k = A_F \exp(-E_a/RT) \qquad \text{(Equation 2.23)}$$

on converting natural logs to common logs and at T_1 and T_2,

$$\log \frac{k_1}{k_2} = \frac{E_a}{2.303R} \left[\frac{1}{T_2} - \frac{1}{T_1} \right] \qquad \text{(Equation 2.24)}$$

where

k : rate constant,

E_a : activation energy

A_F : the 'A' factor which is independent of T

R : reaction rate

T: temperature (K)

The magnitude E_a is an important factor in the reaction mechanism. Reactions that involved the least making or breaking of strong bonds (aqueous dissolution, for example) have the lowest activation energy compared to reactions like solid-state diffusion in minerals at low temperature. (Table 2.1) (Langmuir, 1997). The effects of increasing temperature on the rates of dissolution of some silicate rocks and minerals are given in Figure 2.13. The dissolution rate of minerals increases as temperature increases. Generally, it is believed that the rate of reaction roughly doubled for every 100°C increase in temperature (Woods and Walther, 1983).

Reaction or process	Typical range of E_a values, (Kcal/mol)
Physical adsorption	2 to 6
Aqueous diffusion	<5
Cellular and life-related reactions	5 to 20
Mineral dissolution and precipitation	8 to 36
Mineral dissolution via surface reaction control	10 to 20
Ion exchange	>20
Isotopic exchange in solution	18 to 48
Solid-state diffusion in minerals at low temperatures	20 to 120

Table 2.1: Typical range of E_a values for some reactions or processes (Langmuir, 1997).

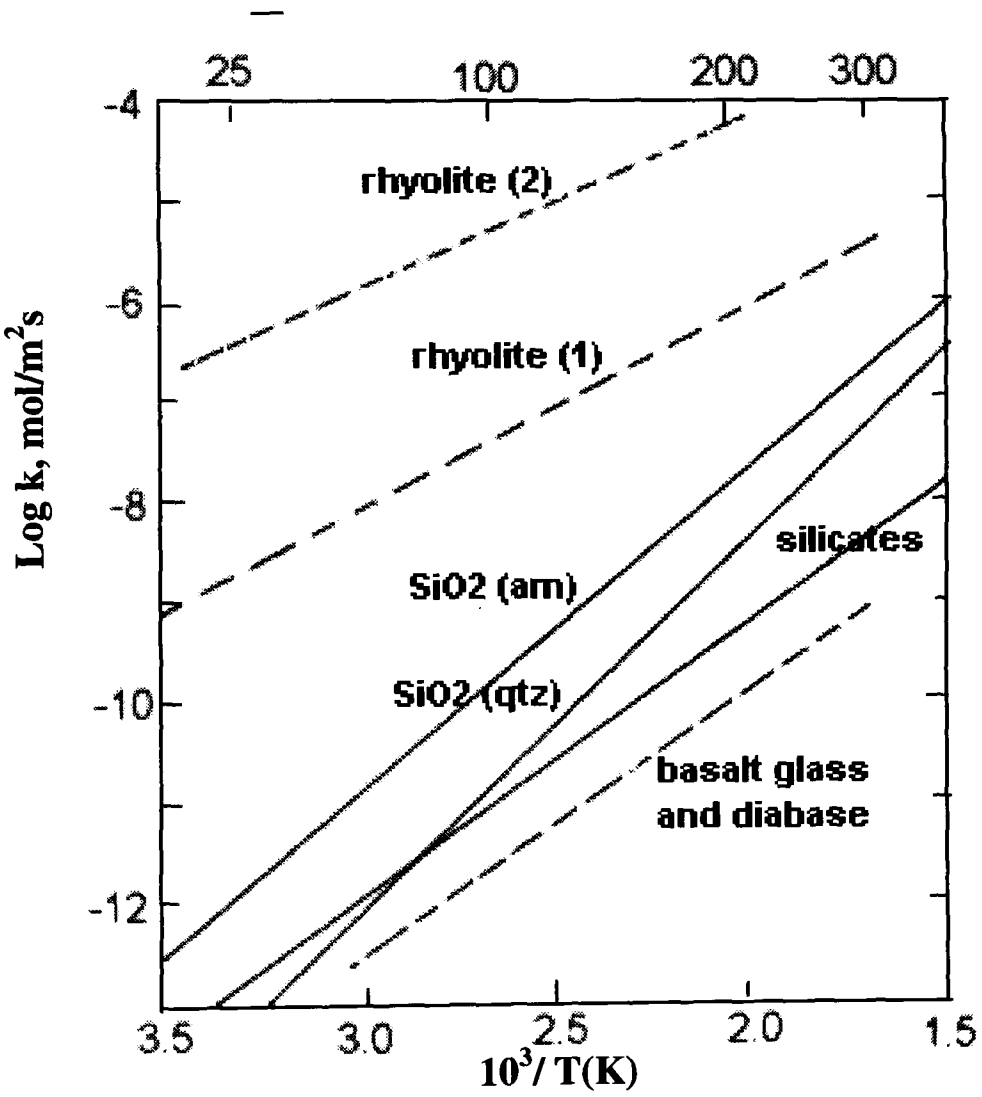

Figure 2.13: An Arrhenius plot of log k versus 1/T (K) for the solution rates of various silicate rocks and minerals. The two sets of lines (dotted and full) indicates that the data obtained from two different sources (Langmuir, 1997).

Leached layer hypothesis

The leached layer hypothesis proposed by Wollast, (1997) and Paces, (1973) states that the dissolution of minerals leads to non-stoichiometric release of elements from the mineral structure, forming a protective layer on the outer part of grains. This layer restricts diffusion of dissolved species from the bulk mineral to the solution. Evidence for and against this hypothesis are given here.

Muir and Nesbitt, (1992) used secondary ion mass spectrometry (SIMS) to study a depth profile (a flow-through experiment with the HCl on labradorite at 23°C and pH 4) and found that Ca and Al were removed from the labradorite at different rates. The cation concentration of the solution affected the relative proportions of Ca and Al removed from the solid. Dissolved Al decreased the relative amount of Al removed but dissolved Ca had no observable effect on the relative release rates of Ca and Al. The authors also concluded that both Ca and Al were removed in preference to Si such that a silica-rich (amorphous SiO_2) was formed (Zone A) at the outer surface and a narrow zone (B), representing a cation exchange zone, separating the fresh plagioclase (C) from the altered layer A (Fig 2.14 left). Hellmann et al, (1990) concluded, based on their flow-through experiments on albite (with the HCl and $Ba(OH_2)$ solutions representing the acids and basic medium and at 25°C/pH 0.57 to 10.2, that leached zones depleted in Na, Al and O developed during the initial, incongruent phase of dissolution. Their X-ray photoelectron spectroscopy (XPS) data suggested that leaching of Al was to greater depths than Na (Fig. 2.13 right).

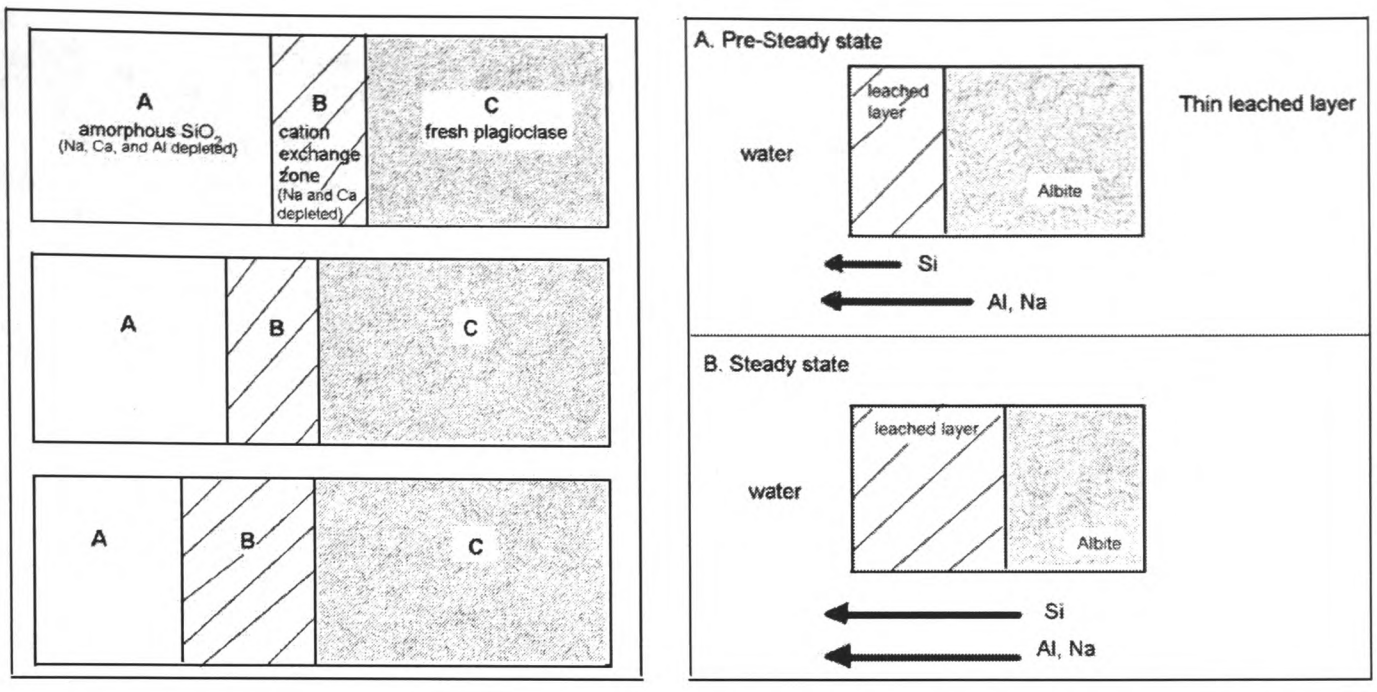

Figure 2.14: (Left) Simplified view of the altered layer formed in response to dissolution in aqueous HCl. "A" indicates the siliceous surface layer, "B" shows the cation exchange zone and "C" represents the unleached plagioclase (Muir and Nesbitt, 1992). (Right): A simplified representation of leached layer formation. (A) Before steady-state is attained, the flux of Na and Al from the surface is greater than the flux of Si because Na-O and Al-O bonds hydrolyse more rapidly than Si-O bonds. The layer thickness increases during this initial period, (B) the attainment of a steady state leached layer requires that Na-O, Al-O and Si-O detachment reactions occur at equal stoichiometric rates. (Hellmann et al, 1990)

At a later stage, Hellmann (2003) proposed a reprecipitated layer instead of the leached layer that he favoured earlier (Hellmann et al, 1990). In flow-through experiments done on labradorite under pH 1 at 22°C, an altered zone was 500nm thick with an interface between amorphous altered zone and crystalline labradorite that is notably sharp was found (Figure 2.15). The zone was depleted of interstitial cations (Ca, Na, K) and Al, whereas it was rich in H, O and Si (measured using secondary ion mass spectrometry, SIMS). It was proposed that the sharp interface was due to interfacial dissolution-reprecipitation, not preferential leaching of cations and interdiffusion with H^+.

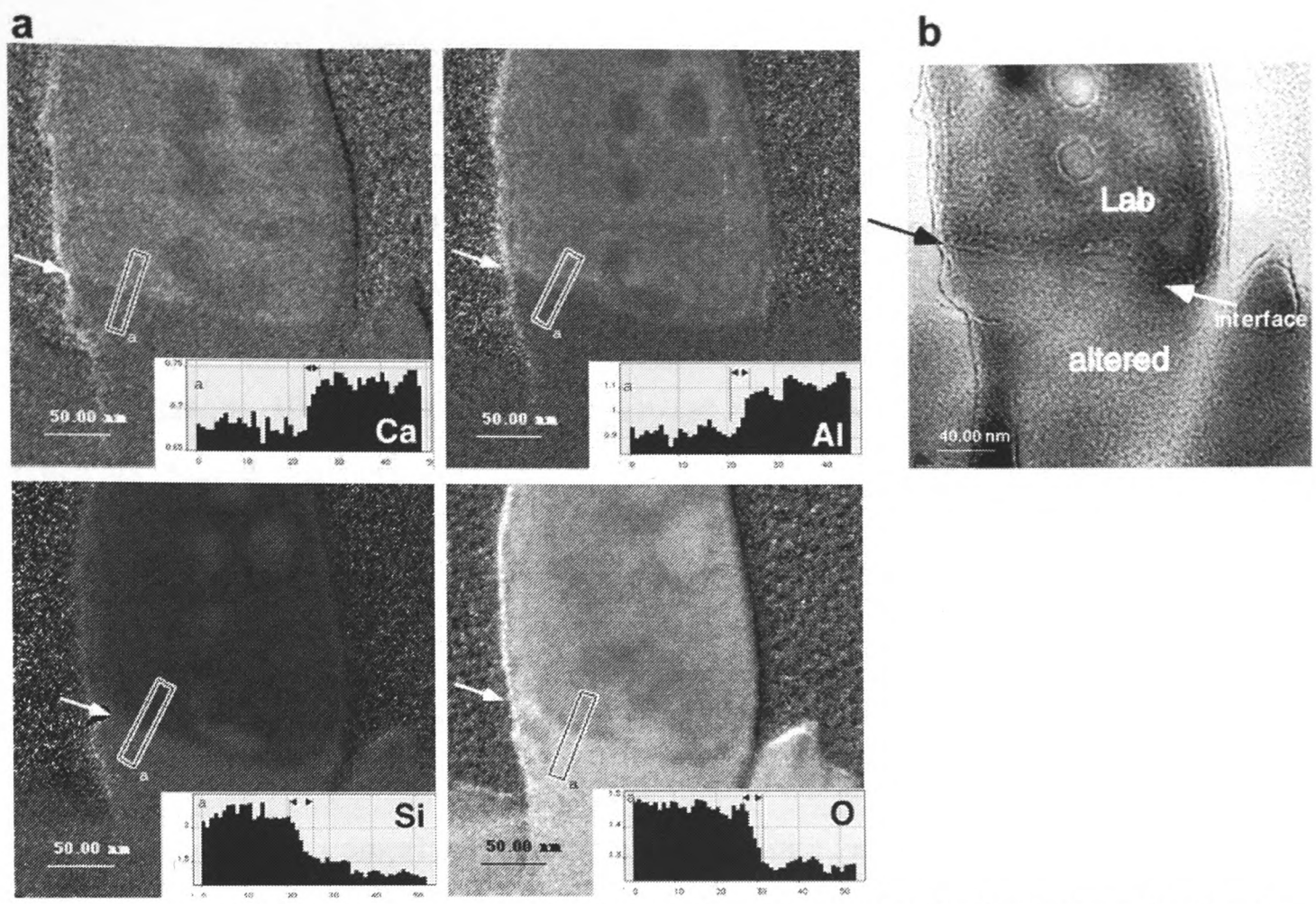

Figure 2.15(a and b): Ultrathin section of labradorite feldspar showing the interfase between the altered zone (bottom) and the unaltered zone (top). The lamellar nature of the thin section is an artefact on the ultramicrotome technique. An energy-filtered transmission electron microscopy (EFTEM) chemical maps of the interfacial boundary (white arrows) separating the altered and altered zones. Qualitative concentrations of Ca, Al, Si and O shown (brightness proportional to concentration). Ca and Al are depleted in the altered zone whereas Si and O re enriched. Inset shows the respective chemical profiles (left to right from altered to non-altered zones. (Hellmann et al, 2003)

Berner and Holdren, (1979), examined the surface morphology using SEM and X-ray photoelectron spectroscopy of sodic plagioclase and potash feldspar from 4 different soils and concluded that the dissolution of feldspars during weathering was controlled by selective chemical reaction at the feldspar-solution interface and not by uniform diffusion through a protective surface layer.

2.3.2 Feldspar dissolution

In this subsection, the discussion will be on the intragranular microtextures (such as exsolution lamellae) and microstructures (such as dislocations) on feldspar surfaces and its relation to weathering. For this purpose, those observed on the well-studied feldspar grains from Shap, in Cumbria, northwest England (Lee, Waldron and Parsons, 1995b; Lee and Parsons, 1995a, 1997) will be discussed as a basis for comparison with the feldspars studied in the present research. However, consideration must be given to the difference in the environment between the temperate climate (Shap) and the tropical climate (present research).

Alkali feldspar phenocrysts in the subsolvus Shap granite comprise pristine exsolution microtextures (cryptoperthites and microperthites). Microperthites are more abundant than cryptoperthites, comprising relatively coarse albite lamellae (c. 0.075-0.5 μm wide by many microns long) called film, in tweed orthoclase (Figure 2.16). Due to the relatively course lamellae, misfit between lattices of albite and orthoclase cannot be accommodated entirely by elastic strain and edge dislocations have formed along the exsolution interfaces. The immediate volume around a dislocation contains excess energy emanating from lattice distortion induced by the dislocation (Lasaga and Blum, 1986) and from the core energy in the dislocation. When a mineral surface is in contact with a solution, this high strain area will offer a favourable site for dissolution. Upon dissolution, the strain energy is released lowering the total free energy of the system.

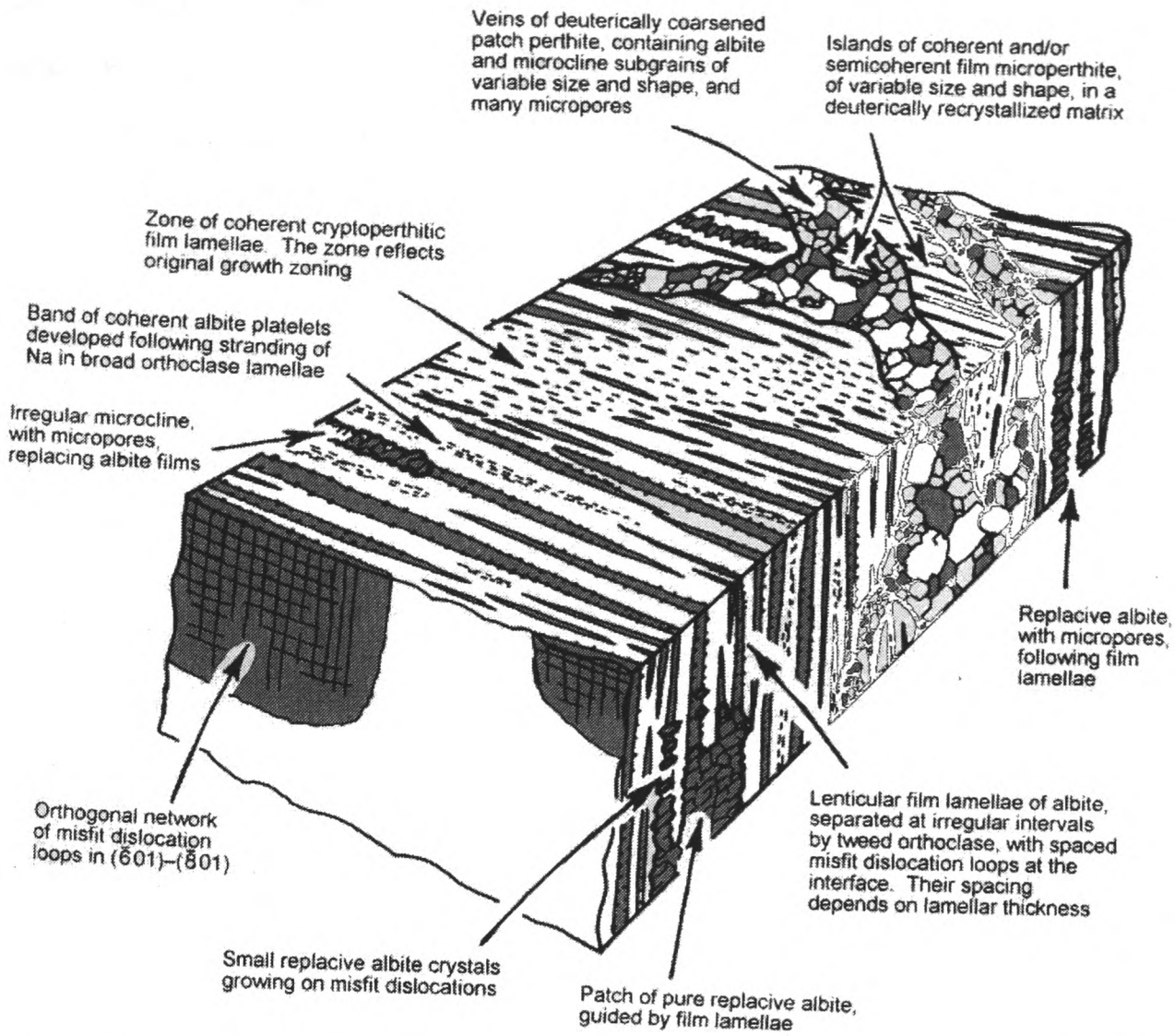

Figure 2.16: Generalised sketch of an ~100-μm-long cleavage fragment of an alkali phenocryst from Shap granite, a typical calc-alkaline granite as it might occur as a detrital fragment. (Parsons et al, 2005).

Several researchers have compared the etching of feldspar surfaces during natural weathering with etching in laboratory acids such as HF-H_2SO_4 (Berner and Holdren, 1977, 1979; Waldron, Lee and Parsons, 1994; Lee and Parsons, 1995a; Lee, Waldron and Parsons, 1995b). Etching alkali feldspar cleavage fragments with hydrofluoric acid vapour dissolves Or- rich feldspar more rapidly than Ab-rich feldspar and leaves the Ab-rich feldspar elevated in relief (Waldron, Lee and Parsons, 1994; Lee and Parsons, 1995a). The difference in relief between Or- and Ab-rich areas in a single feldspar crystal allows crypto- and microperthite textures and crystal defects such as micropores and dislocation microstructures to be imaged with secondary electrons in the SEM. Albite films between the edge dislocations however, dissolved at a greater rate than

orthoclase during natural weathering (Blum, 1994; Lee and Parsons, 1995a) and this discrepancy is a subject of discussions as mentioned by the authors . Lee and Parsons (1995a) provided alkali feldspar grains from Shap and their studies led to a schematic diagram showing the growth of etch pits (Figure 2.17). In the acid-etched semicoherent albite film, etch pits first developed in the interface between albite and orthoclase, grow faster in orthoclase but finally coalesce leading to grain collapse. In the naturally weathered film, the growth is faster in the albite before coalescence.

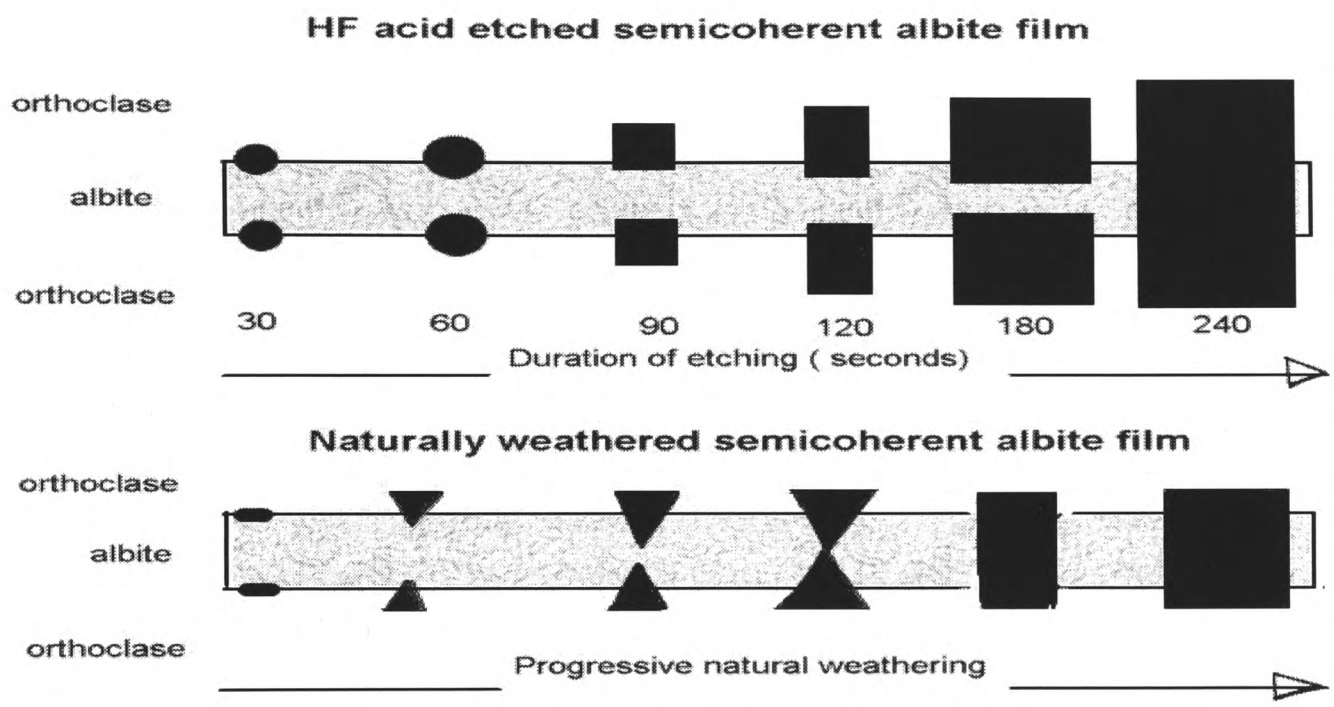

Figure 2.17: Schematic diagram showing the growth of etch pits in and around albite films on (001) microperthite surfaces both HF acid etching and natural weathering (Lee and Parsons, 1995a).

Rates of natural weathering are reported (based on the comparison between the flow-through experiments and the mass-balance measurement in watershed catchments areas) to be up to 3 orders of magnitude slower that those found experimentally (Paces, 1973; Velbel, 1989; Oelkers and Schott, 1995; Lee, Hodson and Parsons, 1998). Velbel (1989) proposed that this, among others, is most likely due to loss of reactive surface to the formation of etch pits in naturally weathered feldspars, and inhomogeneous access of reactive fluids to those surfaces. However, this is very unlikely as the presence of etch will effectively increase the reactive surfaces. Lee and Parsons (1995a) noted that for

Shap feldspars, even before the grains enter the soil, much of the most reactive parts of both the albite and orthoclase have already dissolved as shown by the naturally weathered fragment in Figure 2.18. The narrow mouth and throats of the etch pits can also be easily clogged by reaction products and materials. By comparing the rate of dissolution of experimentally and naturally weathered Shap alkali feldspars, Lee *at al.* (1998) made a conclusion that the dislocation density has a insignificant effect on the dissolution under laboratory conditions but is likely to be a highly important variable during early natural weathering.

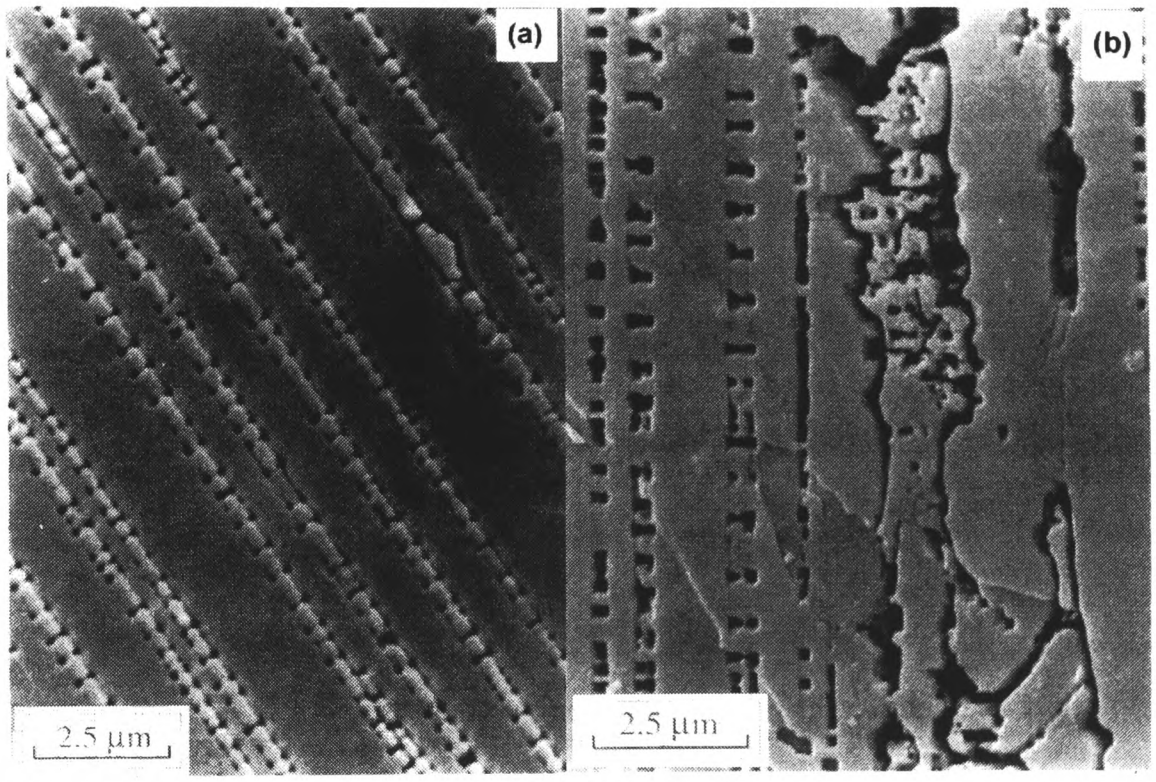

Figure 2.18. SE images of Shap alkali feldspar fragments, on the (001) cleavage surface of microperthite (a) unweathered fragment etched in HF acid vapour for 60s.: albite films are slightly raised relative to surrounding orthoclase and are straddled by numerous pairs of etch pits. (b) Naturally weathered fragment: albite are totally dissolved within the lamellae. The section to the right of the micrograph shows the miroperthite has been partially altered to patch perthite and the interface between them has etched to form a continuous channel. (Lee and Parsons, 1995a).

3. GEOLOGICAL BACKGROUND AND SAMPLING

Introduction

There are two categories of sampling groups used for this study. The first group of samples was taken from newly exposed cut slopes. Soils and rocks samples were taken at appropriate intervals vertically along the cut slope. The second sampling group was taken in boreholes. Again the samples were taken at appropriate intervals along vertical boreholes. In this chapter, the general geology of Peninsular Malaysia is introduced which will touch briefly on the ages and tectonic settings of the granites in Malaysia. The geology of each sampling location together with the sampling method will be discussed further in the following subsection.

3.1 General geology of Malaysia

3.1.1 Ages and Sedimentation

The oldest rocks in Peninsula Malaysia (Figure 3.1) are located in the northwest of the peninsular, comprising late Cambrian sandstone, quartzite and subsidiary beds of grit, siltstone and mudstone (Gobbett, 1972). In the west of Peninsula Malaysia, sedimentation began in late Cambrian and in the east, sedimentation commenced in the early Carboniferous together with widespread volcanism (Geological Survey of Malaysia, 1985). Low-grade regional metamorphism is common in Pre-Jurassic rocks. During the late Mesozoic, molasse-type deposits were deposited in some parts of the peninsula. Continental sedimentation followed in isolated basins during Tertiary. Quaternary deposition is prominent especially in coastal areas and are present up to 15m above mean sea level along the coastal.

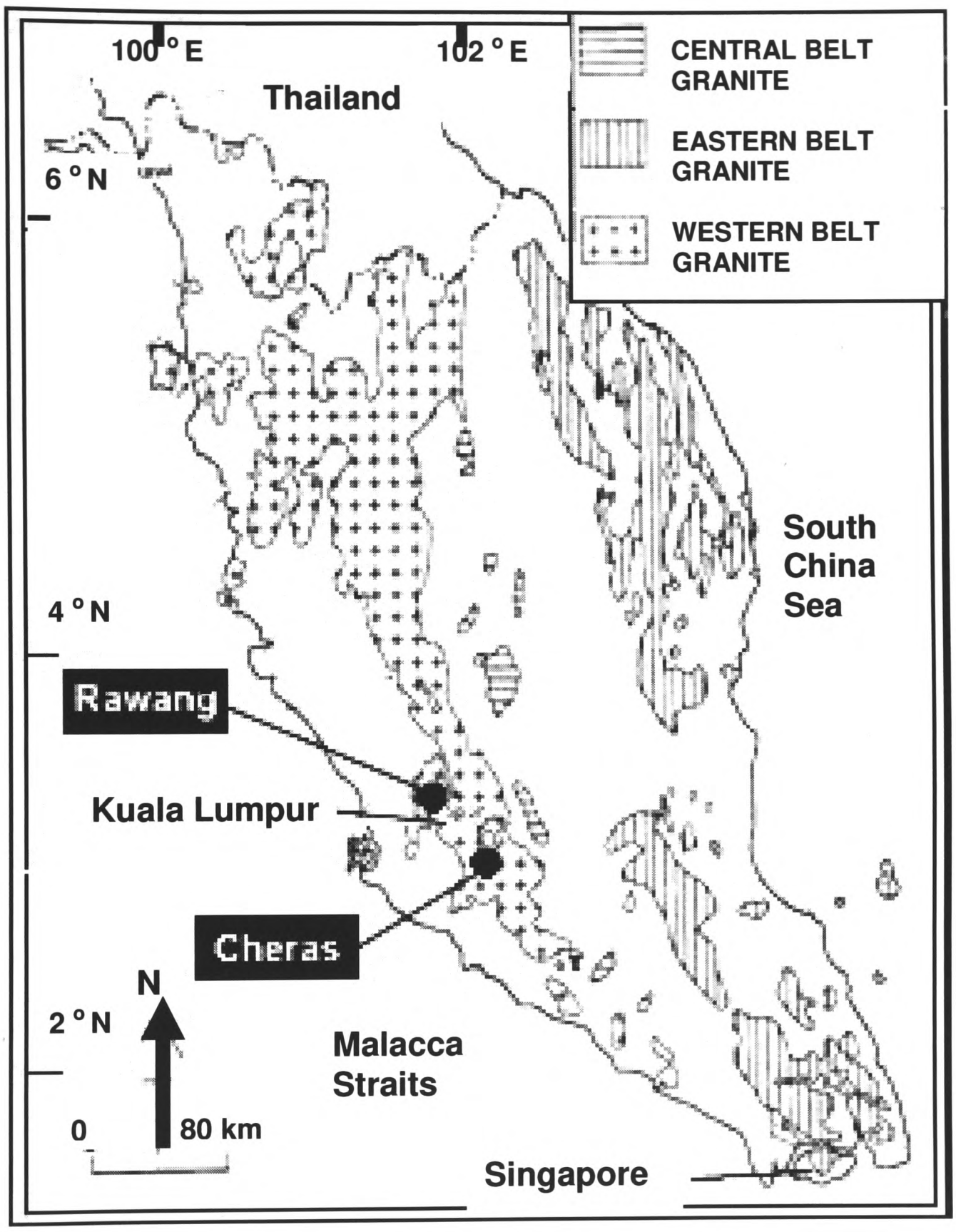

Figure 3.1 Western, Central and Eastern Belts Granites in Peninsula Malaysia (Ghani, 2000). Rawang and Cheras are the two locations where samples were taken for the present study.

3.1.2 Global tectonic setting

During the Silurian to Devonian period (425-380Ma), a major continental collision occurred in southeast China causing widespread folding, metamorphism and granite emplacement and most parts of this region were uplifted and folded (Gobbett, 1972). Between Devonian to Carboniferous (380-340Ma), active subduction caused peninsular Malaysia to rift away from northern Australia. Pebbly mudstone was formed extensively during the Carboniferous to Permian (340-255Ma). The Permian to Triassic (255-200Ma) period marked the emplacement of granites in Peninsular Malaysia. Most of western part of Peninsular Malaysia was covered by an extensive shallow water platform characteristically free of volcanism and tuffs, in contrast to the east where all sediments are tuffaceous. Between the Triassic to Jurassic (220-150Ma) period, pre-rift structures were formed in many localities away from a collision zone and major strike-slip faulting cuts obliquely across the peninsula. Post-collision S type tin granites have been dated at 220-200Ma. Jurassic to Cretaceous (150-80Ma) marked the formation of subalkaline granitoids, which were interpreted, as resulting from pre-rift stages of continental crust reworking. Cretaceous to Neogen (80-20Ma) also marked the formation sub-alkaline granites due to the pre-rift reworking of the continental crust.

The processes mentioned above divided the peninsula into two distinctive blocks: 'Western Peninsula Block' and 'Eastern Peninsula Block'. The Eastern Peninsular Malaysia block comprise of Central and Eastern belts granites. Upper Palaeozoic events of uplifting and multi-phase deformation have caused the block to be severely folded along axes that predominantly strike north-northwest to north. However the Western Peninsula Block remains relatively stable. The present study locations lie within this Western Peninsula Block.

3.1.3 The Granites

Granitic rocks occupy about 50% of the exposed landmass of Peninsular Malaysia. Regionally, they can be categorised as Western Belt granites, Central Belt granite and the Eastern Belt granite (Figure 3.1) (Ghani, 2000).

The Western Belt granite

It is believed that the Western Belt granite was formed between the Triassic to Jurassic (220-150Ma) period (Gobbett, 1972). In comparison with the other two granite belts, the Western Belt granite is more variable in colour compared to the other two belts, normally from gray to pink with the gray variety more abundant. The main rock types are medium grained microcline-microperthite granite, graphic granite, and medium grained and porphyritic granodiorite, tonalite, and granodiorite porphyry, microgranite and quartz veins. Plagioclase is more abundant than alkali feldspar. In porphyritic varieties, phenocrysts are pink microcline microperthite and up to 10 cm long. The most prominent is hornblende-biotite granite (Gobbett, 1972; Schwartz, 1995). There appear to be two trends in the crystallization phase firstly, K-feldspar and biotite tends to dominate while the other is plagioclase and K-feldspar (Ahmad et al, 2002).

Rawang and Cheras are the two locations on this Western Granite belt where samples were taken for the present study (Figure 3.1)

The Central Belt

It is believed that the Central Belt granite was formed during the Jurassic to Cretaceous (150-80Ma) period (Gobbett, 1972). The granite have been considered to be 'S' type granites but detailed studies have revealed that its members have both 'I' and 'S' type features (Ghani, 2000, 2002). Plagioclase occurs as individual euhedral to subhedral laths and very commonly as angular fragments.

The Eastern Belt

The Eastern Belt granite was believed to be formed in Cretaceous to Neogen (80-20Ma) period (Gobbett, 1972), making this belt the youngest granite belt in Peninsular Malaysia. The Eastern Belt is dominated by high-K calc-alkaline granite.

3.2 Sampling and Geological background

3.2.1 Sampling in Cheras

Three vertical profiles were taken along a very recent cut slope and identified as 'Cheras' samples, named after the nearest town in Kuala Lumpur district and about 80m above sea level (3° 2' 46.95" N, 101° 47 ' 9.03" E, Figures 3.1). The surfaces were exposed for about 6 months before the sampling was done. For the present study, very recently exposed surfaces for sampling are very important to ensure that there are no lateral effects of weathering due to the high humidity and hot climate of the tropical monsoon climate. The average temperature is between 24 to 32°C and monthly rainfall can be as high as 1000mm (Figure 3.2). The cut slope is the southern boundary of a leveled area for a 2-storey semi-detached housing development. A sharp 'saprolite'-rock interface was exposed on the cut surface. The term 'saprolite' will later (in Chapter 4) be refined to 'weathering boundary', 'saprolite' and 'top soil'. However, at this stage of the discussion, 'saprolite' composed of the three subdivisions.

Grass is starting to grow (planted by 'hydro-seeding method' to prevent slope failure) on upper part of the slope. Samples, ranging from hard rock to soil, were taken along the weathering profile and placed in airtight plastic bags and marked as CA1 to CA22, CB1 to CB24 and CC1 to CC16. The soil and soft materials were sampled by driving a 5mm inner diameter and 3mm thick plastic PVC (or Polyvinyl chloride) pipes into the soil. The sampler was driven horizontally to a depth of about 15 to 20cm to avoid roots of the grasses planted on the slope surface. There is an active granite quarry, about 15m to the west of the area and rock samples were also taken from this existing quarry (Figure 3.3a).

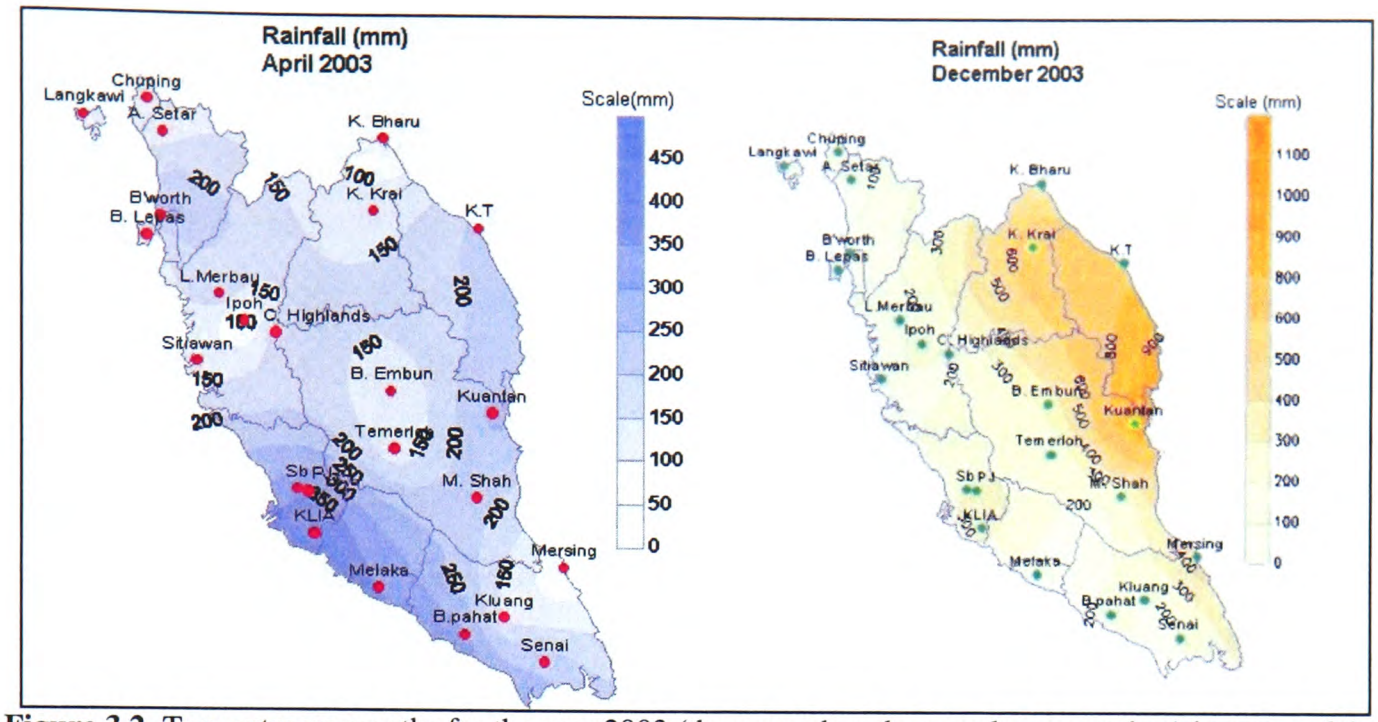

Figure 3.2. Two extreme months for the year 2003 (the year when the samples were taken) in terms of the amount of rainfalls. Monsoon season (November to March) only affects the East Coast. April to September is usually drier months through out the country. (Data: website of the Malaysian Meteorological Department)

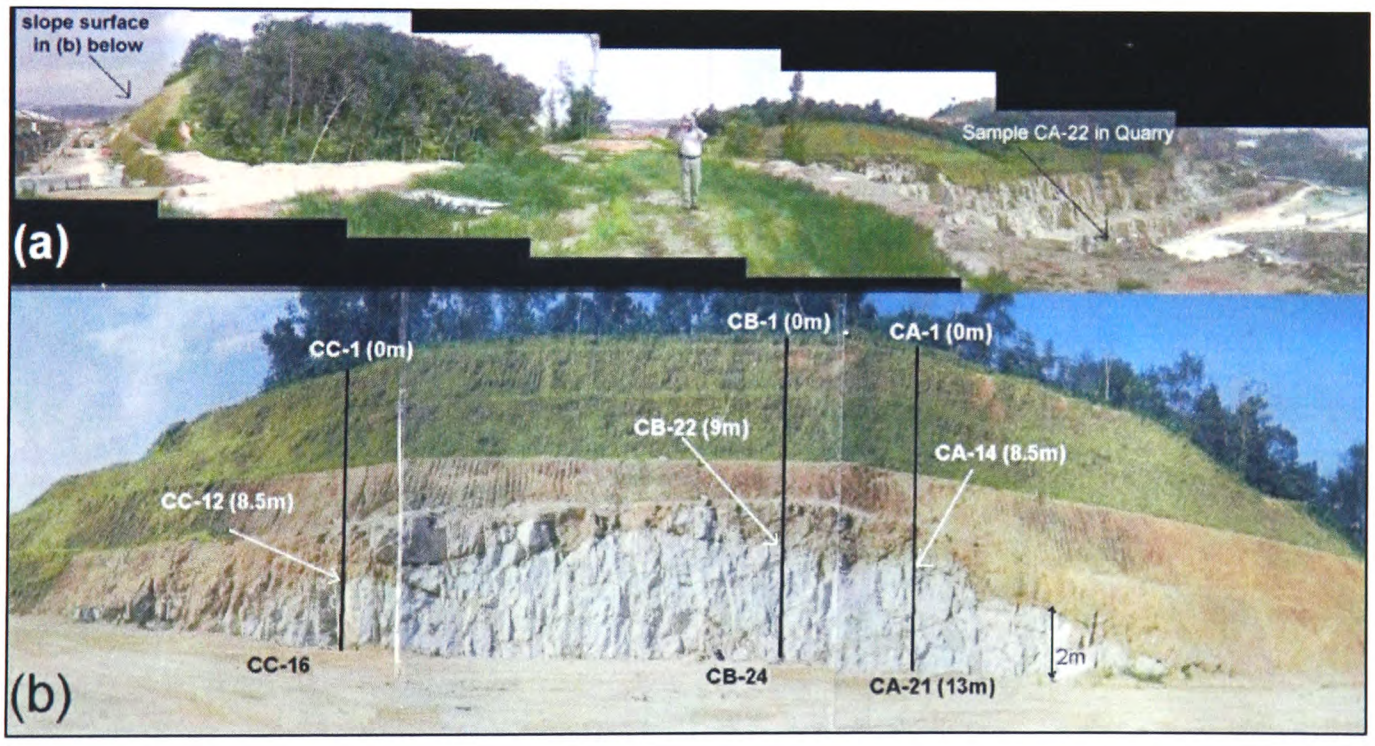

Figure 3.3: Panoramic view of the Cheras site. Samples were marked CA-1 to CA-21, CB-1 to CB-24, and CC-1 to CC-16. Detailed analyses on every sample were done on sampling line CA only. Samples from the sampling lines CB and CC were analysed at random to support the results obtained from samples taken from the CA sampling line.

3.2.2 Sampling in Rawang

Samples from a vertical cut slope and 2 boreholes were taken and identified as 'Rawang' samples, named after the nearest town in Kuala Lumpur district (3° 19' 59.02" N, 101° 34 ' 16.83" E , Figure 3.1). The site is a quarry in saprolite located in between two minor faults. Soil and soft materials on the cut slopes were again sampled by driving a 5mm diameter PVC pipes into the soil and placed in airtight plastic bags and marked as R1 to R6. With the co-operation of some geotechnical consultants and contractors in Malaysia, samples from boreholes in the quarry floor were taken (Figure 3.4). These samples are very important as a confirmation that no lateral weathering effects had occurred on the cut slope. All the soft materials were taken from the face of the cut slope and borehole samples were taken from the quarry floor through deep soft materials before reaching the rock. Drilling was done using a water-wash rotary drilling machine. Water was used as lubricant. When the drilling advanced into the soil, the water washed up broken soil fragments. At every 1.0m depth below ground level, soil samples were taken out with a split-spoon sampler. This sample tube, a thick-walled split-barrel with outside diameter of 50mm, is driven into the ground at the bottom of the borehole by blows from a 63.5kg weight falling through a standard distance of 760mm. The blow counts, N, which is necessary to achieve a penetration of 30mm, gives an indication of the density of the ground. It is regarded as the penetration resistance (British Standard Institution, 1990d). When rock was encountered, the water-wash rotary method could not advance anymore and when the samples brought up showed signs of rock, coring with a diamond bit head was done and a continuous rock core samples were obtained for our purposes. The termination criteria was when the core samples showed no signs of weathering and for both boreholes, the rock core was about 1.5 to 2 m long. The samples taken from the two boreholes were marked as RA-7 to RA 20 for drill hole 5 (DH-5) and RB-7 to RB-20 drill hole 6 (DH-6).

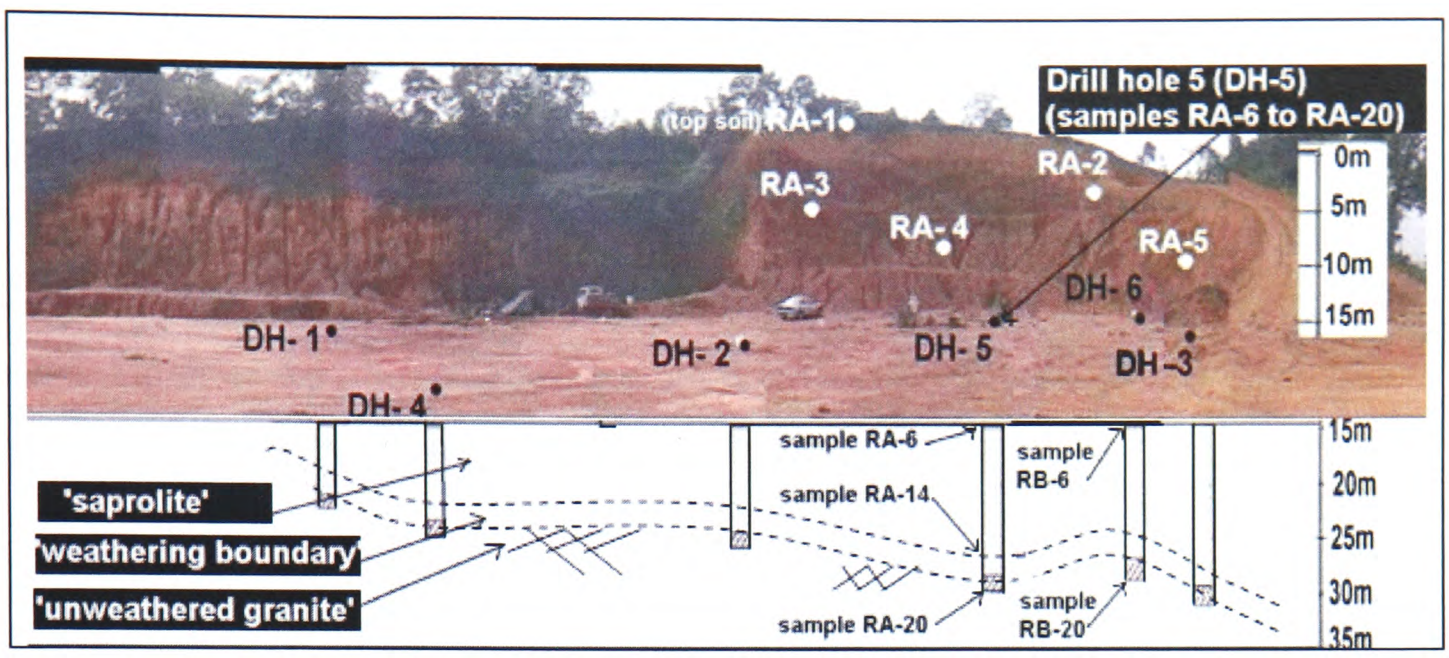

Figure 3.4: Panoramic view of the Rawang site. Samples on cut slopes were marked as RA-1 to RA-5. Drill hole 5 (DH-5): Sample RA-6 was taken on the quarry floor. Samples RA-7 to RA14 were taken from the 'saprolite' zone in drill hole DH-5. Samples RA-15 to RA-20 were taken from the 'weathering boundary' and 'unweathered granite' zones. Drill hole 6 (DH-6): Sample RB-6 was taken on the quarry floor on top of DH-6 and samples RB-7 to RB-20 were taken from the drill hole. Samples taken from DH-6 were not analysed in detail as those taken from DH-5. The 'saprolite', 'weathering boundary' and 'unweathered granite' zones was defined based on the physical and chemical properties of the minerals (will be discussed in Chapter 4). Drill holes DH-1 to DH-4 belong to a local petroleum retailer company involved in the construction of a petrol station on this location. The rock levels depth data in these drill holes were used with their verbal permission.

3.2.1 Geology of Cheras and Rawang

Limestone is located about 15 km to the west and about 2 km to the south is the Kajang Formation, which comprise of schist and phyllite with minor intercalations of limestone (Figure 3.2). The nearest major fault, Jelebu Fault, lies about 15 to 20km east of the sampling site. However, minor quartz veins can be seen in the area. The area lies on the Kuala Lumpur granite, which is a member of the Western Belt granite. The Kuala Lumpur granite was emplaced into the metasedimentary Kajang Formation. Generally, the Kuala Lumpur granite comprises alkali feldspar, plagioclase, biotite, muscocite,

quartz, Fe-Ti oxide and tourmaline and is very felsic with a high amount of SiO_2 (Ghani, 2002).

The fresh samples can be considered as equigranular medium to coarse-grained granite with average grain size 0.5 cm to 1.5 cm across, comprising plagioclase, quartz, K-feldspar, muscovite, biotite and kaolin (Table 3.1). The unaltered plagioclase shows faint Albite twinning and is mostly unzoned. Inclusions of small plagioclase occur in alkali feldspar. The alkali feldspar main type is microcline with distinct cross-hatched twinning. Further study of the unweathered granites (in Chapter 4 of the present study) shows that Cheras granite is an S-type granite. Rawang granite is an I-type granite and is also part of the Kuala Lumpur granite (Figure 3.5) imposing that the Kuala Lumpur granite is a composite intrusion.

Sample	Quartz	Plagio	K-feldspar	Kaolin^{+}	Mica/Illite	Other di-oct. clays
Cheras, 33m depth	32.3	20.6	40.0	2.7	7.8	6.8
Rawang, 30m depth	34.6	67.6	35.6	0	10.7	-

Table 3.1: Mineralogical content (wt %) obtained from XRD analysis, present in 'fresh' granite samples from Cheras and Rawang. Kaolin^{+} could be kaolinite and/or halloysite

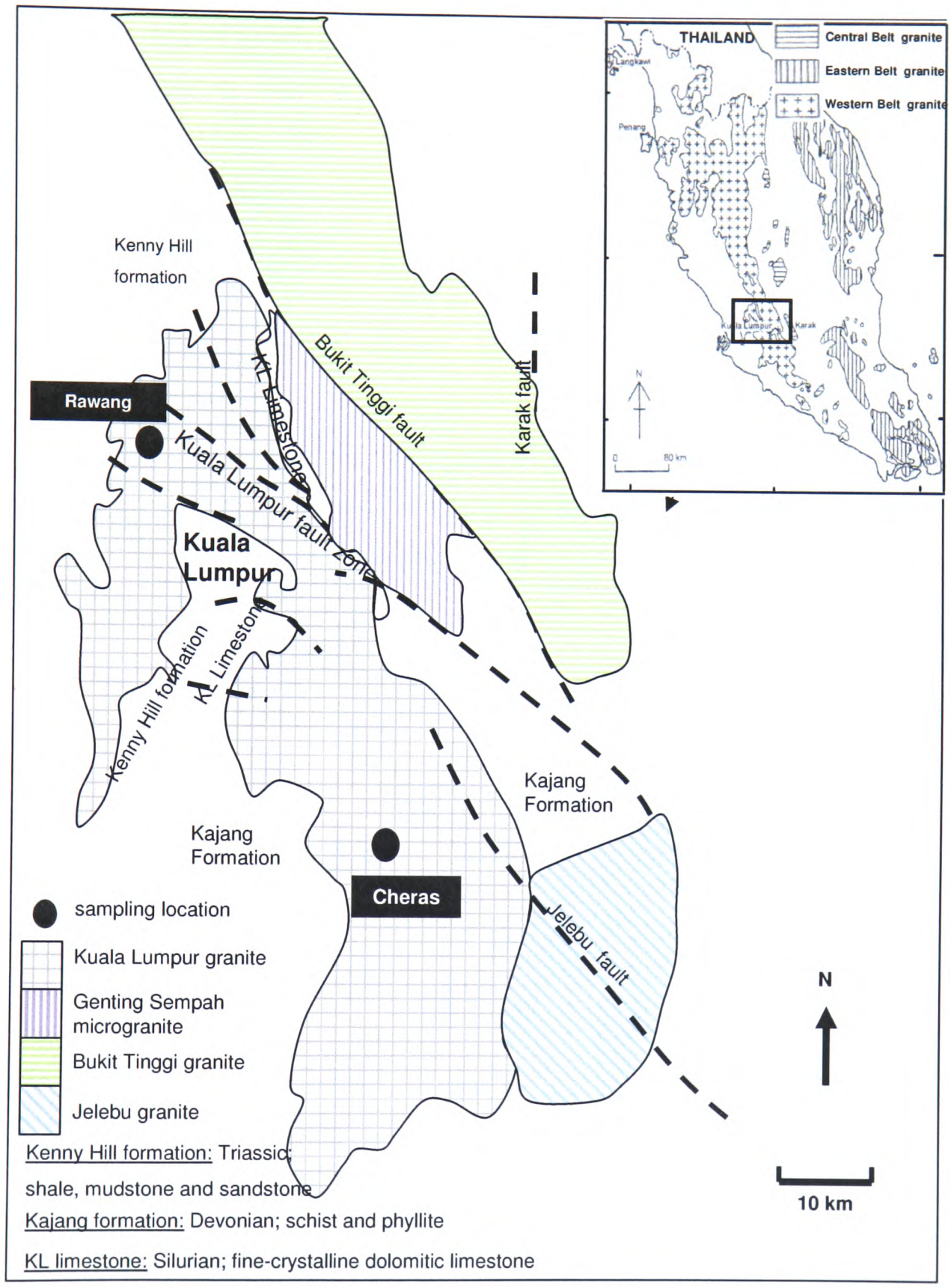

Figure 3.5 Regional geology of Kuala Lumpur area showing the two study areas: Rawang and Cheras. The shaded areas are the different granite formations within the Kuala Lumpur area.

3.3 Summary

The sites were specially chosen to give a clear picture of the different zones produced from the weathering of granite. At Cheras, the 13m height of the cut slope shows a visible sharp distinction between the rock and the saprolite. About 8 to 9m thick of saprolite lies above the rock (Figure 3.3). At Rawang, the saprolite is about 25 to 30m thick (Figure 3.4). The surface of the terrain and the rock-saprolite interface are parallel at Cheras. However, the inferred interface is not so at Rawang.

The Cheras site location next to a quarry gives the opportunity to study the rock below the 13m cut slope. At Rawang the presence of a flat quarry floor next to the 15m thick exposed cut surface (saprolite) gives the opportunity to continue the study of the profile by sinking several drill holes. The holes revealed that the saprolite thickness continues to another 10 to 15m thick before reaching the rock.

4. MINERALOGY AND MAJOR ELEMENT GEOCHEMISTRY

Introduction

The major interest of this research is to study the mechanisms of chemical weathering of granites in a tropical climate. This is done by assessing the mineralogy and major element variations along the depth of the chosen profiles. Any changes in the physical properties of the hand specimens, mineralogical content (by weight%) from 'Quantitative X-ray Powder Diffraction' (QXRPD) analysis, mineral properties under the optical microscope, major elemental content from XRF analysis and microtextures observed under a scanning electron microscope were documented. These variations were also used to categorise the profiles into 4 distinctive zones: unweathered granite, weathering boundary, saprolite and top soil zones. There are 2 approaches in the study of mineral weathering. The first approach is by analysing the mineralogy of samples in the water catchments and the other is looking into the properties of stream or soil/rock samples. In this research, the properties of the soil/rock samples are being looked into.

Studies on the water chemistry in river catchments have improved the understanding of the weathering of parent bedrock. Bluth and Kump (1994) studied the chemistry of over 100 different rivers (for a period of at least 2 years) draining a variety of lithologies and concluded that at a typical 1 to 100cm/y runoff rate, the order of increasing weathering susceptibility is sandstone, granite, basalt, shale and carbonate lithologies. Asano et al (2004) studied the chemistry of water obtained from two different water catchments areas of granitic lithology, forested and bare, for about 5 years duration. Quartz, feldspars and biotite were the dominant minerals of the bedrock. 'Bedrock water samples' were taken from springs and 'soil water samples' were taken using porous-tip polyvinyl chloride (or 'plastic' PVC) tube inserted at depth into the soil profile. Asano and colleagues concluded that from the 'soil water samples', net fluxes of the dominant elements (SiO_2 and Na^+) were similar for both forested and bare areas, even with different profile thicknesses. Net values of SiO_2 and Na^+ for 'bedrock spring fluxes' were three times greater from the forested area than from the bare area suggesting that

the forested area was more leached. About 70-90% of the net fluxes in the forested area and 60-70% in the bare area were derived from the 'bedrock water samples' and it was argued that the contribution of bedrock weathering to water chemistry was very much greater than the weathering of the saprolite zone.

In the present study, both profiles considered are with granite bedrock and it will be shown that the zone defined as the 'weathering boundary' is the active zone of weathering. This zone is the area representing the 'active bedrock weathering zone' in Asano and colleagues' research.

In section 4.1, a brief description of the analysis methods will be given, with an objective of understanding the reasons behind the analyses done. Section 4.2 will discuss the mineralogy of the profiles, focussing on the definition of the weathering zones whereby the profiles were assigned into four zones. The sub-sections 4.2.2, 4.2.3, 4.2.4 and 4.2.5 provide detailed description of these four zones. Under each of these sub-sections, the observations on the major minerals in Cheras and Rawang profiles are noted and discussed. Section 4.3 discusses how these mineralogical observations can be used to define the degree of weathering, noting also similarities and differences between the two profiles and the mineral interactions.

4. 1 Methodology

4.1.1 Quantitative X-ray Powder Diffraction (QXRPD)

The QXRPD analyses were done on powders loaded into cavity holders. The powders were prepared as mixtures of 2.4g of sample and 0.6g of corundum (used as internal standard) using a spray-drying technique. A miniature spray gun sprayed sample suspensions through a hot cylinder and typical product recoveries were about 80% (Figure 4.1a). The analyses were done at the Macaulay Institute, Aberdeen. With this technique, the problems of preferred orientation are effectively eliminated and the

resulting X-ray powder patterns are completely reproducible by different operators (Hillier, 1999). Diffraction patterns were recorded on a Siemens D5000 instrument using cobalt radiation and with a diffracted beam monochromator. The samples were scanned in 0.02 degree steps from 2-75° 2-theta counting for 2 seconds per step. The identification of minerals was based on the positions, intensities and shapes of the various peaks in a diffraction pattern. Kaolinite for example, is identified primarily by two peaks: 7.15Å and 3.58Å (Hillier, 2003). To quantify the concentration of the minerals observed, the peak intensities are measured as integrated peak areas as features like particle size, stacking faults and other forms of order-disorder affect the shape and width but not the integrated peak intensity. Quantitative analysis was made by a reference intensity ratio approach (Hillier 2003) using the 20% added corundum as the reference but based on full patterns of reference minerals rather than individual peaks. Reference patterns for the various minerals identified in each sample are fitted to the observed powder diffraction pattern and the difference minimized by a least squares procedure. The values obtained are at 95% confidence level (Hillier, 2003).

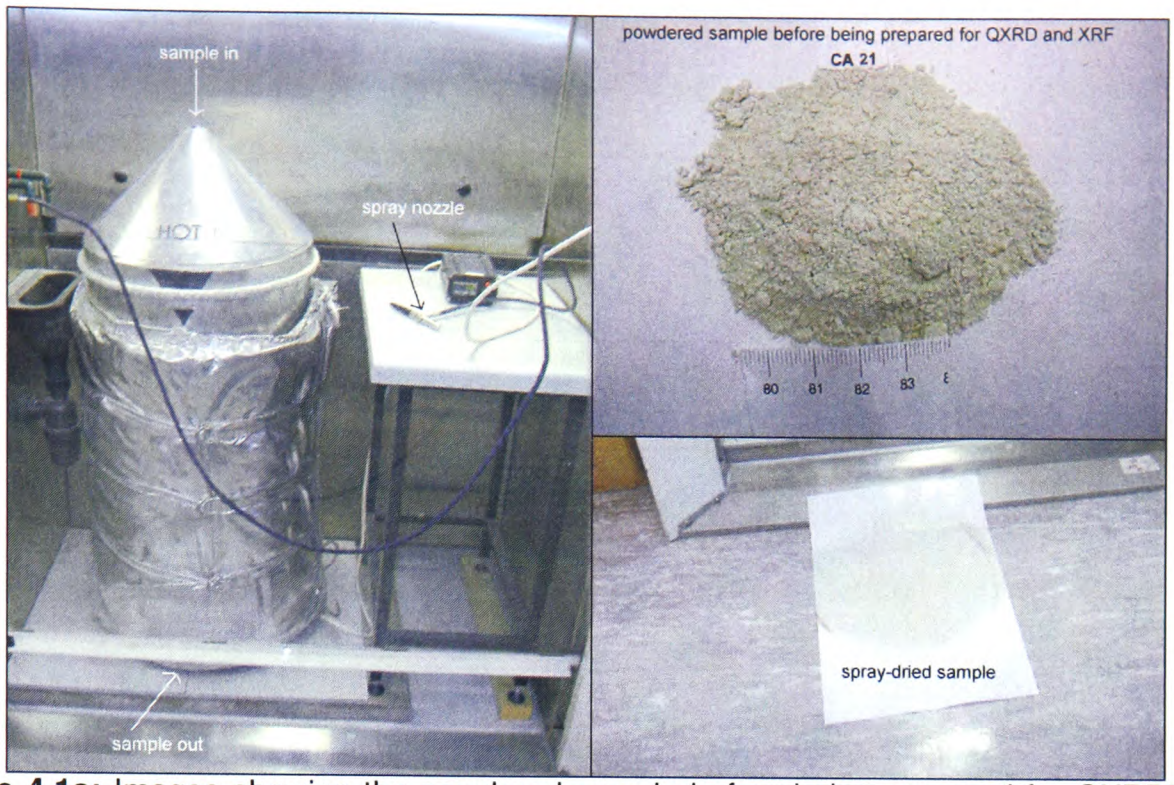

Figure 4.1a: Images showing the powdered sample before being prepared for QXRPD and XRF analyses (right-top). Spray-dry chamber where the liquidified samples passed-through (left) and the spray-dried samples collected for the QXRPD analyses (right-bottom).

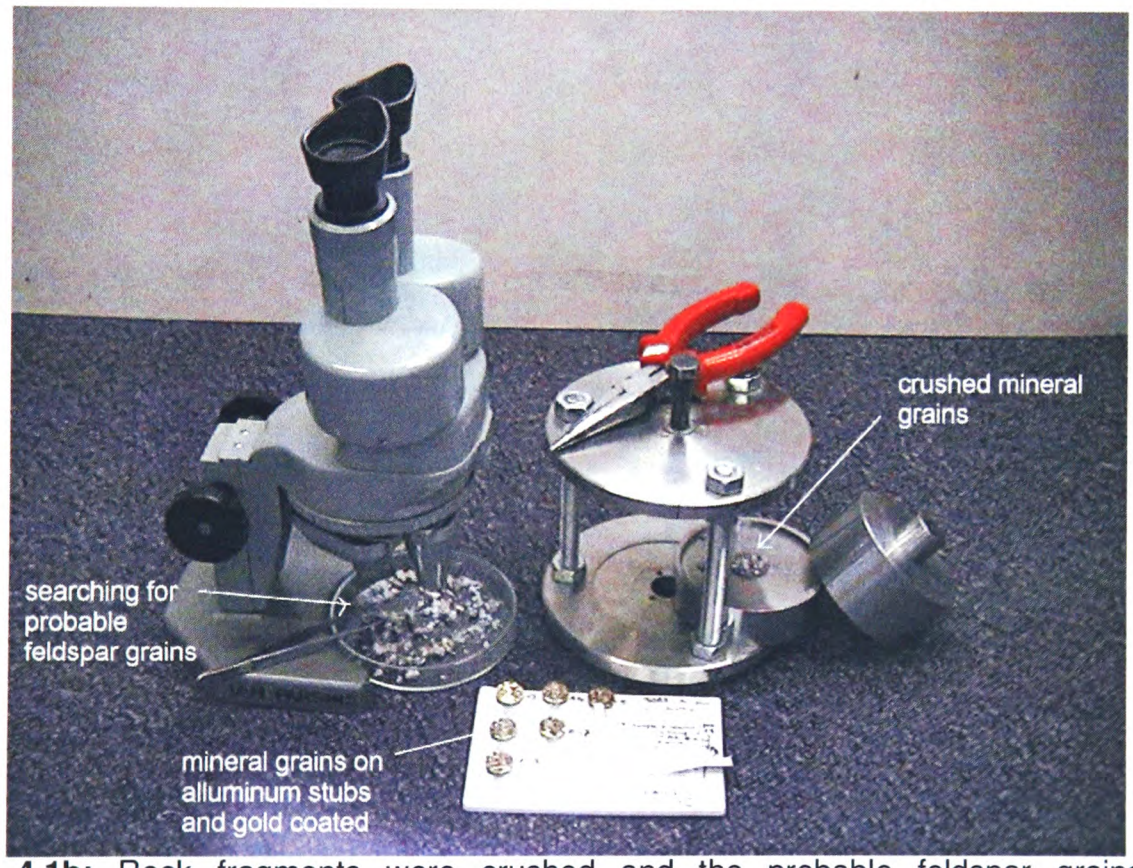

Figure 4.1b: Rock fragments were crushed and the probable feldspar grains were handpicked and mounted on aluminium stubs, ultrasonically washed and rinsed before being gold coated or carbon coated for SEM imaging. The rock crusher was designed and made by Prof. I. Parsons

4.1.2 X-ray Fluorescence spectrometry (XRF)

XRF analyses were carried out on a Philips PW2404 automatic X-ray spectrometer in the Grant Institute of Earth Science at the University of Edinburgh. The techniques used are similar to those described by Fitton et al. (1998), with modifications noted by Fitton & Godard (2004). Major-element concentrations were determined after fusion with a lithium borate flux containing La_2O_3 as a heavy absorber, by a method similar to that developed by Norrish and Hutton (1969). About 50-100g of each sample was very finely ground, using tungsten carbide grinding apparatus, to less than 200μm. The rock powder was dried at 110°C for at least 1 hour, and a nominal but precisely-weighed 1-g aliquot ignited at 1100°C to determine loss on ignition (LOI). The residue was then mixed with Johnson Matthey Spectroflux 105 in a sample: flux ratio of 1:5, based on the unignited sample mass, and fused in a muffle furnace in a Pt5%Au crucible. After the initial fusion, the crucible was reweighed and any flux weight loss was made up with extra flux. After a second fusion over a Meker burner, the molten mixture was swirled several times to ensure homogeneity, cast onto a graphite mold, and flattened with an aluminium plunger into a thin disk. The mold and plunger were maintained at a temperature of 220° C on a hotplate.

Trace-element concentrations were determined on pressed-powder samples. Eight grams of rock powder were mixed thoroughly with eight drops of a 2% aqueous solution of polyvinyl alcohol. The mixture was loaded into a 40-mm diameter aluminium cup in a stainless steel die and compressed against a polished tungsten carbide disc in a hydraulic press at 0.6 tons/cm^2. The fused and pressed samples were analyzed using a Philips PW 2404 automatic X-ray fluorescence spectrometer with a Rh-anode X-ray tube. Background positions were placed as close as possible to peaks and long count times were used at both peak and background positions. Where background count rates were measured on either side of the peak, as in most trace-element determinations, the count time was divided equally between the two positions. Analytical conditions are given in Fitton et al. (1998, 2004)

Corrections for matrix effects on the intensities of major-element lines were made using theoretical alpha coefficients calculated on-line using the Philips software. The coefficients were calculated to allow for the amount of extra flux replacing volatile components in the sample so that analytical totals should be 100% less the measured LOI. Intensities of the longer wavelength trace-element lines (La, Ce, Nd, Cu, Ni, Co, Cr, V, Ba, and Sc) were corrected for matrix effects using alpha coefficients based on major-element concentrations measured at the same time on the powder samples. Matrix corrections were applied to the intensities of the other trace-element lines by using the count rate from the RhK_a Compton scatter line as an internal standard (Reynolds, 1963). Line-overlap corrections were applied using synthetic standards.

The spectrometer was calibrated with USGS and CRPG geochemical reference standards, using the values given by Jochum et al. (1990) for Nb and Zr, and Govindaraju (1994) for the other elements.). Mean and standard deviations (2σ) with standard errors ($2\sigma\sqrt{n}$) were calculated on 5 glass discs made for sample CA-21 as measure of precision and it was found that the maximum error is 3 % relative.

4.1.3 Scanning Electron microscopy (SEM)

The SEM study was done on a Philips XL30CP microscope in the Grant Institute, University of Edinburgh. The resolution of the microscope is 3.5nm at 30kV using the secondary electron (SE) detector while the backscatter (BSE) detector allows you to form an image which depends on the mean atomic number (Z) of the substance in the electron beam. Higher Z means more intense electron scattering so the image is brighter. Thus K-feldspar appears brighter than Na-feldspar. Energy Dispersive Spectroscopy (EDS) analysis, a technique that is based on the characteristic X-ray peaks that are generated when an energetic electron beam interacts with the specimen, was used to determine the relative concentrations of each element in the specimen. This qualitative

analysis uses peak stripping methods where the background is filtered, and the unknown peaks are fit to pure element peaks by linear-least-squares.

Samples were gold coated for topographic imaging using SE and carbon coated for BSE studies. For the SE study, samples that still exhibited their rock characteristics were crushed by applying a gradual increase in pressure in a specially designed steel container Using a binocular microscope, mineral grains (probable feldspar grains in particular) were handpicked and mounted on aluminium stubs using Araldite resin and left overnight for the resin to harden (Figure 4.1b). These grains were picked from the crushed rocks and saprolite samples along the depth of the profiles. These feldspar grains were then cleaned with petroleum ether in an ultrasonic bath to remove any debris. Then, the grains were gold coated before imaging using the SE detector at a working distance of 10mm, with an accelerating voltage of 20kV. When the need arose, the beam was increased to 25kV or 30kV and the working distance reduced to about 7.5mm to improve the resolution of high magnification images. For BSE studies, flat polished thin sections were mounted on SEM stubs with Aquadaq to ensure a good electrical contact between the carbon-coated surface of the sample and the stub to minimise charging of the sample under the electron beam. Images were obtained using the BSE detector at a working distance of 10mm and accelerated voltage of 20kV. BSE imaging was used to get fine scale appearance of the feldspar microtextures using atomic number contrast.

To study the microtextures (e.g. exsolution lamellae) and microstructures (e.g. dislocation etch pits), 'etching' were done on the samples. Samples that still exhibited their rock characteristics were crushed with light blows in a steel mortar. Using a binocular microscope, probable feldspar grains were handpicked from the crushed rocks and samples that already exhibited soil characteristics, and mounted on aluminium stubs using Araldite resin. These feldspar grains were then cleaned in an ultrasonic bath to remove any debris. The etching process involved suspending the mineral grains 20 mm above the surface of concentrated HF for 50 to 120 seconds. They were then rinsed with deionised water to quench the etching process. Samples were then gold coated and

imaged in the SEM using secondary electrons (SE). The reason for etching was to further enhance the visibility of the exsolution lamellae.

4.1.4 Electron microprobe

Mineral analyses were made on a Cameca SX100 electron microprobe at the Grant Institute of Earth Science, University of Edinburgh. EPMA (electron probe micro analysis) works by bombarding a micro-volume of a sample with a focused electron beam, (typical energy of 5-30 keV) and collecting the X-ray photons thereby induced and emitted by the various elemental species. Because the wavelengths of these X-rays are characteristic of the emitting species, the sample composition can be easily identified and quantified using Wavelength Dispersive Spectrometry (WDS). WD spectrometers are based on Bragg's law and use various moveable, shaped diffracting monochromators to separate the characteristic X-rays emitted by the sample. The diffracting crystals and standards for each of the elements analysed is given in Table A1.1 (Appendix A1). Characteristic x-ray lines used for analysis were calibrated using synthetic simple oxides, pure metals, and natural minerals of known composition. Elemental concentrations were measured and calculated using the Cameca's PeakSight (version 3.41) software via the PAP matrix correction algorithm.

Polished thin sections of the samples were carbon-coated and thin strips of carbon tape were placed across the ends of the thin section to minimise charging of the sample by the electron beam. Analyses were done using a defocused beam (50μm) on individual plagioclase and K-feldspar and focussed beam (5μm spot) on biotite, muscovite and chlorite. A large defocused beam was used to minimise the migration of Na and K during analysis and to minimise possible sample bias by integrating the compositions of the host feldspar and any exsolved component. The acceleration voltage used was 15 keV and a probe current of 20nA, with 10-20 second count times on the peaks and 5-10 second count times on each background position. Results of the analyses are given in Tables B1.1 –B1.5 (Appendix B1)

4.1.5 Inductively coupled plasma mass spectrometry (ICP-MS)

ICP-MS analyses were carried out in the Scottish Universities Environmental Research Centre, East Kilbride using an Agilent 7500ce instrument. 0.1g of representative powdered samples was digested using 0.5 ml HNO_3 50% and left overnight on a hot plate. The dried samples were then treated with 5 ml HNO_3 50%, dried and again treated with 1 ml HCl 50% and left for two of hours on a hot plate and finally digested with 5% HNO_3. The mixtures were then diluted 1000 times for the analyses. The REE analyses were carried out in a manner similar to that of Olive et al (2001). The correction procedures involved a repeated analysis of geological reference standards BCR 1, GSP and DRN. With each batch of samples prepared for analyses, the three standards were prepared using similar digestion and dilution protocols.

Repeated analyses on each standards showed that the precision or repeatability has a standard error ($2\sigma\sqrt{n}$) of about 9% and comparisons between the mean values of the repeated analyses of the standards and the published values of the REE concentrations in the standards showed that the accuracy is about 6% relative.

4.2 Mineralogy and geochemistry of the profiles

4.2.1 Definition of the weathering zones

The Cheras and Rawang profiles are divided into four zones, namely 'unweathered granite', 'weathering boundary', 'saprolite' and 'top-soil' zones.

Unweathered granite zone

The lower limit of this zone is not defined as it extends into the granite intrusion below the sampling locations for each profile (Figures 4.2, 4.3 and 4.4). The upper limit is demarcated by the hardness of hand specimens and the appearance of K-feldspar fracture surfaces under the SEM. The rock could not be broken by the force delivered from the weight of a normal geological hammer. No sign of natural dissolution of perthite lamellae could be seen on cleavage surfaces. Observations in the optical microscope were not used as a criterion for this limit. The upper limit was assigned as 0m level and negative values are given below this level. In Cheras, sample CA-18 was taken at 11m depth (from the ground level i.e. top of the hill) of a slope and CA-17 was taken at 10m depth (Figure 4.2). CA-18 fulfilled the criteria for this zone while CA-17 did not and the writer assigned the 10m depth as the 0m level. In Rawang, the recovery of rock core samples in the drilled hole started at 28.50m depth (Figure 4.3). Sample RA-16 is the top 0.02m (approximately) of the rock-core samples and complies with the defined criteria (Figure 4.4-middle right). Sample RA-17 is the upper limit of unweathered granite zone and 28.52m depth below ground level is taken as the 0m level.

Assigned zone	Assigned level, m	Depth below hilltop, m	Sample name	Hand specimen	Optical microscopy		SEM(*)	notes		
								Hand specimen	Optical microscopy	SEM(*)
Top soil	10.0	0.0	CA-1	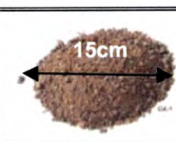	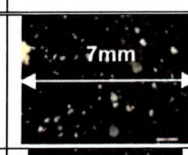	category (i)	Not applicable	Decayed materials	Small fractures of mineral grains within a clay matrix	Exsolution lamellae on K-feldspar fracture surfaces under SEM. Detail of weathering boundary is given in Fig. 4.4
	9.5	0.5	CA-2		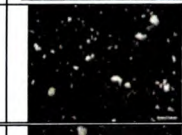					
Saprolite	9.0	1.0	CA-3		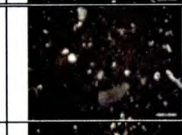			Original mass structure and material fabric are destroyed or crumbles under normal pressure of the hand.		
	8.5	1.5	CA-4		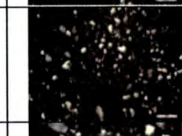					
	8.0	2.0	CA-5		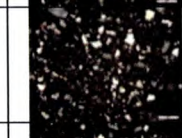					
	7.0	3.0	CA-6		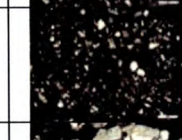					
	6.0	4.0	CA-7		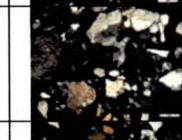	category (ii)			Small fractures of mineral grains within a clay matrix	
	5.0	5.0	CA-8		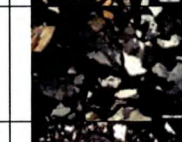					
	4.5	5.5	CA-9		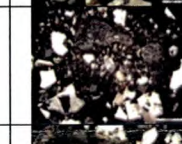					
	4.0	6.0	CA-10		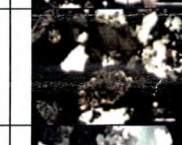					
	3.0	7.0	CA-11		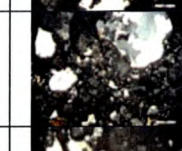					
	2.5	7.5	CA-12		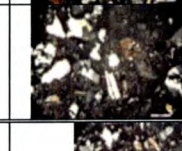					
Weathering boundary	2.5 2.0	7.5 8.0	CA-13		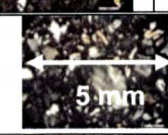			Original mass structure is intact under normal pressure of the hand, crumbles under light hammer blow.	Mineral grains can clearly be observed.	Dissolution exsolution lamellae (due to weathering) are easily observed.
	1.5	8.5	CA-14		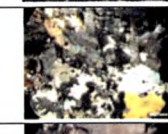					
	1.0	9.0	CA-15	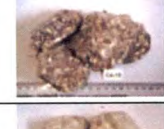						
	0.5	9.5	CA-16				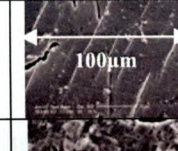			
	0	10.0	CA-17	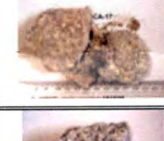						
Unweathered granite	0 -1.0	10.0 11.0	CA-18	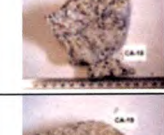	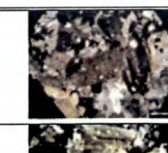		Not applicable	Material will not crumble under light hammer blow.		Need HF acid etching in laboratory to observe exsolution lamellae
	-1.5	11.5	CA-19		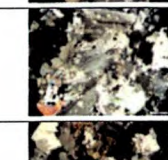					
	-2.0	12.0	CA-20		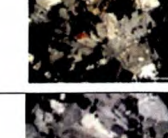					
	-3.0	13.0	CA-21		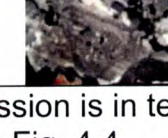					

Figure 4.2: Zones assigned to the Cheras profile. Detail discussion is in text. (*) Exsolution lamellae on K-feldspar fracture surfaces under SEM. Detail of weathering boundary is given in Fig. 4.4

Assigned zone	Assigned level, m	Depth below hilltop m	Sample name	Hand specimen	Optical microscopy	SEM(*)	notes		
							Hand specimen	Optical microscopy	SEM(*)
Top soil	28.52	0	RA-1	15 cm	7mm	Not applicable	Original mass structure and material fabric are destroyed or crumbles under normal pressure of the hand. decayed materials	Fractures of grains within a clay matrix	Generally, difficult to hand-pick feldspar grains under naked eye/binocular microscope
Saprolite	23.52	5.0	RA-2						
	20.52	8.0	RA-3						
	18.52	10.0	RA-4						
	15.52	13.0	RA-5						
	13.52	15.0	RA-6						
	11.52	17.0	RA-7						
	9.52	19.0	RA-8						
	8.52	20.0	RA-9						
	7.02	21.5	RA-10						
	5.52	23.0	RA-11						
	4.02	24.5	RA-12						
	2.52	26.0	RA-13						
	1.02	27.5	RA-14						
Weathering boundary	1.02	27.5	RA-15	5 cm	5 mm		Crumbles under light hammer blow.	Mineral grains can clearly be observed.	(due to weathering) are easily observed.
	0.02	28.50							
	0	28.52	RA-16	5 cm	100µm				
Unweathered granite	0	28.52	RA-17			Not applicable	Material will not crumble under light hammer blow.		Need HF acid etching in laboratory to observe exsolution lamellae
	-0.02	28.54							
	-0.48	29.0	RA-18	15 cm					
	-0.98	29.5	RA-19	15 cm					
	-1.48	30.0	RA-20	15 cm					

Figure 4.3: Zones assigned to the Rawang profile. Detail discussion is in text. (*) Exsolution lamellae on K-feldspar fracture surfaces under SEM. Detail of weathering boundary is given in Fig. 4.4

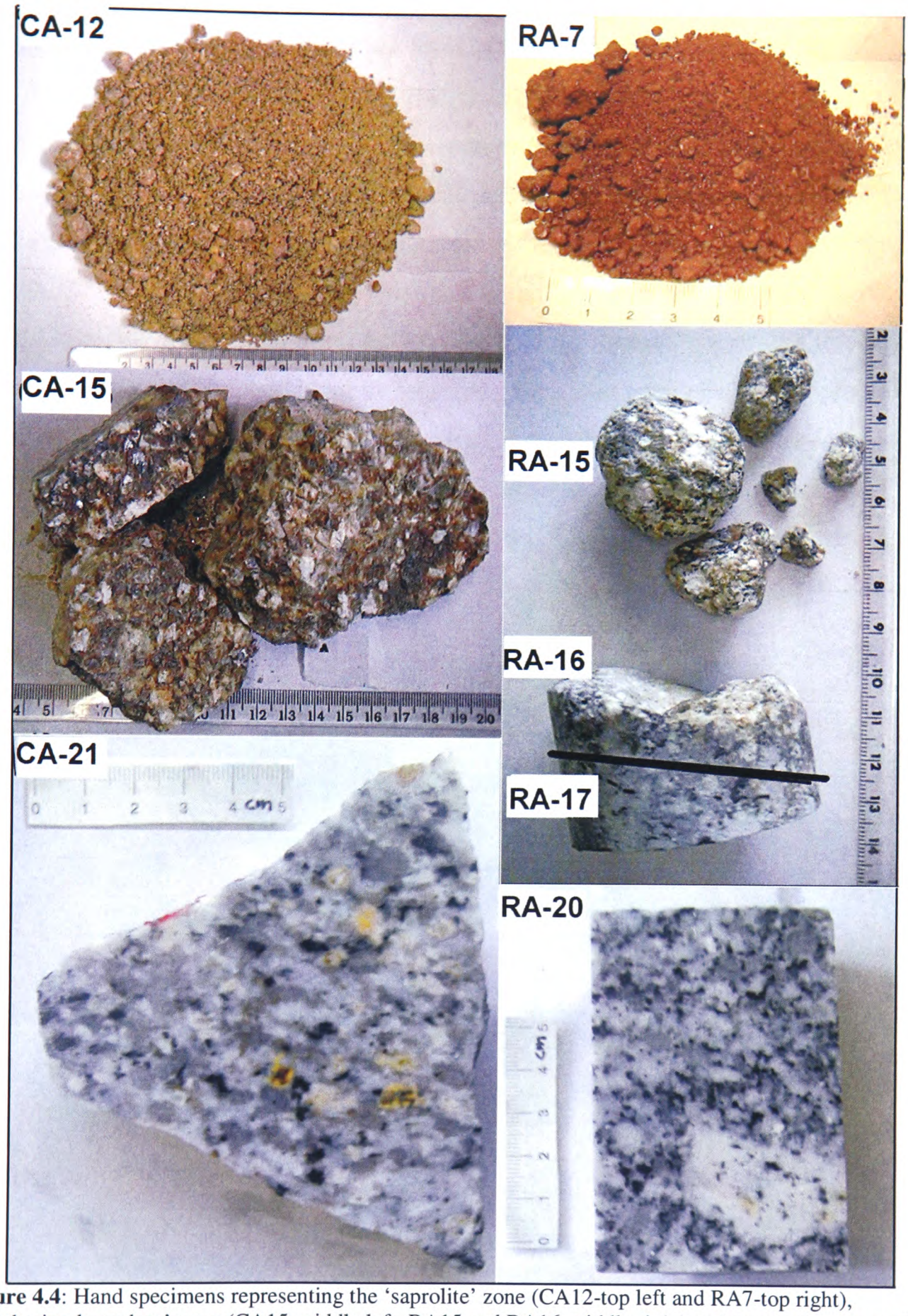

Figure 4.4: Hand specimens representing the 'saprolite' zone (CA12-top left and RA7-top right), 'weathering boundary' zone (CA15-middle left, RA15 and RA16-middle right) and 'unweathered granite' zone (CA21-bottom left, RA17-middle right and RA20-bottom right) of the Cheras and Rawang profiles. Sample RA-15 was obtained in a sampling barrel as loose materials above RA16 (middle right). The black line between RA16 and RA17 will be discussed in detail in Fig. 4.11)

Weathering boundary zone

The lower limit of this zone is the upper limit of the unweathered granite zone. The upper limit is demarcated by the abrupt change in the appearance of the mineral grains under the optical microscope between this zone and the saprolite zone (Figures 4.2, 4.3). The mineral grains in this zone are either fresh or slightly weathered whereas above it, majority of the mineral grains are completely weathered. In the hand specimen, the rock can be broken by the force delivered from the weight of a normal geological hammer. This zone always contains lumps of the original rock (fragments preserving the rock texture) SEM images were not used to determine the upper limit of this zone. In terms of the mineral content, plagioclase decreases to <1% (i.e. trace) and kaolin content increases to >30% (Tables 4.1, 4.2). In the Cheras profile, the boundary is marked above sample CA-13 at about 8.0m depth and in the Rawang profile, above sample RA-15, at about 27.5m (Figure 4.3). The thickness of this zone in the Cheras profile is about 2m and in the Rawang profile is about 1m.

In Table 4.1, the samples CA-13 and CA-14 are 'out-of-order' because CA-14 is produced by weathering on a joint cutting below CA-13 (Figure 4.5.).

Assigned zone	Assigned level (m)	Depth below ground level, bgl (m)	sample name	quartz (wt %)	plagioclase (wt%)	K-feldspar (wt%)	kaolin[(1)] (wt%)	gibbsite (wt%)	muscovite (wt%)	hematite (wt%)	goethite (wt%)
Saprolite	10.0	0.0	CA-1	60	N.D.	1	26	8	4	trace	1
	9.5	0.5	CA-2	54	N.D.	1	36	6	2	trace	1
	9.0	1.0	CA-3	61	N.D.	1	24	13	2	trace	trace
	8.5	1.5	CA-4	47	N.D.	trace	27	19	7	trace	1
	8.0	2.0	CA-5	56	N.D.	N.D.	17	22	4	trace	trace
	7.0	3.0	CA-6	65	N.D.	trace	20	9	6	trace	trace
	6.0	4.0	CA-7	61	trace	3	24	N.D.	12	N.D.	N.D.
	5.0	5.0	CA-8	60	trace	6	25	N.D.	9	N.D.	N.D.
	4.5	5.5	CA-9	52	trace	6	35	N.D.	7	N.D.	N.D.
	4.0	6.0	CA-10	56	N.D.	9	30	N.D.	6	N.D.	N.D.
	3.0	7.0	CA-11	53	trace	6	35	N.D.	7	N.D.	N.D.
	2.5	7.5	CA-12	41	trace	5	47	N.D.	7	N.D.	N.D.
Weathering boundary	2.0	8.0	CA-13	42	18	29	3	N.D.	8	N.D.	N.D.
	1.5	8.5	CA-14	44	trace	29	15	N.D.	12	N.D.	N.D.
	1.0	9.0	CA-15	35	22	31	2	N.D.	10	N.D.	N.D.
	0.5	9.5	CA-16	39	16	31	5	N.D.	8	N.D.	N.D.
	0.0	10.0	CA-17	46	23	22	3	N.D.	7	N.D.	N.D.
Unweathered granite	-1.0	11.0	CA-18	43	19	30	2	N.D.	7	N.D.	N.D.
	-1.5	11.5	CA-19	31	20	42	2	N.D.	6	N.D.	N.D.
	-2.0	12.0	CA-20	48	17	25	trace	N.D.	10	N.D.	N.D.
	-3.0	13.0	CA-21	39	25	24	2	N.D.	10	N.D.	N.D.
	-23.0	33.0	CA-22	34	22	34	2	N.D.	8	N.D.	N.D.

Table 4.1 Quantitative XRPD analysis results of Cheras. [(1)]Kaolin generally refers to kaolinite, halloysite, and less common dickite and nacrite (Dixon, 1989) but here it refers to kaolinite and halloysite. Dotted lines represent the demarcations into sub-categories (refer to Figure 4.2). The samples highlighted are 'out-of-order' because CA-14 is produced by weathering on a joint cutting below CA-13 (refer to figure 4.5). (note, N.D: Not detected).

Assigned zone	Assigned level (m)	Depth bgl, (m)	sample name	quartz (wt %)	plagioclase (wt%)	K-feldspar (wt%)	kaolin[(1)] (wt%)	gibbsite (wt%)	hematite (wt%)	goethite (wt%)	biotite (wt%)	chlorite (wt%)	anatase (wt%)
Saprolite	28.52	0.0	RA-1	50	N.D.	N.D.	35	4	N.D.	3	N.D.	N.D.	trace
	23.52	5.0	RA-2	45	N.D.	N.D.	23	25	N.D.	2	N.D.	N.D.	N.D.
	20.52	8.0	RA-3	43	N.D.	N.D.	21	22	2	2	N.D.	N.D.	N.D.
	18.52	10.0	RA-4	56	N.D.	N.D.	24	14	1	1	N.D.	N.D.	trace
	15.52	13.0	RA-5	40	N.D.	N.D.	12	40	1	2	N.D.	N.D.	N.D.
	13.52	15.0	RA-6	47	N.D.	N.D.	47	3	1	2	N.D.	N.D.	trace
	11.52	17.0	RA-7	56	N.D.	N.D.	25	13	2	1	N.D.	N.D.	trace
	9.52	19.0	RA-8	29	N.D.	N.D.	70	N.D.	N.D.	1	N.D.	N.D.	trace
	8.52	20.0	RA-9	30	N.D.	N.D.	69	N.D.	N.D.	1	N.D.	N.D.	trace
	7.02	21.5	RA-10	35	N.D.	N.D.	63	N.D.	N.D.	1	N.D.	N.D.	trace
	5.52	23.0	RA-11	55	N.D.	N.D.	42	N.D.	N.D.	3	N.D.	N.D.	1
	4.02	24.5	RA-12	7	N.D.	N.D.	93	N.D.	N.D.	-	N.D.	N.D.	N.D.
	2.52	26.0	RA-13	37	N.D.	N.D.	62	N.D.	N.D.	1	N.D.	N.D.	trace
	1.02	27.50	RA-14	28	trace	9	36	N.D.	trace	1	2	N.D.	trace
Weathering boundary	0.02	28.50	RA-15	39	17	27	2	N.D.	N.D.	N.D.	5	6	N.D.
	0	28.52	RA-16	25	25	35	2	N.D.	N.D.	N.D.	4	6	N.D.
Unweathered granite	-0.02	28.54	RA-17	26	24	38	1	N.D.	N.D.	N.D.	5	4	N.D.
	-0.48	29.0	RA-18	34	28	25	1	N.D.	N.D.	N.D.	6	4	N.D.
	-0.98	29.5	RA-19	33	25	25	1	N.D.	N.D.	N.D.	6	6	N.D.
	-1.48	30.0	RA-20	33	25	27	trace	N.D.	N.D.	N.D.	7	5	N.D.

Table 4.2: Quantitative XRPD analysis results of Rawang. [(1)]Kaolin generally referred to kaolinite, halloysite, and less common dickite and nacrite (Dixon, 1989) but here it refers to kaolinite and halloysite. Dotted lines represent the demarcations into sub-categories (refer to Figure 4.3). (note, N.D: Not detected).

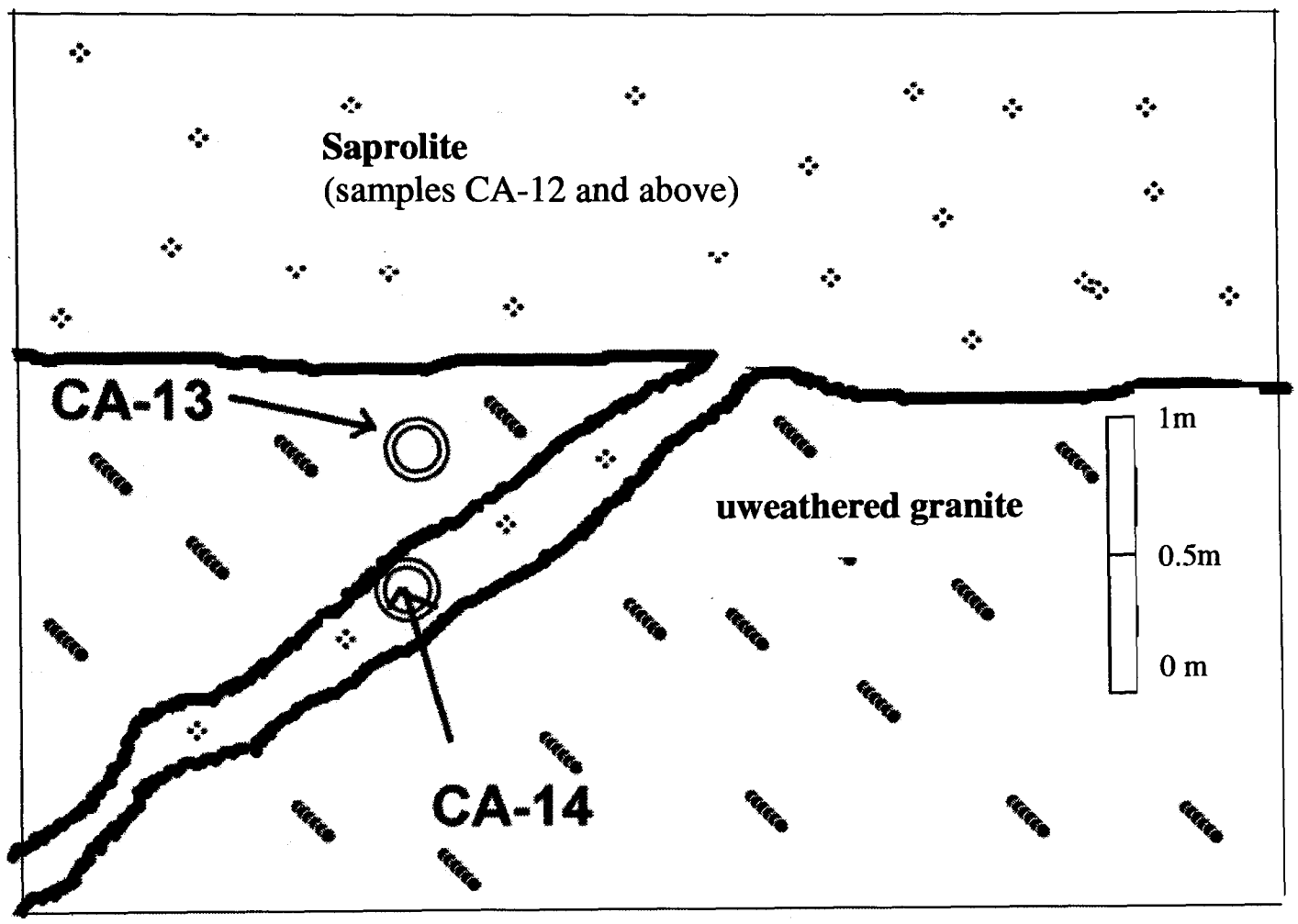

Figure 4.5 Sketch showing sample CA-14 is produced by weathering on a joint cutting below CA-13 making the QXRPD results obtained from the samples CA-13 and CA-14 were 'out-of-order' (refer to Table 4.1)

Saprolite zone

'Saprolite' is generally defined as soft, friable, clay-rich, thoroughly decomposed rock formed in place by chemical weathering of igneous or metamorphic rock. It is normally formed in humid, tropical, or subtropical climates. 'Laterite' is generally being defined as highly weathered red soil rich in iron and aluminum oxides, formed in a tropical to temperate climate where intense chemical weathering is common. 'Residual soil' on the other hand, is generally defined as soil developed in place as the product of decomposition and disintegration of bedrock. In this study, the term 'saprolite' is used to identify the zone above the weathering zone. The lower limit of this zone is the upper limit of the weathering boundary zone while the upper limit is about 0.5 below the ground level which formed the top soil. Rock remnants in hand specimen can be broken easily by normal pressure between human fingers (Figure 4.4). Feldspar grains from most of the samples within this zone could not be easily identified to be hand-picked for SEM study. The thickness of this zone in the Cheras profile is 8m and in the Rawang profile is 27.5m

A comparison between some of the different terminologies normally used to describe the weathering profile is given in Table 4.3

Engineering scale of the weathering grades scale of rock mass			Common term
Grade	Description	Term	
VI	All rock materials are converted to soil. The mass structure and material fabric are destroyed.	Residual soil	Solum
V	All rock materials are disintegrated to soil. The original mass structure is still largely intact.	Completely weathered	Saprolite
IV	More than half of the rock materials is decomposed or disintegrated to soil. Fresh or discoloured rock is present either as a continuous framework or as corestone.	Highly weathered	
III	Less than half of the rock materials is discomposed or disintegrated to soil. Fresh or discoloured rock is present either as a continuous framework or as corestone.	Moderately weathered	Weathered bedrock
III	Discoloration indicates weathering of rock material and discontinuity surfaces. All rock material may be discoloured by weathering.	Slightly weathered	
I	No visible sign of rock material weathering: perhaps a slight discolouration at discontinuity surfaces	Fresh	Bedrock

Terminology used in this study	
Term	Description
Top soil	Hand specimen: contains decayed materials
Saprolite	Hand specimen: original mass structure and material fabric are destroyed or crumbles under normal pressure of the hand. Optical microscope: fractures of grains within a clay matrix SEM: generally, difficult to hand-pick feldspar grains.
Weathering boundary	Hand specimen: original mass structure is still intact and stays intact under normal pressure of the hand but crumbles under light hammer blow. Optical microscopy: Mineral grains can clearly be observed. SEM: dissolution exsolution lamellae of K-feldspar fracture surfaces are easily observed.
Unweathered granite	Hand specimen: material will not crumble under light hammer blow. Optical microscopy: Mineral grains can clearly be observed. SEM: exsolution lamellae on K-feldspar fracture surfaces can only be visible when etched in a laboratory with conc. HF

Table 4.3: Comparison between the different terminologies described by Fookes (1997) on the left of the thick margin and the writers adopted terminology (right).

4.2.1.4 Top soil zone

This layer was organic-rich top soil which contains plant roots and decayed leaves. The thickness of this layer was about 0.1 to 0.5m.

4.2.2 The unweathered granite zone

Petrology

The rocks within this zone in both Cheras and Rawang are medium to coarse grained granite as shown in the hand specimens (Figure 4.4). Modal composition based on the QXRPD analysis for the Cheras area is 31-48 wt% (quartz), 23-42wt% (alkali feldspar), 17-25wt% (plagioclase) with minor amounts of muscovite (Table 4.1). Some biotite grains can be observed under optical microscopy. For the Rawang area, the composition is 25-34wt% (quartz), 24-38wt% (alkali feldspar), 24-28wt% (plagioclase) and about 5 - 8 wt% (biotite) (Table 4.2). Occasionally, up to about 5cm long feldspar phenocrysts can be seen in Rawang compared to smaller, about 1 to 2cm long, phenocrysts in Cheras. In both areas the plagioclases are equigranular, euhedral to subhedral and show Albite and Pericline twinning. Most of the alkali feldspars in Cheras are microcline with the characteristic cross-hatched twinning with some microperthites. In Rawang, most of the K-feldspars are anhedral to subhedral microperthites.

Cheras S-type and Rawang I type granites

The subdivision of S- and I-type granites was first proposed by Chappell and White (1974) in the Lachlan Fold Belt granite, in Australia (Chappell and White, 1974, 2001). S-type granites are derived from magmas generated by partial melting of a sedimentary source rock. The rocks contain Al-rich minerals such as muscovite in addition to biotite, feldspars and quartz (Best, 2003). I-type granites on the other hand, are derived from magmas generated by partial melting of mafic and intermediate igneous rocks and the metaluminous granites contains more Na and Ca than the S-type. Among the minerals present are Al-poor biotite, together with the feldspars and quartz, and may have titanite. The silica wt% in S-type granites is higher than the I-type.

The Cheras unweathered granite contains muscovite together with biotite and other minerals (Tables 4.1) compared to the absence of muscovite in the Rawang granite and are generally richer in silica content (Table 4.2). Anatase (TiO_2) was detected by the QXRPD analysis in the Rawang granite, but not in the Cheras granite. The feldspar end-member composition of the unweathered granite and weathering boundary zone samples, calculated from the bulk XRF analysis, of the Cheras granite is lower in Ca content than the Rawang granite (Table 4.6, Figure 4.6a). From the electron microprobe analysis on the biotite grains, it was found that biotites in the Cheras granite are poorer in aluminium content than the Rawang granite (Figure 4.6b, Table B1.4 in appendix B1). With these findings, and also the presence of microcline in Cheras and orthoclase in Rawang, it can be said that the Cheras granite is an S-type while the Rawang granite is I-type.

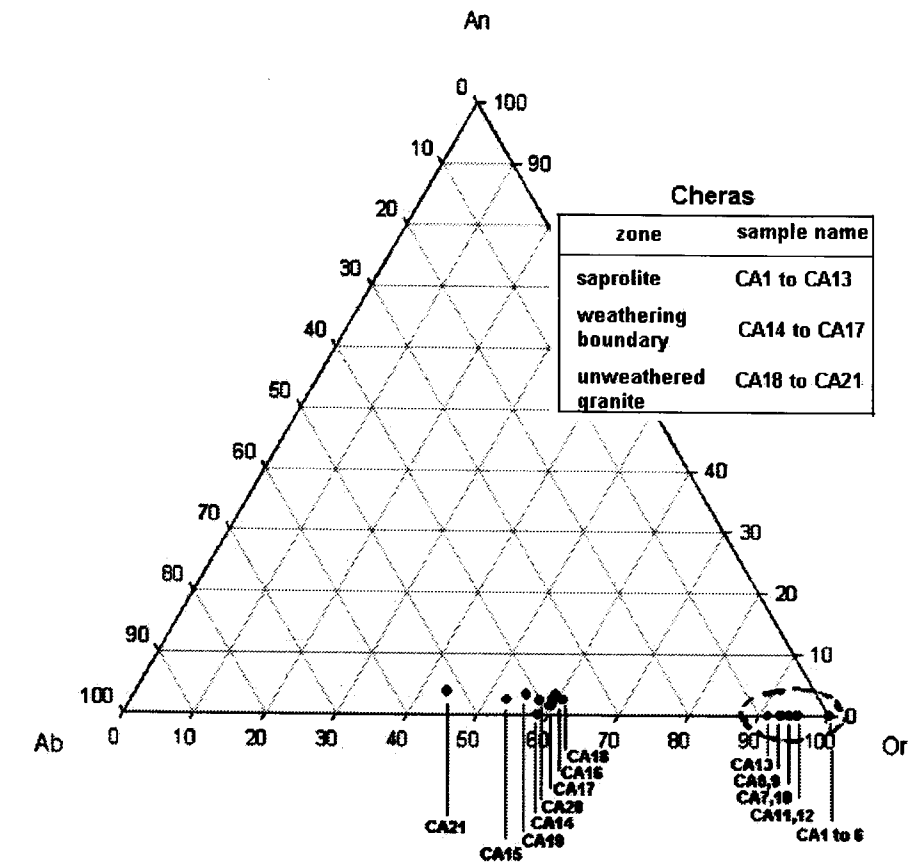

Figure 4.6a: Ternary plots of feldspar end-members of the bulk composition from the XRF analysis calculated using CIPW norms.

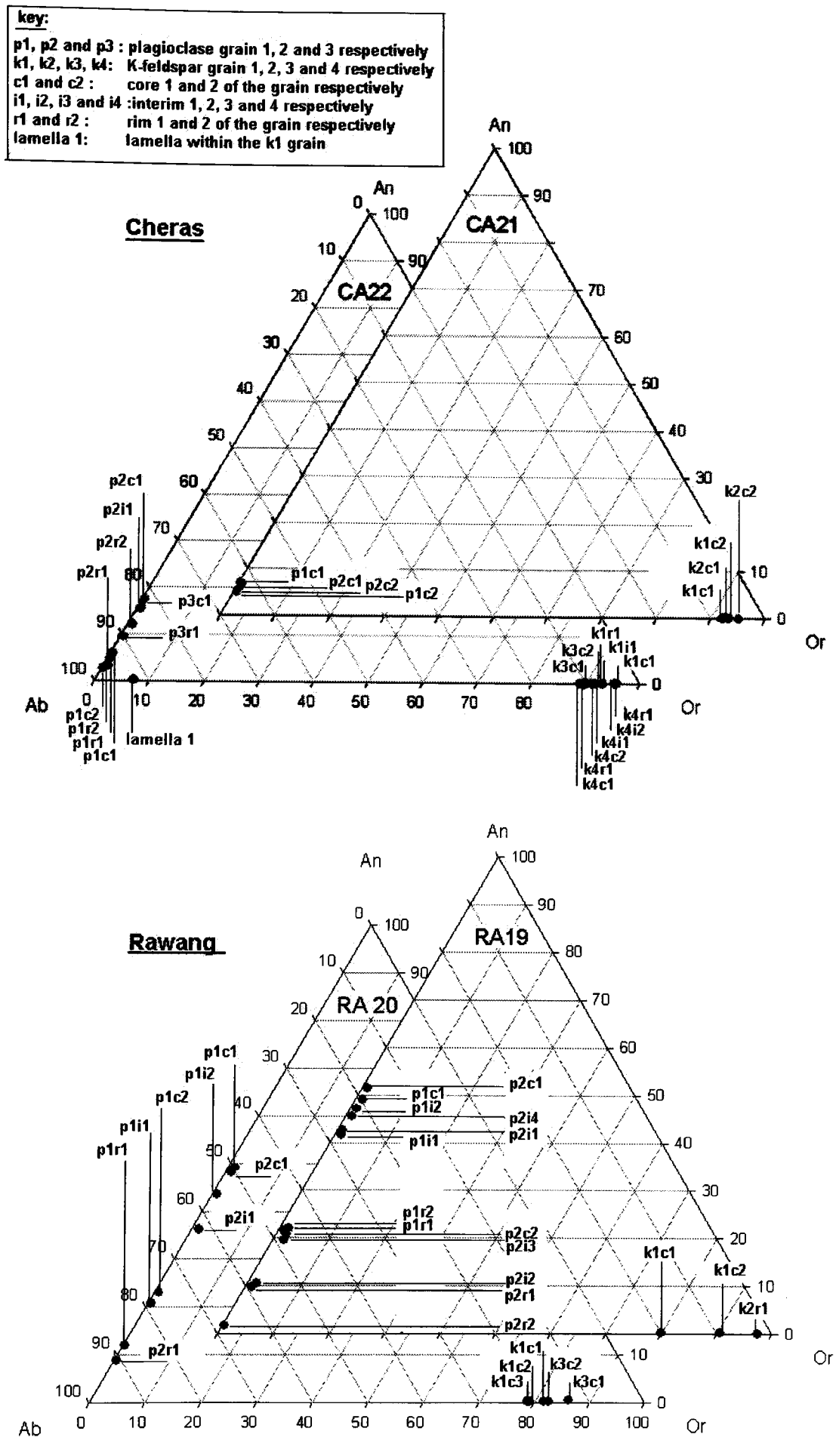

Figure 4.6b Ternary plots of feldspar end member composition from the electron probe analyses.

Assigned zone	Assigned level(m)	Depth bgl, (m)	Sample name	SiO_2 (wt%)	Al_2O_3 (wt%)	Fe_2O_3 (wt%)	MgO (wt%)	CaO (wt%)	Na_2O (wt%)	K_2O (wt%)	TiO_2 (wt%)	MnO (wt%)	P_2O_5 (wt%)	LOI (wt%)	Total (wt%)	Ba (ppm)	Nb (ppm)	Zr (ppm)	Y (ppm)	Sr (ppm)	Rb (ppm)
Top soil	10.0	0.0	CA-1	75.98	18.32	1.66	-	-	-	0.30	0.19	0.00	0.04	4.38	100.87	8.00	25.34	98.51	39.92	-	42.68
	9.5	0.5	CA-2	74.59	21.80	2.18	-	-	-	0.33	0.21	0.01	0.02	1.72	100.85	6.00	27.95	93.06	34.25	-	47.88
	9.0	1.0	CA-3	76.09	20.10	1.43	-	-	-	0.28	0.11	0.00	0.01	2.77	100.79	5.00	16.03	67.27	24.56	-	37.07
	8.5	1.5	CA-4	67.23	26.74	1.95	-	-	-	0.80	0.19	0.01	0.02	2.88	99.82	10.40	32.96	97.60	52.35	-	123.76
	8.0	2.0	CA-5	72.92	21.80	1.35	-	-	-	0.67	0.14	0.01	0.01	2.56	99.45	5.90	23.64	83.79	34.74	-	116.42
	7.0	3.0	CA-6	79.17	18.28	1.38	-	-	-	0.67	0.15	0.01	0.01	1.31	100.98	5.70	21.54	78.85	35.03	-	101.63
Saprolite	6.0	4.0	CA-7	75.31	16.07	1.24	0.11	-	0.07	1.77	0.13	0.01	0.02	5.16	99.90	37.78	27.30	73.57	37.11	1.90	258.50
	5.0	5.0	CA-8	76.01	15.52	0.99	0.12	-	0.11	2.22	0.15	0.01	0.02	5.32	100.48	31.56	28.62	76.80	48.24	2.90	284.70
	4.5	5.5	CA-9	71.71	18.80	0.95	0.09	-	0.09	1.89	0.19	0.02	0.02	5.85	99.61	25.14	33.30	91.24	46.06	3.30	256.90
	4.0	6.0	CA-10	72.76	16.34	1.13	0.06	-	0.06	1.47	0.10	0.01	0.02	6.87	98.84	19.21	19.26	75.99	41.49	2.30	218.40
	3.0	7.0	CA-11	72.69	17.99	1.14	0.06	-	0.05	1.68	0.14	0.01	0.02	5.76	99.53	29.75	23.94	94.88	38.01	2.80	293.90
	2.5	7.5	CA-12	76.19	15.80	1.06	0.10	-	0.04	1.22	0.12	0.01	0.01	5.01	99.56	19.31	24.85	65.08	31.75	2.30	222.50
	2.0	8.0	CA-13	74.64	15.05	1.13	0.05	-	0.35	5.54	0.13	0.02	0.03	3.20	100.13	65.19	24.24	65.49	47.15	8.80	568.40
	1.5	8.5	CA-14	76.84	13.35	0.80	0.15	-	2.39	5.13	0.10	0.02	0.04	1.17	99.98	56.55	18.14	50.13	81.63	15.90	543.70
Weathering boundary	1.0	9.0	CA-15	75.12	13.76	1.46	0.21	0.27	2.74	4.94	0.17	0.06	0.08	1.07	99.87	93.29	30.25	82.76	118.79	18.20	600.40
	0.5	9.5	CA-16	78.67	12.24	0.81	0.13	0.15	2.18	5.09	0.11	0.02	0.04	1.20	100.63	72.21	18.85	58.82	46.06	12.50	534.30
	0.0	10.0	CA-17	75.34	13.53	1.22	0.16	0.31	2.51	6.01	0.15	0.03	0.06	0.83	100.14	68.70	24.34	77.41	62.35	17.80	611.20
	-1.0	11.0	CA-18	76.24	12.88	1.02	0.19	0.30	2.46	6.20	0.10	0.04	0.05	0.58	100.06	80.34	18.65	65.99	47.45	18.70	625.90
	-1.5	11.5	CA-19	76.01	12.63	1.09	0.23	0.38	2.62	5.31	0.12	0.04	0.06	1.63	100.11	52.24	21.80	61.24	53.21	18.20	563.60
Unweathered granite	-2.0	12.0	CA-20	77.02	12.52	0.93	0.15	0.27	2.55	5.59	0.09	0.02	0.06	0.62	99.82	105.94	16.81	58.42	38.90	15.90	575.00
	-3.0	13.0	CA-21	77.33	12.40	0.97	0.12	0.47	3.57	4.53	0.11	0.03	0.06	0.70	100.29	46.11	19.46	57.81	42.28	17.30	470.20
	-23.0	33.0	CA-22	72.73	15.11	0.95	0.17	0.47	2.90	7.05	0.12	0.03	0.06	0.61	100.20	288.43	19.26	58.21	49.43	35.40	645.60

Table 4.4: Results of XRF analyses on samples at different depth below ground level (bgl) in the Cheras profile.

Assigned zone	Assigned level(m)	Depth bgl, (m)	sample name	SiO_2 (wt%)	Al_2O_3 (wt%)	Fe_2O_3 (wt%)	MgO (wt%)	CaO (wt%)	Na_2O (wt%)	K_2O (wt%)	TiO_2 (wt%)	MnO (wt%)	P_2O_5 (wt%)	LOI (wt%)	Total (wt%)	Ba (ppm)	Nb (ppm)	Zr (ppm)	Y (ppm)	Sr (ppm)	Rb (ppm)
Top soil (~1m depth)	28.52	0.0	RA-1	64.40	20.54	5.27	-	-	-	0.11	0.94	0.01	0.09	9.32	100.68	78.60	27.25	329.29	15.36	12.76	18.91
Saprolite	23.52	5.0	RA-2	65.81	23.57	6.18	-	-	-	0.10	1.12	0.01	0.08	4.21	101.07	67.10	17.53	187.19	11.35	5.18	81.23
	20.52	8.0	RA-3	70.29	19.92	4.24	-	-	-	0.52	0.73	0.00	0.06	4.83	100.58	76.50	19.23	201.50	13.11	7.71	80.41
	18.52	10.0	RA-4	62.34	26.60	5.33	-	-	-	1.16	0.89	0.01	0.07	3.75	100.15	79.20	24.54	252.09	18.39	3.77	138.04
	15.52	13.0	RA-5	55.91	35.31	4.42	-	-	-	0.60	0.68	0.01	0.08	2.71	99.72	44.60	19.23	169.56	13.40	1.95	63.28
	13.52	15.0	RA-6	64.38	19.41	4.31	-	-	-	0.27	0.75	0.01	0.05	9.91	99.09	87.40	23.14	225.19	16.83	12.05	40.54
	11.52	17.0	RA-7	63.03	18.61	4.56	-	-	-	0.27	0.83	0.01	0.05	11.60	98.97	87.80	25.24	257.03	23.68	5.79	39.72
	9.52	19.0	RA-8	56.55	26.83	2.91	-	-	-	0.43	0.44	0.01	0.05	12.12	99.33	100.90	14.02	131.46	17.51	11.75	69.40
	8.52	20.0	RA-9	56.62	26.59	3.31	-	-	-	0.34	0.53	0.01	0.04	12.10	99.53	76.30	16.73	161.90	19.37	6.80	53.39
	7.02	21.5	RA-10	59.22	24.48	3.66	-	-	-	0.29	0.70	0.01	0.05	11.54	99.94	106.60	21.74	220.45	19.66	11.14	47.68
	5.52	23.0	RA-11	70.18	16.89	4.64	-	-	-	0.25	0.80	0.01	0.07	8.61	101.06	105.30	25.14	264.19	28.77	10.23	34.11
	4.02	24.5	RA-12	54.58	28.89	2.27	-	-	-	0.34	0.44	0.01	0.03	12.20	98.77	47.10	14.42	128.54	56.76	6.80	57.26
	2.52	26.0	RA-13	61.43	23.62	2.84	-	-	-	0.33	0.48	0.00	0.05	9.98	98.73	46.50	16.33	153.13	69.68	0.64	52.78
	1.02	27.50	RA-14	62.42	22.02	3.98	0.24	0.05	-	2.92	0.69	0.02	0.12	7.50	99.96	454.60	22.14	193.34	134.37	35.88	288.88
Weathering boundary	0.02	28.50	RA-15	72.16	13.44	2.70	0.95	0.90	1.99	5.43	0.48	0.04	0.16	1.40	99.64	479.90	15.83	146.18	58.71	62.63	301.83
	0	28.52	RA-16	67.27	15.76	2.24	0.73	1.31	2.83	6.59	0.40	0.03	0.13	1.20	98.48	insufficient sample					
Unweathered granite	-0.02	28.54	RA-17	70.09	15.85	1.93	0.64	1.42	2.87	7.41	0.37	0.03	0.12	0.71	101.44	1,060	11.42	103.24	45.70	114.93	342.02
	-0.48	29.0	RA-18	71.74	14.48	2.72	0.96	2.00	2.87	5.05	0.51	0.05	0.15	0.80	101.33	431.90	15.63	141.44	49.61	87.47	284.19
	-0.98	29.5	RA-19	67.15	13.58	2.79	1.03	1.84	2.57	5.16	0.51	0.05	0.15	0.90	101.72	719.30	16.03	164.52	37.28	96.36	309.28
	-1.48	30.0	RA-20	69.59	14.13	3.25	1.19	1.88	2.60	5.59	0.60	0.05	0.18	0.80	99.86	571.80	17.93	171.87	40.31	86.26	328.05

Table 4.5: Results of XRF analyses on samples at different depth below ground level (bgl) in the Rawang profile.

Assigned zone	Assigned Level, (m)	Depth bgl,(m)	sample name	Si	Ti	Al	Mg	Ca	Mn	Fe	Ba	Na	K	Calculated values Or	Ab	An
Saprolite	10.0	0.0	CA-1	13.08	-	3.72	-	-	0.0006	0.24	-	-	0.07	100.00	-	-
	9.5	0.5	CA-2	12.58	-	4.33	-	-	0.0010	0.31	-	-	0.07	100.00	-	-
	9.0	1.0	CA-3	12.88	-	4.01	-	-	0.0004	0.20	-	-	0.06	100.00	-	-
	8.5	1.5	CA-4	11.70	-	5.48	-	-	0.0016	0.28	-	-	0.18	100.00	-	-
	8.0	2.0	CA-5	12.55	-	4.42	-	-	0.0010	0.19	-	-	0.15	100.00	-	-
	7.0	3.0	CA-6	13.18	-	3.59	-	-	0.0010	0.19	-	-	0.14	100.00	-	-
	6.0	4.0	CA-7	13.28	-	3.34	0.03	-	0.0021	0.18	-	0.02	0.40	94.32	5.68	-
	5.0	5.0	CA-8	13.36	-	3.22	0.03	-	0.0019	0.15	-	0.04	0.50	93.00	7.00	-
	4.5	5.5	CA-9	12.83	-	3.96	0.02	-	0.0026	0.14	-	0.03	0.43	93.24	6.76	-
	4.0	6.0	CA-10	13.22	-	3.50	0.02	-	0.0011	0.12	-	0.02	0.34	94.17	5.83	-
	3.0	7.0	CA-11	12.97	-	3.78	0.02	-	0.0014	0.17	-	0.02	0.38	95.66	4.34	-
	2.5	7.5	CA-12	13.38	-	3.27	0.03	-	0.0012	0.16	-	0.01	0.27	95.24	4.76	-
	2.0	8.0	CA-13	13.21	-	3.14	0.01	-	0.0028	0.17	-	0.12	1.25	91.24	8.76	-
Weathering boundary	1.5	8.5	CA-14	13.38	-	2.74	0.04	-	0.0027	0.12	-	0.81	1.14	58.53	41.47	-
	1.0	9.0	CA-15	13.19	-	2.85	0.05	0.05	0.0091	0.21	-	0.93	1.11	52.95	44.62	2.43
	0.5	9.5	CA-16	13.58	-	2.49	0.03	0.03	0.0034	0.12	-	0.73	1.12	59.67	38.85	1.48
	0	10.0	CA-17	13.21	-	2.80	0.04	0.06	0.0039	0.18	-	0.85	1.34	59.58	37.84	2.58
Unweathered granite zone	-1.0	11.0	CA-18	13.33	-	2.65	0.05	0.06	0.0055	0.15	-	0.83	1.38	60.86	36.67	2.47
	-1.5	11.5	CA-19	13.37	-	2.62	0.06	0.07	0.0055	0.16	-	0.89	1.19	55.26	41.42	3.32
	-2.0	12.0	CA-20	13.43	-	2.57	0.04	0.05	0.0027	0.14	-	0.86	1.24	57.68	39.98	2.34
	-3.0	13.0	CA-21	13.42	-	2.54	0.03	0.09	0.0050	0.14	-	1.20	1.00	43.75	52.44	3.81
	-23.0	33.0	CA-22	12.85	-	3.15	0.04	0.09	0.0045	0.14	-	0.99	1.59	59.48	37.19	3.33

Table 4.6a: Feldspar end-member composition in Cheras, calculated from the XRF analyses. Values have been converted to 32O (Oxygen 32). The end members are calculated using the equations: Or = 100xK/(Ca+Na+K); Ab=100xNa/(Ca+Na+K); An=100xCa/(Ca+Na+K) (Dear, Howie and Zussman, 1992).

Assigned zone	Assigned level,(m)	Depth bgl,(m)	Sample name	Si	Ti	Al	Mg	Ca	Mn	Fe	Ba	Na	K	Calculated values Or	Ab	An
Saprolite	28.52	0	RA-1	12.15	-	4.57	-	-	0.0018	0.83	-	-	0.03	100.00	-	-
	23.52	5.0	RA-2	11.80	-	4.98	-	-	0.0020	0.93	-	-	0.02	100.00	-	-
	20.52	8.0	RA-3	12.52	-	4.18	-	-	0.0005	0.63	-	-	0.12	100.00	-	-
	18.52	10.0	RA-4	11.28	-	5.67	-	-	0.0012	0.81	-	-	0.27	100.00	-	-
	15.52	13.0	RA-5	10.03	-	7.47	-	-	0.0009	0.66	-	-	0.14	100.00	-	-
	13.52	15.0	RA-6	12.35	-	4.39	-	-	0.0016	0.69	-	-	0.07	100.00	-	-
	11.52	17.0	RA-7	12.38	-	4.31	-	-	0.0020	0.75	-	-	0.07	100.00	-	-
	8.52	20.0	RA-9	11.10	-	6.14	-	-	0.0013	0.54	-	-	0.09	100.00	-	-
	7.02	21.5	RA-10	11.49	-	5.60	-	-	0.0008	0.59	-	-	0.07	100.00	-	-
	5.52	23.0	RA-11	12.89	-	3.66	-	-	0.0014	0.71	-	-	0.06	100.00	-	-
	4.02	24.5	RA-12	10.76	-	6.71	-	-	0.0015	0.37	-	-	0.08	100.00	-	-
	2.52	26.0	RA-13	11.76	-	5.33	-	-	0.0006	0.45	-	-	0.08	100.00	-	-
	1.02	27.5	RA-14	11.79	-	4.90	0.07	0.01	0.0038	0.63	-	-	0.70	98.58	-	1.42
Weathering boundary	0.02	28.50	RA-15	12.96	-	2.85	0.25	0.17	0.0053	0.41	-	0.69	1.24	58.94	32.85	8.21
	0.00	28.52	RA-16	12.39	-	3.42	0.20	0.26	0.0045	0.35	-	1.01	1.55	54.94	35.88	9.18
Unweathered granite zone	-0.02	28.54	RA-17	12.47	-	3.32	0.17	0.27	0.0047	0.29	-	0.99	1.68	57.16	33.64	9.20
	-0.48	29.0	RA-18	12.69	-	3.02	0.25	0.38	0.0067	0.40	-	0.98	1.14	45.55	39.31	15.14
	-0.98	29.5	RA-19	12.64	-	3.01	0.29	0.37	0.0073	0.44	-	0.94	1.24	48.60	36.83	14.57
	-1.48	30.0	RA-20	12.60	-	3.01	0.32	0.36	0.0081	0.49	-	0.91	1.29	50.26	35.54	14.20

Table 4.6b: Feldspar end-member composition in Rawang, calculated from the XRF analyses .

Assigned zone	Assigned Level, (m)	Depth bgl, (m)	sample name	quartz (wt %)	Or[(a)] (wt%)	Ab[(b)] (wt%)	An[(c)] (wt%)	corundum (wt%)	hypersthene (wt%)	ilmenite (wt%)	magnetite (wt%)	apatite (wt%)	zircon (wt%)	Normative values in [(a), (b) and (c)] being summed up to 100% Or (wt%)	Ab (wt%)	An (wt%)
Unweathered Granite (Cheras)	-1.0	11.0	CA-18	36.98 (42.66)	36.71^{n} $(30.06)^{(+)}$	20.82^{n} $(18.90)^{(++)}$	1.16^{n}	1.68	1.30	0.19	0.45	0.12	0.01	62.55^{n}	35.47^{n}	1.98^{n}
	-1.5	11.5	CA-19	39.01 (31.03)	31.45^{n} $(41.57)^{(+)}$	22.17^{n} $(19.83)^{(++)}$	1.49^{n}	2.01	1.44	0.23	0.48	0.14	0.01	57.07^{n}	40.23^{n}	2.70^{n}
	-2.0	12.0	CA-20	39.77 (48.02)	33.11^{n} $(24.57)^{(+)}$	21.58^{n} $(17.19)^{(++)}$	0.95^{n}	1.91	1.11	0.17	0.41	0.14	0.01	59.51^{n}	38.79^{n}	1.71^{n}
	-3.0	13.0	CA-21	37.81 (39.43)	26.84^{n} $(23.49)^{(+)}$	30.21^{n} $(25.34)^{(++)}$	1.94^{n}	0.90	1.05	0.21	0.42	0.14	0.01	45.50^{n}	51.21^{n}	3.29^{n}
	-23.0	33.0	CA-22	27.31 (33.65)	41.88^{n} $(34.37)^{(+)}$	24.54^{n} $(21.68)^{(++)}$	1.94^{n}	1.96	1.14	0.23	0.42	0.14	0.01	61.26^{n}	35.90^{n}	2.84^{n}
Unweathered Granite (Rawang)	-0.04	28.54	RA-17	20.24 (25.66)	44.66^{n} $(38.32)^{(+)}$	24.29^{n} $(24.14)^{(++)}$	6.29^{n}	0.64	2.80	0.70	0.84	0.28	0.01	52.50^{n}	37.00^{n}	10.50^{n}
	-0.5	29.0	RA-18	29.38 (34.14)	30.21^{n} $(24.47)^{(+)}$	24.29^{n} $(27.58)^{(++)}$	8.97^{n}	0.94	4.10	0.97	1.19	0.35	0.03	52.01^{n}	33.90^{n}	14.09^{n}
	-1.0	29.5	RA-19	26.18 (33.29)	31.07^{n} $(24.56)^{(+)}$	21.75^{n} $(25.43)^{(++)}$	8.18^{n}	0.66	4.35	0.97	1.22	0.35	0.03	41.15^{n}	46.31^{n}	12.54^{n}
	-1.5	30.0	RA-20	26.53 (33.31)	33.47^{n} $(26.46)^{(+)}$	22.00^{n} $(24.93)^{(++)}$	8.18^{n}	0.73	5.02	1.14	1.42	0.42	0.03	56.14^{n}	32.90^{n}	10.96^{n}

Table 4.6c: CIPW normative minerals calculated using a program written by Hollocher, K. Geology Department, Union College, Schenectady, NY, 12308 (Appendix C).

(42.66) : mineral composition (wt%) obtained from QXRPD;

$(30.06)^{(+)}$: mineral composition (wt%) obtained from QXRPD were for K-feldspar ;

$(18.90)^{(++)}$: mineral composition (wt%) obtained from QXRPD were for plagioclase

36.71^{n} : normative value

Alkali feldspar exsolution textures

Alkali feldspars may have two types of microtextures: pristine and alteration (Parsons and Brown, 1984; Hodson, Lee and Parsons, 1997). Pristine microtextures form by solid-state diffusion accompanying cooling. The most important thing during this transformation is the ordering of framework cations (Si and Al) and exsolution, leading to regular lamellar perthitic intergrowths. During exsolution, Ab- and Or-rich phases separate from initially homogeneous feldspar. This process produces lamellae. The lamellae are usually oriented near to (601). Only end member bulk chemical compositions and rapidly cooled alkali feldspars do not contain exsolution lamellae. If exsolution occurs on very fine scale, producing crypto-perthite/ mesoperthite/ antiperthite for Or-rich/median/Ab-rich bulk composition respectively, the feldspar framework structure remains continuous across interfaces between Ab- and Or-rich lamellae and the intergrowth is said to be coherent. Because of the differences in cell dimensions of Ab- and Or-rich phases, coherency introduces elastic strain. Coarser exsolution microtextures cannot retain coherency and edge dislocations form along lamellar boundaries in order to reduce misfit between the structures of the two phases. Alteration is formed by interaction of feldspars with fluids already present in the cooling body of rock, termed 'deuteric alteration' or introduced from outside, termed 'hydrothermal alteration' (Figure 2.16). During deuteric alteration coherent intergrowths recrystalize, by a dissolution-reprecipitation process, to produce coarse, irregular 'patch' or 'vein' perthites (Worden et al, 1990; Lee, Waldron and Parsons, 1995b) composed of incoherent albite and K-feldspar subgrains. Micropores develop at their boundaries giving feldspars their characteristic turbidity. Most alkali feldspars in granites contain mixture of pristine and deuteric microtexture (Figure 2.16). The type of microtexture has a strong effect on the way grains weather (see also Lee and Parsons, 1995a; Lee, Hodson and Parsons, 1998).

Hydrofluoric acid vapour dissolves Or- rich feldspar more rapidly than Ab-rich feldspar and leaves the Ab-rich feldspar elevated in relief (Waldron, Lee and Parsons 1994). The difference in relief between Or- and Ab-rich areas in a single feldspar crystal allow

crypto- and microperthite textures and crystal defects such as micropores and dislocation microstructures to be imaged with secondary electrons in the SEM.

The exsolution lamellae observed on the grain surfaces are shown in Figure 4.7. The untreated feldspar surface did not show any observable microtextures. The treated feldspar surfaces showed the presence of regular albite exsolution lamellae with the albite standing out as ridges. Grooves seen along the margins correspond with regions of high coherency strain. Paired deep etch pits formed on the outcrop of misfit dislocations and these could probably be in the form of nanotunnels (Fitz Gerald, Parsons and Cayzer, 2006). Thin, straight exsolution lamellae with etch pits can be observed and in general, alkali feldspars from Rawang have exsolution lamellae that are longer and thinner than those from Cheras.

Zoning in plagioclase

In Cheras, compositional zoning was observed in some grains (Figure 4.8a). Electron probe analyses showed a decrease in the anorthite content (an increase in the albite content) from the core towards the rim. This compositional gradient created fine-scale oscillatory zoning and forms when the boundary layer of solid solution growing from the magma becomes depleted in the high-T component ($CaAl_2Si_2O_8$) and enriched in the low-T component ($NaAlSi_3O_8$) (Best, 2003). The first-formed crystals fail to react with magma during cooling and continuing crystallization.

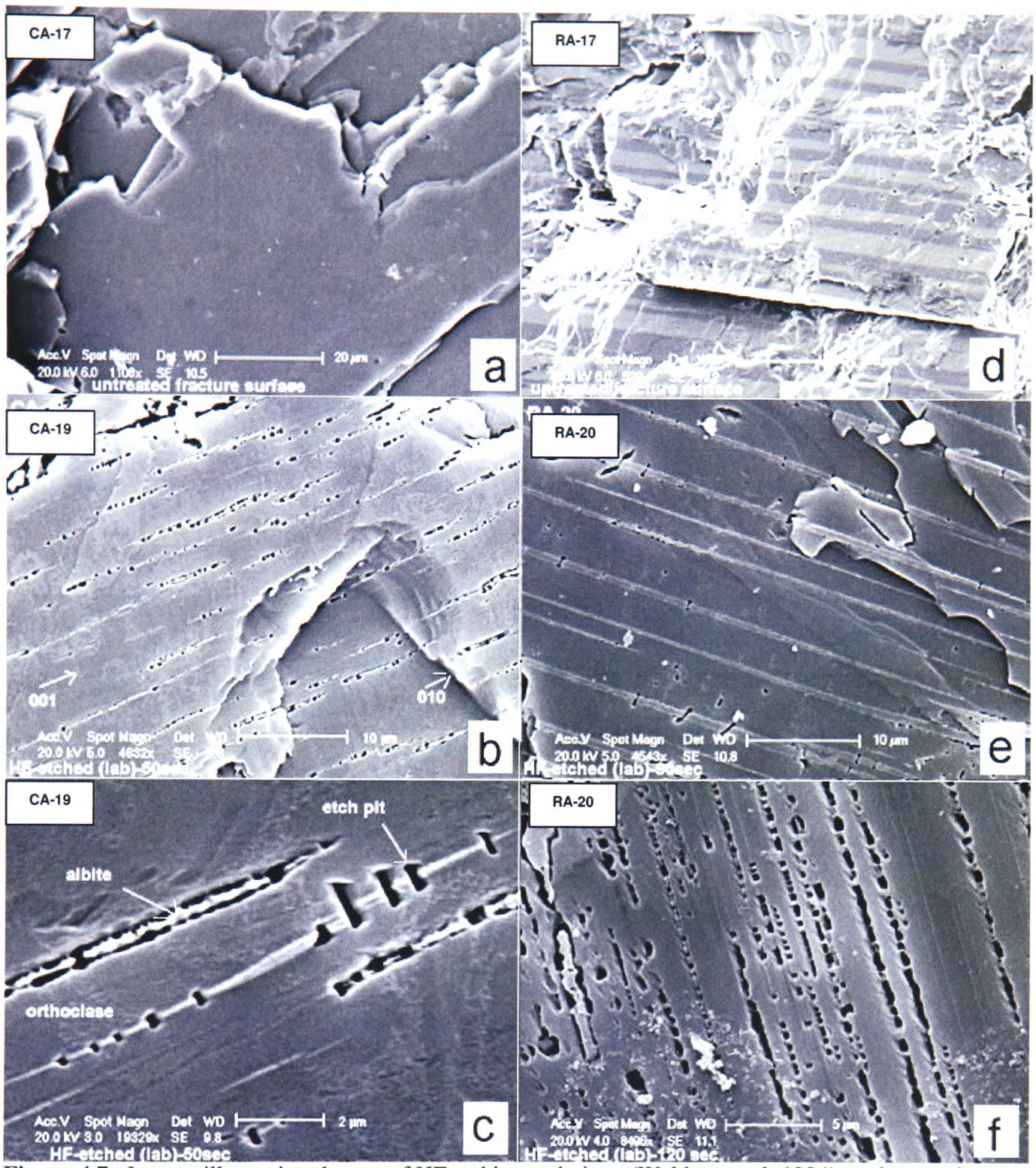

Figure 4.7 Images illustrating the use of HF etching technique (Waldron et.al, 1994) to characterize feldspar microtextures in unweathered samples from Cheras (left) and Rawang (right). (a) Untreated feldspar cleavage surface, (b,c) regular albite exsolution lamellae on the etched surface. Albite stands out as ridges. Grooves along the margins correspond with regions of high coherency strain. Paired deep etch pits have formed on the outcrop of misfit dislocations, probably in the form of nanotunnels (Fitz Gerald et al., 2006). (d) Albite twinning in a plagioclase grain, (e,f) Thin, straight exsolution lamellae with etch pits. In general, alkali feldspars from Rawang have exsolution lamellae that are longer and thinner than those from Cheras.

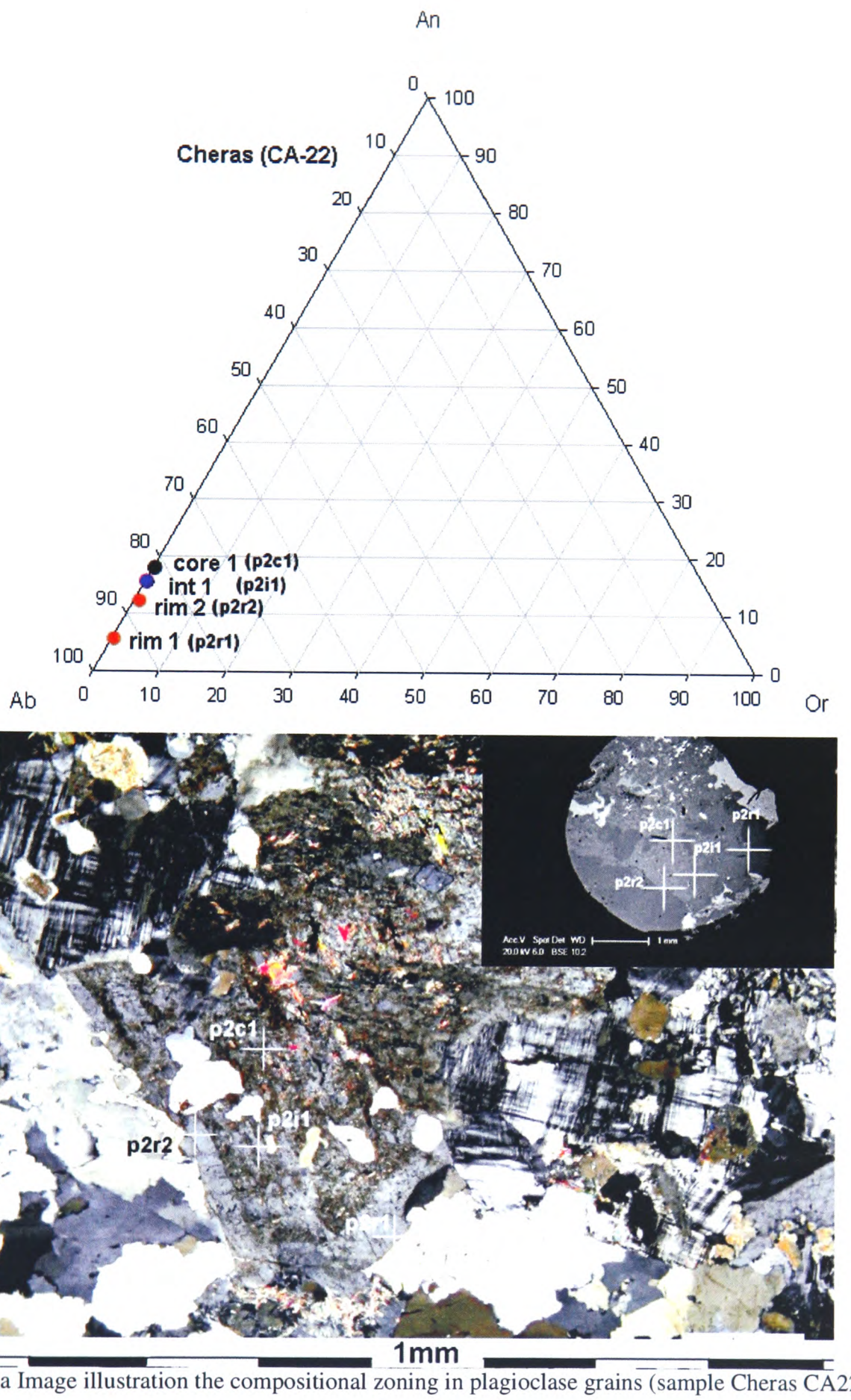

Figure 4.8a Image illustration the compositional zoning in plagioclase grains (sample Cheras CA22). Inset: BSE image of the grain. The Ca content in anorthite (An) decreases from the core towards the rim..

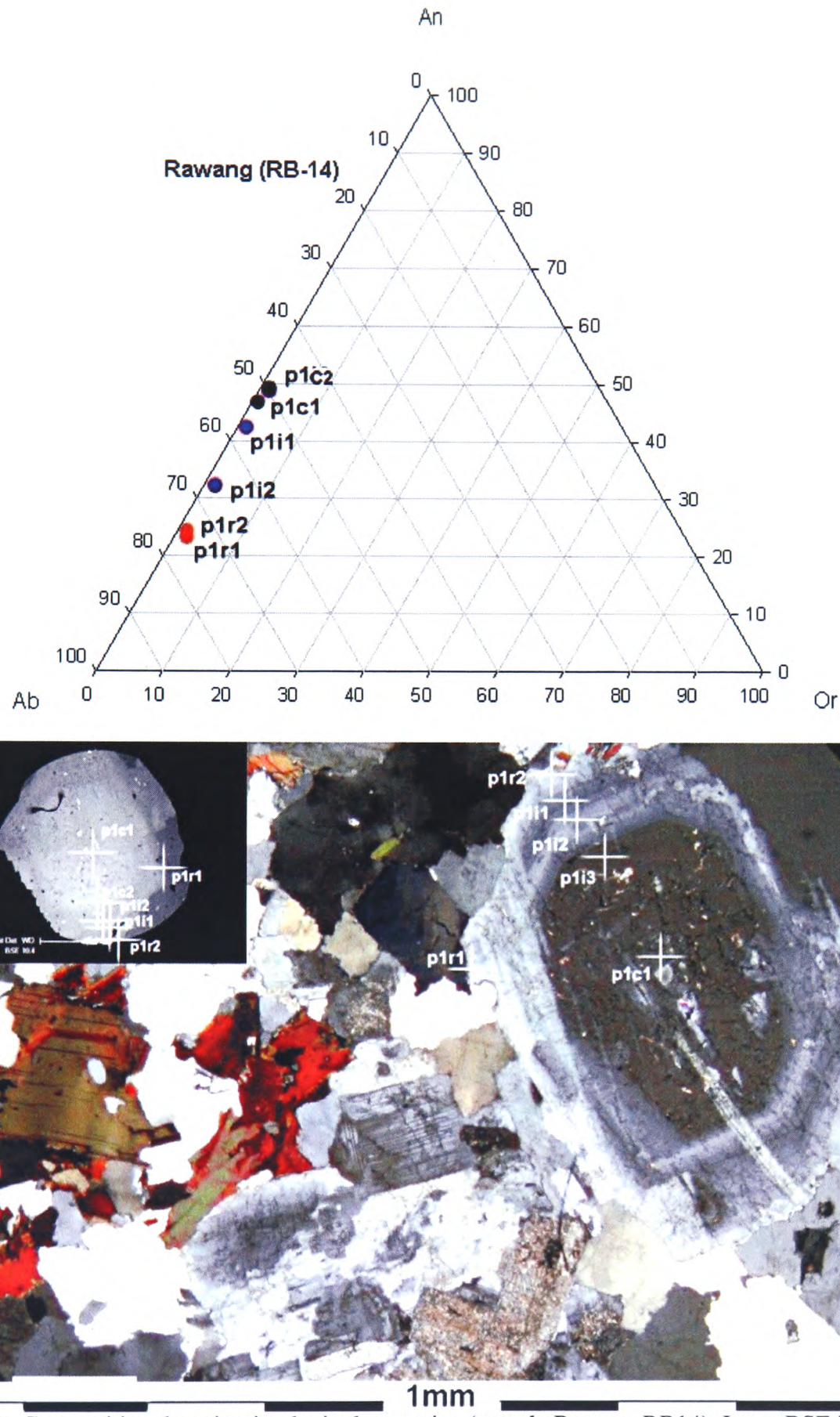

Figure 4.8b. Compositional zoning in plagioclase grains (sample Rawang RB14). Inset: BSE image of the grain. . Sample Rawang RB14 was at 29m depth (bgl) in a drilled hole (RB) about 1m adjacent to drill hole RA.

In Rawang, the end member composition is $Or_{0-2}Ab_{48-98}An_{2-51}$. Compositional zoning was clearly observed (Figure 4.8b) and again with the decrease in anorthite content from the core towards the rim.

Mineralogy

Alkali feldspar: From the ternary plots of feldspar end members based on the electron probe analyses of the bulk composition of individual grains (Table 4.7) obtained by traversing using large beam (Tables B1-1 and B1-2 in appendix B1), the alkali feldspars in Cheras and Rawang shows that they crystallized originally from magma as K-sanidine but now, following ordering and exsolution, they are low albite-microcline microperthites (Cheras) and low albite-orthoclase (Rawang). As mentioned in Section 4.1, the electron microprobe analyses were done with defocused beam and the analyses for K-feldspar (Table 4.7) give the bulk composition of the perthitic feldspar (except for the case labelled 'lamella'). Generally the mineral composition for alkali feldspar in Cheras and Rawang are $Ab_{4-11}Or_{89-96}An_{0-0.1}$ and $Ab_{8-21}Or_{79-97}An_{0.2-0.5}$ respectively.

Next page: **Table 4.7.** Feldspar end-member values calculated (Appendix B2) from electron microprobe analyses results (Appendix B1) . Samples 'RB' were taken in a drilled hole about 1m adjacent to the drilled hole for samples 'RA' in Rawang. Sample RB13 was at 28m depth and RB14 at 29m depth below ground level.(abbreviation used; *kfs1 core1*: k feldspar grain number 1 at core of the grain 1, rim: at the rim of the grain, iterm: in between the core and the rim, *plaq*: plagioclase grain)

Sample description	Or	Ab	An
Cheras K-feldspar			
CA21_kfs1_core1	92.09	7.91	-
CA21_kfs1_core2	93.33	6.61	0.07
CA21_kfs2_core1	92.35	7.59	0.06
CA22_kfs1lamella1	7.11	92.66	0.23
CA21_kfs2_core2	95.15	4.85	-
CA22_kfs4_core1	88.93	11.01	0.07
CA22_kfs4_core2	90.94	9.06	-
CA22_kfs4_rim1	95.63	4.37	-
CA22_kfs4_interm1	91.57	8.43	-
CA22_kfs4_interm2	95.27	4.73	-
CA22_kfs4_rim2	89.65	10.26	0.10
CA22_kfs1_core1	95.72	4.28	-
CA22_kfs1interm1	93.16	6.71	0.13
CA22_kfs1_rim1	92.90	7.10	-
CA22_kfs3_core1	90.08	9.79	0.13
CA22_kfs3_core2	91.63	8.34	0.03
Range, excl lamella:	89-96	4-11	0-0.1
Cheras plagioclase			
CA21_plag1_core1	0.66	92.68	6.67
CA21_plag2_core1	0.26	92.80	6.93
CA21_plag2_core2	0.69	93.38	5.94
CA22_plag1_rim1	0.53	94.89	4.58
CA22_plag1_core1	0.32	93.74	5.94
CA22_plag1_core2	0.27	97.07	2.66
CA22_plag1_rim2	0.79	95.93	3.27
CA22_plag2_rim1	0.42	94.12	5.45
CA22_plag2_rim2	0.81	87.10	12.09
CA22_plag2interm1	0.68	83.87	15.44
CA22_plag2_core1	0.42	82.05	17.53
CA22_plag3_rim1	0.45	90.06	9.48
CA22_plag3_core1	0.40	82.96	16.64
Range:	0.3-0.8	82-97	3-18
Rawang K-feldspar			
RA19_kfs1_core1	79.81	19.93	0.26
RA19_kfs1_core2	90.52	9.28	0.20
RA20_kfs1_core1	81.61	18.12	0.27
RA20_kfs1_core2	79.10	20.61	0.29
RA20_kfs1_core2b	78.64	21.10	0.26
RA20_kfs3_core1	85.97	13.57	0.46
RA20_kfs3_core2	82.37	17.43	0.20
RB-13_kfs1_core1	83.95	15.78	0.26
RB-13_kfs1_core2	88.06	11.78	0.16
RB-13_kfs2_rim1	84.60	15.14	0.26
RB-13_kfs2_int1	87.73	12.01	0.26
RB-13_kfs2_int2	92.20	7.61	0.20
RB-13_kfs2_core1	79.34	20.26	0.39
Range:	79-97	8-21	0.2-0.5

Sample description	Or	Ab	An
Rawang plagioclase			
RA19_plag1_rim1	1.88	77.20	20.92
RA19_plag1_rim2	1.75	76.30	21.95
RA19_plag1_int1	1.22	57.18	41.61
RA19_plag1_int2	1.18	51.72	47.10
RA19_plag1_core1	1.46	49.64	48.90
RA19_plag2_rim1	1.14	88.99	9.87
RA19_plag2_int1	1.01	56.41	42.58
RA19_plag2_rim2	0.46	97.84	1.69
RA19_plag2_int2	1.68	87.66	10.65
RA19_plag2_int3	2.07	78.23	19.70
RA19_plag2_int4	1.07	53.30	45.64
RA19_plag2_core1	0.84	47.67	51.49
A19_plag2_core2	1.01	77.34	21.65
RA20_plag1_core1	1.33	49.61	49.06
RA20_plag1_rim1	0.39	87.63	11.98
RA20_plag1_interm1	0.58	78.69	20.73
RA20_plag1_interm2	0.94	55.54	43.52
RA20_plag1_dark1	0.84	76.12	23.03
RA20_plag2_core1	1.03	50.79	48.17
RA20_plag2_interm1	1.30	62.57	36.12
RA20_plag2_rim1	0.46	90.58	8.95
RB-13_plag1_rim1	1.09	74.15	24.75
RB-13_plag1_int1	1.05	59.53	39.42
RB-13_plag1_int2	1.32	56.35	42.33
RB-13_plag1_core1	1.44	54.83	43.74
RB-13_plag2_rim1	0.52	96.26	3.23
RB-13_plag2_rim2	0.23	80.00	19.77
RB-13_plag2_int1	1.16	62.18	36.65
RB-13_plag2_int2	1.40	77.05	21.55
RB-13_plag2_int3	0.72	51.13	48.15
RB-13_plag2_core1	0.85	50.23	48.92
RB-13_plag2_core2	0.58	64.80	34.62
RB-14_plag1_rim1	1.99	74.76	23.25
RB-14_plag1_rim2	1.45	74.52	24.02
RB-14_plag1_int1	1.37	56.56	42.06
RB-14_plag1_int2	1.91	66.19	31.89
RB-14_plag1_ core2	1.61	50.02	48.38
RB-14_plag1_core1	1.11	52.55	46.34
RB-14_plag2_rim1	0.80	91.70	7.50
RB-14_plag2_rim2	1.40	75.59	23.01
RB-14_plag2_int1	1.08	51.34	47.58
RB-14_plag2_int2	1.09	52.65	46.25
RB-14_plag2_core1	1.19	50.98	47.83
RB-14_plag2_core2	1.09	51.21	47.70
Range:	0-2	48-98	2-51

Both Rawang and Cheras are sub-solvus, two feldspar granites, which crystallized separate plagioclase and alkali feldspar phases from magma. During subsequent cooling the alkali feldspars exsolved a third feldspar phase, albite in perthitic intergrowth with orthoclase (in Rawang) or with microcline (in Cheras). The analyses in Table 4.7 were carried out with a large beam diameter and therefore, in principle, give crystal compositions prior to exsolution.

The feldspars show the variation characteristic of I-type (Rawang) and S-type (Cheras) granites (Chappell and White, 1974). Plagioclase in Rawang has more An than Cheras and is strongly zoned (Table 4.7). Two crystal rim analyses with very low An (1.69 and 3.23 mol%) are probably albite exsolved from alkali feldspar, but otherwise plagioclase is in the range Ab_{48-92} mol%. In Cheras the compositional range is limited to Ab_{82-97}. In Rawang Or in plagioclase is higher (average 1.2 mol%) than Cheras (average 0.5 mol%). Like plagioclase, alkali feldspars in Rawang have a larger range in composition (Or_{79-97}, mean Or_{84}) than Cheras (Or_{89-96}, mean Or_{93}) and a higher An content ($An_{0.2-0.5}$, mean $An_{0.3}$) than Cheras (maximum $An_{0.23}$, many with Ca below detection limit). The presence of orthoclase in Rawang and microcline in Cheras is also consistent with their I- and S-type character.

In broad terms the compositional variation suggests higher crystallization temperatures for Rawang, consistent with its I-type character and its mafic mineral assemblage. However, an attempt to obtain crystallization temperatures using two-feldspar thermometry (I. Parsons pers. comm., 2008) was only partially successful. The thermometer of Elkins and Grove (1990) was used within the computer package SOLVCALC (Wen and Nekvasil, 1994). When dealing with zoned mineral assemblages such as Rawang feldspar pairs it is difficult to determine which pair of compositions represent equilibrium. A combination of the most An-rich plagioclase found in Rawang with the most Ab-rich alkali feldspar gave a crystallization temperature of 758°C at 3 kbars pressure, which is reasonable, but many other combinations failed the tests built into the Wen and Nekvasil package. All feldspar pairs tried from Cheras gave

implausibly low temperatures in the range 294 to 436°C at the same pressure. The reason for these low temperatures lies with the extremely low Or content of the Cheras plagioclase and the low An content of the alkali feldspar (Table 4.7). All two-feldspar thermometers are extremely sensitive to these minor components. The assemblage found might be explained by intercrystal subsolidus re-equilibration in Cheras. This is consistent with the pervasive development of microcline in Cheras, rather than orthoclase as in Rawang, which is generally taken to be a result of fluid–feldspar reactions in the microcline stability field, at or below 450 °C (Brown and Parsons 1989). S-type granites are general considered to crystallise from more water-rich magmas than I-type.

Plagioclase: Electron probe analysis showed that the unweathered plagioclase grains in the Cheras and Rawang granites have compositions in the range $Ab_{82\text{-}97}An_{3\text{-}18}$ $Or_{0.3\text{-}0.8}$ and $Ab_{48\text{-}98}An_{2\text{-}51}Or_{0\text{-}2}$ respectively (Table 4.7, Figure 4.8).

Micas: In Cheras, muscovite was detected by QXRPD and confirmed with optical microscopy. Its content ranged from about 6 to 10wt% (Table 4.1). In Rawang, biotite made up about 3 to 7wt% (Table 4.2) and muscovite was absent, and this was confirmed by optical microscopy.

Other: In both the Cheras and Rawang granites, traces of kaolin were found to be present using QXRPD, about 0.5 to 2 wt% in Cheras (Tables 4.2) and about 0.3 to 1.1 wt% in Rawang (Table 4.2). Kaolin here refers to undifferentiated kaolin group minerals, comprising kaolinite and halloysite. Normally kaolin occurs in unweathered granites because of hydrothermal activity. In Rawang, chlorite made up about 3 to 6wt%. Accessory minerals present in the Cheras granite were zircon, apatite, monazite and epidote, and in Rawang anatase, zircon, apatite and monazite. Some of these minerals observed under optical microscopy are shown in Figure 4.9.

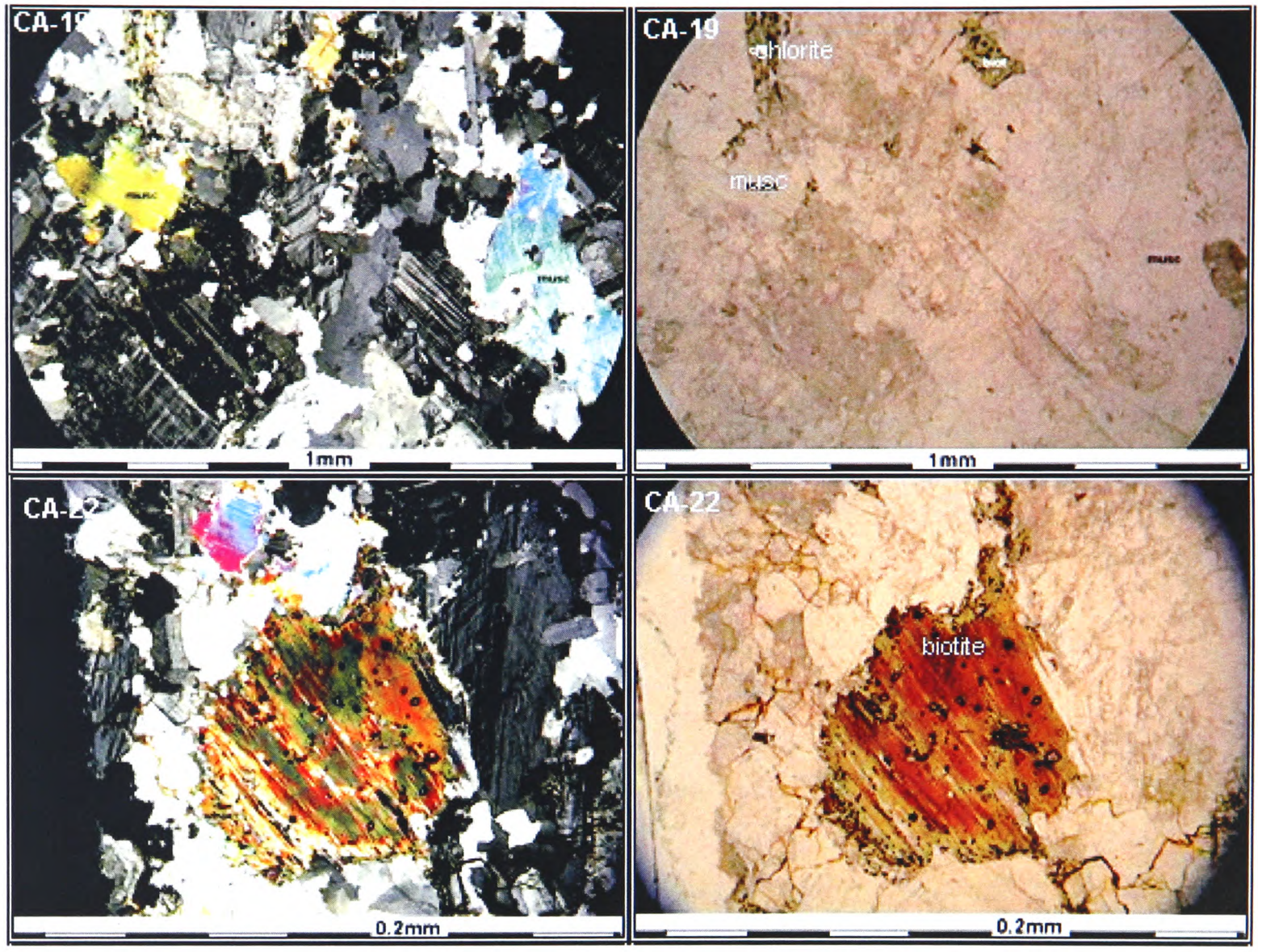

Figure 4.9a. Optical micrograph of Cheras unweathered granite zones showing the occurrence of muscovite and biotite with zircon as inclusions. Images on the right column are under plane polarised light.

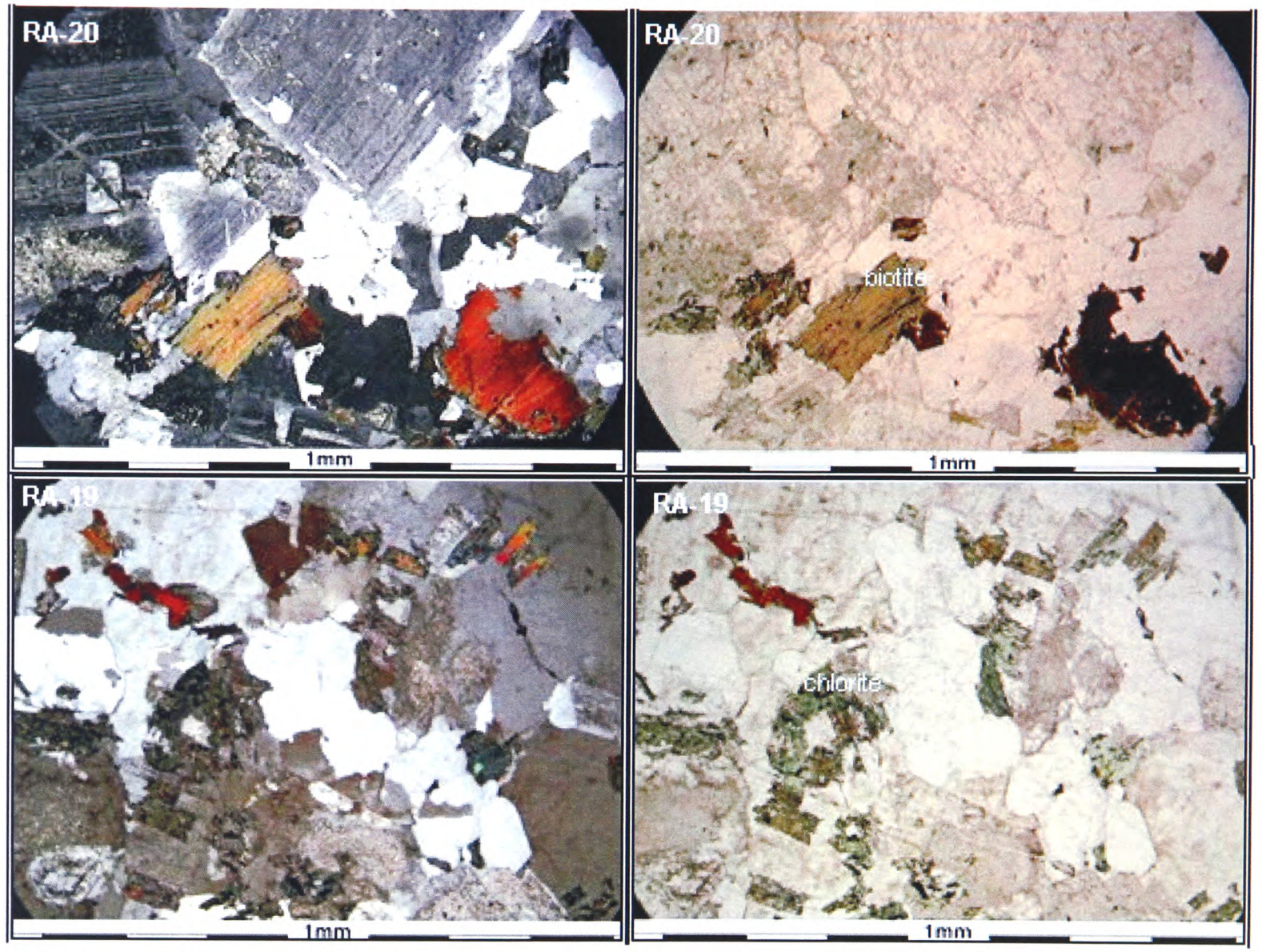

Figure 4.9b. Optical micrograph of Rawang unweathered granite zones._showing the occurrence of biotite and chlorite. Images on the right column are under plane polarised light.

Major Element Geochemistry

Both the Cheras and Rawang granites are rich in silica with about 72 to 77 wt% in Cheras (Table 4.4) and 67 to 72 wt% in Rawang (Table 4.5). Alumina content ranges from 13 to 15wt% in Cheras and 14 to 16wt% in Rawang. CIPW Mineral norms were calculated for unweathered granites (Table C1-1 to C1-10 in appendix C), tabulated in Table 4.6c. The CIPW norm gives Ab, Or and An but does not show how they are distributed. The electron probe analyses are more informative.

4.2.3 The weathering boundary zone

Mineralogy

Alkali feldspar: In both Cheras and Rawang profiles, alkali feldspar shows an initial stage of weathering. K-feldspar cleavage surfaces (Figure 4.10) have been naturally etched showing that albite in exsolution lamellae has dissolved. In some grains, albite is still present inside the exsolution lamellae while in others, albite has totally etched away. Note that this behaviour is different to the etching seen using HF as the etching agent, when K-feldspar dissolves most rapidly (Figure 4.7). Some grains were relatively unaffected by the dissolution processes (Figures 4.11). Generally, the amount (in wt%) of K-feldspar present within this zone was the same as in the unweathered zone in Cheras (Table 4.1) and in Rawang (Table 4.2).

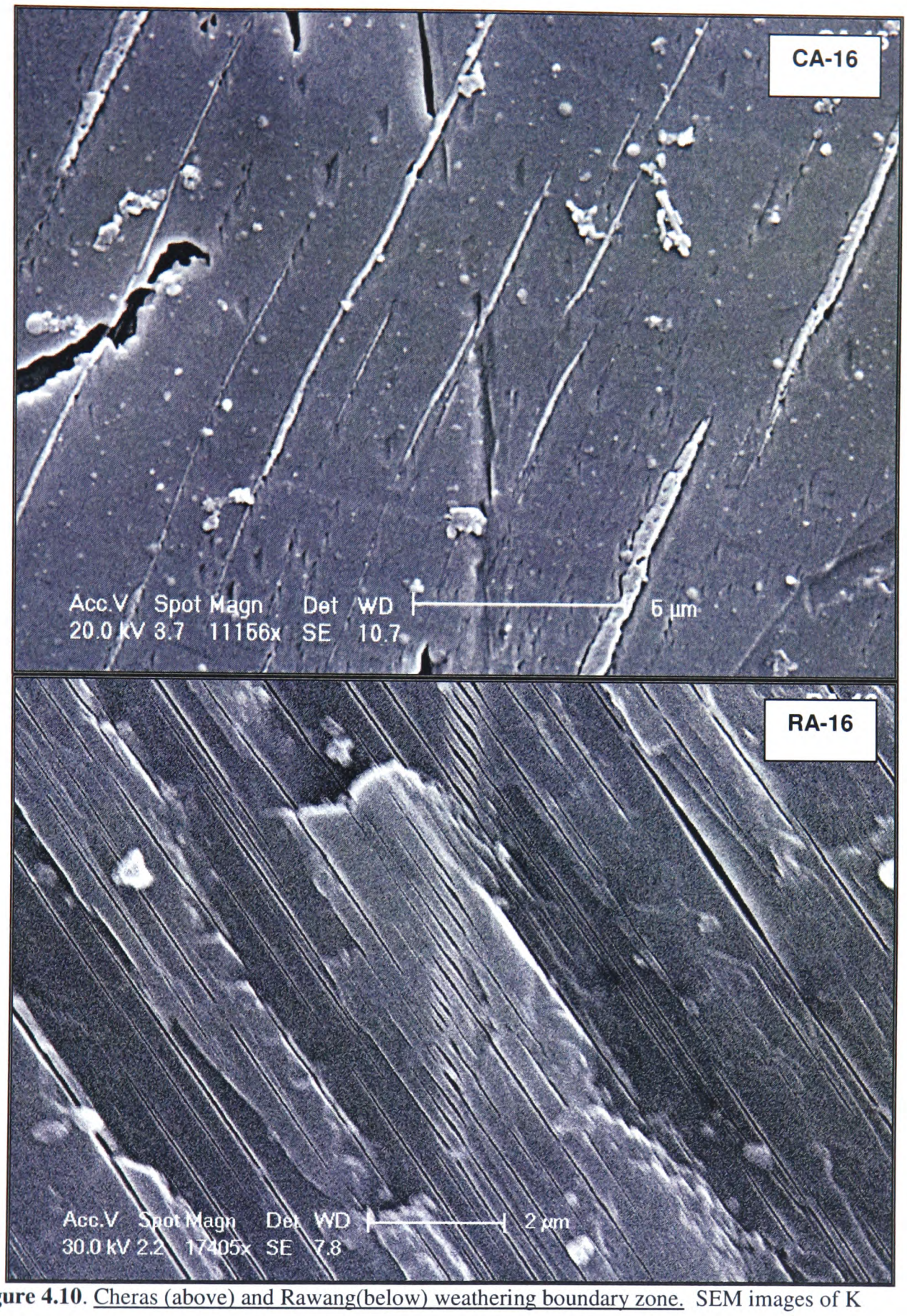

Figure 4.10. Cheras (above) and Rawang(below) weathering boundary zone. SEM images of K feldspar cleavage surfaces. The surfaces have been naturally etched by the weathering agents at different rates. (Top): Albite is still present in the exsolution lamellae and (bottom): completely dissolved.

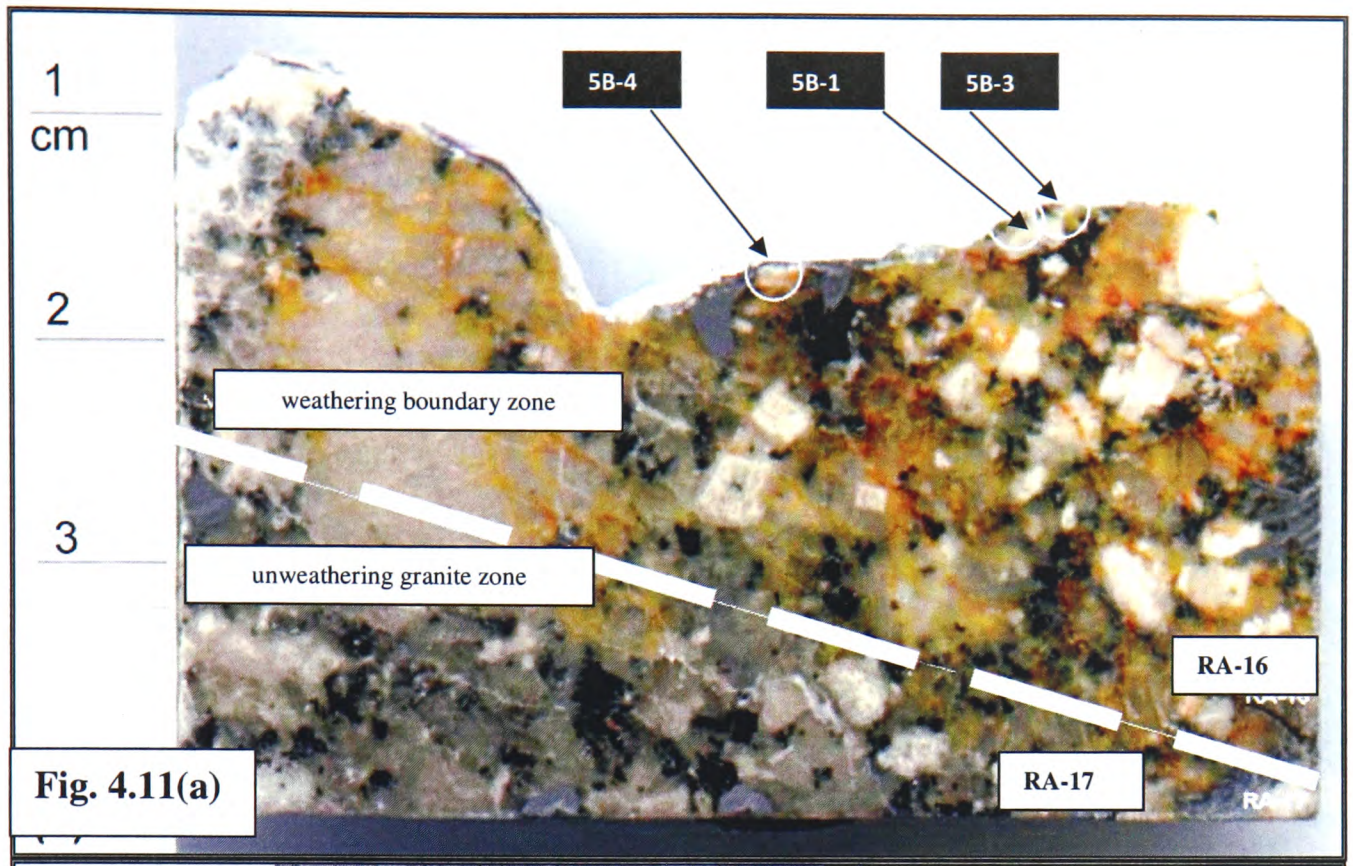

Fig. 4.11(a)

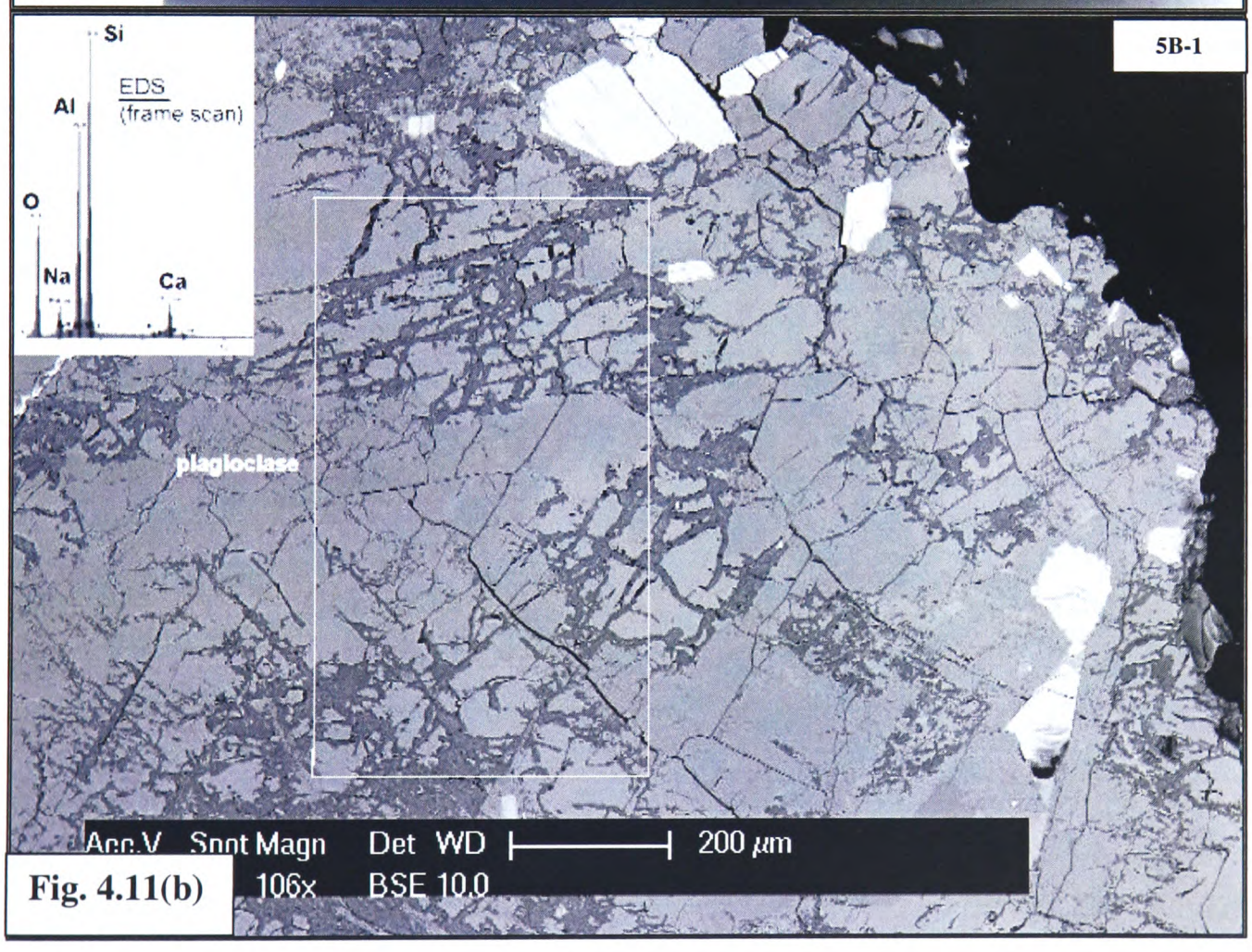

Fig. 4.11(b)

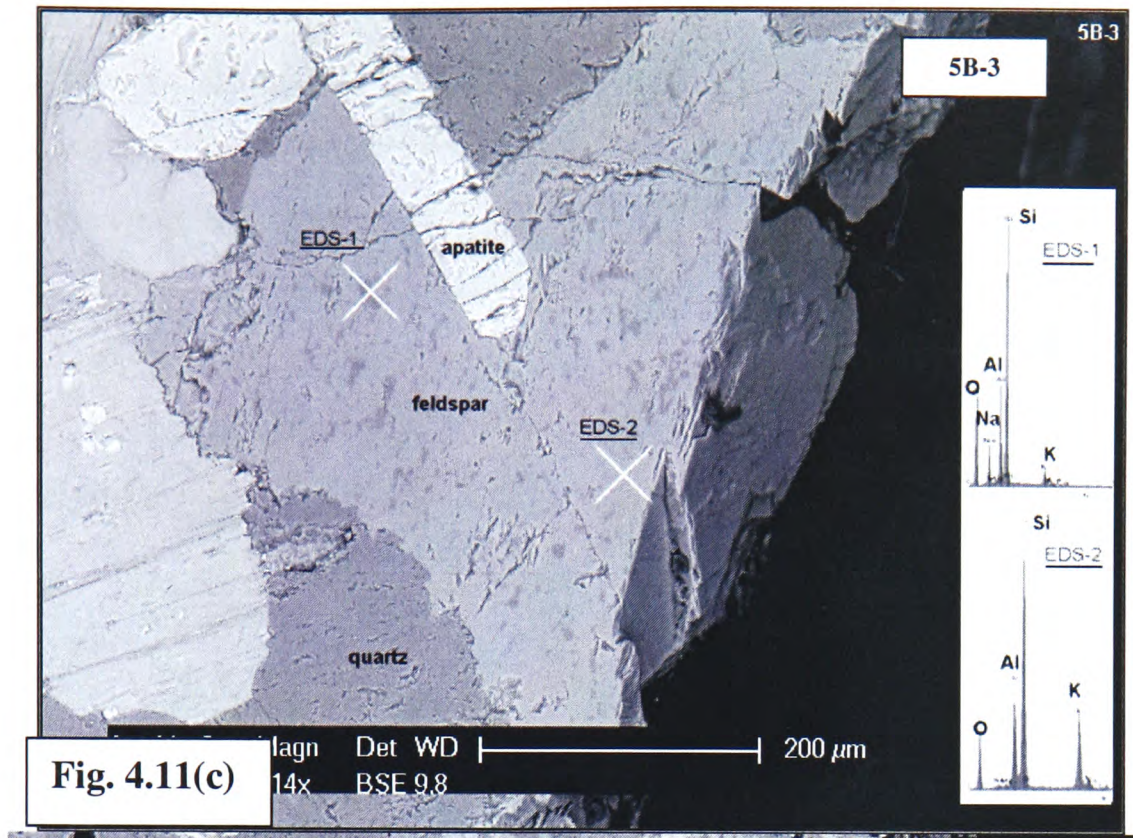

Fig. 4.11(c)

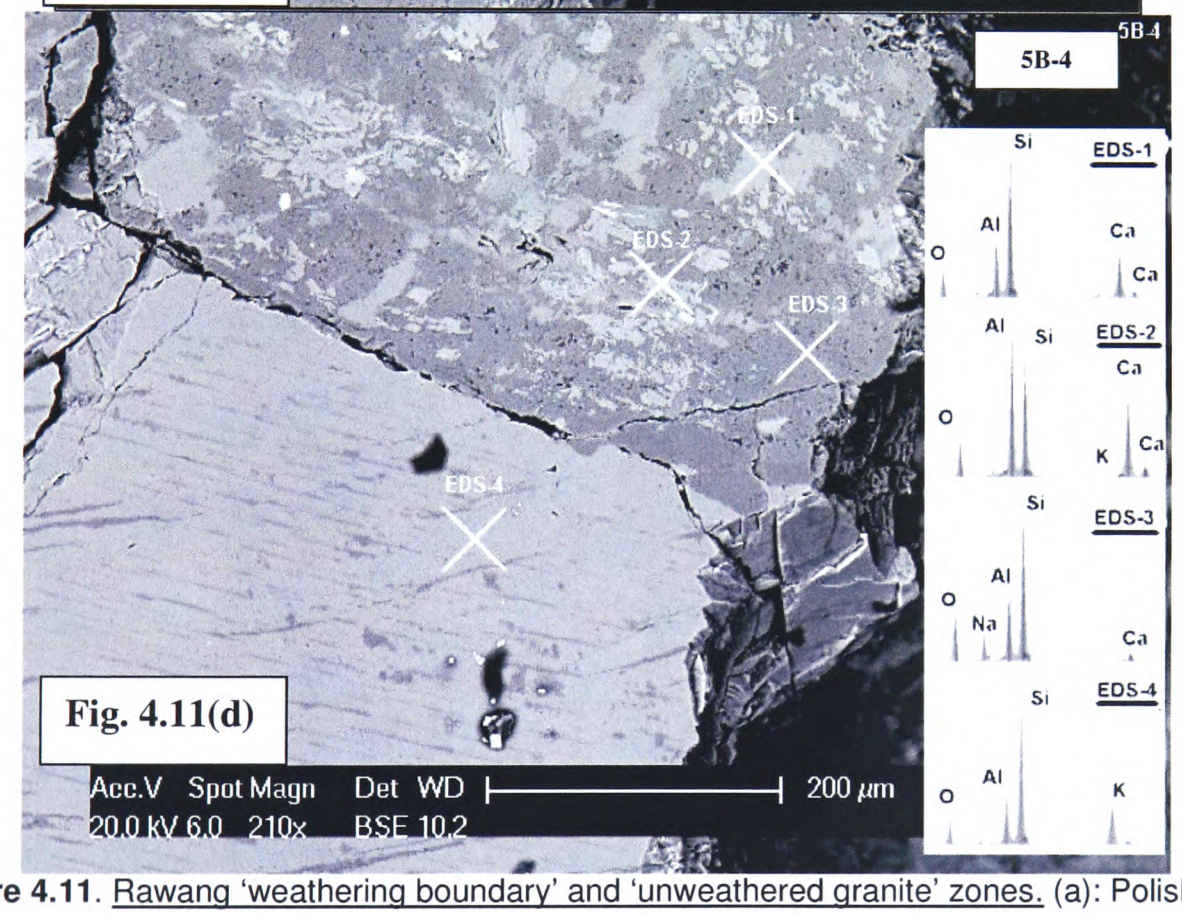

Fig. 4.11(d)

Figure 4.11. Rawang 'weathering boundary' and 'unweathered granite' zones. (a): Polished section showing the arbitrary line between the two zones and locations of BSE images to be taken. (b): BSE image of plagioclase grain with a network of fractures filled with clay minerals, (c) patch perthite alkali-feldspar which was not affected by weathering processes, and (d) plagioclase and perthitic K-feldspar , also not affected by weathering. The white thick lines on Fig. 4.11a corresponds with line on Fig. 4.4. Figures 4.11b,c and d are BSE images.

Plagioclase:

Plagioclase and perthitic albite dissolve, leading to the decrease in Na_2O, before K-feldspar dissolves (Figure 4.12). Under SEM, dissolution can be seen to have occurred along the twins and this could probably due to coherency strain in the twin walls. K-feldspar gradually disappears as we approach the saprolite. The plagioclase grains develop a network of fractures and in some cases, are totally altered and these networks are clearly visible in the BSE images (Figure 4.11b). In both Cheras and Rawang profiles, the amount of plagioclase decreases sharply within the boundary zone (Tables 4.1, 4.2).

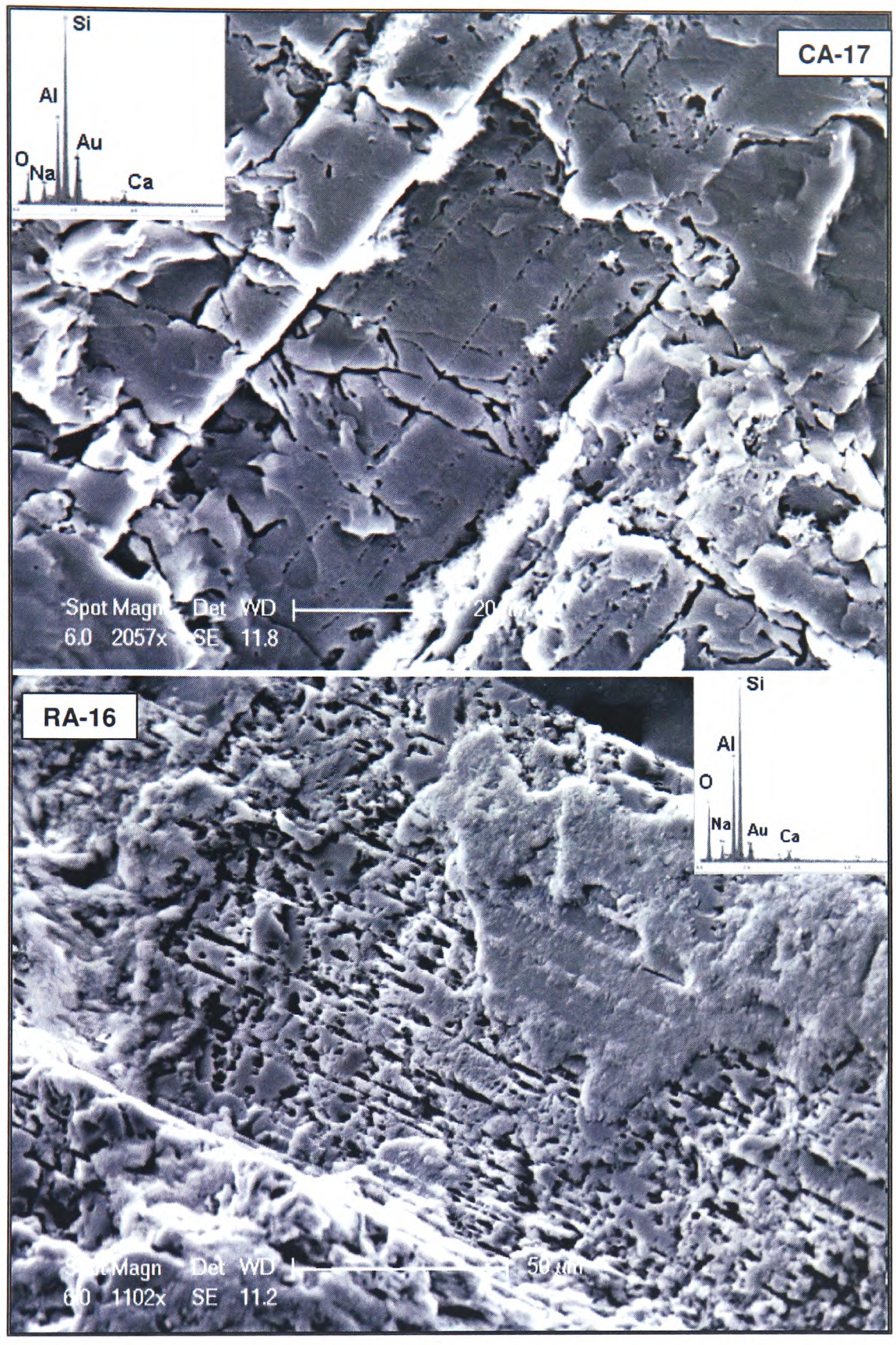

Figure 4.12 .Cheras and Rawang weathering boundary zones. SEM image of weathered plagioclase in Cheras CA-17 (top) and Rawang, RA-16 (bottom). Dissolution occurs where twin boundaries intersect the cleavage surface, presumably because of coherency strains.

Clay minerals and oxides: Generally, the amount of kaolinite is slightly higher than in the unweathered granite zone 2.00 to 5.36 wt % compared to 0.65 to 1.90wt% in Cheras, (Table 4.1) and 1.84 to 2.40wt % compared to 0.30 to 1.16wt% in Rawang, (Table 4.2). In Cheras, halloysite can be observed on the K-feldspar fracture surfaces (Figure 4.13), sometimes growing together with hematite (Figure 4.14). Hematite (α-Fe_2O_3) can also be seen covering the surface of alkali feldspar grains (Figure 4.15). In Rawang, halloysite were present in fractures and appeared as a thin layer on the feldspar surface presumably because it grew into a confined space (Figure 4.16). Similarly, smectite was present in confined spaces (Figure 4.17) or grew freely in cavities and feldspar surfaces (Figures 4.23 and 4.24). Smectite was observed only in Rawang. From the trends of kaolin observed in Figures 4.6 and 4.7, it can be said that the formation of clay minerals and oxides by the weathering process was at its beginning stage. Hematite, halloysite and smectite were identified from the EDS analyses (in the scanning electron microscope) and by their morphology (Welton, 1984; S. Hillier pers. comm. 2008).

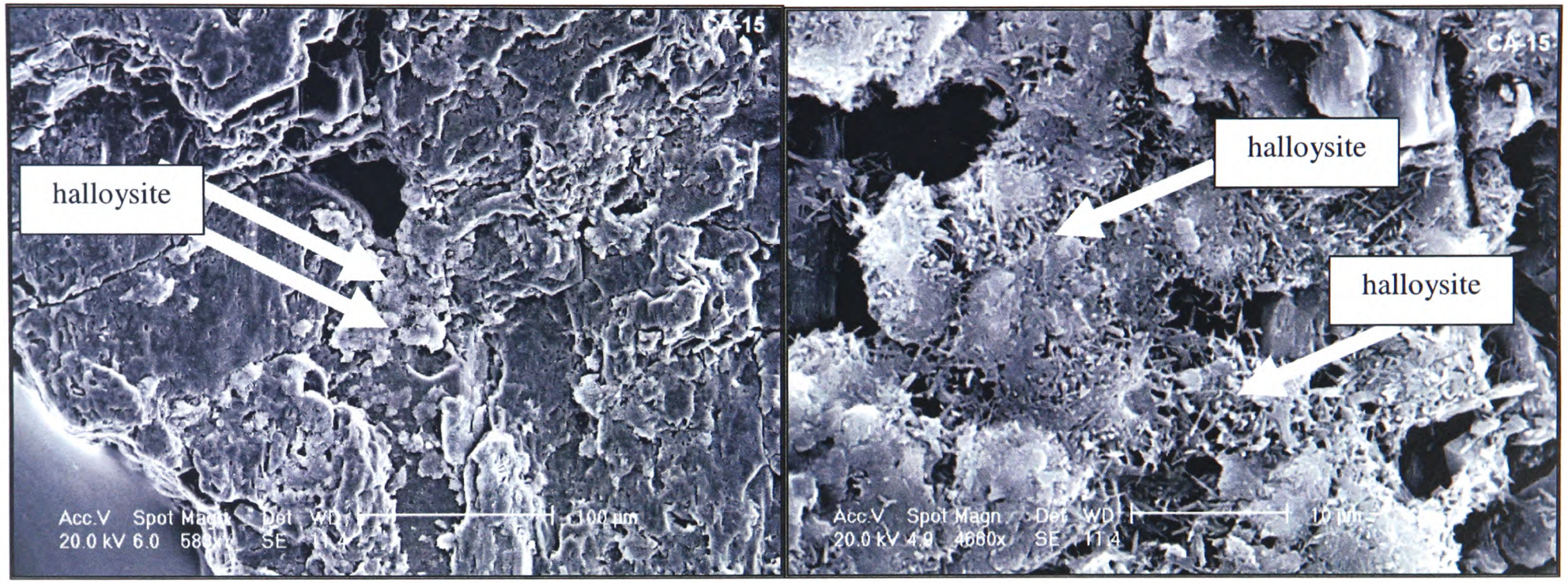

Figure 4.13. Cheras weathering boundary zone. SEM image showing the distribution of halloysite seen on feldspar grain surface (left). High magnification of the plagioclase surface (right).

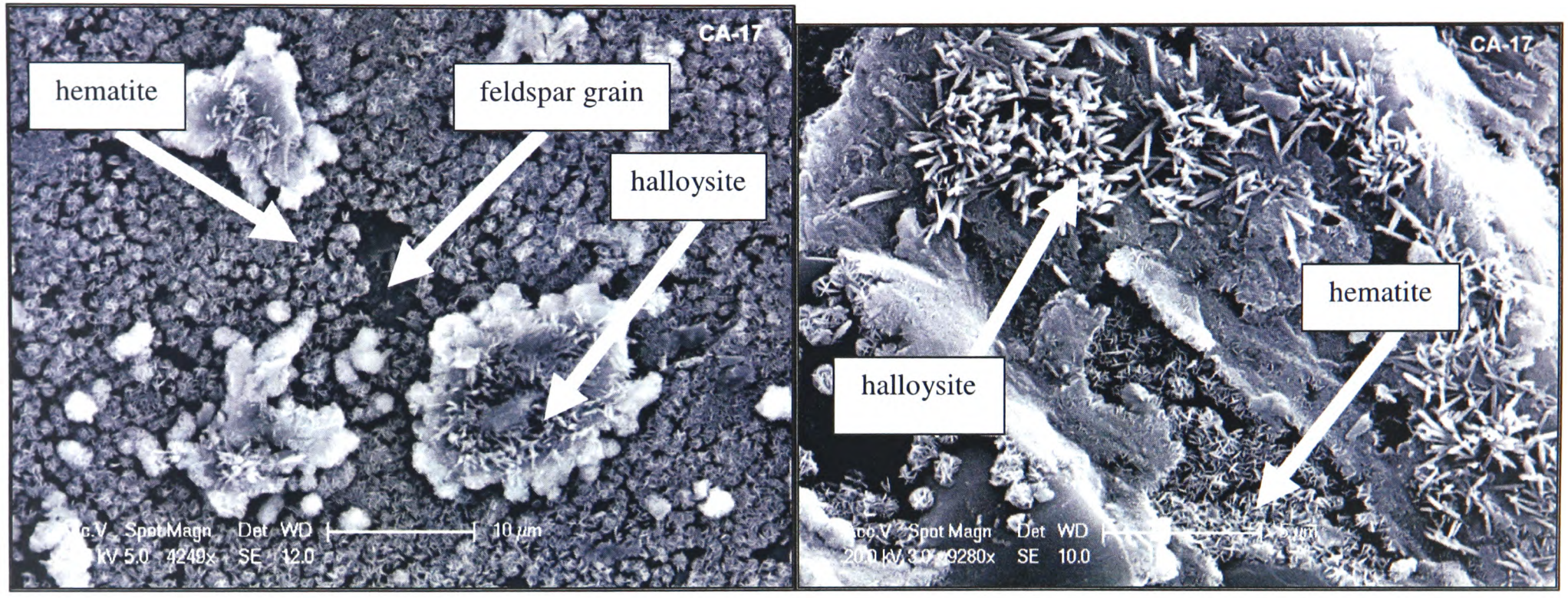

Figure 4.14. Cheras weathering boundary zone. SEM image of halloysite and hematite growing on feldspar grain. (Left): Distribution of halloysite-hematite clusters on the surface. (Right): high magnification

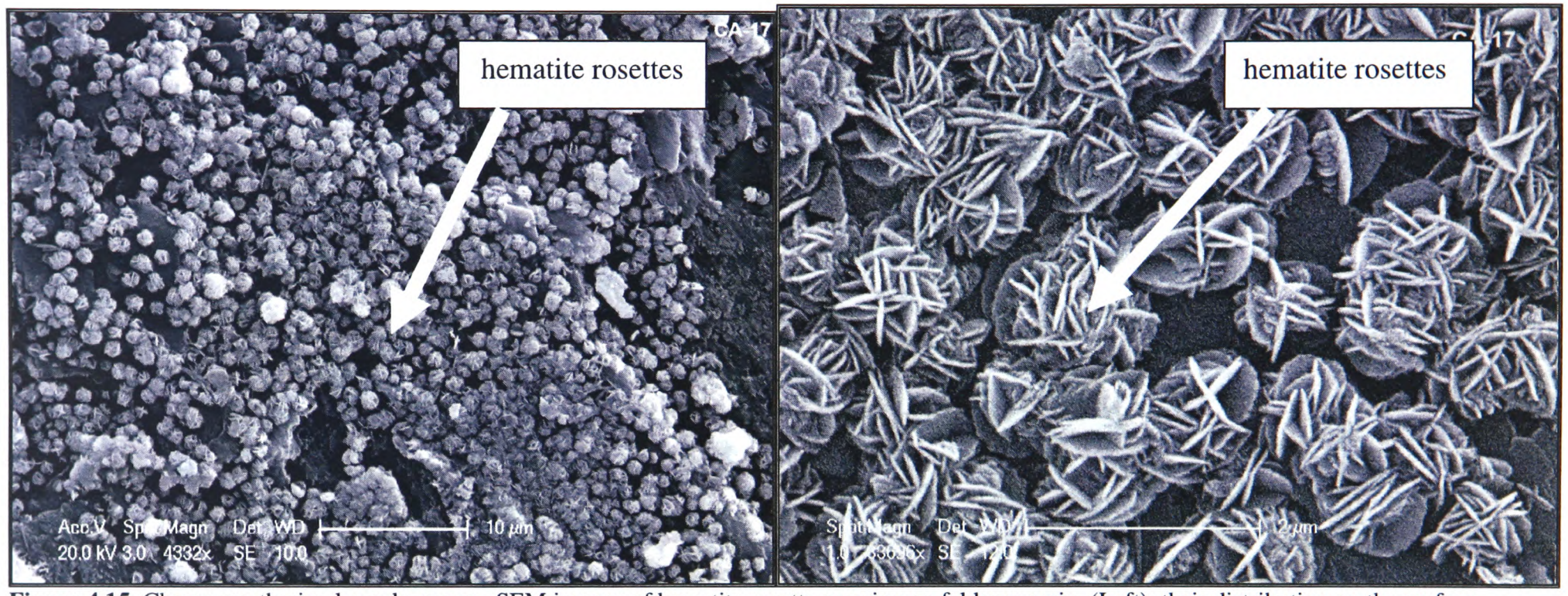

Figure 4.15. Cheras weathering boundary zone. SEM images of hematite rosetts growing on feldspar grain. (Left): their distribution on the surface. (Right): Rosetts at high magnification.

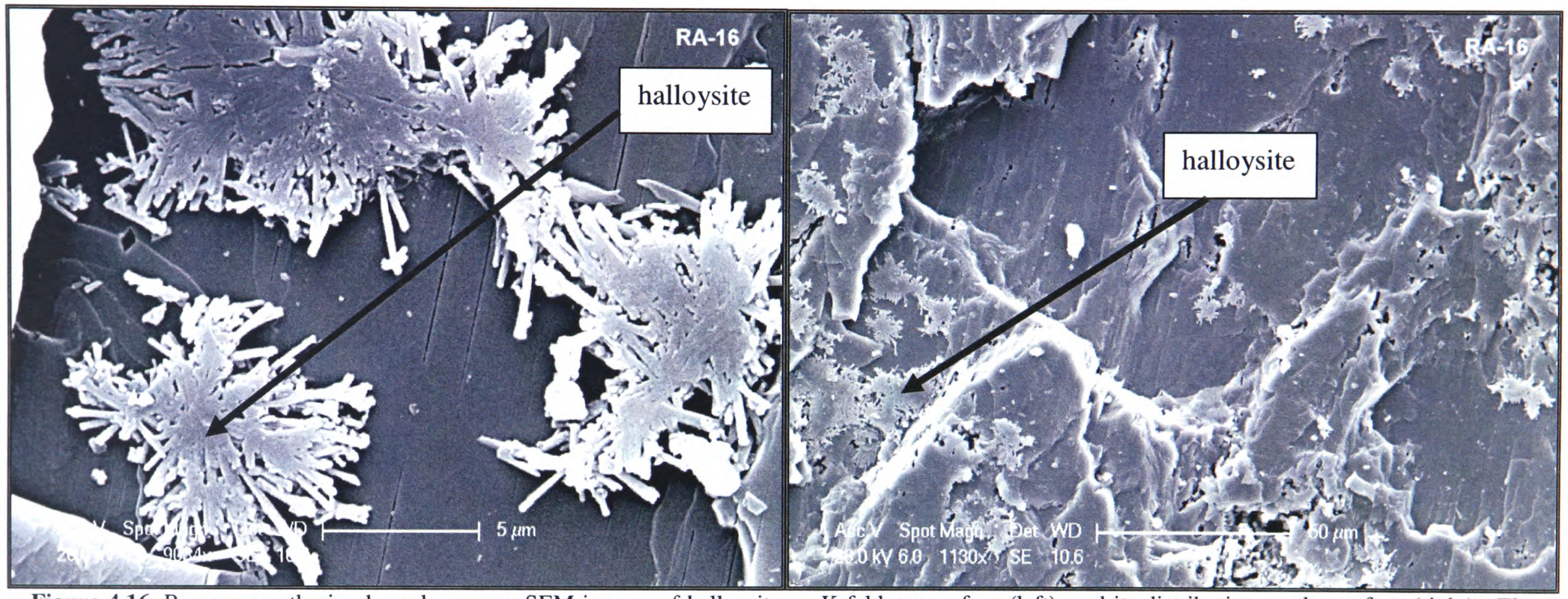

Figure 4.16. Rawang weathering boundary zone. SEM images of halloysite on K-feldspar surface (left), and its distribution on the surface (right). The halloysite seems to be flattened and probably be grew in-between fractures.

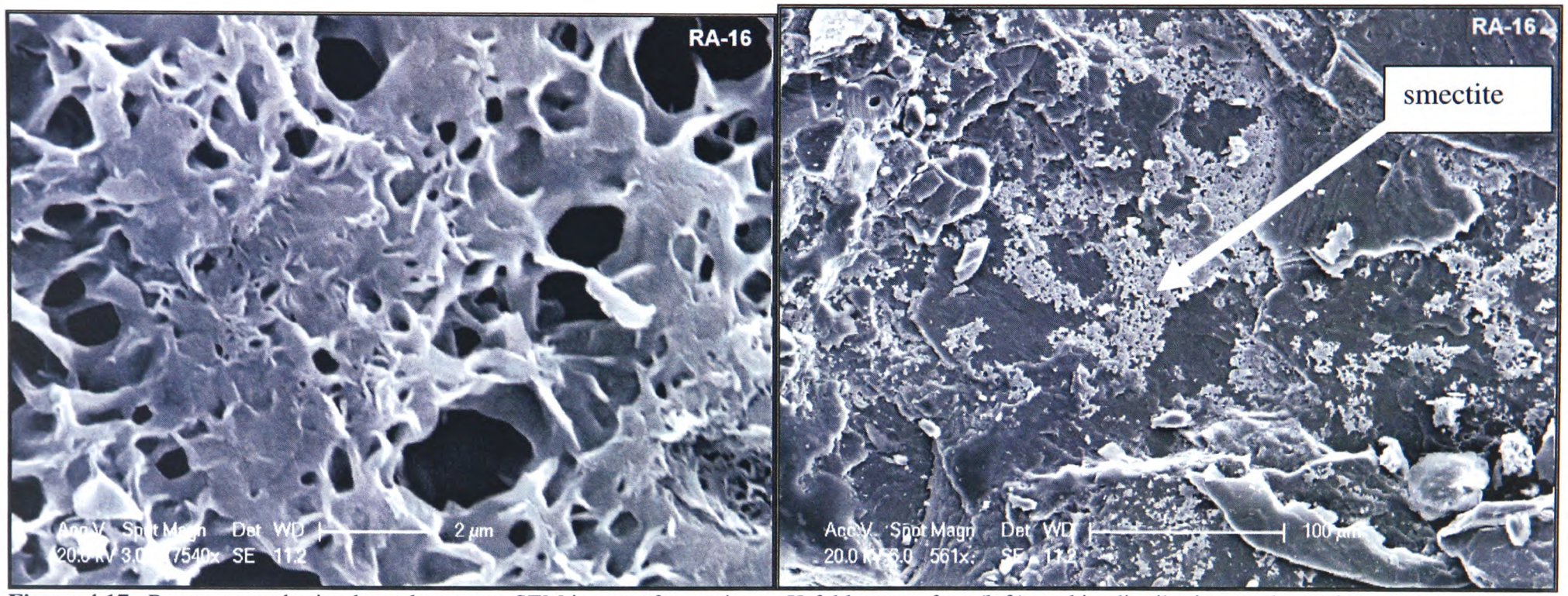

Figure 4.17. Rawang weathering boundary zone. SEM image of smectite on K-feldspar surface (left), and its distribution on the surface (right). The smectite seems to be flattened and probably be grew in fractures, similar to halloysite in Figure 4.21.

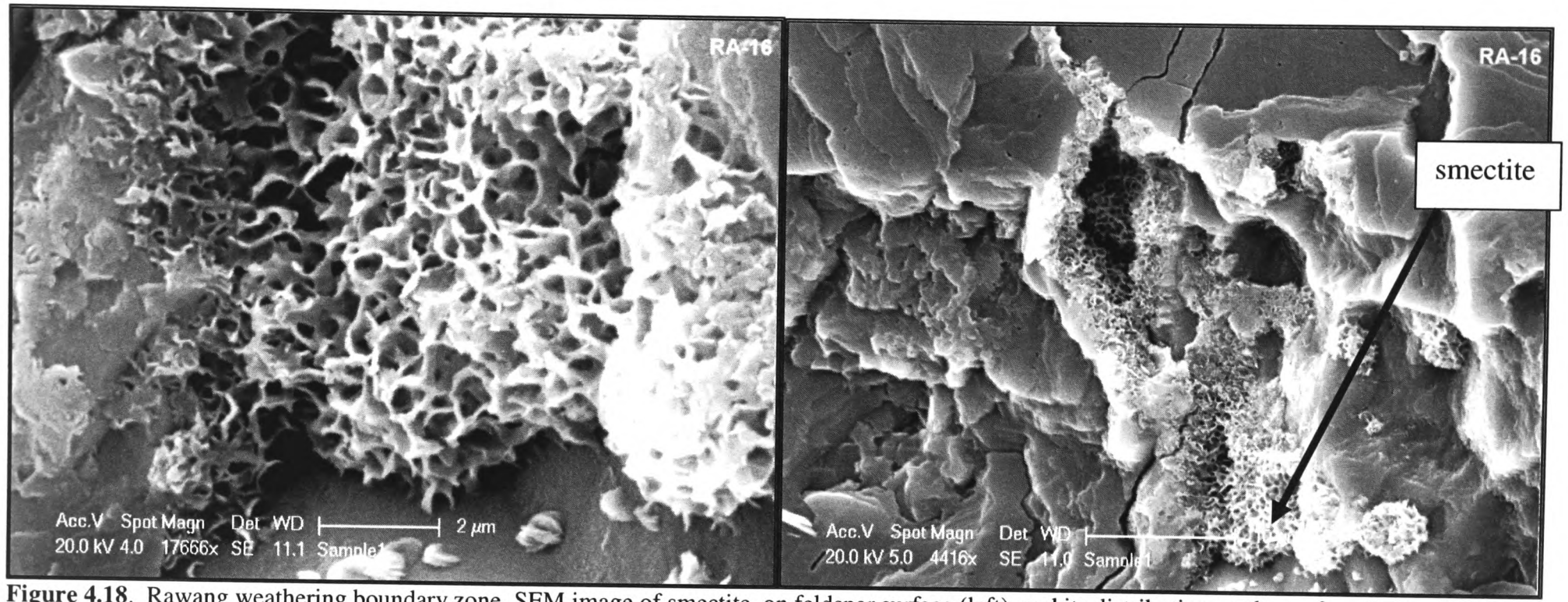

Figure 4.18. Rawang weathering boundary zone. SEM image of smectite on feldspar surface (left), and its distribution on the surface (bottom). The smectite has grown in open spaces in between mineral grains.

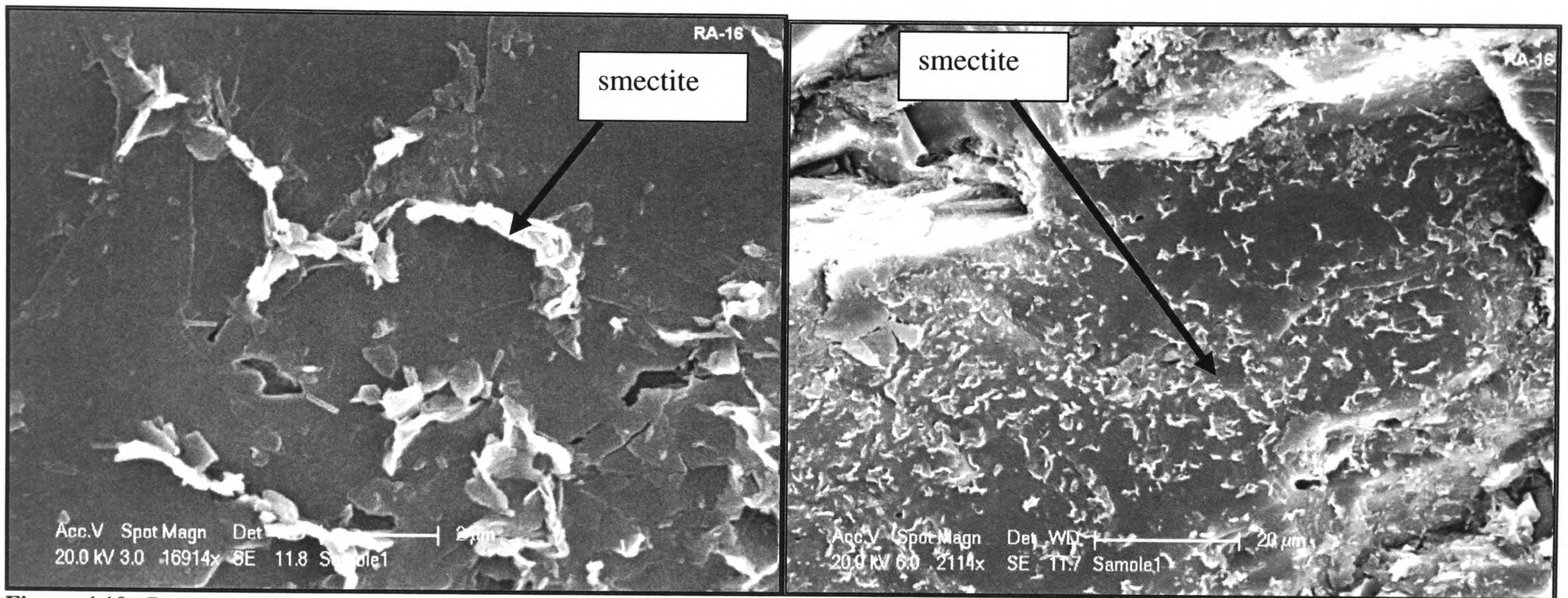

Figure 4.19. Rawang weathering boundary zone. Another SEM image of smectite, with a different morphology, growing on K-feldspar surface (left), and its distribution on the surface (right).

Others: Accessory minerals surviving in the boundary zone, detected by the optical microscope, in Cheras were zircon, apatite, monazite and epidote and in Rawang were anatase, zircon, apatite and monazite

Major Element Geochemistry

Generally, the XRF analysis of major elements Cheras granite showed a constant amount of major elements within a boundary zone. An apparent variation in the amount of certain elements can only be observed when comparing with that in the saprolite zone. In the Rawang granite, due to the difficulty in obtaining samples from this zone, the general trend of the major elements geochemistry could not be observed (Figures 4.9). This is mainly because the analysed samples in this zone are residual rock fragments of weathered materials.

4.2.4 The saprolite zone

Mineralogy

Alkali feldspar. In the Cheras profile, traces of this mineral were detected right to the topsoil (Table 4.1). Based on the amount present from the QXRPD analysis, it can be grouped into 2 categories: (i) trace: about 1wt% or less and (ii) small amount: about 3 to 10wt%. Sample CA13 is not part of the saprolite as discussed earlier (Figure 4.5). Alkali feldspar was not found in the saprolite from Rawang (Table 4.2).

Plagioclase. Traces of the mineral were detected, from the QXRPD analysis, below the 4m and 27.5m depths (below the ground level) in the Cheras and Rawang profiles respectively while K-feldspar declines almost to zero (Tables 4.2 and 4.3). This suggests that the traces of plagioclase (detected by the QXRPD analysis) between 7.5m to 4m depth in the Cheras profile were actually perthitic albite that remained as exsolution lamellae in the alkali feldspar. This is based on the SEM, optical microscopy and QXRPD analyses. This albite is similar to that observed on some of the alkali feldspar fracture surfaces in the weathering granite zone (Figure 4.20).

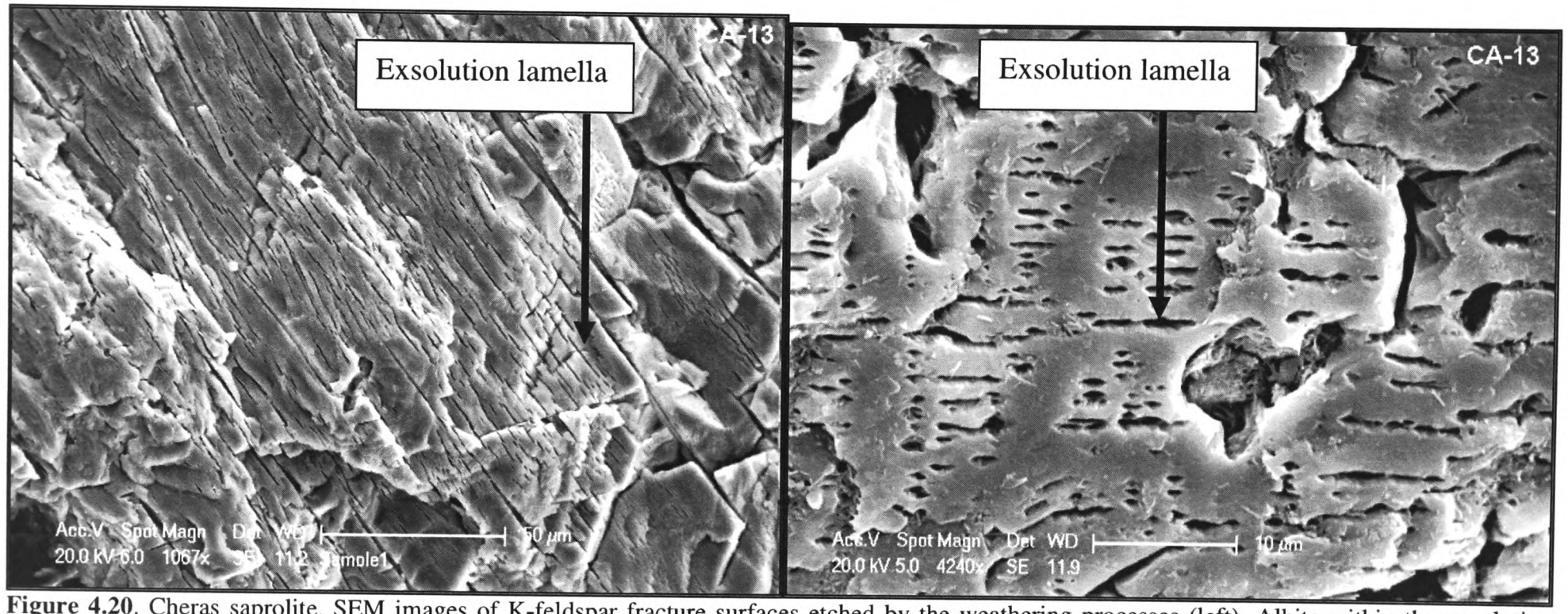

Figure 4.20. Cheras saprolite. SEM images of K-feldspar fracture surfaces etched by the weathering processes (left). Albite within the exsolution lamellae has been dissolved. Higher magnification showing the 'empty' exsolution lamellae (right).

Clay minerals. In both Cheras and Rawang profiles, kaolin was at its maximum amount just above the weathering zone and gradually decreased upwards, then there was a slight enrichment (Cheras: Table 4.1, Rawang: Table 4.2). Halloysite could be observed in abundance under SEM from the upper part of the 'weathering boundary' zone to about this level (Figures 4.21, 4.22). It could be seen easily when powdered samples were sprinkled randomly onto the SEM stubs. In the Cheras profile, apart from kaolinite and halloysite, no other clay mineral was detected.

In the Rawang profile, vermiform kaolinite was seen under SEM at 26.0m depth, (Figure 4.23). Smectite was not seen in the Rawang saprolite, only in the weathering boundary zone.

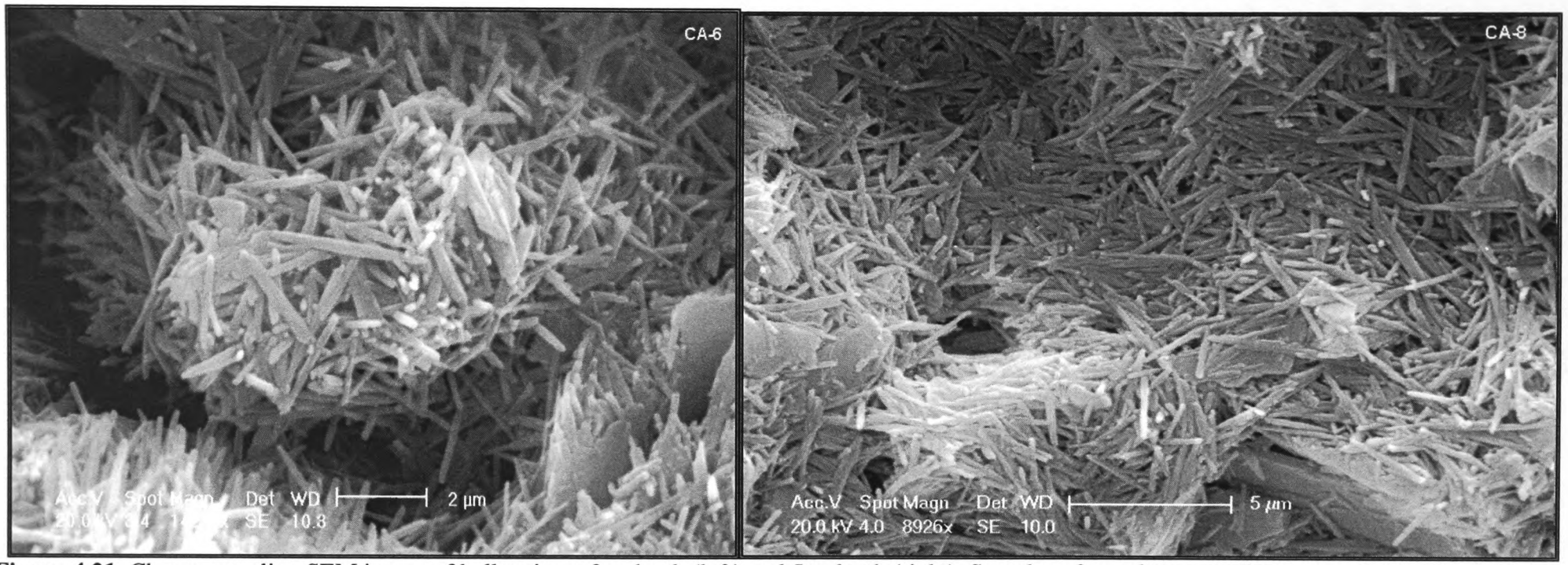

Figure 4.21. Cheras saprolite. SEM image of halloysite at 3m depth (left) and 5m depth (right). Samples of powdery saprolite were sprinkled randomly onto SEM stubs before being gold-coated for the SEM imaging.

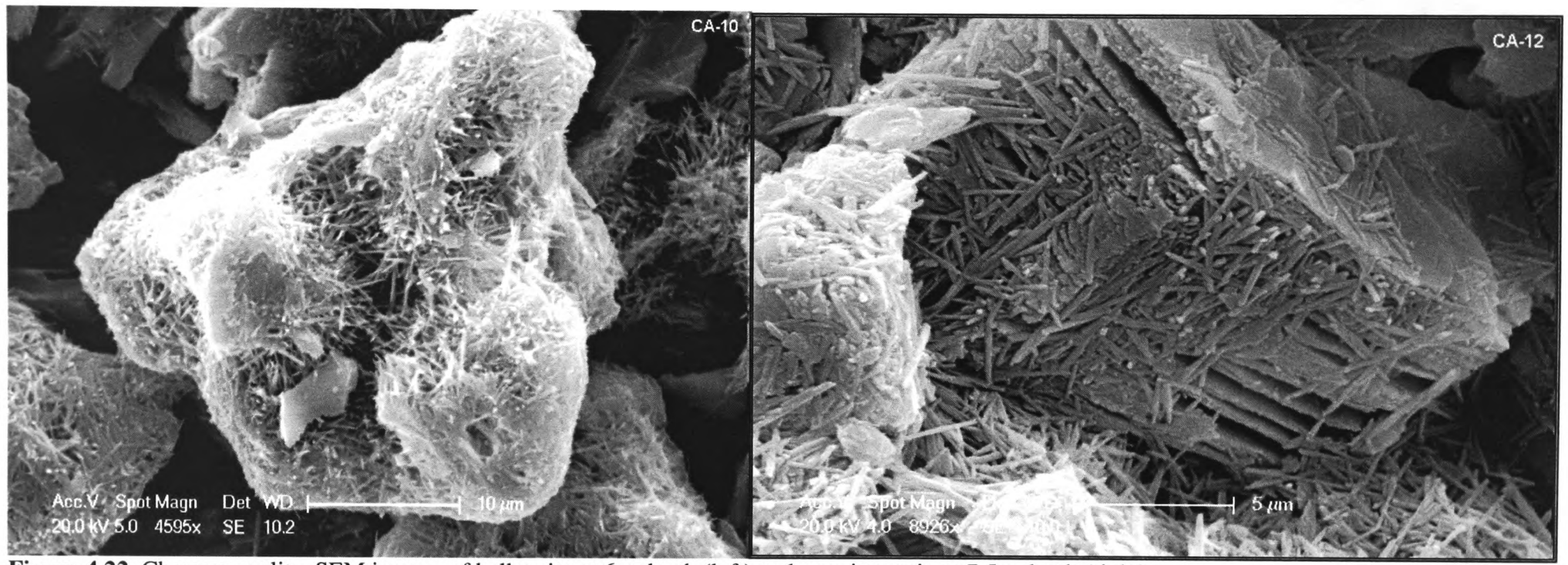

Figure 4.22. Cheras saprolite. SEM images of halloysite at 6m depth (left) and on mica grain at 7.5m depth (right).

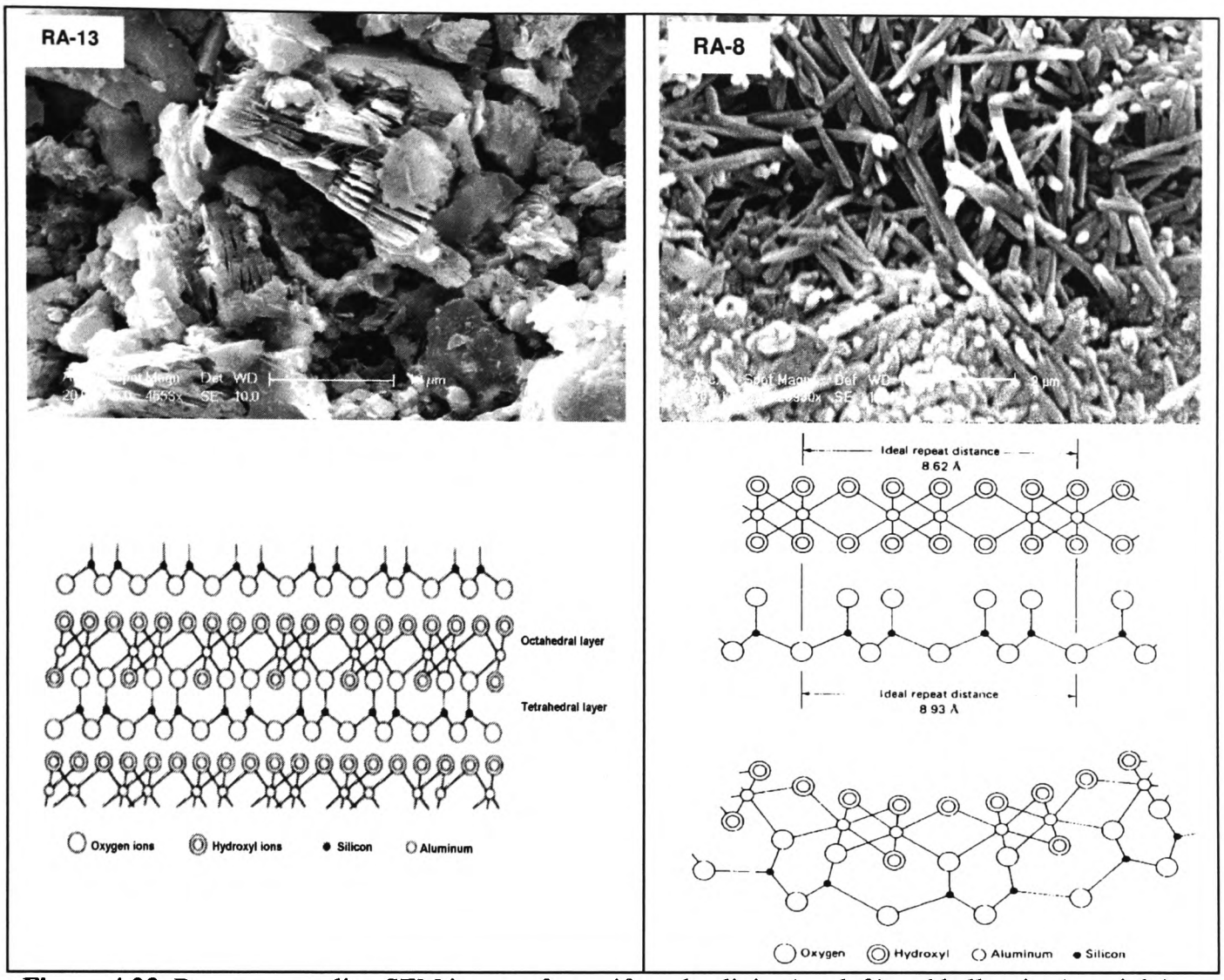

Figure 4.23. Rawang saprolite. SEM image of vermiform kaolinite (top left) and halloysite (top right). (Bottom left): The kaolinite structure- a cross section showing oxygen at the top of the tetrahedra replacing some hydroxyls in the octahedral layer. (Bottom right): The halloysite structure- schematic illustration of how the mismatch between the octahedral and the tetrahedral layers causes curvature of the structure, which results in the tubular structure (Drever, 1997)

Oxides and hydroxides. Small amount of hematite was present above the 3m depth in the Cheras profile (Table 4.1) and above the 17m depth in the Rawang profile (Table 4.2). A trace of anatase was present throughout the saprolite in the Rawang profile.

In the Cheras profile, gibbsite and goethite were present above the 3m depth to the topsoil (Table 4.1) and in the Rawang profile from 19m depth to the topsoil (Table 4.2)

Micas. In the Cheras saprolite, muscovite was present throughout the section (Table 4.1). In the Rawang profile, biotite was present only in the lower part of the saprolite.

Their presence agrees with the Goldich series, muscovite being very resistive to weathering and biotite with almost the same degree of susceptibility to weathering as Na–rich plagioclase.

Others. Chlorite and other accessory minerals like zircon and apatite were observed in the optical microscope for both Cheras and Rawang profiles. Only chlorite were detected using XRD and is only present in the Rawang unweathered and weathering boundary zones (Table 4.2).

4.3 Discussion

4.3.1 Determination of the degree of weathering

Sampling was done at approximately regular intervals through the depth of an exposed surface in the Cheras profile and part exposed surface and part vertically drilled hole in the Rawang profile. Presence of rock fractures down the depth, might for example induce drastic increase in the rate of weathering at a particular location rather than the other. Due to this reason, questions may arise as to whether the degree of weathering of each sample taken relates solely to the depth. Study of normally used chemical weathering indices proposed by previous researchers on each of the samples and relating them to the depth is a method of tackling the problem.

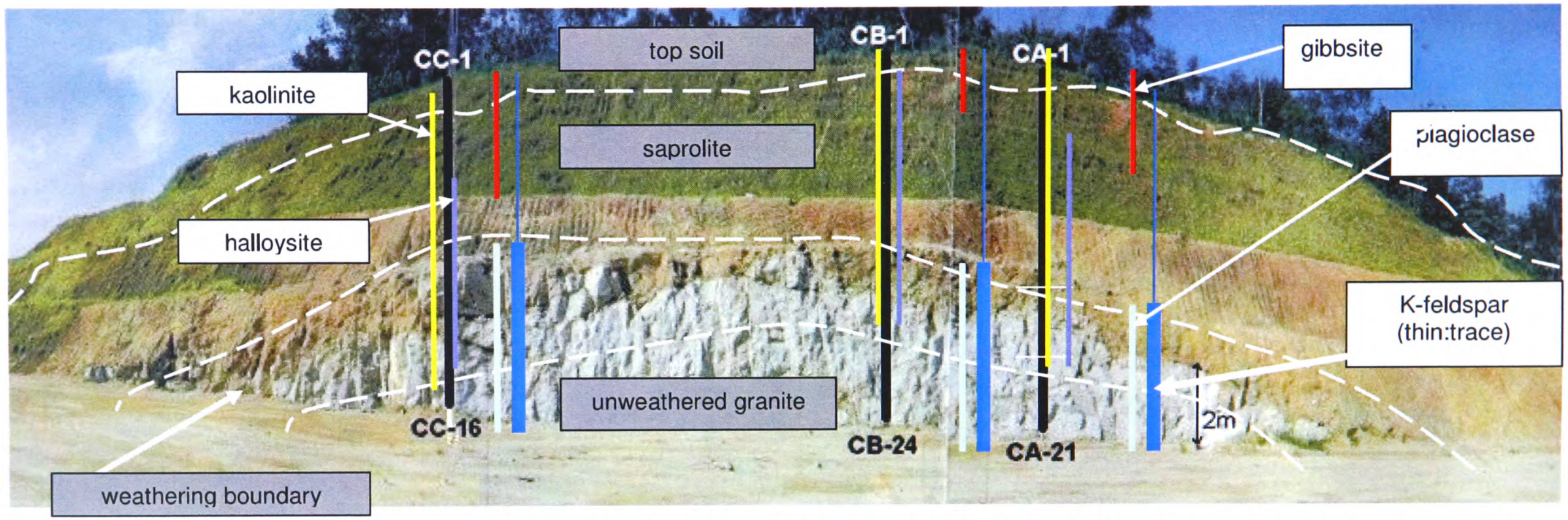

Figure 4.24. Distribution of some important minerals in the Cheras profile based on their presence observed under SEM. Observations of halloysite were made on (i) powdery samples sprinkled randomly on SEM stubs, (ii) powdery samples were mixed with distilled water and the mixture was placed on SM stubs and (iii) mineral grains placed randomly on SEM stubs. CA-1 to CA-21, CB-1 to CB-24 and CC-1 to CC-16 are sample names. Only selected samples in vertical lines CB and CC were analysed. However, all samples along the vertical line CA were analysed.

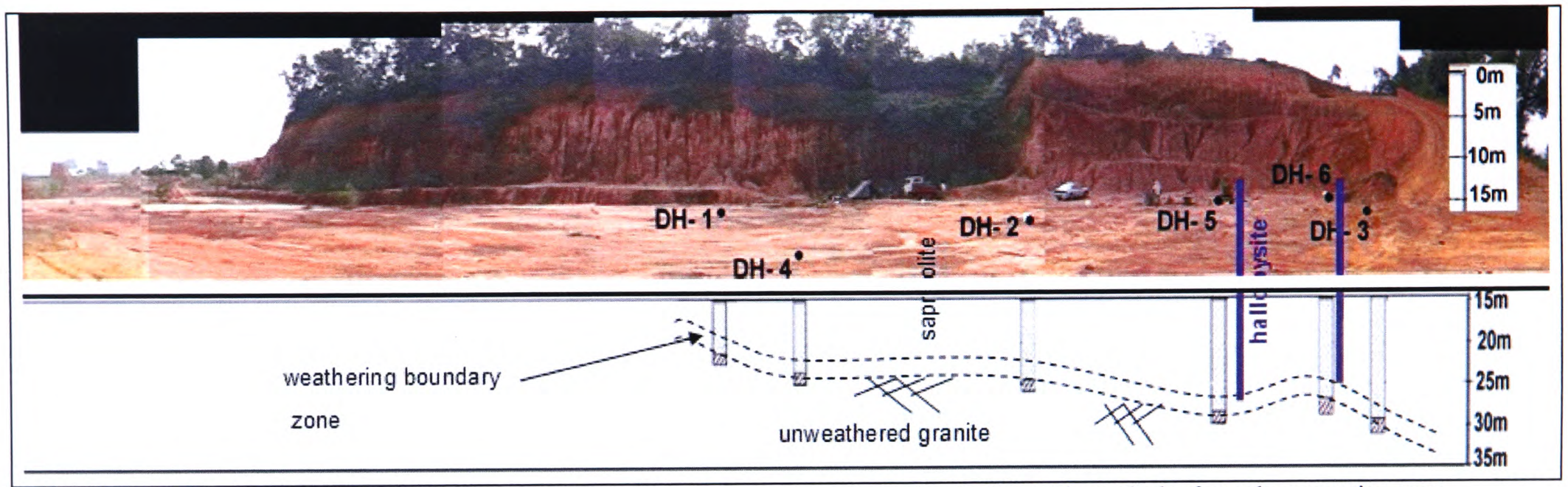

Figure 4.25. Distribution of halloysite in the Rawang profile based on their presence observed under SEM. The methods of sample preparation were similar to that of the Cheras profile. Only DH-5 (for samples marked 'RA') and DH-6 (for samples marked 'RB') were analysed as the writer had access only to these two boreholes. Halloysite distribution could not be interpreted as following the rock topography (as in the Cheras profile) because the samples taken on the exposed slope were not vertically above the drill holes.

There are several chemical indices based on the molecular proportions proposed by earlier researchers to classify the degree of weathering of samples on a weathering profile. Nesbitt and Young (1982) proposed a 'chemical index of alteration' (CIA), to measure the degree of weathering of sedimentary and volcanic rocks near Lake Huron, Canada (Equation 4.1). The changes in CIA reflect changes in the proportion of feldspar and the various clay minerals in the profile. Voicu and Bardoux (2002) used a 'mineralogical index of alteration' (MIA) to study the behaviour of major and trace elements under tropical weathering in Guyana (Equation 4.2). MIA relates to CIA with the argument that CIA values range from 50 to 100 and cannot be directly applied for normative calculations. The MIA value of 0-20% indicates unweathered, 20-40% weakly, 40-60% moderately and 60-100% extremely weathered rock. The 'chemical index of weathering' (CIW) (Equation 4.3), is similar to CIA (Equation 4.1) but eliminates the K_2O. CIW was proposed by Harnois (1988) after reviewing several of the then existing methods of calculating chemical weathering indices. 'Plagioclase index of alteration' (PIA) was proposed by Fedo et al (1995) again, on reviewing several existing methods and was developed especially for plagioclase weathering by subtracting the K-feldspar content from the system (Equation 4.4).

$$CIA = [Al_2O_3/ (Al_2O_3 + CaO + Na_2O + K_2O)] \times 100 \quad \text{(Equation 4.1)}$$

$$MIA = 2 \times (CIA - 50) \quad \text{(Equation 4.2)}$$

$$CIW = (100) [Al_2O_3/ (Al_2O_3+CaO+Na_2O)] \quad \text{(Equation 4.3)}$$

$$PIA = (100) [Al_2O_3-K_2O)/ (Al_2O_3+CaO+Na_2O-K_2O)] \quad \text{(Equation 4.4)}$$

A comparison of the indices discussed above was made of the samples taken from Cheras and Rawang (Table 4.8, Figures 4.26 and 4.27). In the present study, weathering in relation to the feldspar content is emphasized. Generally, it can be observed that the weathering indices decrease with increasing depth in the profile, as the active weathering front is approached.

Determination of a new index of weathering

In this study, the writer aimed to find an index of weathering that is directly related to the dissolution of the feldspar minerals, and in addition wanted to establish to establish some inexpensive, reliable indices for field engineers and consultants to immediately identify where a particular sample on a slope fits in a weathering profile.

K-feldspar index of alteration 1' (KIA1) is to determine the dissolution of K-feldspars with regards to the combined amounts of all the feldspars present along the depth without considering the clay minerals they formed (Equation 4.5, Figure 4.27). The indices discussed previously considered the presence of Al_2O_3 in their equations (Equations 4.1 to 4.4). 'K-feldspar index of alteration 2' (KIA2) considers the dissolution of K-feldspar with respect to $K_2O + Na_2O + CaO + MgO$. The differences between KIA1 and KIA 2 shows that MgO is being retained, in smectite, which is abundant on the upper part of the weathering boundary and the lower part of the saprolite (Figure 4.27). Smectite is also related to the presence of water in the atomic structure. The boundary zone and the lower part of the saprolite is the place where water accumulates with the high annual rainfall as they are immediately above the impermeable unweathered granite zone.

$$KIA1 = (100)\,[(K_2O)/(K_2O + Na_2O + CaO)] \quad \text{(Equation 4.5)}$$

$$KIA2 = (100)\,[(K_2O)/(K_2O + Na_2O + CaO + MgO)] \quad \text{(Equation 4.6)}$$

$$NIA3 = (100)\,[(Na_2O)/(K_2O + Na_2O + CaO + MgO)] \quad \text{(Equation 4.7)}$$

$$KIA4 = (100)\,[(K_2O + Na_2O)/(K_2O + Na_2O + CaO + MgO)] \quad \text{(Equation 4.8)}$$

Depth bgl (m)	CIA (Mol %)	CIW (Mol %)	PIA (Mol %)	MIA (Mol %)	KIA1 (Mol %)	KIA-2 (Mol %)	(KIA1-KIA2) (Mol %)	NIA3 (Mol %)	KIA4 (Mol %)
0.0.0	98.24	100.00	100.00	96.48	100.00	100.00	-	-	100.00
0.50	98.41	100.00	100.00	96.81	100.00	100.00	-	-	100.00
1.00	98.53	100.00	100.00	97.06	100.00	100.00	-	-	100.00
1.50	96.88	100.00	100.00	93.76	100.00	100.00	-	-	100.00
2.00	96.80	100.00	100.00	93.61	100.00	100.00	-	-	100.00
3.00	96.18	100.00	100.00	92.37	100.00	100.00	-	-	100.00
4.00	88.80	99.29	99.19	77.60	94.32	82.93	11.38	5.00	87.93
5.00	85.72	98.85	98.64	71.43	93.00	83.24	9.77	6.26	89.50
5.50	89.56	99.22	99.12	79.13	93.24	84.47	8.78	6.12	90.59
6.00	90.62	99.40	99.34	81.23	94.17	86.42	7.75	5.35	91.77
7.00	90.47	99.54	99.49	80.94	95.66	88.57	7.09	4.02	92.59
7.50	91.96	99.59	99.55	83.91	95.24	80.51	14.73	4.02	84.53
8.00	69.61	96.32	94.02	39.22	91.24	89.52	1.72	8.60	98.11
8.50	58.48	77.25	66.49	16.95	58.53	56.27	2.25	39.88	96.15
9.00	57.08	73.35	62.73	14.16	51.69	49.17	2.52	41.44	90.60
9.50	56.65	76.03	63.57	13.30	58.80	56.81	1.99	36.99	93.80
10.00	54.72	74.25	59.96	9.45	58.08	56.05	2.03	35.60	91.65
11.00	53.25	73.72	57.31	6.50	59.39	56.97	2.42	34.33	91.30
11.50	54.02	71.64	57.91	8.03	53.49	50.74	2.74	38.03	88.77
12.00	53.83	72.77	57.99	7.66	56.36	54.44	1.92	37.73	92.17
13.00	51.61	64.83	52.72	3.22	42.14	41.07	1.07	49.22	90.29

Table 4.8a. Cheras profile. weathering indices (mol %) against depth (m) below ground level. Molecular % (Mol %) = weight % (wt%)/ molecular weight.

Chemical Index of Alteration (CIA)=$[Al_2O_3/(Al_2O_3+CaO+NA_2O+K_2O)]100\%$ (Nesbitt et al, 1982); Chemical Index Of Weathering (CIW)=$[Al_2O_3/(Al_2O_3+CaO+NA_2O)]100$ % (Harnois,1988); Plagioclase Index Of Alteration (PIA)=$[Al_2O_3-K_2O)/(Al_2O_3+CaO+Na_2O-K_2O_3)100\%$ (Fedo et al, 1995); Mineralogical Index Of Alteration (MIA)= $2 \times (CIA - 50)$ (Voicu et al, 2002); K-feldspar Index Of Alteration-1 (KIA1)= $K_2O/(K_2O+Na_2O+CaO)$; K-feldspar Index Of Alteration-2 (KIA2) = $K_2O/(K_2O+Na_2O+CaO+MgO)$; Na-feldspar Index Of Alteration-3 (NIA3)= $Na_2O/(K+Na+Ca+Mg)$; K-feldspar Index Of Alteration-4 (KIA4= $K_2O+Na_2O/(K+Na+Ca+Mg)$

depth bgl (m)	CIA (Mol %)	CIW (Mol %)	PIA (Mol %)	MIA	KIA1 (Mol %)	KIA-2 (Mol %)	KIA1-KIA2 (Mol %)	NIA3 (Mol %)	KIA4 (Mol %)
0.00	99.41	100.00	100.00	98.83	100.00	100.00	-	-	1.00
5.00	99.55	100.00	100.00	99.09	100.00	100.00	-	-	1.00
8.00	97.27	100.00	100.00	94.55	100.00	100.00	-	-	1.00
10.00	95.48	100.00	100.00	90.96	100.00	100.00	-	-	1.00
13.00	98.19	100.00	100.00	96.38	100.00	100.00	-	-	1.00
15.00	98.51	100.00	100.00	97.02	100.00	100.00	-	-	1.00
16.90	98.44	100.00	100.00	96.89	100.00	100.00	-	-	1.00
18.90	98.30	100.00	100.00	96.60	100.00	100.00	-	-	1.00
19.90	98.63	100.00	100.00	97.27	100.00	100.00	-	-	1.00
21.40	98.75	100.00	100.00	97.49	100.00	100.00	-	-	1.00
22.90	98.45	100.00	100.00	96.91	100.00	100.00	-	-	1.00
24.40	98.75	100.00	100.00	97.50	100.00	100.00	-	-	1.00
25.90	98.52	100.00	100.00	97.05	100.00	100.00	-	-	1.00
27.40	87.15	99.59	99.52	74.30	97.20	81.89	15.31	-	0.82
28.40	55.48	73.24	60.64	10.96	54.47	44.55	9.92	24.83	0.69
28.50	52.66	69.13	55.09	5.33	50.32	44.52	5.80	29.08	0.74
28.52	50.84	68.46	51.74	1.69	52.34	47.34	5.00	27.87	0.75
28.60	51.15	63.40	51.88	2.30	39.56	33.65	5.91	29.04	0.63
29.40	50.80	64.20	51.37	1.60	42.42	35.41	7.01	26.83	0.62
30.00	50.69	64.74	51.22	1.38	44.01	36.11	7.91	25.53	0.62

Table 4.8b. Chemical indices for the Rawang profile.

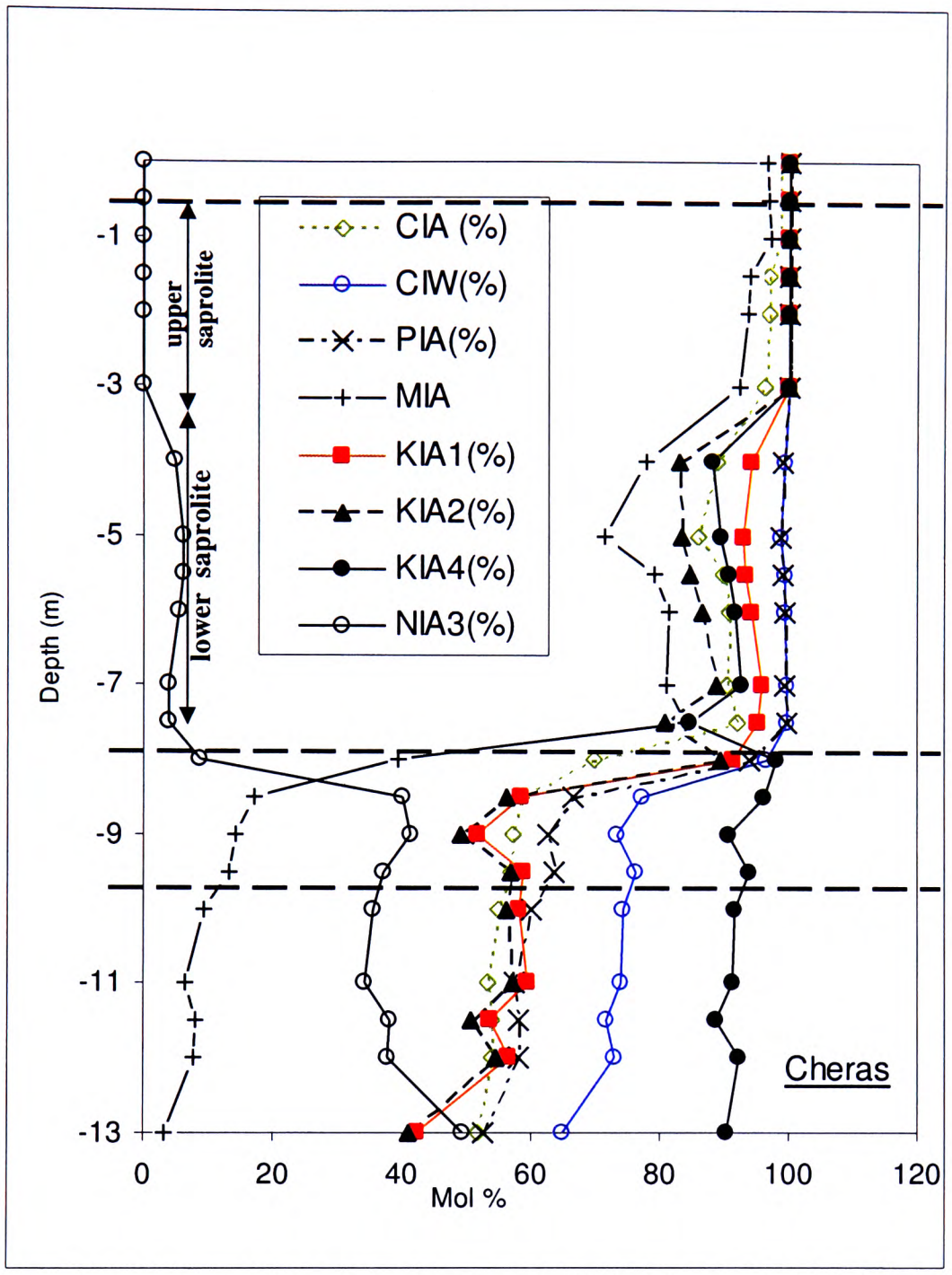

Figure 4.26a: Cheras: Plots of the weathering indices (mol %) against depth (m) below ground level.

MIA and NIA3 give a very clear picture of the different stages of weathering compared to other Indices.

Chemical Index of Alteration (CIA)=$[Al_2O_3/(Al_2O_3+CaO+Na_2O+K_2O)]100\%$(Nesbitt et al, 1982)

Chemical Index Of Weathering (CIW)=$[Al_2O_3/(Al_2O_3+CaO+Na_2O)]100$ % (Harnois,1988),

Plagioclase Index Of Alteration (PIA)=$[Al_2O_3-K_2O)/(Al_2O_3+CaO+Na_2O-K_2O_3)]100\%$ (Fedo et al, 1995)

Mineralogical Index Of Alteration (MIA)= $2 \times (CIA - 50)$ (Voicu et al, 2002),

K-feldspar Index Of Alteration-1 (KIA1)= $K_2O/(K_2O+Na_2O+CaO)$,

K-feldspar Index Of Alteration-2 (KIA2)= $K_2O/(K_2O+Na_2O+CaO+MgO)$,

Na-feldspar Index Of Alteration-3 (NIA3)= $Na_2O/(K+Na+Ca+Mg)$

K-feldspar Index Of Alteration-4 (KIA4= $K_2O+Na_2O/(K+Na+Ca+Mg)$

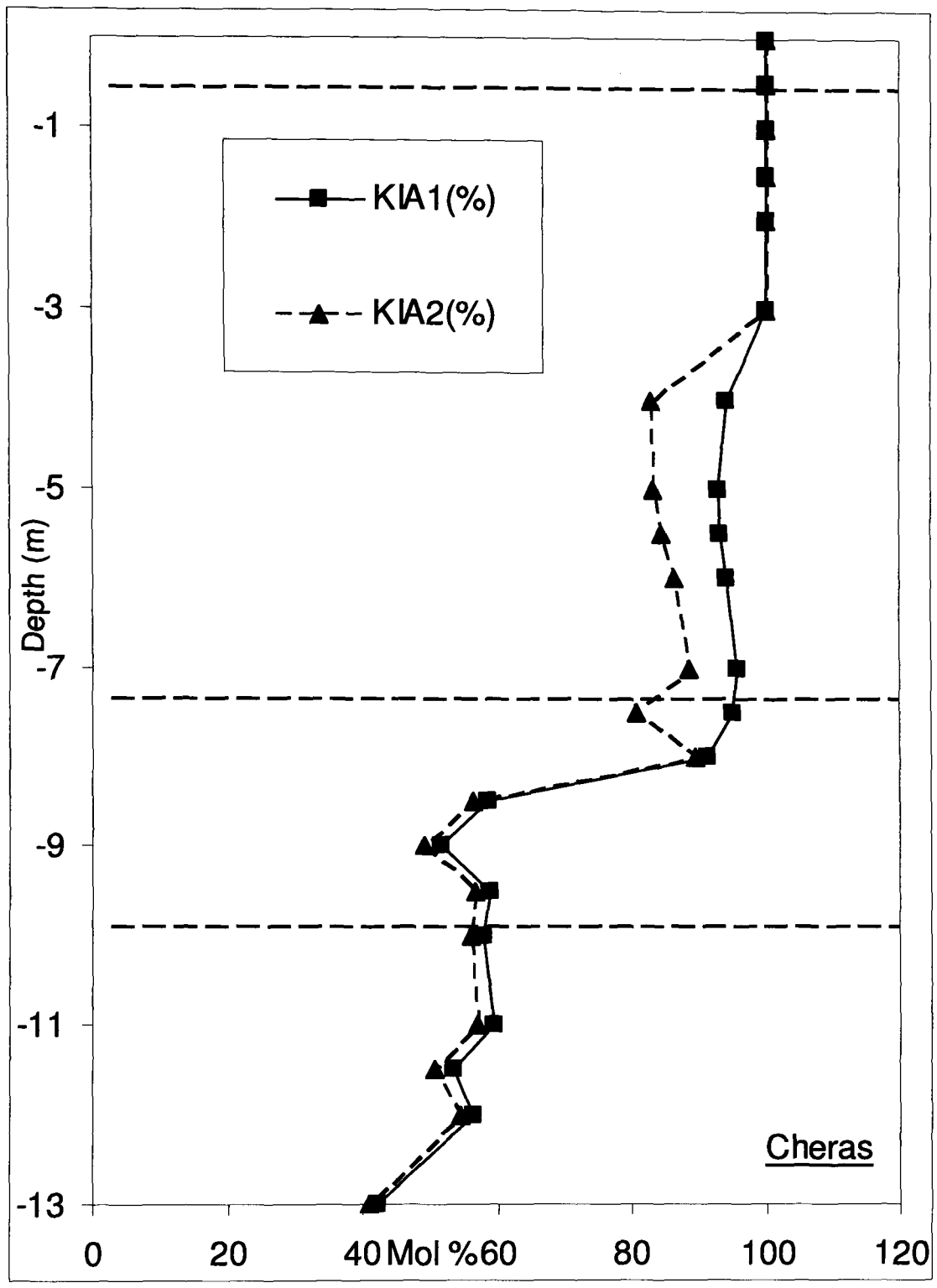

Figure 4.26b: Cheras**:** Plots of the KIA1, KIA2 and the the difference between KIA1 and KIA 2. (KIA1-KIA2) represents the absence of MgO in KIA1 between 3m to about 8m depth. This is related to the formation of clay minerals like smectite found in this region.

K-feldspar Index Of Alteration-1 (KIA1)= $K_2O/(K_2O+Na_2O+CaO)$,

K-feldspar Index Of Alteration-2 (KIA2)= $K_2O/(K_2O+Na_2O+CaO+MgO)$

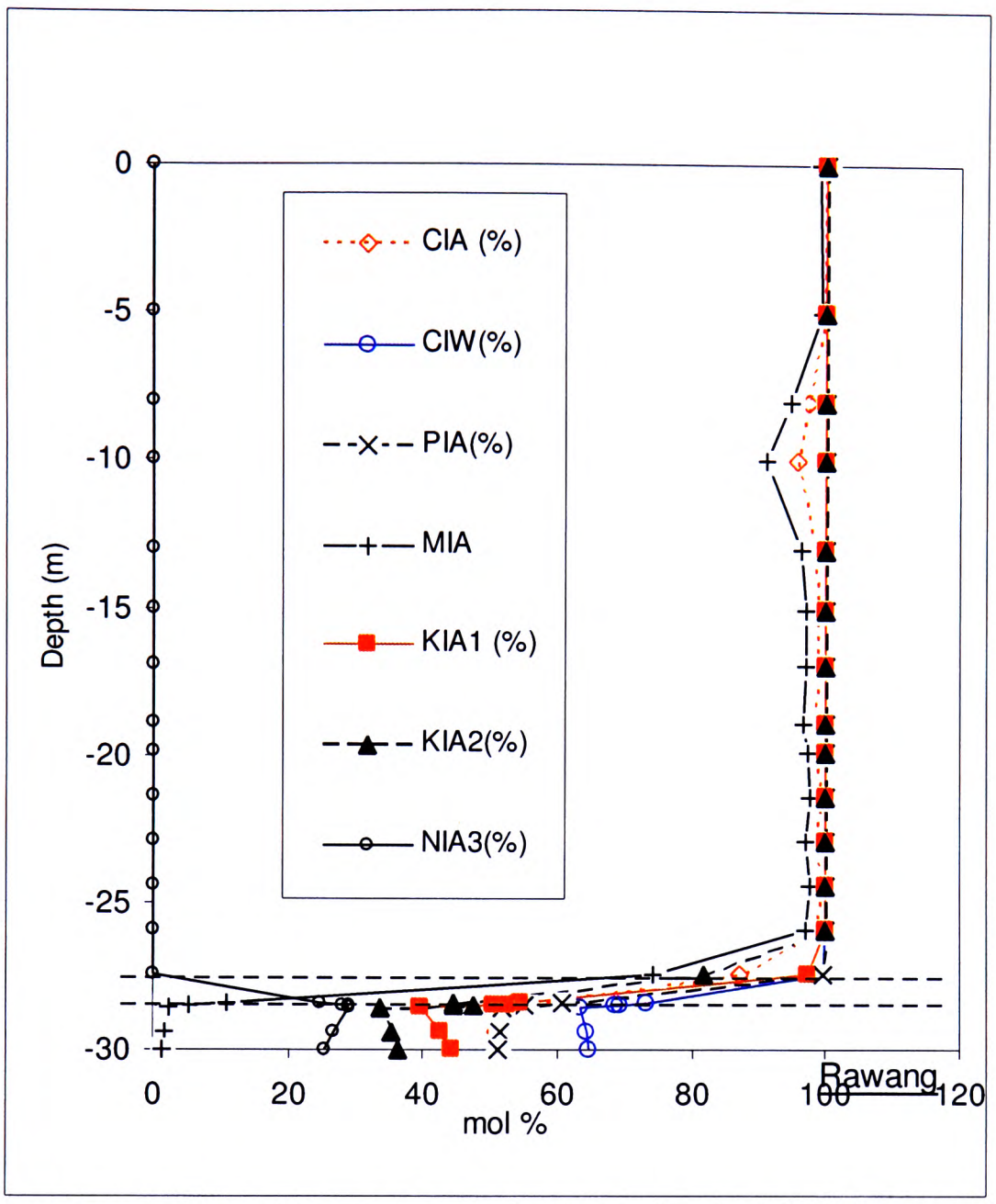

Figure 4.27a: Rawang **:** Plots of the weathering indices (%) against depth (m) below ground level. MIA and NIA3 do not appear to differentiate the different stages of weathering compared to other Indices as that in Cheras (Figure 4.26a). This is due to the sampling conditions at Rawang where not many samples could be taken from the weathering boundary zone which subsequently caused the apparent abrupt change between the saprolite and weathering boundary zone.

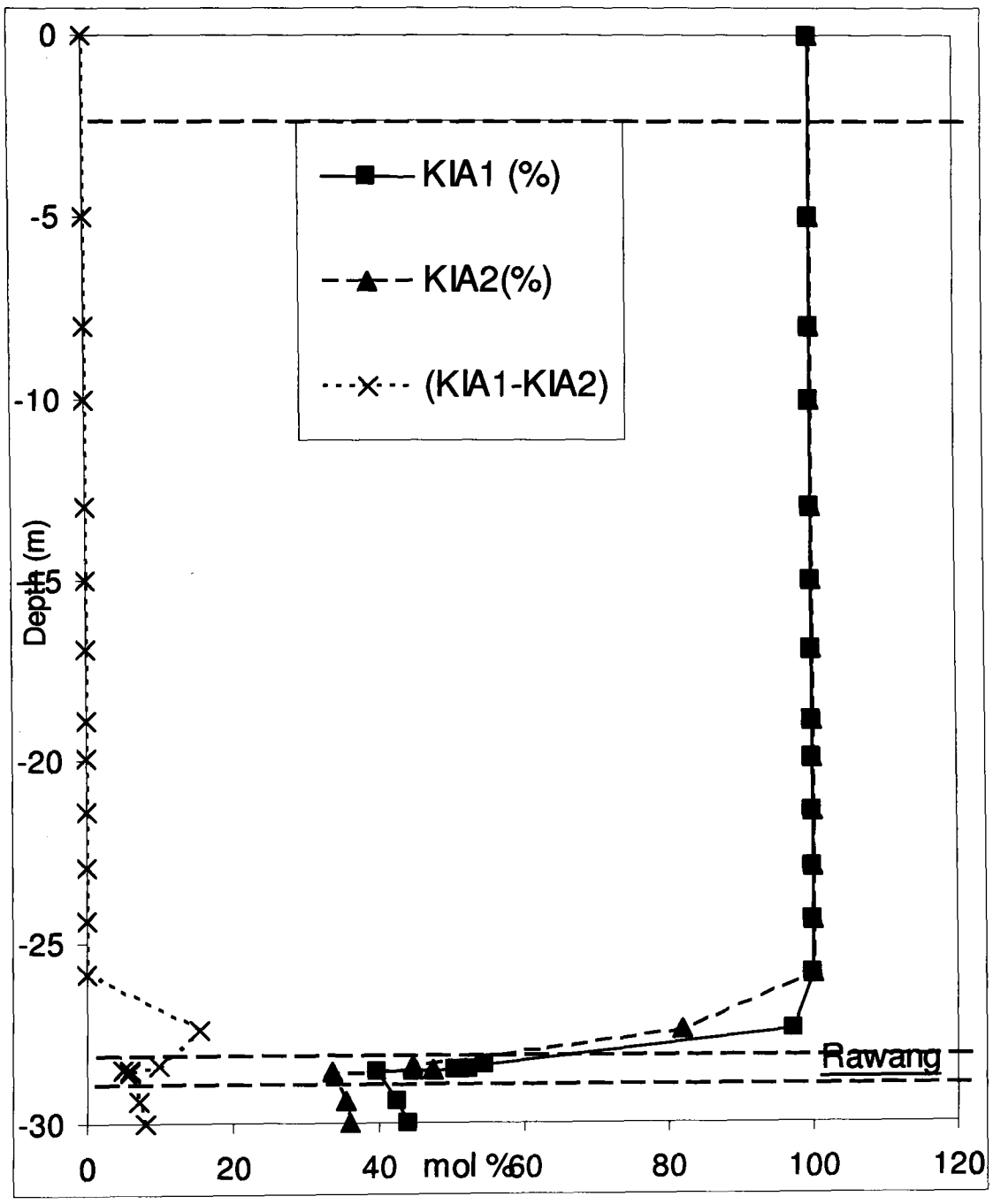

Figure 4.27b. Rawang: Plots of the KIA1, KIA2 and the the difference between KIA1 and KIA 2. (KIA1-KIA2) represents the absence of MgO in KIA1 between 3m to about 8m depth.

'Na-feldspar index of alteration 3' (NIA3) considers the dissolution of plagioclase with respect to all the feldspars and this index shows a clear differences between the three zones of weathering compared to the other indices (apart from MIA). MIA can be considered as another version of CIA. It manipulates the CIA values to show the difference degree of weathering zones.

'K-feldspar index of alteration 4' (KIA4) considers the dissolution of K-feldspars and plagioclase against all the feldspars.

In all of these indices, the different zones of weathering can be observed by grouping the values into clusters representing the different zones. Any of these indices can be use to represent the different zones. The writer believes that NIA3 is the best index to be used, especially for the weathering of granite similar to the Cheras granite. The character of the two unweathered granites (Cheras being S-type and Rawang, I-type) having different composition of Si-, Al- and Ca- rich minerals) will impose influence the calculation of the other indices. CIA, MIA, CIW and PIA use the Al_2O_3 as a major factor, while KIA1, KIA2, NIA3 and KIA4 do not take the Al_2O_3 into consideration. The Na content in both unweathered granites is almost similar (Tables 4.4 and 4.5). NIA3 enhances the differences between the different degrees of weathering. The relation between these indices can also be manipulated to correlate the occurrences of the minerals present with the degree of weathering. The accumulation of MgO can be related to the occurrences of smectite and the amount of water present in the weathering boundary and the lower part of the saprolite. NIA3 values are able to be grouped into two distinctive groups in the saprolite zone. The NIA3 indices can immediately inform the field engineers as to whether a particular sample is in the upper part or lower part of the saprolite zone (Figure 4.26a).

4.3.2. Exposed slope surface and drilled hole

Generally, the trends of the minerals and elements present along the completely exposed slope surface and part drilled-part exposed are similar. This suggests that the profiles

have not been significantly modified by the man-made cut surface (at Cheras) or by the use of drilling fluids (at Rawang).

4.3.3 General overview

The main difference between the two types of the unweathered granites is the mineralogical content. Cheras unweathered granite is the S-type granite containing more Al-rich minerals (e.g. muscovite) and higher in SiO_2 (wt %) content. Rawang unweathered granite is an I-type granite having more CaO content, less Al-rich minerals (e.g. biotite) and the wt% of silica is lower. The weathering boundary zone is the active weathering zone whereby active mineral alterations with chemical reactions and transportation begin. In this region, the clay mineral content (kaolinite) starts to form and the feldspars begin to dissolve. The thickness of this active zone is about 2.5m in Cheras granite and about 1m in Rawang granite. This study could not define the factors responsible for this thickness. The depth of the 'bedrock' or the unweathered granite being the place where weathering process starts is one of the main factors. The presence of a weathering medium (water) is very important to the weathering process and the depth will influence the amount of water present. One of the major difference between Cheras and Rawang granites considered is the depth of the profile (Cheras being 10m thick of top soil, saprolite and weathering boundary zones combined compared to about 28.5m thick in Rawang).

In the saprolite and top soil zones, there are traces or total absence of feldspars and maximum presence of clay minerals (kaolinite). So feldspar is effectively completely replaced by clay minerals and Al hydroxides.

The following section will discuss the possible pathways for elemental removal through the saprolite, focussing on the transformation of feldspars in the unweathered granite to secondary minerals in the saprolite.

4.3.4 Mineral relationship

Feldspars to kaolinite: Dissolution controlled by microtextures, especially dislocations and along exsolution lamellae, plays a major role in the degradation of K-feldspars (Lee and Parsons, 1995a; Lee, Hodson and Parsons, 1998). The dissolved elements will recrystallize as, among others, clay minerals. K-feldspar could react with carbonic acid and water to form kaolinite with quartz as by-products (Equation 4.9) or dissolve in water to reprecipitate gibbsite (Equation 4.10).

$$2KAlSi_3O_{8\,(S)} + 2H_2CO_3 + H_2O_{(l)} \Rightarrow Al_2Si_2O_5(OH)_{4\,(s)} + 2K^+_{(aq)} + 2HCO_3^-{}_{(aq)} + 4SiO_{2\,(s)} \quad \text{(Eq. 4.9)}$$

K-feldspar carbonic acid kaolinite bicarbonate ion quartz

$$KAlSi_3O_{8\,(S)} + 8H_2O_{(l)} \Rightarrow Al(OH)_{3\,(s)} + K^+_{(aq)} + OH^-_{(aq)} + 3H_4SiO_{2\,(s)} \quad \text{(Eq. 4.10)}$$

K-feldspar water gibbsite

Small amounts of residual K-feldspar and plagioclase present along the depth from the weathering boundary zone to the saprolite zone corresponds to the high kaolin content suggesting that a substantial amount of K-feldspar and plagioclase had dissolved and most probably, recrystalized as kaolin. However, K-feldspar is not the only mineral that would form kaolinite on dissolution (for example, equations 4.11).

$$2NaAlSi_3O_8 + 2H_2CO_3 + 9H_2O \Rightarrow 2Na^+_{(aq)} + Al_2Si_2O_5(OH)_4 + 4H_4SiO_4 + 2HCO_3^-{}_{(aq)} \quad \text{(Eq. 4.11)}$$

albite kaolinite silicic acid

When feldspar dissolves, K^+ (aq) and Na^+ are released and may be taken up by plants (at shallow depth below ground level) or flushed into some catchment areas. This is reflected in the reduction of K_2O, Na_2O and CaO content from the upper part of the weathering boundary zone to the top soil.

Feldspars to gibbsite and smectite: Gibbsite can be the product of reaction of K-feldspar (Equation 4.10) or plagioclase (Equation 4.12) and was present in the upper part of the

saprolite zones corresponding to the decline in the K-feldspar content. Smectite was observed in SEM samples only in the Rawang weathering zone and most likely were the direct product of the plagioclase dissolution (Equation 4.13) during the drastic decline of plagioclase in this zone. Gibbsite is the extreme end of the weathering cycle and is the result of the weathering of plagioclase, micas and all alumino silicates.

$$NaAlSi_3O_8 + 7H_2O + H^+_{(aq)} \Rightarrow Al(OH)_3 + Na^+_{(aq)} + 3H_4SiO_4 \quad \text{(Eq. 4.12)}$$

albite water gibbsite silicic acid

$$2.25NaAlSi_3O_8 + 2H_2CO_3 + 6H_2O \Rightarrow 2Na^+_{(aq)} + Na_{0.25}Al_2Al_{0.25}Si_{3.75}O_{10}(OH)_2\ nH_2O + 3H_4SiO_4 + 2HCO_3^-{}_{(aq)} \quad \text{(Eq. 4.13)}$$

albite smectite (Na-beidellite)

Micas to Hematite: Hematite is a secondary mineral and can be formed as a weathering product of iron-bearing minerals such as the dehydration of goethite or from the dissolution of minerals such as biotite and chlorite. The higher amount of hematite in the Rawang profile compared to the Cheras profile (area marked '+' in Figures 4.34 and 4.35) is due to presence of only minor amount of biotite in the latter profile. A review of chlorite weathering was given by Wilson (2004) who noted that chlorite (from various types of bedrocks) transformed to vermiculite and subsequently, to kaolin and hematite. From the electron probe analysis of biotite (Table B1.4 in appendix B1) and chlorite (Table B1.5 in appendix B1) the FeO content was about 20 to 40 wt% and this could be the contribution to the formation of hematite. The writer could not relate the formation of hematite with goethite as both goethite and hematite were present in a same depth range in the Cheras profile while goethite did not show any reduction in amount during the formation of hematite in the Rawang profile.

4.3.5 Thermodynamic relation to mineral weathering reactions

In this section the writer will discuss the formation of clay minerals found in the saprolites of both the Cheras and Rawang granites in relation to the reactions between the chemicals present and water. Water acts as the medium of weathering. To relate this situation to the field, two alternative assumptions have to be considered. First, water does not leave the system. In this situation, weathering can be said to be a process in a closed system. The second assumption is that water does leave the system, and the weathering process is in an open system. However, for equilibrium to be achieved weathering must be in a closed system, at least for a certain period of time and there is a medium for the chemical interactions to occur. The weathering processes that occur naturally are in an open system.

In the field, let us assume that the unweathered granite upper boundary is the ground surface at the beginning of the weathering process (time, t=0) (Figure 4.28), which for granites would occur when roof rocks have been removed by tectonic uplift.

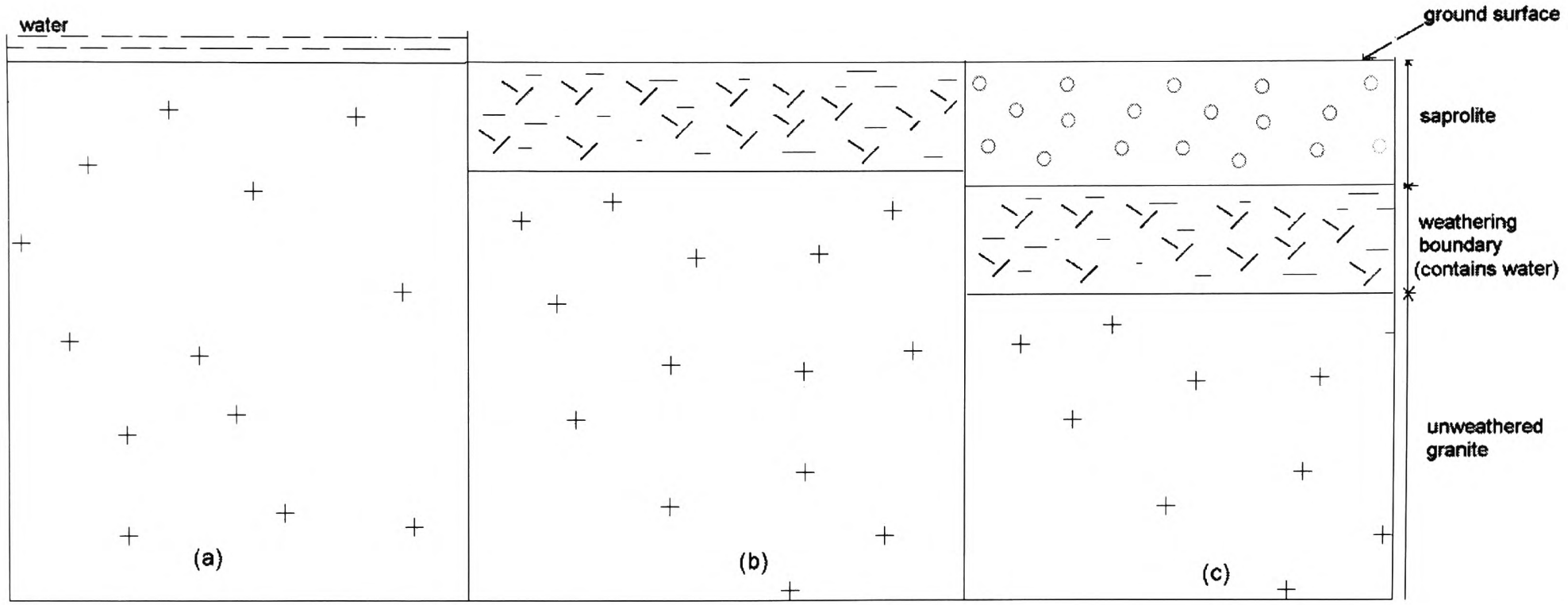

Figure 4.28. Schematic drawing of the progression of the weathering boundary zone. (a) It begins with the unweathered granite is the ground level. Water has to be present to act as a medium of the chemical interactions. (b) As the weathering progress, the weathering boundary zone develops and progress to be thicker. Again water has to be present as the chemical interaction medium. (c) Weathering progresses with the dissolution of the minerals in the unweathered granite and subsequently, a saprolite zone develops.

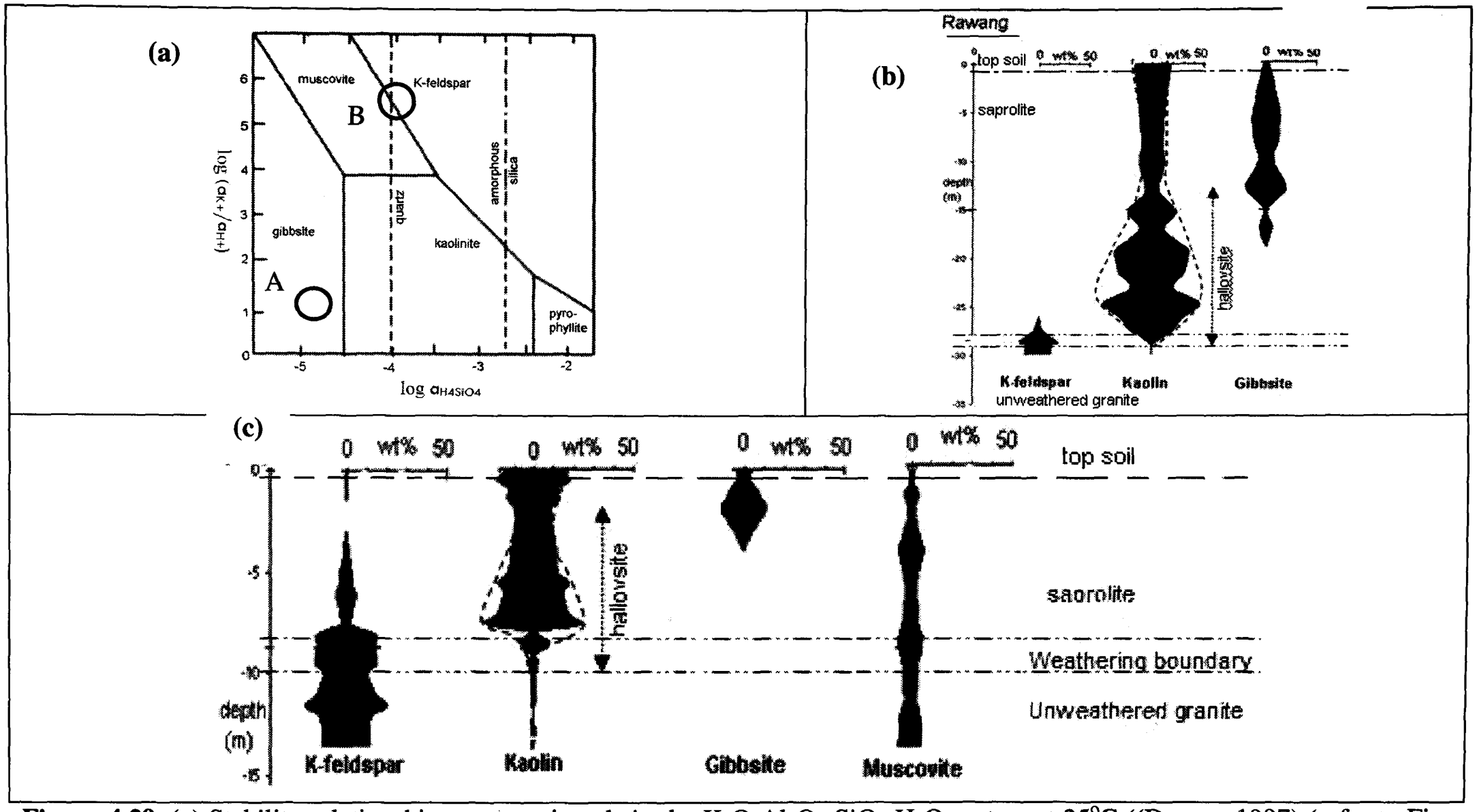

Figure 4.29. (a) Stability relationship among minerals in the K_2O-Al_2O_3-SiO_2-H_2O system at 25°C ((Drever, 1997) (refer to Fig. 2.2) (b) mineralogical content of K-feldspar, kaolinite and gibbsite from the QXRPD analysis of Rawang granite and (c) Mineralogical content of K-feldspar, kaolinite, gibbsite and muscovite from the QXRPD analysis of Cheras granite.

The K-feldspar grains on the unweathered granite reacts with water and will, at equilibrium, transform into gibbsite. This water might come from rain or some other sources and a thin film of water is good enough to start a reaction on this nano-scale. It should also be noted that the mean annual rainfall in Malaysia is about 2,540mm (100in) with the driest recorded is 1,650mm and the wettest is 5100mm. As time increases, the surface of the unweathered granite goes deeper into the ground with the formation and thickening of the weathering boundary zone. Along the way, new fresh mineral grains are exposed to the reactants in the solutions and new K-feldspar grains will provide the SiO_2 needed for the formation of clay minerals. On further reactions, the gibbsite will react with the K-feldspar to form kaolinite.

As the weathering zone moves downward, a saprolite zone develops. The saprolite zone is not a very active zone although some minor chemical weathering processes might still occur with the presence of small amounts of K-feldspar. As water flows within the weathering boundary zone, it carries along the soluble components from the zone leaving behind saprolite. Leaching is very active within the weathering boundary zone and can be an analogy of the flow-through experiments done on mineral grains as discussed in Chapter 2. Although not all reactions happen in the weathering boundary zone, there are no more (or maybe trace, for example on the remaining K-feldspar found in the Cheras saprolite) breakdown reactions in the saprolite, except for some conversion of kaolinite to gibbsite. As it is no more an active region, gibbsite is left in the saprolite zone. Subsequently, as the weathering boundary zone goes down the clay minerals formed will be left in the saprolite zone (Figure 4.29).

Similarly, albite reacts with water to form gibbsite (Equation 4.12). These gibbsite will also react with SiO_2 provided by albite and K-feldspar to form kaolinite. The direct product of albite dissolution (Equation 4.13) produced smectite in Rawang. Smectite's presence was detected qualitatively (from SEM study) in Rawang granite but not in the Cheras granite. This could probably be due to the higher amount of plagioclase in Rawang granite (24.14-27.58 wt %) compared to the Cheras granite (18.90-25.34 wt %).

In relation to the movement of the reaction medium, gibbsite is formed with a high degree of flushing for the removal of cations and silica so as it would not react with the available SiO_2 to form kaolinite. Kaolinite is formed in a less rapid flushing as gibbsite is needed for the reaction with SiO_2. Smectite formation would be in rather stagnant water for an appreciable build-up of SiO_2 can occur. The supply of the SiO_2 comes from the newly exposed feldspar grains.

The sequence of minerals encountered with depth through the saprolite which are gibbsite, kaolinite and ultimately, K-feldspar (Figures 4.24, 4.29) matches with the expected sequence as water progressively reacts with granites as discussed ealier in Chapter 2 (Section 2.1.1).

The mechanism of the weathering of these newly exposed grains will be discussed in Chapter 6. At equilibrium, the reaction will reach the K-feldspar or albite stable phases and weathering will cease. However, this situation will never arise as the fresh unweathered granite surface keeps supplying the reactants needed.

4.3.6 Quantifying the degree of weathering

Most of the analyses done in this study were conducted in the laboratory. It would be very helpful if one could infer the grade of weathering from analyses which are cheap and prompt. In this section the writer intends to quantify the field descriptions (which are qualitative) by giving ratings to the character of the materials. The results of the QXRPD and XRF analyses which are already in numerical terms will be grouped and given ratings based on the characters and the generalisation inferred from this study. The total ratings of the field descriptions will be compared to the total ratings of the laboratory analyses results. A rough guide of the grades will be produced from the field descriptions. The QXRPD and XRF analyses results will be the 'standards' to which the new guide is referred to. This guide, with further input, is hoped to be helpful to engineers especially in the slope stability studies. It should be noted that not all

exposures encountered by field researchers are a complete profile with obvious boundaries between the unweathered granite, weathering boundary, saprolite and top soil zones.

Imposed ratings

From the analyses done in this study, the writer defined 4 types of ratings that can be developed. They are:

1. Mineralogical rating: This rating is based on the quantitative results of the QXRPD analysis
2. Chemical rating: This rating is based on the quantitative results of the XRF analysis
3. Textural ratings: based on the qualitative description of the optical microscopy and Scanning Electron Microscopy studies.
4. Field ratings: based on the qualitative field descriptions.

Mineralogical ratings

The weight percentage content of the minerals obtained from QXRPD analysis are grouped into 4 groups based on their character that it shows in both Cheras and Rawang profiles (Table 4.9a).

Plagioclase		K-feldspar		kaolin		Justification
Range (wt %)	Rating	Range (wt %)	Rating	Range (wt %)	Rating	
0-5	0	0-3	0	>30	0	Top soil/ completely weathered
6-10	1	4-10	1	21-30	1	Upper part of saprolite
11-15	2	11-20	2	11-20	2	Lower part of saprolite
16-20	3	21-30	3	4-10	3	Weathering boundary
>20	4	>30	4	0-3	4	Unweathered granite

Table 4.9a: Mineralogical ratings given for different range of the QXRPD results and the justification for the ratings given.

The first group representing approximately completely weathered feldspars and completely developed clay minerals having the plagioclase content between 0 to 5 wt%, K-feldspar content between 0 to 3 wt % and Kaolin content of more than 30wt%. This group is given '0' rating. Similarly, group 2 is ranged to represent the upper part of the saprolite and is given '1' rating, lower part of saprolite: '2' rating, weathering boundary: '3' rating and unweathered granite: '4' rating. The ratings are then given to the QXRPD analysis results obtained from the Cheras and Rawang granites (Table 4.9b).

Cheras *depth (m)*	zone	plagioclase (wt%)	rating	K-feldspar (wt%)	rating	kaolin (wt%)	rating	Total ratings
0		-	0	1.34	0	26.03	1	1
(0.50)		-	0	0.57	0	36.31	0	0
(1.00)		-	0	0.53	0	23.76	1	1
(1.50)		-	0	0.25	0	26.67	1	1
(2.00)		-	0	-	0	16.94	2	2
(3.00)	Saprolite	-	0	0.1	0	20.16	1	1
(4.00)		0.15	0	3.06	1	23.49	1	2
(5.00)		0.05	0	6.19	1	25.13	1	2
(5.50)		0.07	0	6.36	1	34.9	0	1
(6.00)		-	0	8.93	1	29.71	1	2
(7.00)		0.01	0	5.47	1	34.71	0	1
(7.50)		0.23	0	5.27	1	46.53	0	1
(8.00)		17.92	3	29.03	3	3.07	4	10
(8.50)	Weathering boundary	0.1	0	28.68	3	15.37	2	5
(9.00)		21.87	4	30.98	4	2	4	12
(9.50)		16.19	3	31.08	4	5.36	3	10
(10.00)		23.09	4	22.23	3	2.55	4	11
(11.00)	Unweathered granite	18.9	3	30.06	4	1.67	4	11
(11.50)		19.83	3	41.57	4	1.7	4	11
(12.00)		17.19	3	24.57	3	0.65	4	10
(13.00)		25.34	4	23.49	3	1.49	4	11

Rawang *depth (m)*	zone	plagioclase (wt%)	rating	K-feldspar (wt%)	rating	kaolin (wt%)	rating	Total ratings
0		-	0	-	0	34.81	0	0
(5.00)		-	0	-	0	23.15	1	1
(8.00)		-	0	-	0	20.63	1	1
(10.00)		-	0	-	0	23.7	1	1
(13.00)		-	0	-	0	12.07	2	2
(15.00)		-	0	-	0	46.51	0	0
(17.00)		-	0	-	0	24.59	1	1
(19.00)		-	0	-	0	69.98	0	0
(20.00)	Saprolite	-	0	-	0	69.2	0	0
(21.50)		-	0	-	0	63.18	0	0
(23.00)		-	0	-	0	42.15	0	0
(24.50)		-	0	-	0	93.01	0	0
(26.0)		-	0	-	0	61.88	0	0
(27.50)		0.26	0	9.32	1	36.07	0	1
(28.40)		16.91	1	26.9	3	2.4	4	8
(28.50)	Weathering boundary	24.5	2	34.95	4	1.84	4	10
(28.52)		24.14	2	38.32	4	1.13	4	10
(28.54)	Unweathered granite	27.58	2	24.47	3	0.76	4	9
(29.00)		25.43	2	24.56	3	0.91	4	9
(30.00)		24.93	2	26.46	3	0.3	4	9

Table 4.9b: Mineralogical ratings given for different QXRPD results of the Cheras and Rawang granite. The total ratings will be later used as a comparison with the field ratings.

Chemical ratings

The weight percentage content of the minerals obtained from XRF analysis of the major elements are grouped into 4 groups based on their trend observed both Cheras and Rawang profiles (Table 4.10a).

Na_2O		K_2O		Justification
Range (wt %)	Rating	Range (wt %)	Rating	
0.0- 0.09	0	0.0-0.9	0	Top soil/ completely weathered
0.10-1.49	1	1.0-1.9	1	Upper part of saprolite
1.50-1.99	2	2.0-3.9	2	Lower part of saprolite
2.00-2.49	3	4.0-5.9	3	Weathering boundary
>2.50	4	>6.0	4	Unweathered granite

Table 4.10a: Chemical ratings given for different range of the XRF results and the justification for the ratings given.

The first group representing completely weathered feldspars and completely developed clay minerals having the Na_2O content between 0 to 0.09 wt% and K_2O content between 0 to 0.9 wt percent. This group is given '0' rating. Similarly, group 2 is ranged to represent the upper part of the saprolite and is given '1' rating, lower part of saprolite: '2' rating, weathering boundary: '3' rating and unweathered granite: '4' rating. The ratings are then given to the XRF analysis results obtained from the Cheras and Rawang granites (Table 4.10b).

Cheras		Na_2O		K_2O		
depth (m)	zone	(wt%)	rating	(wt%)	rating	Total ratings
0	Saprolite	-	0	0.3	0	0
(0.50)		-	0	0.33	0	0
(1.00)		-	0	0.28	0	0
(1.50)		-	0	0.8	0	0
(2.00)		-	0	0.67	0	0
(3.00)		-	0	0.67	0	0
(4.00)		0.07	1	1.77	1	2
(5.00)		0.11	1	2.22	2	3
(5.50)		0.09	1	1.89	1	2
(6.00)		0.06	1	1.47	1	2
(7.00)		0.05	1	1.68	1	2
(7.50)		0.04	1	1.22	1	2
(8.00)	Weathering boundary	0.35	1	5.54	3	4
(8.50)		2.39	3	5.13	3	6
(9.00)		2.74	4	4.94	3	7
(9.50)		2.18	3	5.09	3	6
(10.00)	Unweathered granite	2.51	4	6.01	4	8
(11.00)		2.46	3	6.2	4	7
(11.50)		2.62	4	5.31	3	7
(12.00)		2.55	4	5.59	3	7
(13.00)		3.57	4	4.53	3	7

Rawang		Na_2O		K_2O		
depth (m)	zone	(wt%)	rating	(wt%)	rating	Total ratings
0	Saprolite	-	0	0.11	0	0
(5.00)		-	0	0.1	0	0
(8.00)		-	0	0.52	0	0
(10.00)		-	0	1.16	1	1
(13.00)		-	0	0.6	0	0
(15.00)		-	0	0.27	0	0
(17.00)		-	0	0.27	0	0
(19.00)		-	0	0.43	0	0
(20.00)		-	0	0.34	0	0
(21.50)		-	0	0.29	0	0
(23.00)		-	0	0.25	0	0
(24.50)		-	0	0.34	0	0
(26.0)		-	0	0.33	0	0
(27.50)	Weathering boundary	-	0	2.92	2	2
(28.40)		1.99	2	5.43	3	5
(28.50)		2.83	4	6.59	4	8
(28.52)	Unweathered granite	2.87	4	7.41	4	8
(28.54)		2.87	4	5.05	3	7
(29.00)		2.57	4	5.16	3	7
(30.00)		2.6	4	5.59	3	7

Table 4.10b: Chemical ratings given for different XRF results of the Cheras and Rawang granite. The total ratings will be later used as a comparison with the field ratings.

Textural ratings

The qualitative descriptions based on the textures of the grains observed from the optical microscopy study and the SEM analysis of the feldspar grains are used for textural ratings. 3 groups are allocated for the optical microscopy observations and 4 groups for the SEM on the feldspar grains observations (Table 4.11a).

Optical microscopy		SEM on feldspar grains	
descriptions	ratings	descriptions	ratings
Very fine mineral grains	0	No feldspar grains identifiable from SEM study. Difficult to hand-pick feldspar grains from crushed weathered granite	0
Fractures of grains within a clay matrix	1	Naturally formed perthitic lamellae have been dissolved	1
Mineral grains can clearly be observed.	2	Naturally formed perthitic lamellae with albite still present	2
		No naturally formed exsolution lamellae observed on K-feldspar grain surface, can only be visible when etched in a laboratory with conc. HF	3

Table 4.11a: Textural ratings to the qualitative description obtained from the optical microscopy and SEM studies and the justification for the ratings given.

The first group representing completely weathered feldspars is when no mineral grains can be identified in the optical microscope and no feldspar grains are identifiable in the SE microscope. The second and third group defined from SEM study relates to the presence or absence albite within the exsolution lamellae. These two groups do not strictly coincide with the optical microscopy categories. This is because, the '1' to '3'ratings in the SEM study can only be observed when mineral grains can clearly observed in the optical microscope (i.e. '2' rating in the optical microscopy study). For this rating purpose, the optical microscopy category is only grouped into 3 groups. The justification for the SEM study category is based on the presence or absence of naturally formed lamellae on the K-feldspar surfaces. The ratings are then given to the XRF analysis results obtained from the Cheras and Rawang granites (Table 4.11b).

Cheras depth (m)	zone	rating (Optical Mic)	rating (SEM)	Total ratings
0	top soil	0	0	0
(0.50)		0	0	0
(1.00)	saprolite	0	0	0
(1.50)		0	0	0
(2.00)		0	0	0
(3.00)		0	0	0
(4.00)		1	0	1
(5.00)		1	0	1
(5.50)		1	0	1
(6.00)		1	0	1
(7.00)		1	0	1
(7.50)	Weathering boundary	1	0	1
(8.00)		2	1	3
(8.50)		2	1	3
(9.00)		2	1	3
(9.50)		2	1	3
(10.00)		2	1	3
(11.00)	Unweathered granite	2	3	5
(11.50)		2	3	5
(12.00)		2	3	5
(13.00)		2	3	5

Rawang Depth (m)	zone	Rating (Optical Mic)	Rating (SEM)	Total ratings
0	top soil	0	0	0
(5.00)		0	0	0
(8.00)	saprolite	0	0	0
(10.00)		0	0	0
(13.00)		0	0	0
(15.00)		0	0	0
(17.00)		0	0	0
(19.00)		0	0	0
(20.00)		0	0	0
(21.50)		0	0	0
(23.00)		0	0	0
(24.50)		0	0	0
(26.0)		0	0	0
(27.50)	Weathering boundary	0	0	0
(28.40)		2	2	4
(28.50)		2	2	4
(28.52)	Unweathered granite	2	3	5
(28.54)		2	3	5
(29.00)		2	3	5
(30.00)		2	3	5

Table 4.11b: Textural ratings given for different qualitative descriptions (Optical microscopy and Scanning Electron Microscopy, SEM studies) of the Cheras and Rawang granite. The total ratings will be later used as a comparison with the field ratings

Field ratings

The field description is based on the visual inspection on the properties of the rock/soil. A 'simple visual description' is targeted to inexperienced field personnel while the other description is based on the engineering scale of weathering grades of rock mass proposed by Fookes (1997) with a little modifications proposed in by the British Standard Institution (1981). 3 groups were allocated for the 'simple visual description' and 4 groups for the other description (Table 4.12a).

The first group representing completely weathered mineral grains is given '0' rating. In the 'Simple description', the presence or absence of decayed materials defines this group. Due to its simplicity, only 4 groups can be defined for '0' to '3' ratings. However, the ratings based on the 'engineering scale of weathering' is defined based on the fabric and discolouration of the materials and this detail description can be defined into 6 groups with '0' to '5' ratings. The ratings are then given to the samples obtained from the Cheras and Rawang granites (Table 4.12b).

Simple visual description		Based on 'Engineering scale of weathering grades of rock mass (Fookes,1997)' and Scale of weathering grades of rock mass '(BS5930: 1981)	
descriptions	ratings	Descriptions	ratings
original mass structure and material fabric are destroyed or crumbles under normal pressure of the hand., decayed materials present	0	All rock materials are converted to soil. The mass structure and material fabric are destroyed. The soil has not been significantly transported.	0
original mass structure and material fabric are destroyed or crumbles under normal pressure of the hand BUT decayed materials absent	1	All rock materials are disintegrated to soil. The original mass structure is still largely intact.	1
original mass structure is still intact and stays intact under normal pressure of the hand but crumbles under light hammer blow.	2	More than half of the rock materials is discomposed or disintegrated to soil. Fresh or discoloured rock is present either as a discontinuous framework or as corestone.	2
material does not crumble under light hammer blow	3	Less than half of the rock materials is discomposed or disintegrated to soil. Fresh or discoloured rock is present either as a continuous framework or as corestone.	3
		Discoloration indicates weathering of rock material and discontinuity surfaces. All rock material may be discoloured by weathering.	4
		No visible sign of rock material weathering: perhaps a slight discolouration at discontinuity surfaces	5

Table 4.12a: Textural ratings to the qualitative description obtained from the laboratory analyses and the justification for the ratings given. Note:' underlined words are the additional criteria proposed in (BS5930: 1981).

Cheras depth (m)	zone	Rating based on 'Simple field description'	Rating based on Fookes (1997) and (BS5930: 1981)	Total ratings
0	top soil	0	0	0
(0.50)		0	0	0
(1.00)	saprolite	1	0	1
(1.50)		1	0	1
(2.00)		1	0	1
(3.00)		1	0	1
(4.00)		1	1	2
(5.00)		1	1	2
(5.50)		1	1	2
(6.00)		1	1	2
(7.00)		1	1	2
(7.50)	Weathering boundary	1	2	3
(8.00)		2	2	4
(8.50)		2	3	5
(9.00)		2	3	5
(9.50)		2	4	6
(10.00)		2	4	6
(11.00)	Unweathered granite	3	5	8
(11.50)		3	5	8
(12.00)		3	5	8
(13.00)		3	5	8

Rawang Depth (m)	zone	Rating (Simple field description)	rating (Fookes,1997) and '(BS5930: 1981)]	Total ratings
0	top soil	0	0	0
(5.00)		0	0	0
(8.00)	saprolite	1	0	1
(10.00)		1	0	1
(13.00)		1	0	1
(15.00)		1	1	2
(17.00)		1	1	2
(19.00)		1	1	2
(20.00)		1	1	2
(21.50)		1	2	3
(23.00)		1	2	3
(24.50)		1	2	3
(26.0)		1	2	3
(27.50)	Weathering boundary	2	4	6
(28.40)		3	4	7
(28.50)		3	5	8
(28.52)	Unweathered granite	3	5	8
(28.54)		3	5	8
(29.00)		3	5	8
(30.00)		3	5	8

Table 4.12b: Field ratings given for different qualitative descriptions of the Cheras and Rawang granite. The total ratings will be later used as a comparison with the field ratings

Analysing the ratings

The total ratings of each the 4 types are tabulated and plotted against depth for the Cheras and Rawang granites (Table 4.13, Figure 4.30).

Groupings for the Field Ratings are developed and tabulated based on the trend shown by the Field Rating in relation to the other 3 ratings. Generally, the writer propose '0' rating as top soil (E), '1' as top part of saprolite (D), '2' as lower part of saprolite (C), '3' to'6' as the weathering boundary (B) and above '6' as 'fresh' granite (A). Should an exposed outcrop be rated between '3' to '6', the material should be considered as within the boundary zone. The grouping proposed need to be refined with classification of more samples at different locations. Engineering parameters like the 'particle size distribution' and the 'index properties' like the plasticity of the materials should also be included. These indices can be obtained from the laboratory tests provided in the British Standard Institution (1990c). With this, the writer would foresee that a relation with the properties can be correlated.

Cheras depth (m)	mineralogical rating	chemical ratings	textural ratings	field ratings	Groups for field ratings
0	1	0	0	0	E
-0.5	0	0	0	0	
-1	1	0	0	1	D
-1.5	1	0	0	1	
-2	2	0	0	1	
-3	1	0	0	1	
-4	2	2	1	2	C
-5	2	3	1	2	
-5.5	1	2	1	2	
-6	2	2	1	2	
-7	1	2	1	2	
-7.5	1	2	1	3	B
-8	10	4	3	4	
-8.5	5	6	3	5	
-9	12	7	3	5	
-9.5	10	6	3	6	
-10	11	8	3	6	
-11	11	7	5	8	A
-11.5	11	7	5	8	
-12	10	7	5	8	
-13	11	7	5	8	

Rawang depth (m)	Mineralogical rating	chemical ratings	textural ratings	field ratings	Groups for field ratings
0	0	0	0	0	E
-5	1	0	0	0	
-8	1	0	0	1	D
-10	1	1	0	1	
-13	2	0	0	1	
-15	0	0	0	2	C
-17	1	0	0	2	
-19	0	0	0	2	
-20	0	0	0	2	
-21.5	0	0	0	3	
-23	0	0	0	3	
-24.5	0	0	0	3	
-26	0	0	0	3	
-27.5	1	2	0	6	B
-28.4	8	5	4	7	A
-28.5	10	8	4	8	
-28.52	10	8	5	8	
-28.54	9	7	5	8	
-29	9	7	5	8	
-30	9	7	5	8	

Table 4.13: Summary of the 4 ratings. These results are plotted in Figure 4.30. Groupings for the Field Ratings are developed and tabulated in the shaded column. The writer is proposing '0' Field rating as top soil (E), '1' as top part of saprolite (D), '2' as lower part of saprolite (C), '3' to'6' as the weathering boundary (B) and above '6' as 'fresh' granite (A). The grouping proposed need to be refine with classification of more samples at different locations.

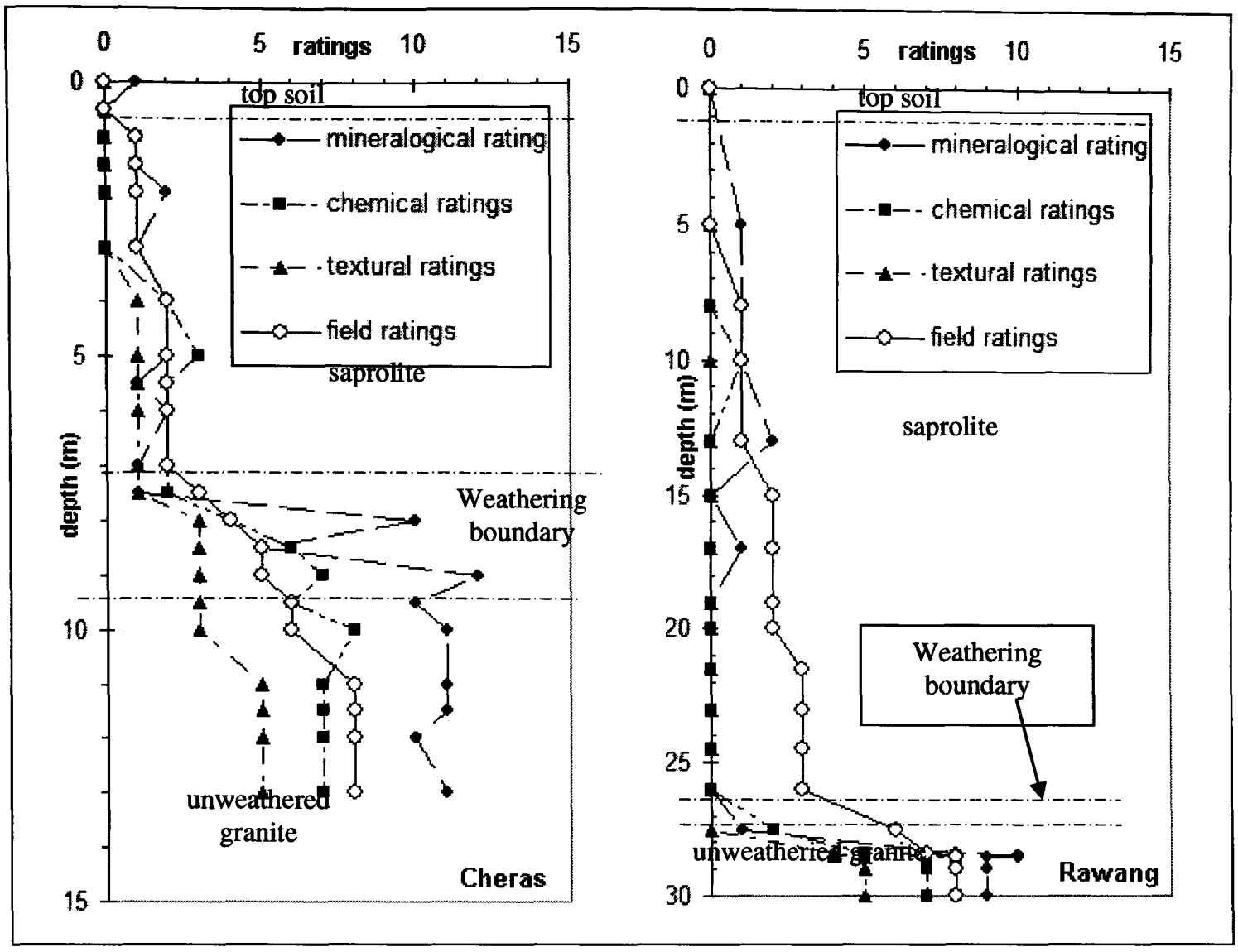

Figure 4.30. Comparison between the 4 types of ratings proposed. The field ratings can be generalised to be similar to the other ratings. The field ratings can therefore be used as a rough guide to identify the condition or the degree of weathering at which some exposed material on site is encountered.

4.4 Conclusion

The analyses of minerals and chemicals of samples from the weathering profiles of the Cheras and Rawang granites have brought about a categorization of the weathering profiles into 4 'zones': top soil, saprolite, weathering boundary and unweathered granite zones. The reactions within the active weathering boundary zone dictate the formation of secondary minerals. There are other parameters involved in the weathering processes but few assumptions were proposed to confine the scope of discussion. The discussion above has enlightened the understanding of the development of secondary minerals

especially clays in a deep weathering profile. The determination of the degree of weathering using the chemical properties was refined by just considering the weathering of feldspar minerals rather that the need to consider the formation of clay minerals. The numerical values (QXRPD and XRF) together with the textural analyses obtained from the laboratory can be used to translate the qualitative descriptions obtained from field inspection into numerical values. These values appear to be reliable to provide a general idea on the weathering grade. The field inspection is cheap and prompt. This 'quantifying of the field description' obviously can be improved further.

5. MOBILITY OF ELEMENTS

5.1 Introduction

Weathering is essentially a leaching process and thus, one way of determining the extent of weathering is to monitor the mobility of different elements. Trace and REE are particularly important because they are known to be sensitive to different geochemical processes. Rate of loss of elements in a weathering profile can be determined by comparing the concentration of elements at different depths to that of the parent material. Elements that are lost relative to parent rock are considered mobile while those that accumulate are immobile. This can be expressed in terms of percentage change of the element concentrations against an immobile element in the parent material (Equation 5.1) (Nesbitt and Markovics 1997; Nesbitt, Markovics and Price, 1980; Kronberg, Nesbitt and Fyfe, 1987; Nesbitt 1979). Often, mobile elements are those contained in early weatherable minerals, thus the results of element mobility should match the mineralogical data.

$$\text{Percentage change} = 100\{[(\chi_s/I_s)/(\chi_p/I_p)]-1\} \qquad \text{(Equation 5.1)}$$

Where

χ^s: concentration of any element (χ) in sample (s)

χ^p: concentration of any element (χ) in the parent rock (p)

I^s: concentration of an immobile element (I) in sample (s)

I^p: concentration of an immobile element (I) the parent rock (p)

Nesbitt and Markovics (1997), Nesbitt (1979) preferred TiO_2 as the immobile element rather than Zr. Their argument was that since Zr might not be evenly distributed in all samples, it could introduce inter-sample error in the percentage calculation. This is not so for TiO_2 as it is much more abundant as its presence is in wt% rather than ppm. Panahi, Young and Rainbird (2000) studied the alteration of an Archean granite in Canada, using Ar, Hf and TiO_2 to study chemical mobility on a 13m depth weathering profile. Zr and TiO_2 were also used as immobile elements by

among others, Viers and Wasserburg (2004) in their study on the chemical behaviour in a lateritic profile in Cameroon; Singh et al, (2005) in their study on the weathering of the Ganga alluvial plain, and Voicu and Bardoux, (2002) in their study on geochemical behaviour under tropical weathering in Guina Shield. The use of TiO_2 for this purpose in granites is also questionable because TiO_2 is mostly contained in titano-magnetic minerals and ilmenite, which could weather easily while in basalts, significant TiO_2 is contained in pyroxene and thus, less mobile.

In this chapter, the writer intends to use the 'percentage change' method discussed above to understand the mobility of the elements present in the deep profile, especially in relation to feldspars. As the descriptions of the raw data have been addressed in Chapter 4, the following section will describe the mobility of the major and trace elements. However, the amount of the elements present is presented on the same plot for comparison purposes.

5.2 Mobility of major and trace elements relative to Zr

The mobility of major and trace elements is expressed in terms of percentage change of the element concentrations as in Equation 5.1, normalised to Zr present in the unweathered granite. The writer used Zr for several reasons. The main reason is that Zr is preferentially retained in the material as weathering progresses. The absolute concentrations of Zr are higher in the upper part of the profiles compared to the lower part. This shows that Zr is retained in the weathered material as weathering progresses. Figure 5.1 shows the difference between the distributions of Zr compared to Ba. The writer also observed the plots of the percentage change when normalised to both Zr and TiO_2 and in Cheras, the writer did not observe any difference in terms of the positive or negative percentage change of the major and trace elements. So, in terms of the trends, there is no difference when they are normalised to Zr or TiO_2. TiO_2 could not be used for the Rawang granite due to the presence of anatase in the saprolite, but not in the unweathered and weathering boundary zones (Table 4.2) implying mobility of TiO_2 and its precipitation as a low-T phase during weathering. The mineral zircon was observed to be present in both Cheras and Rawang granites (optical microscopy). Due to these, the writer preferred zirconium, Zr and

comparison can be made between Cheras and Rawang in the later sections of this report. For a clearer picture, it is useful to clarify what the percentage change means: the percentage change of Al_2O_3 at 5m depth for example, with respect to TiO_2 means the amount (wt%) of Al_2O_3 at 5m depth divided by the amount of TiO_2 (wt%) at the 5m depth (i.e. Al_2O_3 at 5m depth is normalised to TiO_2 also at 5m depth). This means that the normalised value of Al_2O_3 at 5m depth is the amount of Al_2O_3 with respect to a unit value of TiO_2. The percentage change of Al_2O_3 at 5m depth is the normalised value of Al_2O_3 at 5m depth divided by the normalised value of Al_2O_3 at 13m depth (which is considered as parent rock for Cheras, and at 30m depth for Rawang) multiplied by 100. The value obtained is the relative change of Al_2O_3 at 5m depth to the parent rock relative to a 'constant' amount of TiO_2, which is one unit. As the normalising process produces a value relative to a unit value of the adopted relative immobile element, the use of Zr with the amount in ppm, compared the with major elements (amount in wt %) is acceptable.

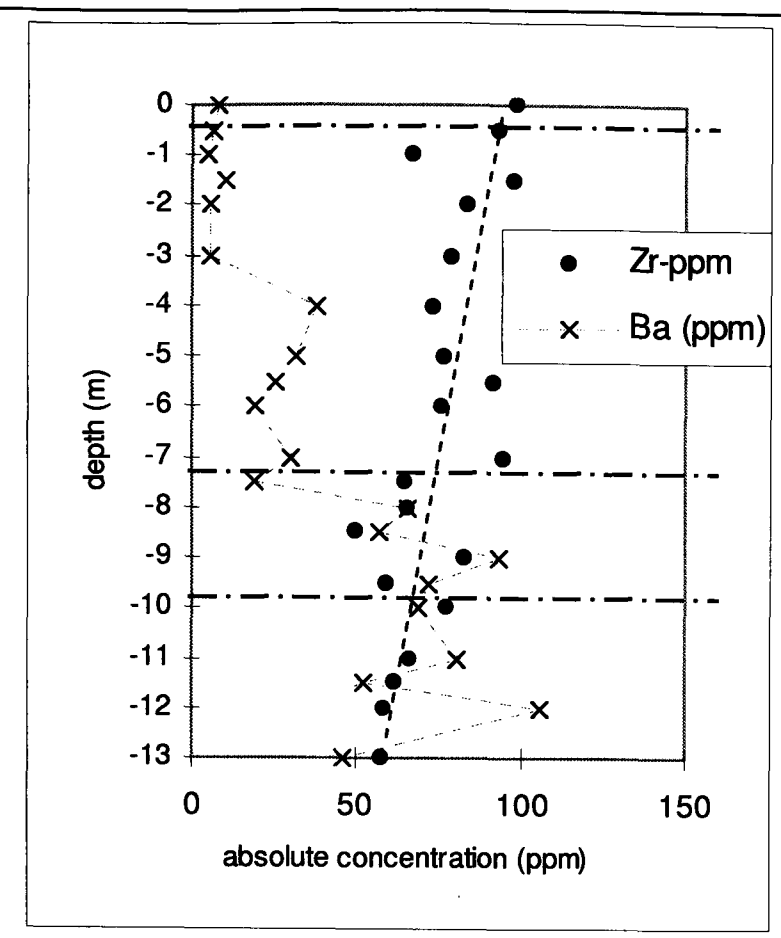

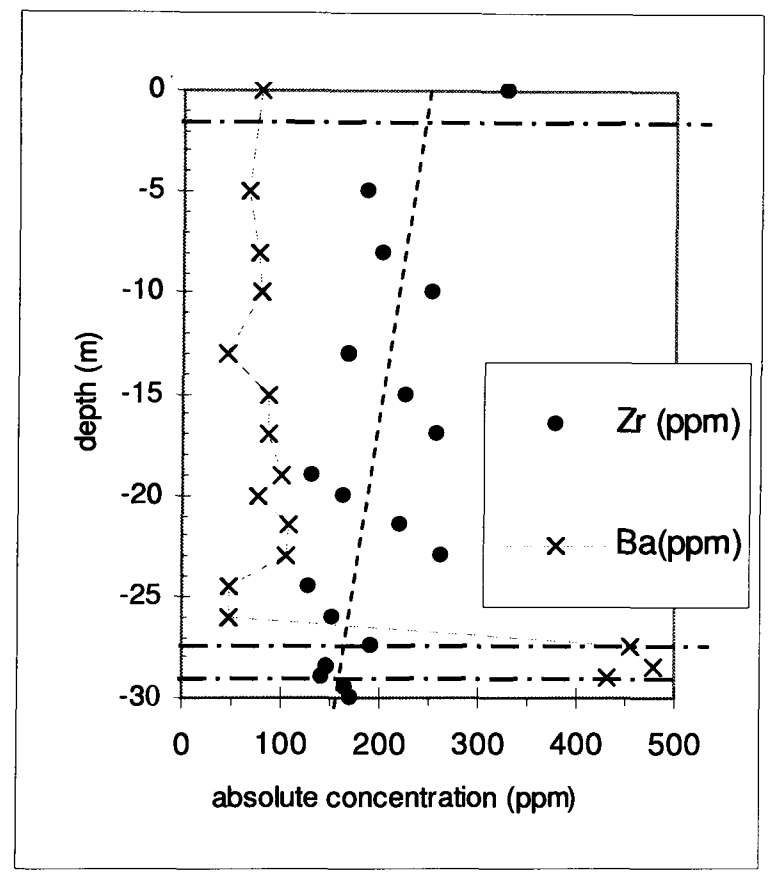

Figure 5.1: Absolute concentrations of Zr and Ba plotted against depth (top: Cheras and bottom: Rawang). The absolute concentrations of Zr are obviously retained in the weathered materials as weathering progresses. Absolute concentrations of Ba are also plotted as a comparison to show that Zr is less mobile than Ba.

5.2.1 Mobility of elements relative to Zr in Cheras

SiO_2 shows a negative percentage change (mobile) almost through-out the depth (Figure 5.2a). At the weathering boundary zone, positive and negative percentage change occurs but the amount (wt%) of SiO_2 is basically constant.
The development of clay minerals in the weathering boundary zone is reflected in the positive percentage change (immobile) of Al_2O_3 at 0.5 to 4m depth (Figure 5.2b). Clay minerals formation contributes to the accumulation of the Al_2O_3.

Positive percentage change (immobile) of Fe_2O_3 shows positive values reflects the oxidation activity in the upper part (0 to 2m depth) of the saprolite (Figure 5.2c). This correspond to the high amount (in wt%) of Fe_2O_3 in this region.

The mobility of CaO, Na_2O and K_2O is obvious when the percentage change decrease and reach -100% just above the weathering boundary zone (Figures 5.2d, e and f). The mobility of the elements reflects the replacement of feldspar by clay minerals.

Negative percentage change of P_2O_5 shows that it is mobile from the upper part of the weathering boundary zone (8.5m depth) to the top soil (Figures 5.2h). The mobility of P_2O_5 is reflected in the presence of the mineral apatite. Apatite was observed present in optical microscopy study, in the unweathered granite and some of the samples from the weathering boundary zone. However, apatite was not detected in the quantitative XRD analyses.

(a)

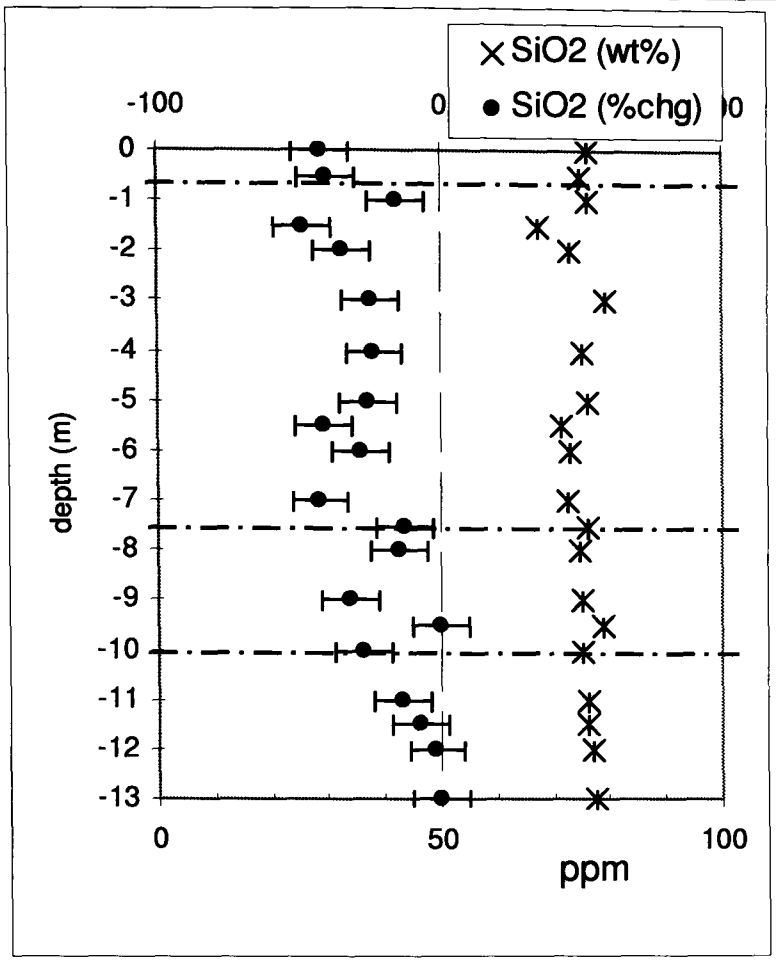

(b)

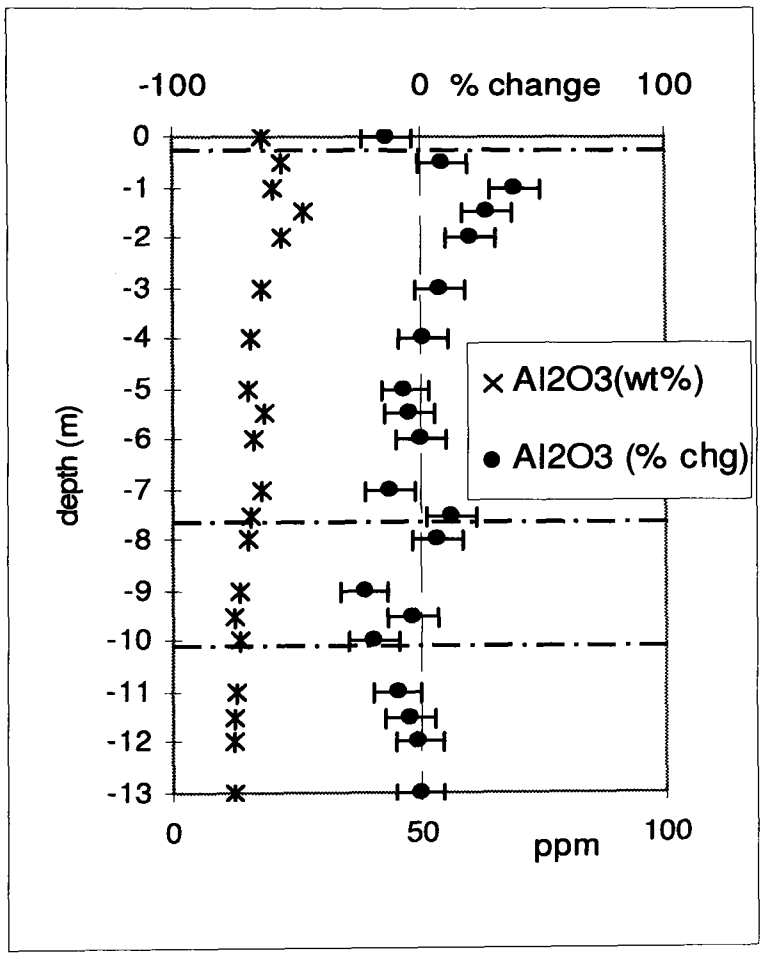

Figure 5.2.Cheras major element percentage change with respect to Zr of the parent rock (sample CA-21 at 13m depth) **(a)**: SiO_2, **(b)**: Al_2O_3

(c)

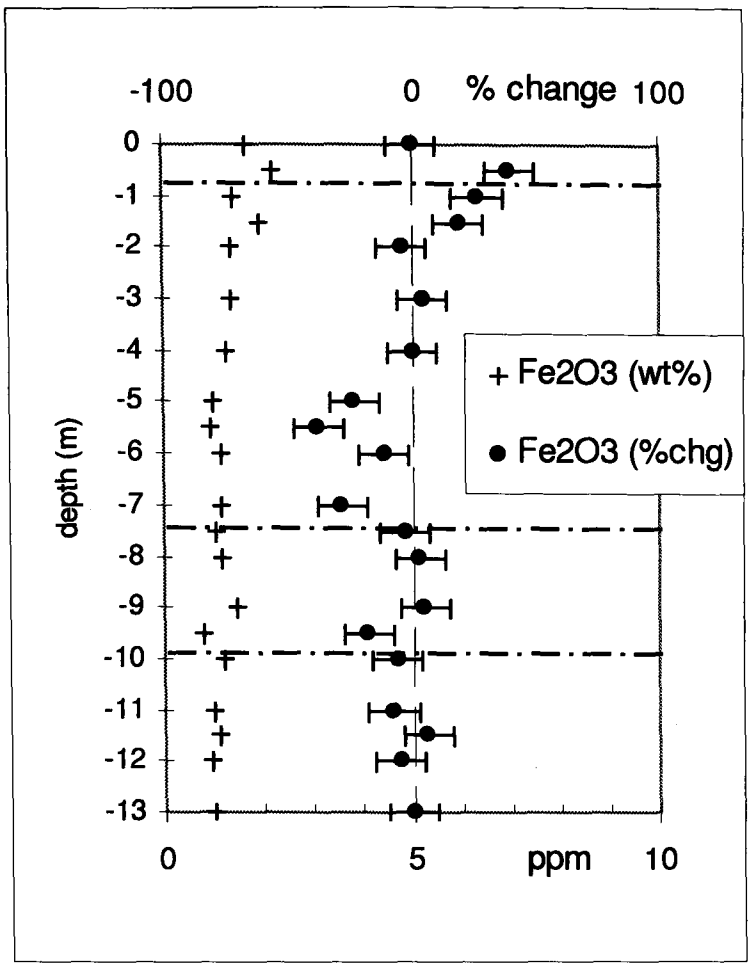

(d)

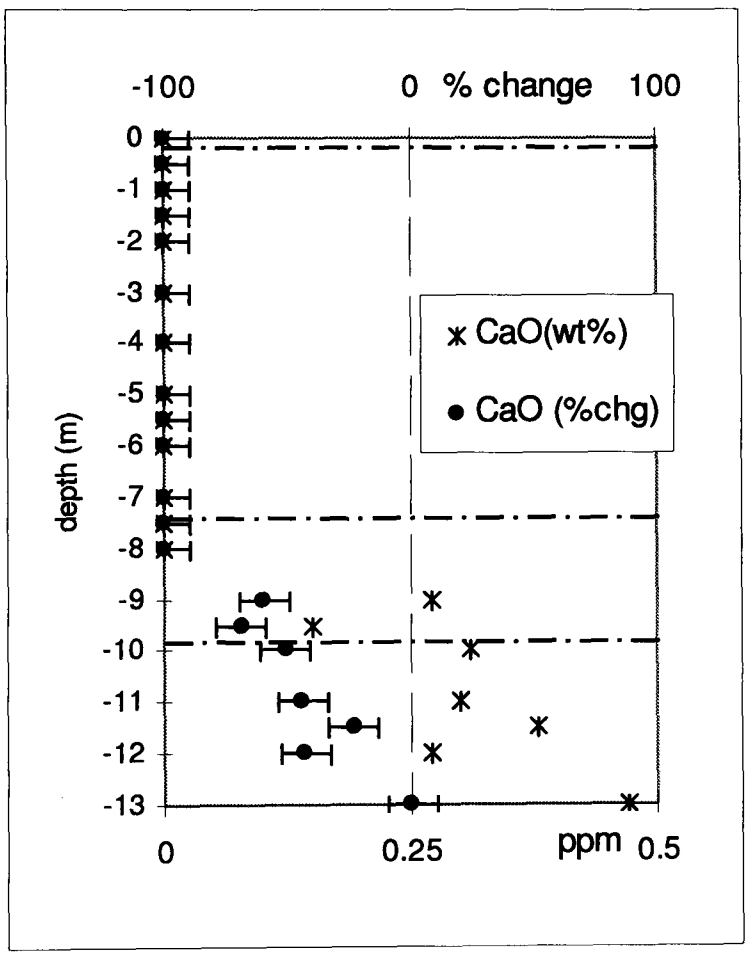

Figure 5.2.Cheras major element percentage change with respect to Zr of the parent rock (sample CA-21 at 13m depth) **(c)**: Fe_2O_3, **(d)**: CaO

(e)

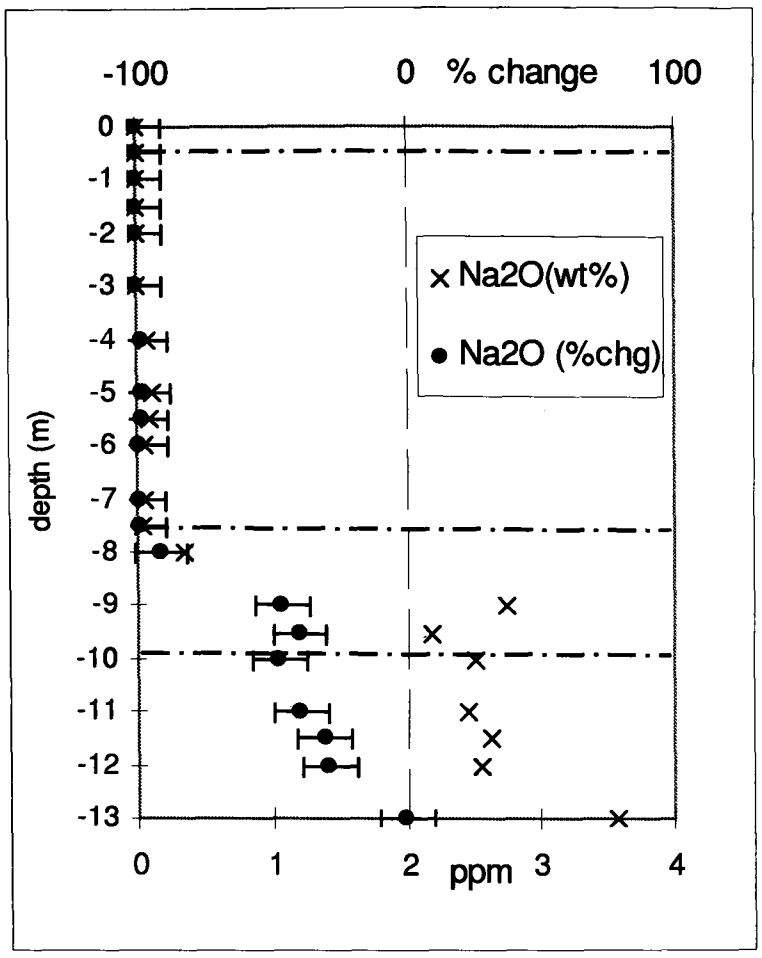

(f)

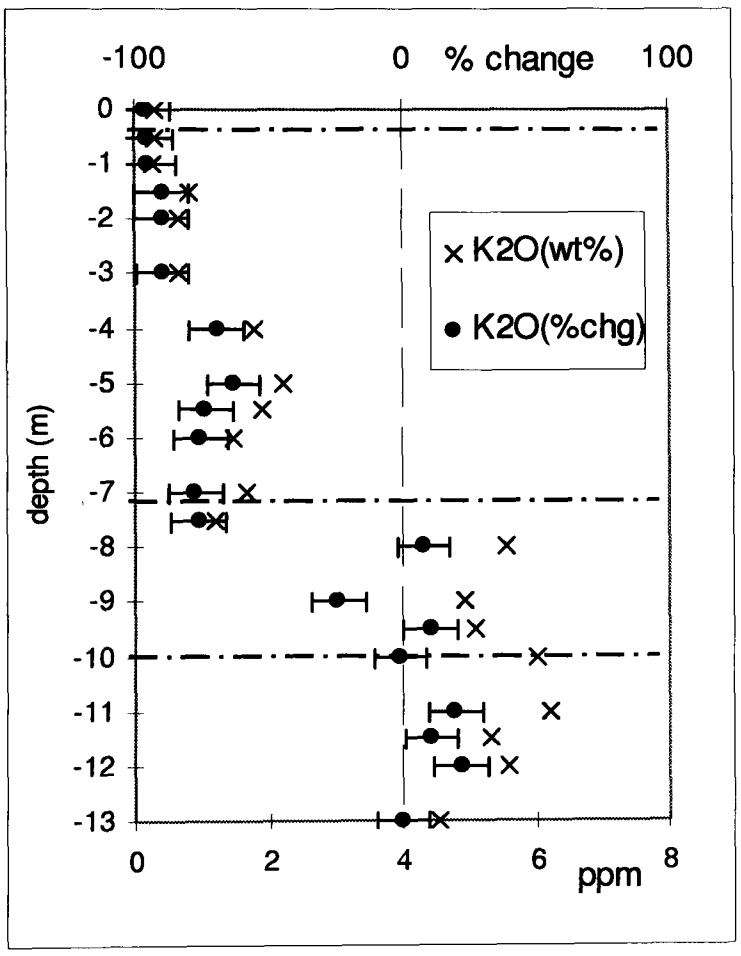

Figure 5.2.Cheras major element percentage change with respect to Zr of the parent rock (sample CA-21 at 13m depth) **(e)**: Na_2O **(f)**: K_2O

(g)

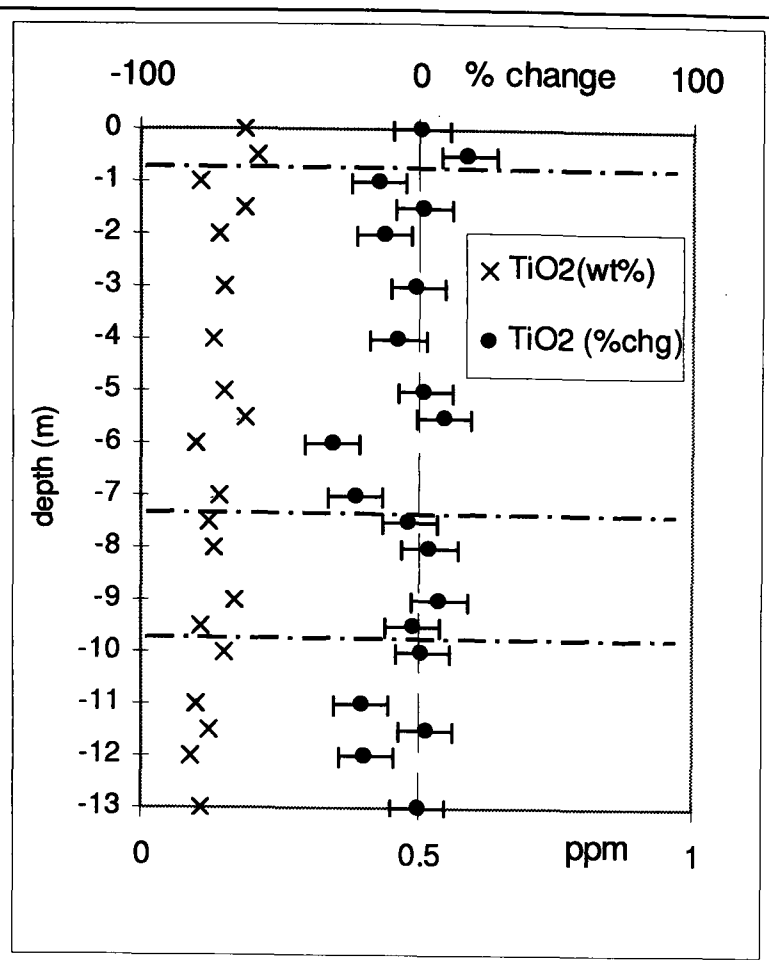

(h)

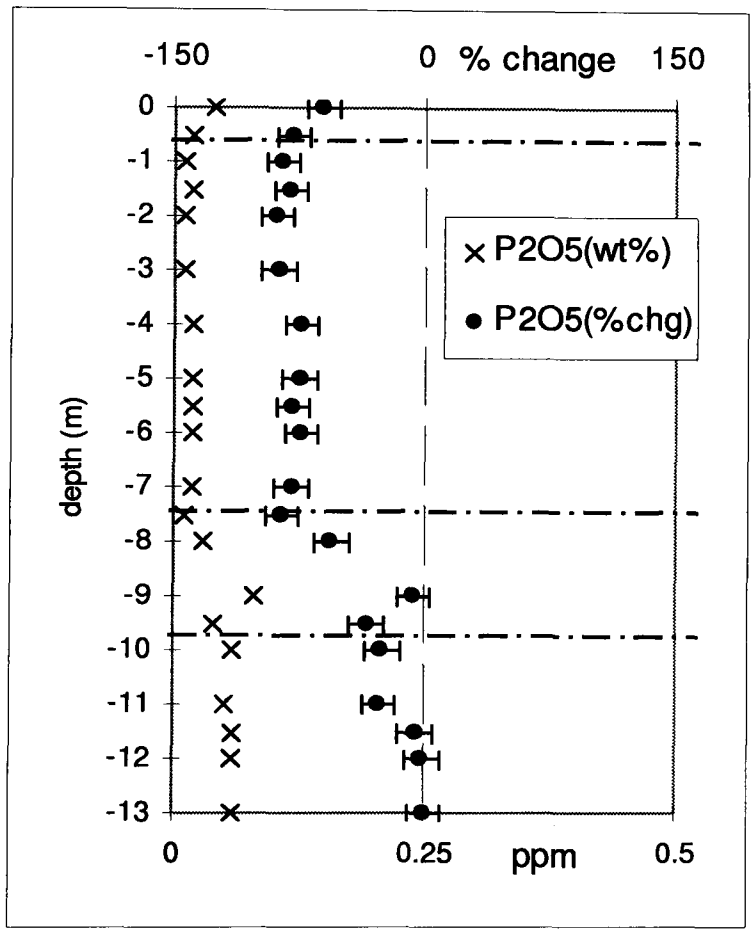

Figure 5.2. Cheras major element percentage change with respect to Zr (**g**): TiO_2 (**h**): P_2O_5

The trace elements, Ba, Y, Sr, and Rb are all mobile elements (Figure 5.3) in the saprolite and/or weathering boundary zone. Ba, Sr and Rb are present in feldspars: Ba and Rb are predominantly in K-feldspar while Sr is predominantly in plagioclase.

Nb is the only element that accumulates above the unweathered granite. Nb has been noted to be hosted by cassiterite (Deer et al, 1992; Cerny et al, 2004). The presence of rare cassiterite grains in the Cheras unweathered granite observed in the optical microscopy study explains the relative immobility of Nb. Its behaviour is indistinguishable from that of zirconium.

(a)

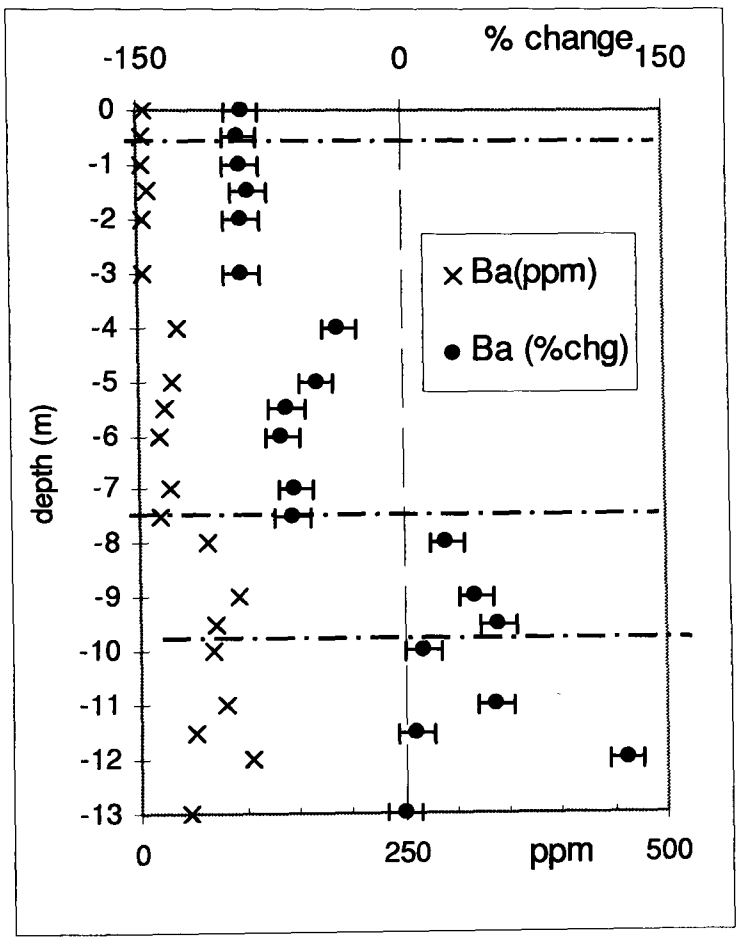

Figure 5.3.Cheras trace element percentage change with respect to Zr of the parent rock (sample CA-21 at 13m depth) **(a)**: Ba

(b)

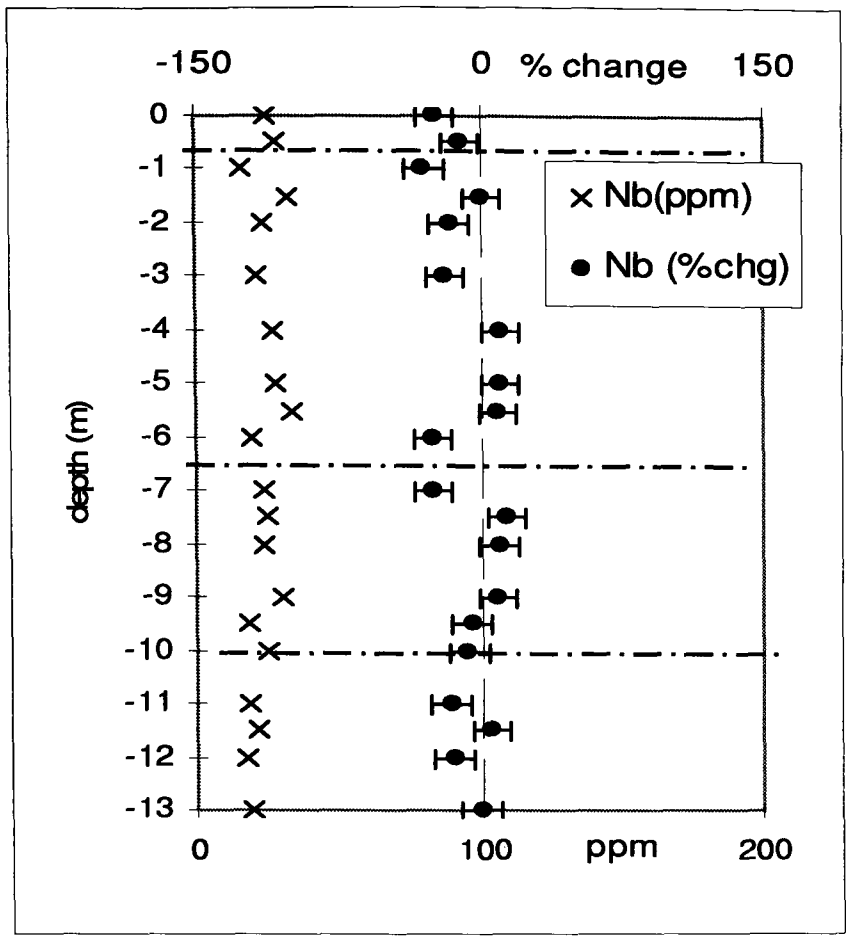

(c)

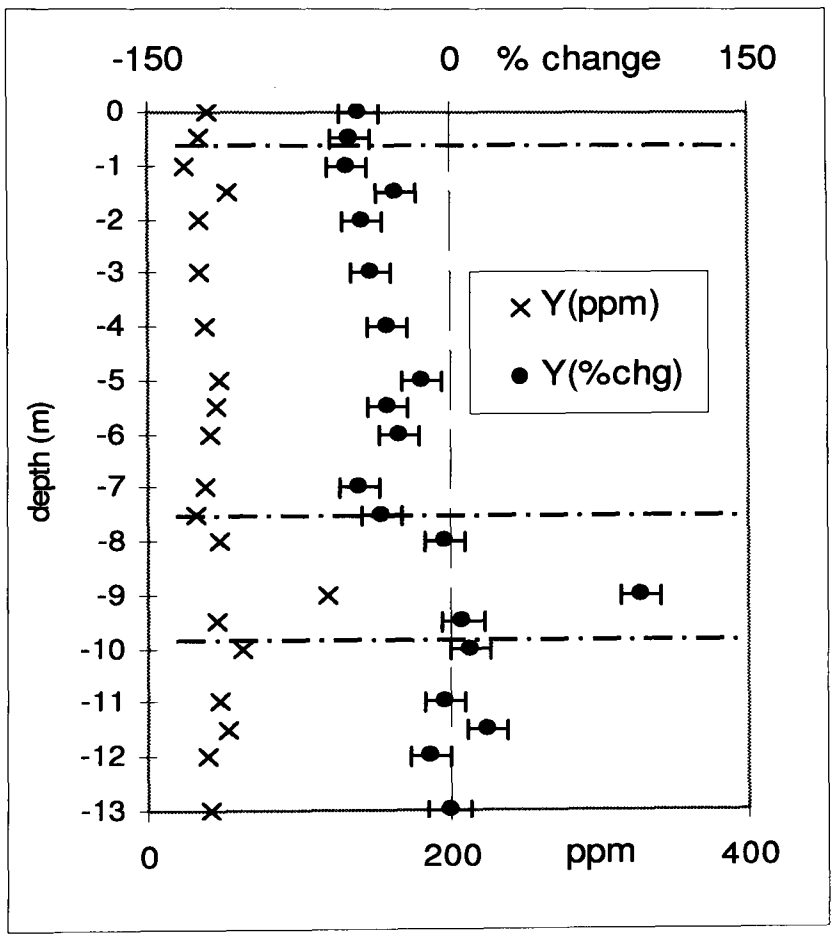

Figure 5.3.Cheras trace element percentage change with respect to Zr of the parent rock (sample CA-21 at 13m depth) (**b**): Nb, (**c**): Y

(d)

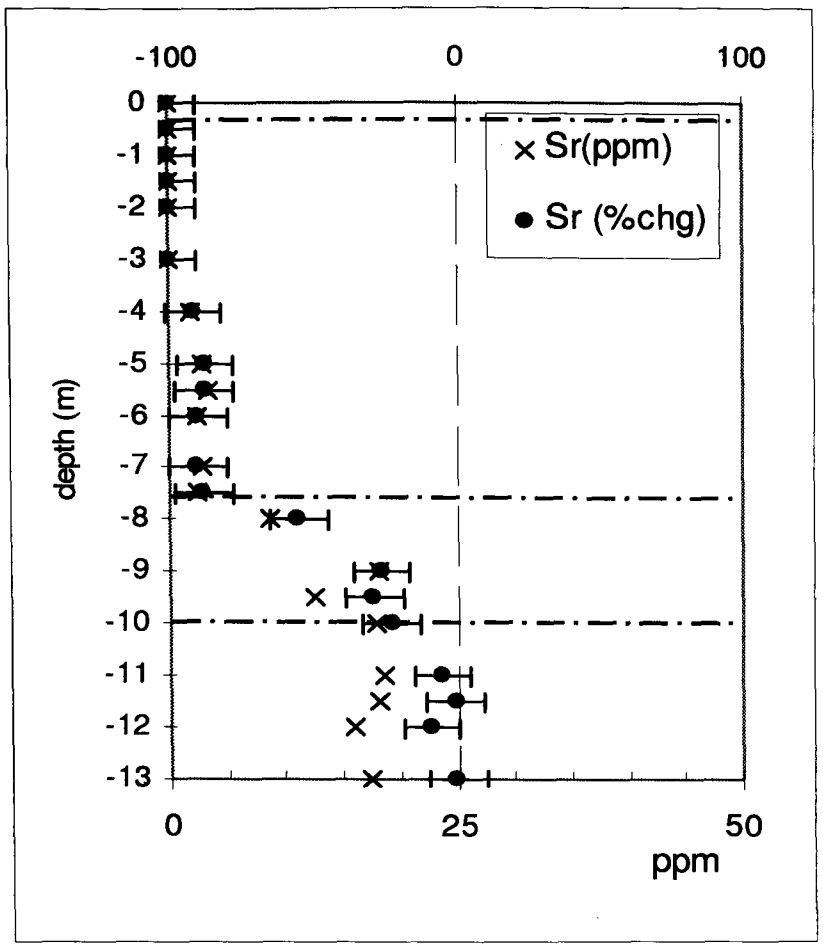

(e)

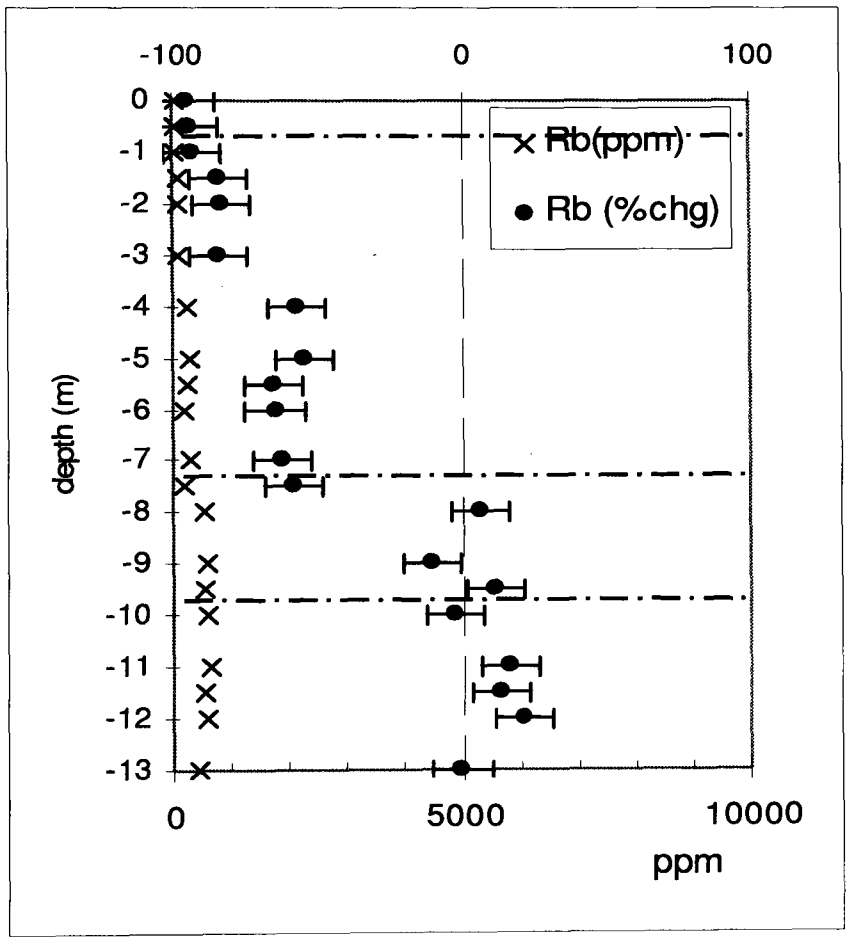

Figure 5.3.Cheras trace element percentage change with respect to Zr of the parent rock (sample CA-21 at 13m depth) **(d)**: Sr **(e)**: Rb

5.2.2 Mobility of major and trace elements relative to Zr in Rawang

The mobility of the major and trace elements in Rawang is similar to that in Cheras. The similar trends can be observed in Figures 5.4 and 5.5.

All the trace elements are relatively mobile elements (Figure 5.5) in the saprolite and/or weathering boundary zone

(a)

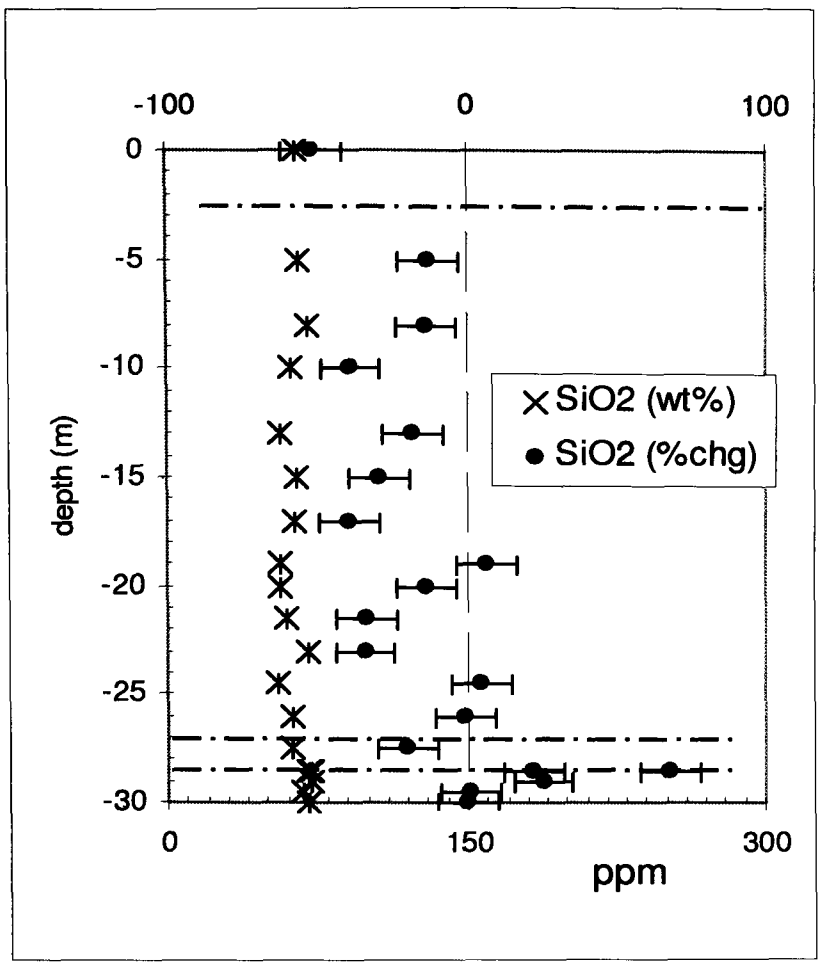

(b)

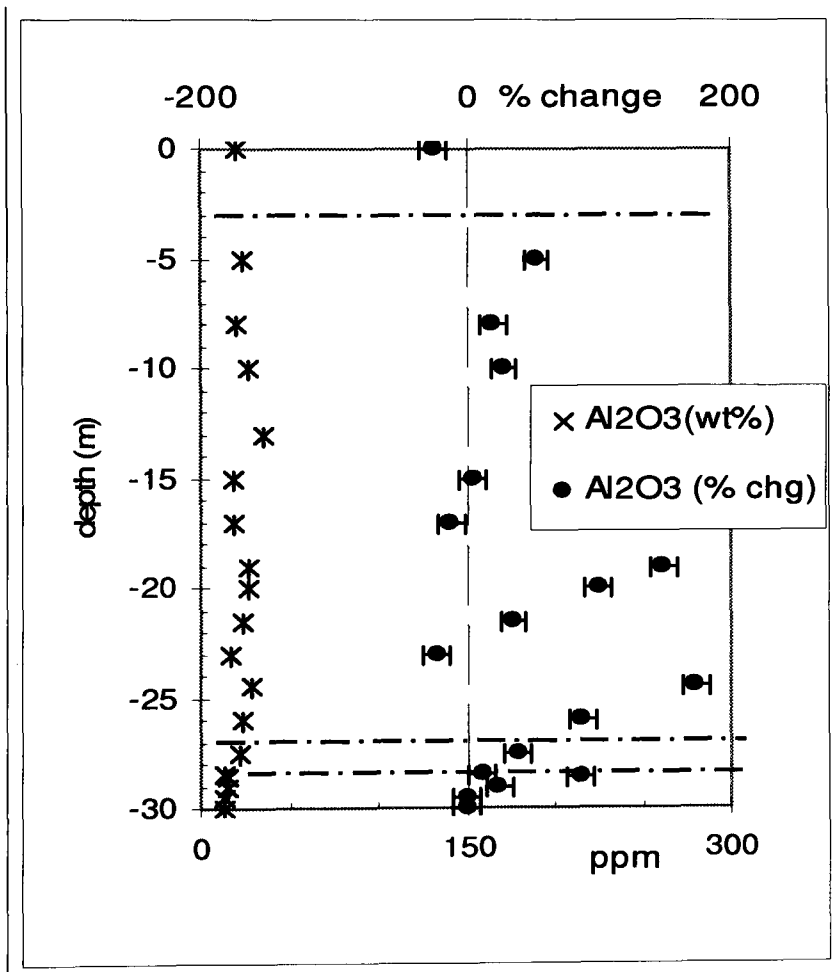

Figure 5.4.Rawang major element percentage change with respect to Zr of the parent rock (sample RA-20 at 30m depth) **(a)**: SiO_2, **(b)**: Al_2O_3

(c)

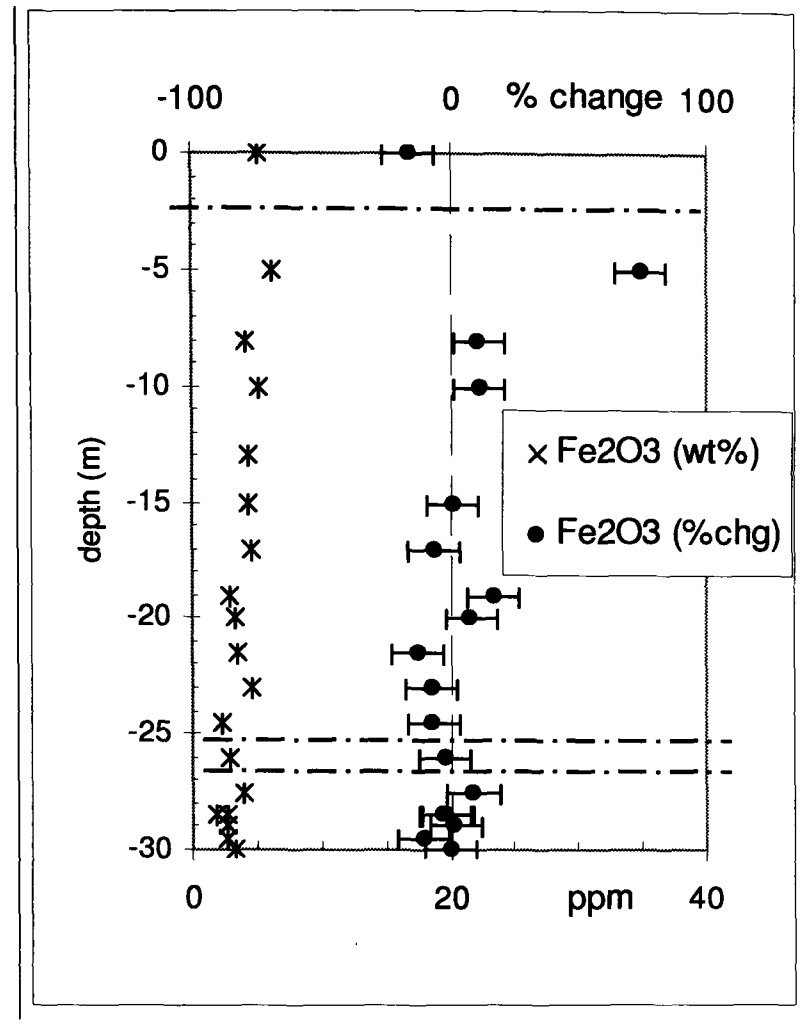

(d)

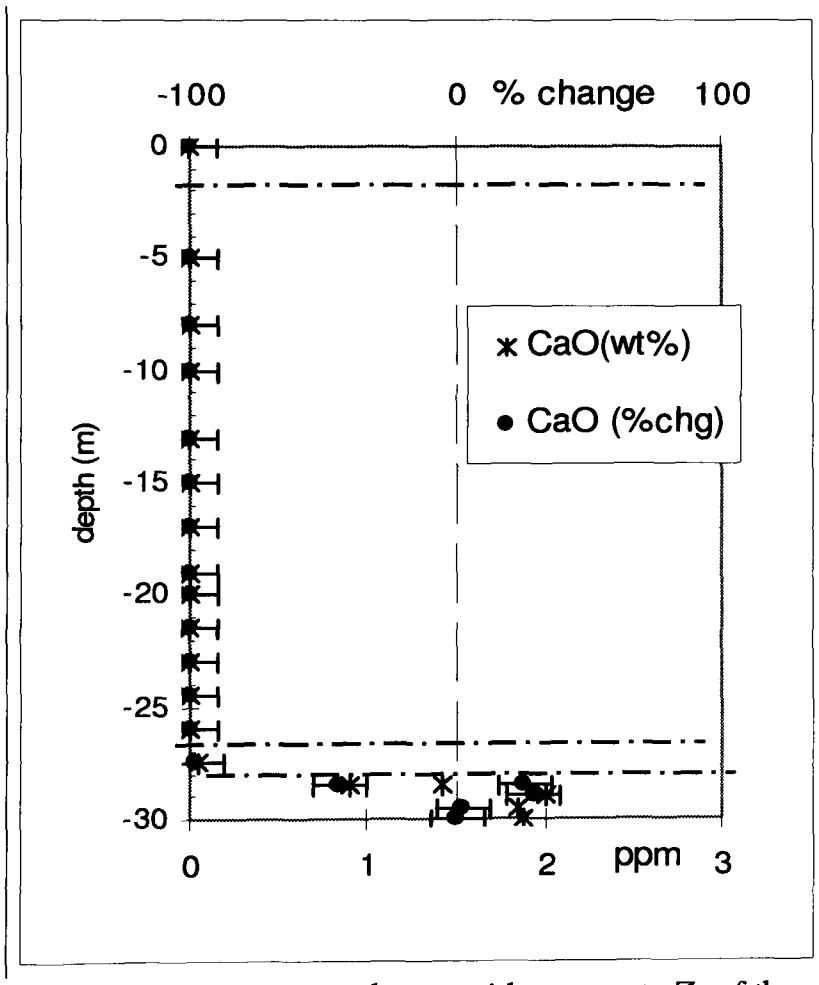

Figure 5.4.Rawang major element percentage change with respect to Zr of the parent rock (sample RA-20 at 30m depth) (**c**): Fe_2O_3, (**d**): CaO

(e)

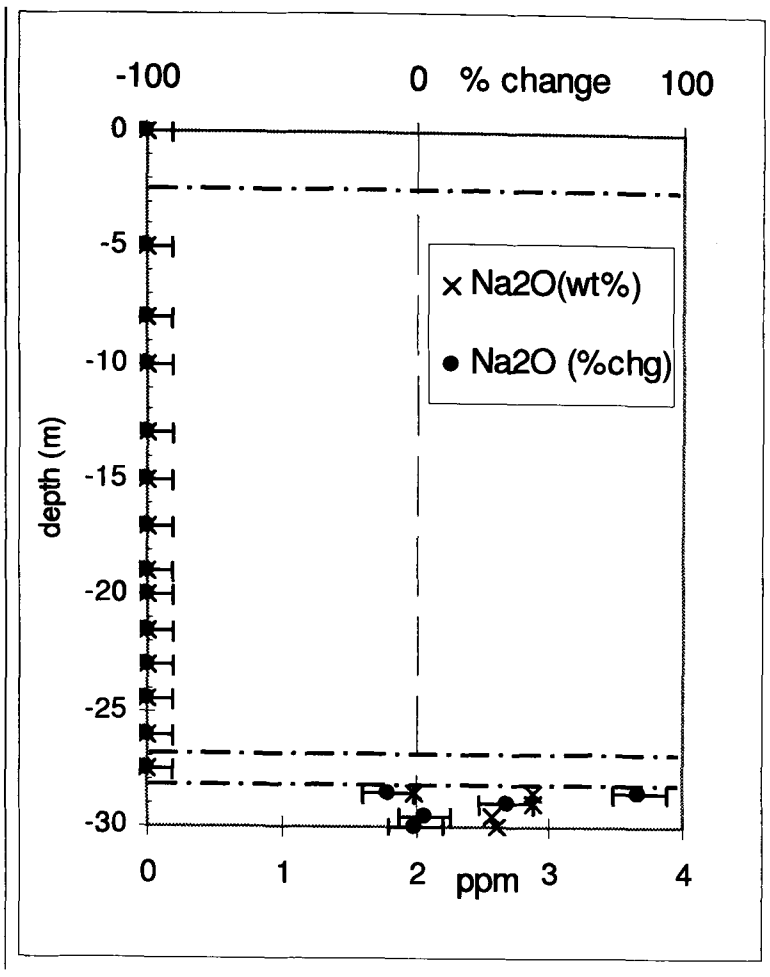

(f)

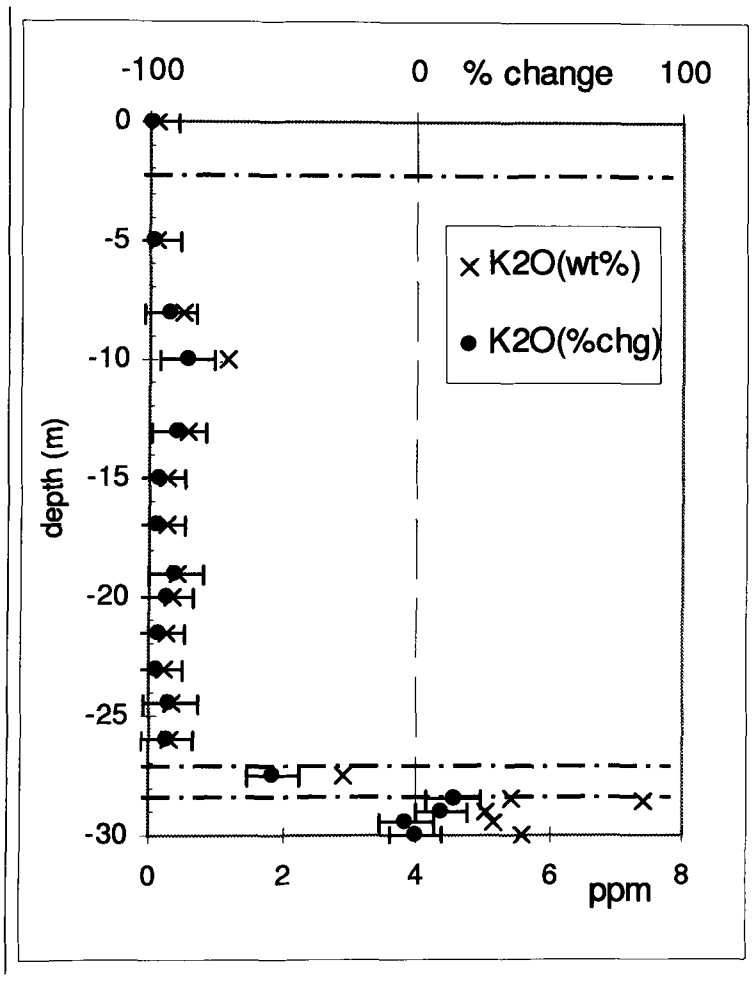

Figure 5.4.Rawang major element percentage change with respect to Zr of the parent rock (sample RA-20 at 30m depth) (**e**): Na_2O (**f**): K_2O

(g)

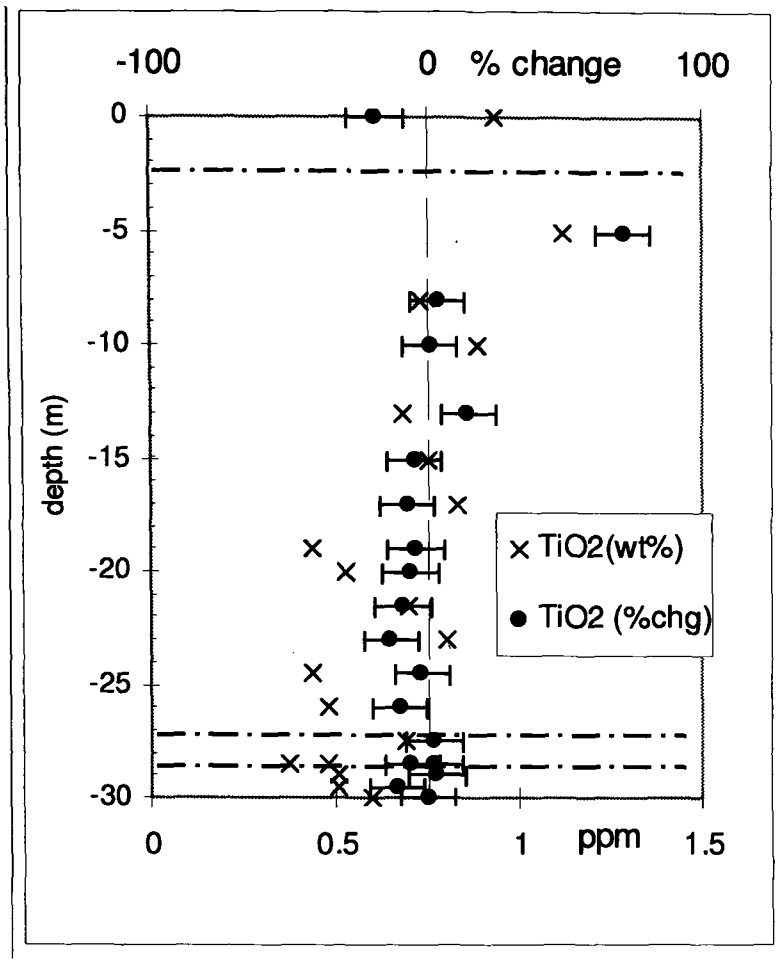

(h)

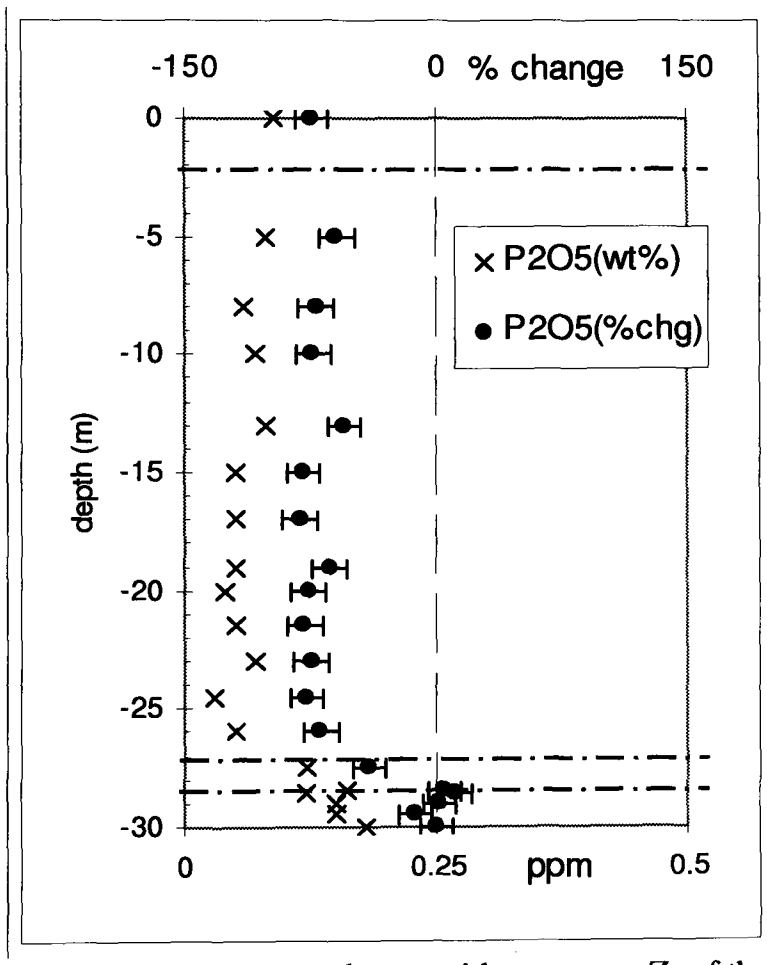

Figure 5.4.Rawang major element percentage change with respect to Zr of the parent rock (sample RA-20 at 30m depth) **(g)**: TiO_2 **(h)**: P_2O_5

(a)

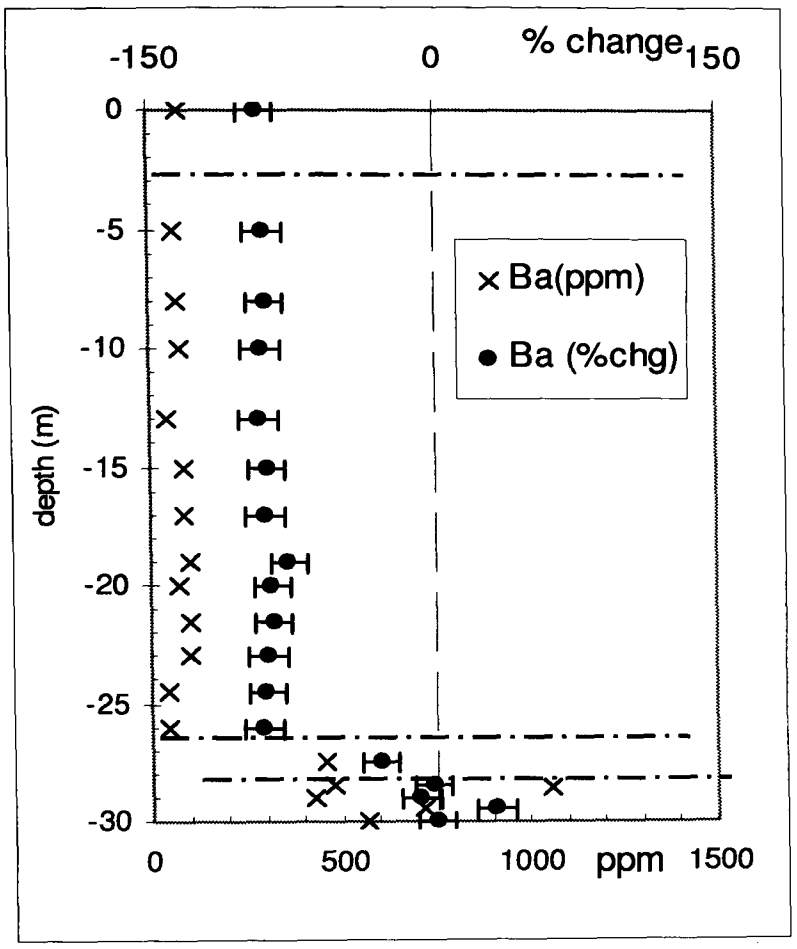

(b)

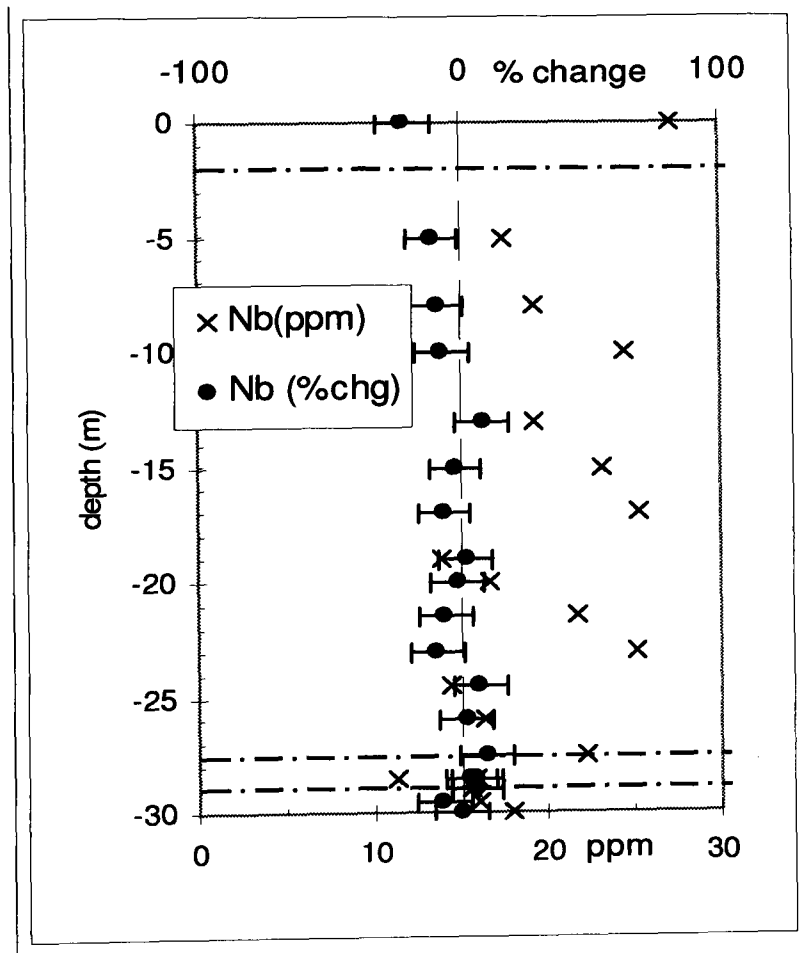

Figure 5.5.Rawang trace element percentage change with respect to Zr of the parent rock (sample RA-20 at 30m depth) (**a**): Ba, (**b**): Nb

(c)

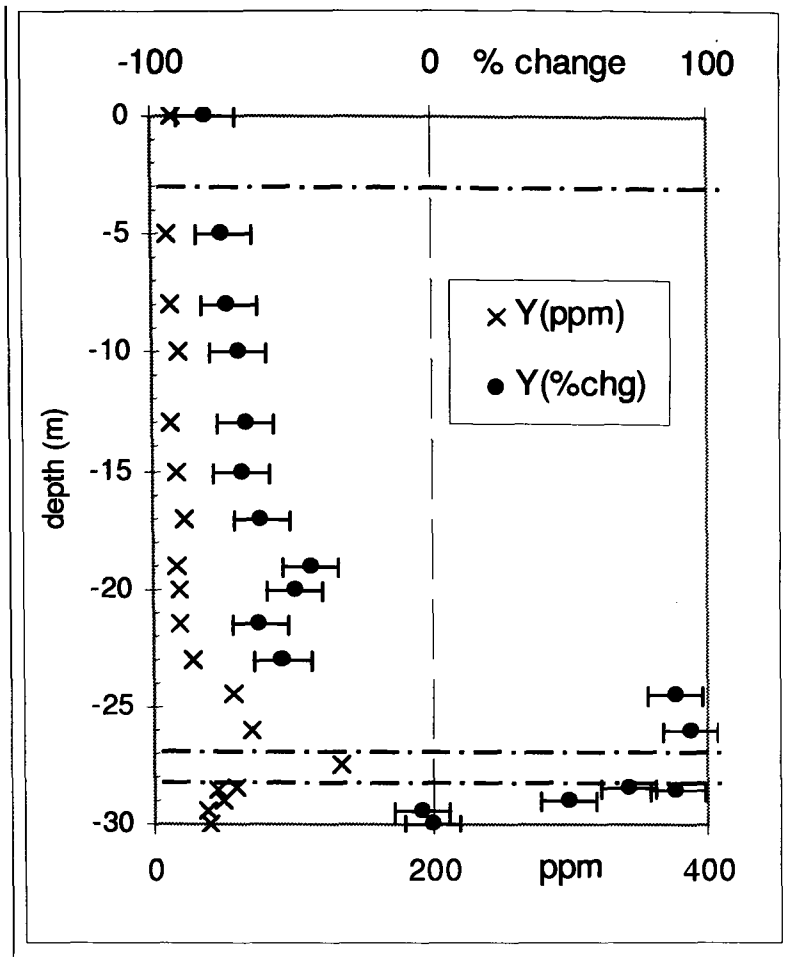

(d)

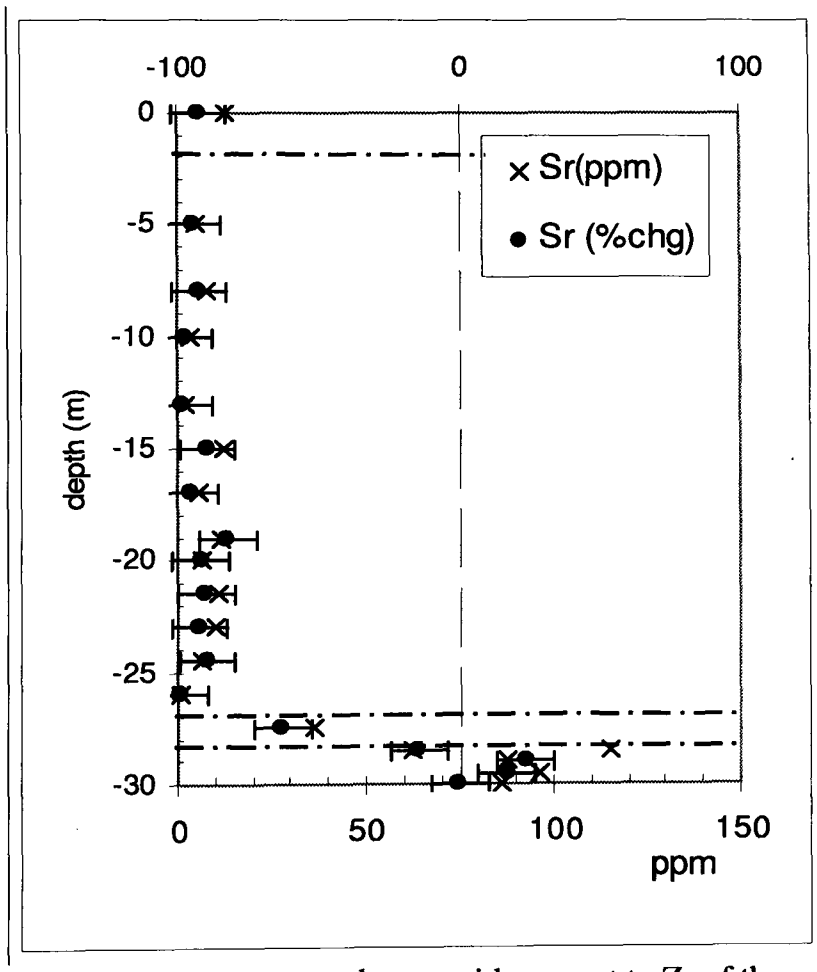

Figure 5.5.Rawang trace element percentage change with respect to Zr of the parent rock (sample RA-20 at 30m depth) **(c)**: Y **(d)**: Sr

(e)

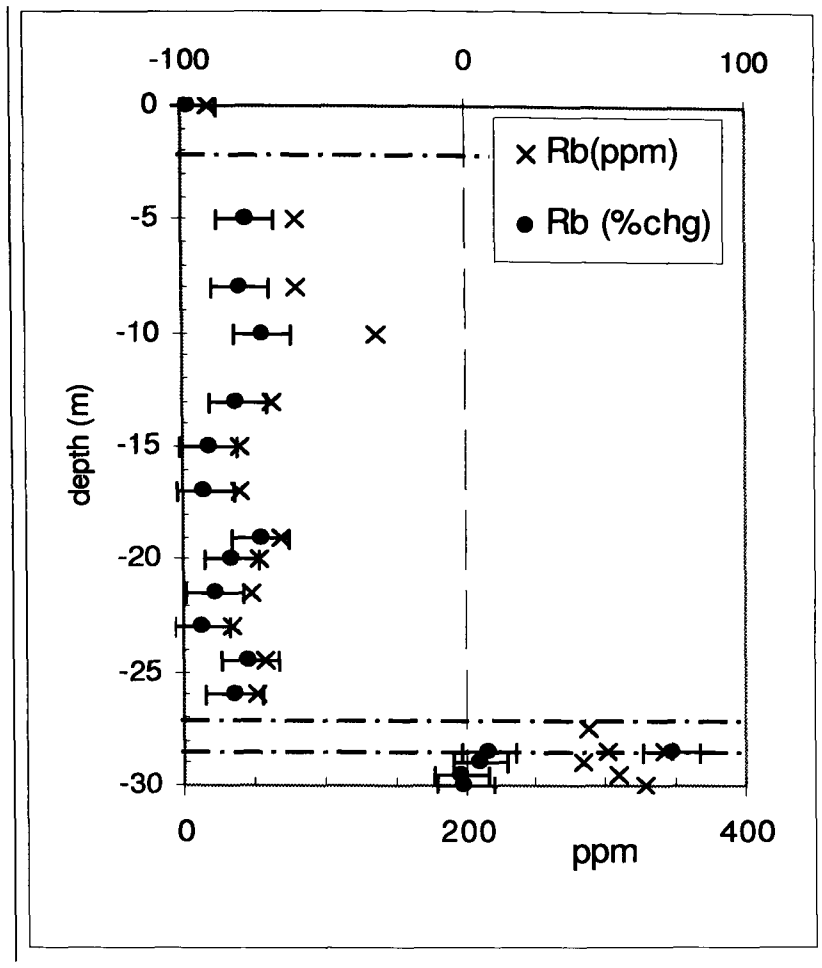

Figure 5.5.Rawang trace element percentage change with respect to Zr of the parent rock (sample RA-20 at 30m depth) (e): Rb

5.3 Mobility of REE relative to Zr

Generally, there are two methods of presenting the data in the REE analyses. First is normalization of the data obtained to a reference that is external to the system under investigation, such as Chondrite and 'North Atlantic Shale Composition', NASC. Secondly, normalization to a reference that is part of the system under investigation. To study the percentage change of the REE, Equation 5.1 is used with respect to a relatively immobile element in each sample and the parent material is used as the reference.

5.3.1 Mobility of REE relative to Zr in Cheras

REE in Cheras

The concentration of the REE in Cheras is given in Table 5.1. The relative mobility of REE to Zr presented as percentage are plotted in Figures: 5.6 (a) to 5.6(n)

Percentage change of elements

Generally, in the top soil and saprolite zones all RE elements shows negative percentage change or mobility relative to Zr. In the weathering boundary zone, all the LREE (La to Sm) shows positive percentage changes or immobility relative to Zr while the HREE (Eu to Lu) generally shows a negative percentage change or mobility relative to Zr.

Zone	Depth bgl, (m)	Sample name	La (ppm)	Ce (ppm)	Pr (ppm)	Nd (ppm)	Sm (ppm	Eu (ppm)	Gd (ppm)	Tb (ppm)	Dy (ppm)	Ho (ppm)	Er (ppm)	Tm (ppm)	Yb (ppm)	Lu (ppm)
Top soil	0.0	CA-1	6.12	23.11	1.39	4.62	1.18	0.02	1.13	0.25	1.78	0.37	1.24	0.22	1.50	0.22
	0.5	CA-2	4.51	15.90	0.96	3.10	0.76	0.01	0.75	0.14	0.94	0.20	0.65	0.12	0.82	0.13
Saprolite	1.0	CA-3	4.42	17.34	0.93	3.00	0.69	0.01	0.52	0.10	0.59	0.13	0.40	0.07	0.55	0.09
	1.5	CA-4	6.66	29.95	1.63	5.52	1.37	0.02	1.05	0.20	1.28	0.26	0.83	0.15	1.05	0.16
	2.0	CA-5	5.26	25.40	1.10	3.59	0.87	0.01	0.81	0.17	1.19	0.25	0.82	0.15	1.02	0.16
	3.0	CA-6	8.40	37.74	2.05	6.97	1.59	0.02	1.26	0.23	1.37	0.27	0.85	0.15	1.05	0.16
	4.0	CA-7	12.74	198.42	3.35	11.42	2.95	0.05	2.36	0.50	3.12	0.69	1.91	0.35	2.58	0.42
	5.0	CA-8	17.84	59.17	4.72	16.28	4.03	0.06	2.61	0.46	2.68	0.55	1.48	0.26	1.87	0.30
	5.5	CA-9	21.15	71.62	5.53	19.24	4.79	0.10	3.22	0.56	3.12	0.64	1.66	0.29	2.06	0.34
	6.0	CA-10	17.46	64.20	4.45	15.25	3.80	0.12	2.90	0.61	4.05	0.92	2.52	0.44	3.03	0.48
	7.0	CA-11	11.59	50.77	2.97	10.04	2.36	0.11	1.74	0.37	2.56	0.61	1.77	0.33	2.38	0.39
	7.5	CA-12	12.95	50.94	3.40	11.75	2.78	0.09	1.75	0.30	1.76	0.37	1.00	0.18	1.26	0.21
Weathering boundary	8.0	CA-13	19.52	275.54	5.29	18.86	4.91	0.15	3.59	0.72	4.34	0.94	2.52	0.44	2.99	0.47
	8.5	CA-14	42.81	68.70	12.48	45.48	12.76	0.53	9.92	1.92	11.53	2.37	6.04	1.04	6.91	1.05
	9.0	CA-15	35.17	60.54	9.11	32.87	9.75	0.37	9.57	2.03	13.10	2.87	7.50	1.26	8.08	1.28
	9.5	CA-16	21.02	42.12	5.56	19.35	5.04	0.17	3.64	0.69	4.10	0.84	2.18	0.37	2.51	0.40
	10.0	CA-17	26.16	61.09	7.23	25.52	6.62	0.19	4.73	0.87	5.25	1.08	2.79	0.47	3.10	0.49
Unweathered granite	11.0	CA-18	13.47	30.81	3.66	12.83	3.60	0.16	2.88	0.59	3.80	0.83	2.20	0.39	2.60	0.42
	11.5	CA-19	19.91	46.53	5.56	19.78	5.53	0.17	4.48	0.90	5.56	1.16	2.99	0.52	3.40	0.52
	12.0	CA-20	23.14	56.65	6.79	24.00	6.78	0.16	5.22	1.04	6.07	1.20	3.01	0.50	3.40	0.50
	13.0	CA-21	17.05	39.64	4.69	16.71	4.56	0.15	3.65	0.74	4.55	0.96	2.49	0.42	2.87	0.44

Table 5.1. REE content in samples at different depth below ground level (bgl) in Cheras. Ample CA-14 (at 8.5m depth) is not used on the plots as it is an 'out-of-order' sample as in Figure 4.5 (Chapter 4).

(a)

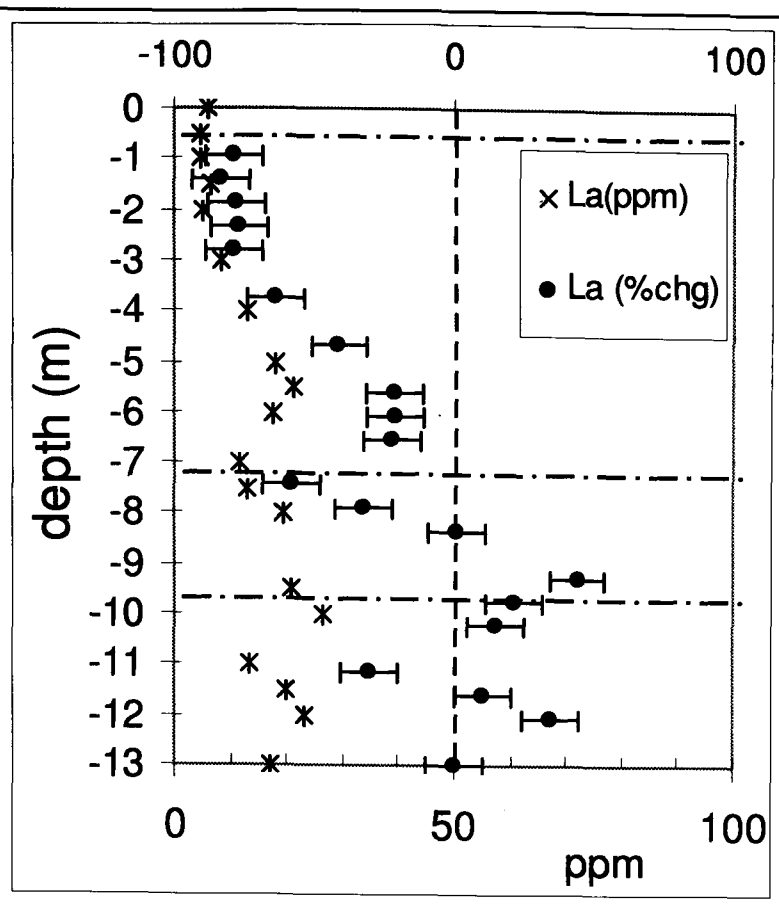

(b)

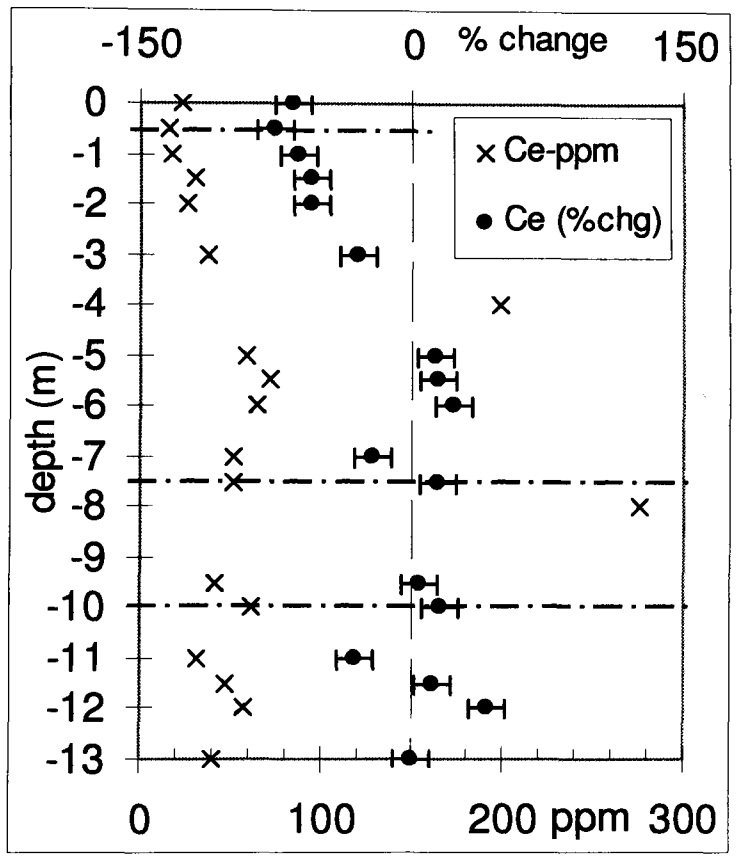

Figure 5.6.Cheras REE percentage change with respect to Zr of the parent rock (sample CA-21 at 13m depth) (**a**): La, (**b**): Ce. The points were plotted at 10% error.

(c)

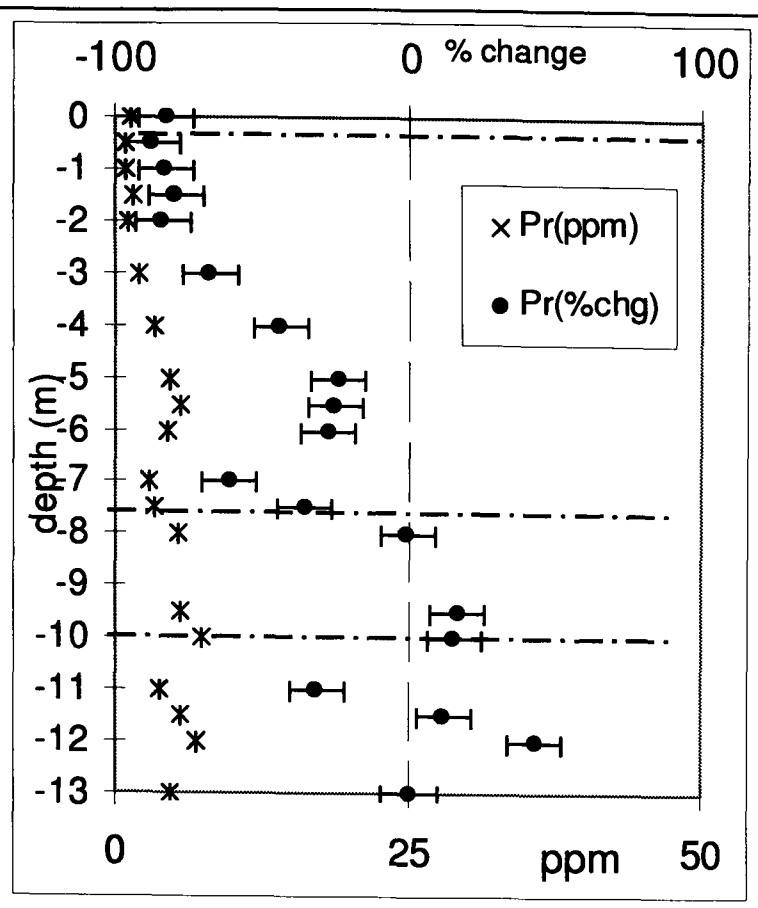

(d)

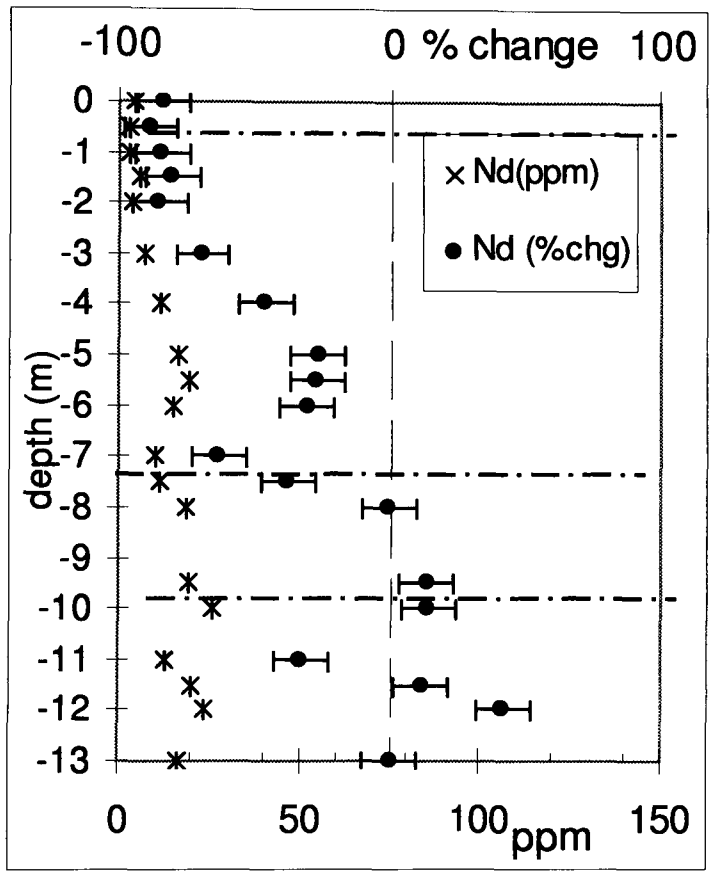

Figure 5.6.Cheras REE percentage change with respect to Zr of the parent rock (sample CA-21 at 13m depth) (**c**): Pr, (**d**): Nd

(e)

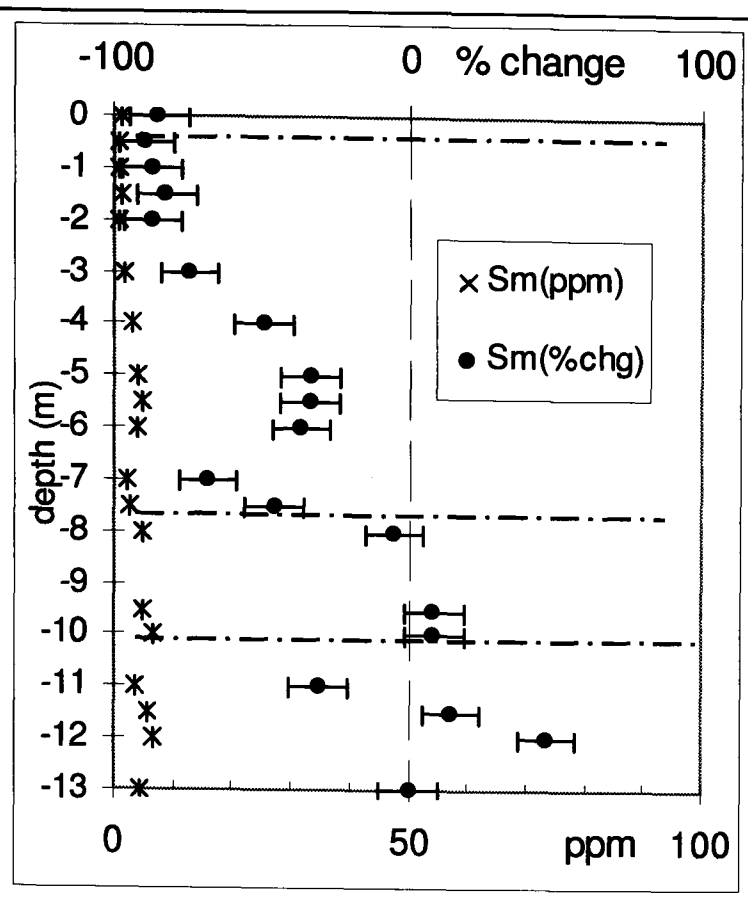

(f)

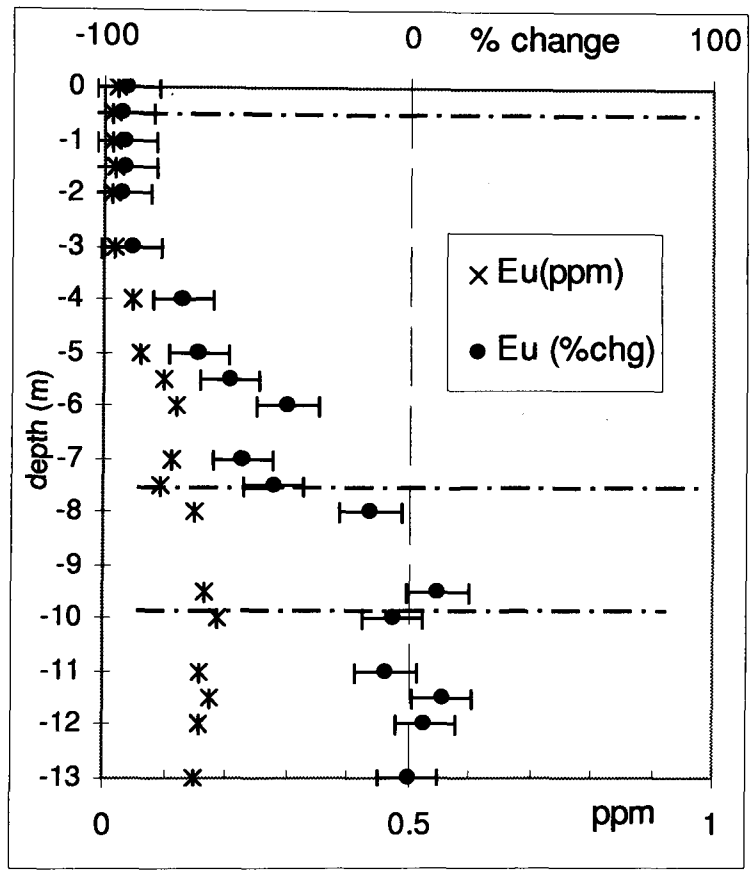

Figure 5.6.Cheras REE percentage change with respect to Zr of the parent rock (sample CA-21 at 13m depth) **(e)**: Sm, **(f)**: Eu

(g)

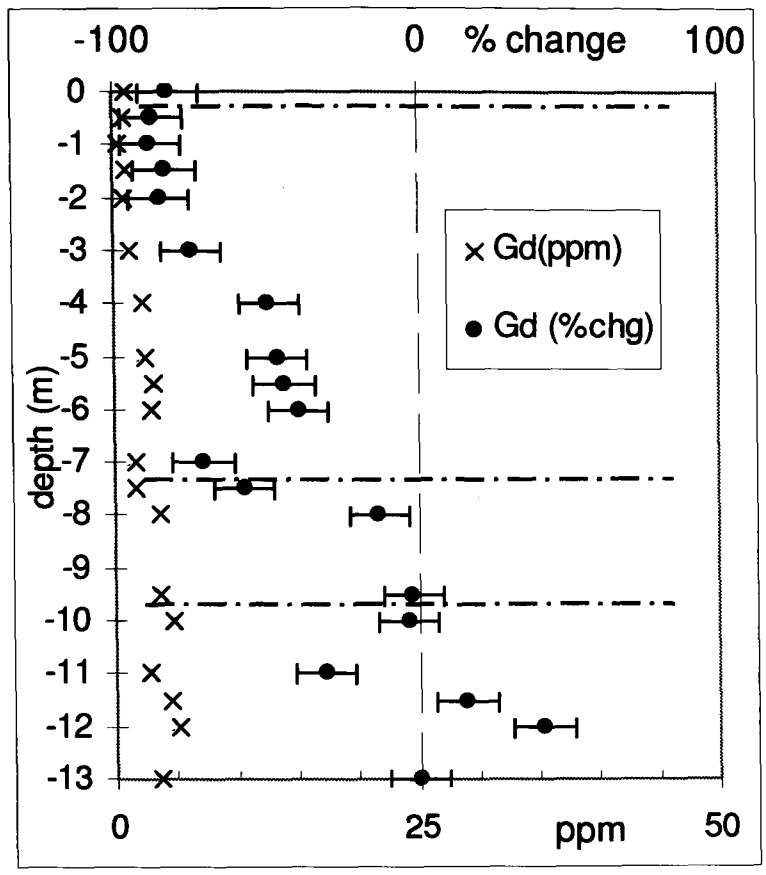

(h)

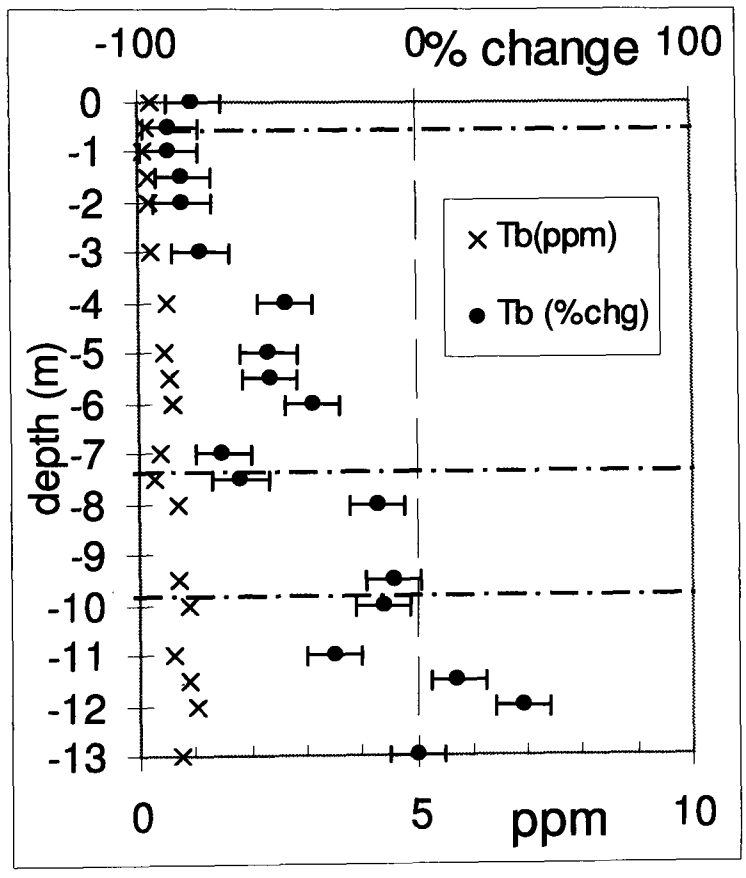

Figure 5.6.Cheras REE percentage change with respect to Zr of the parent rock (sample CA-21 at 13m depth) (**g**): Gd, (**h**): Tb

(i)

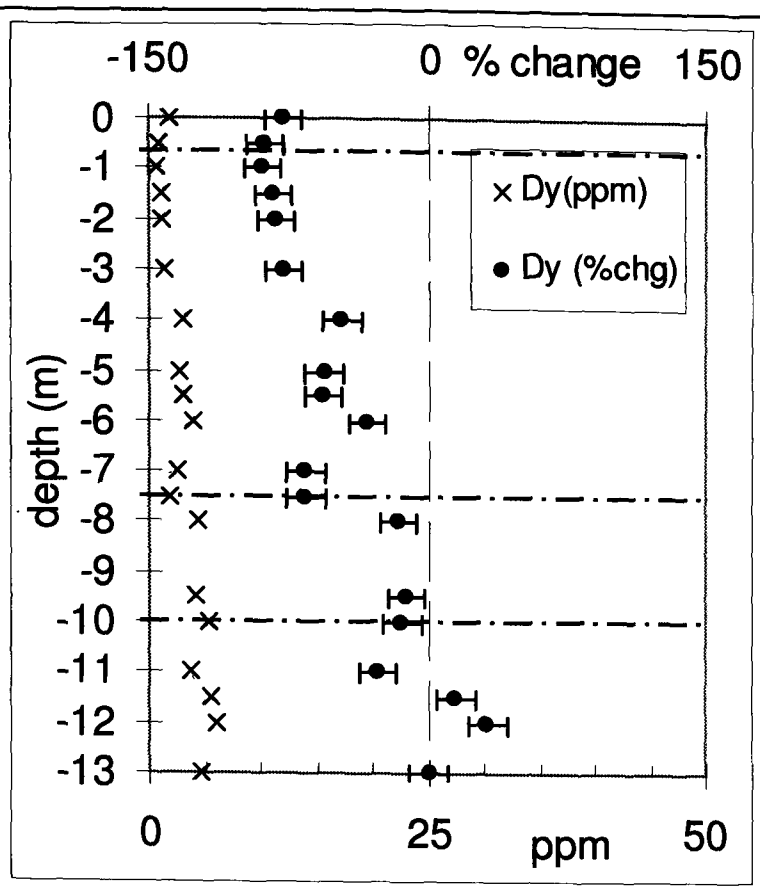

(j)

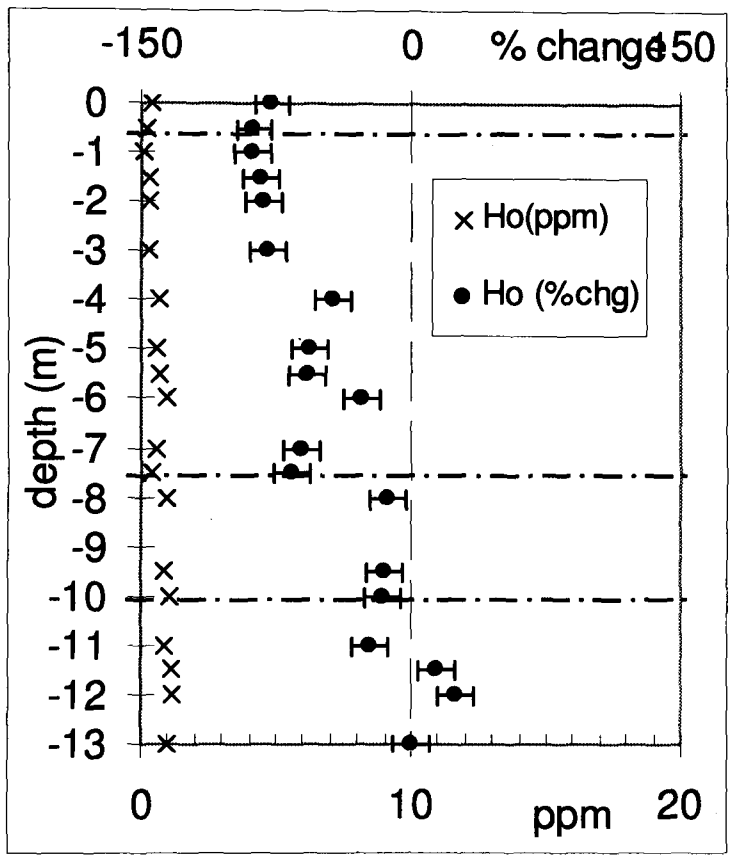

Figure 5.6.Cheras REE percentage change with respect to Zr of the parent rock (sample CA-21 at 13m depth) **(i)**: Dy, **(j)**:Ho

(k)

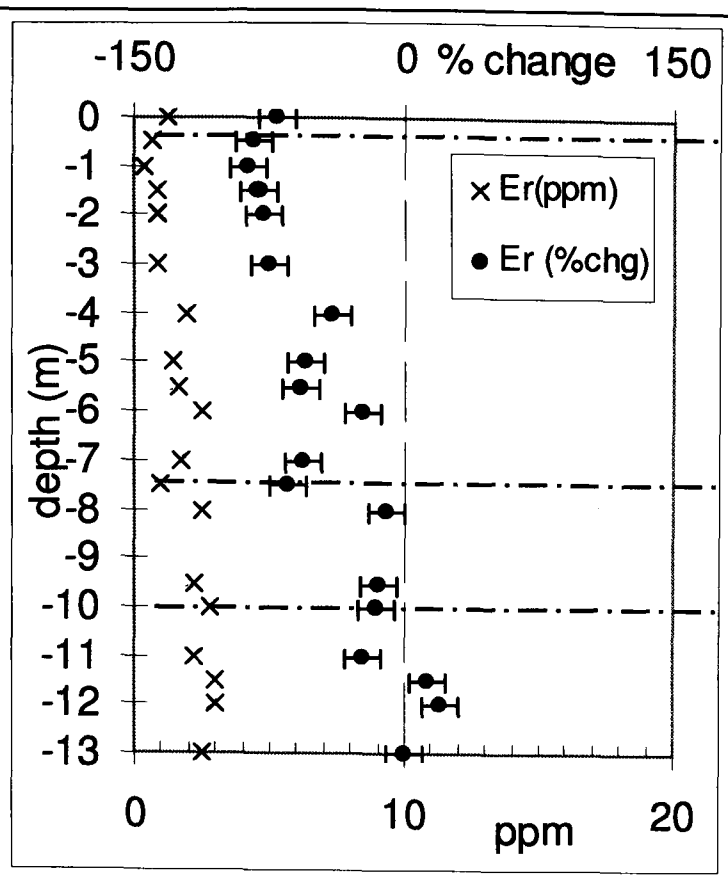

(l)

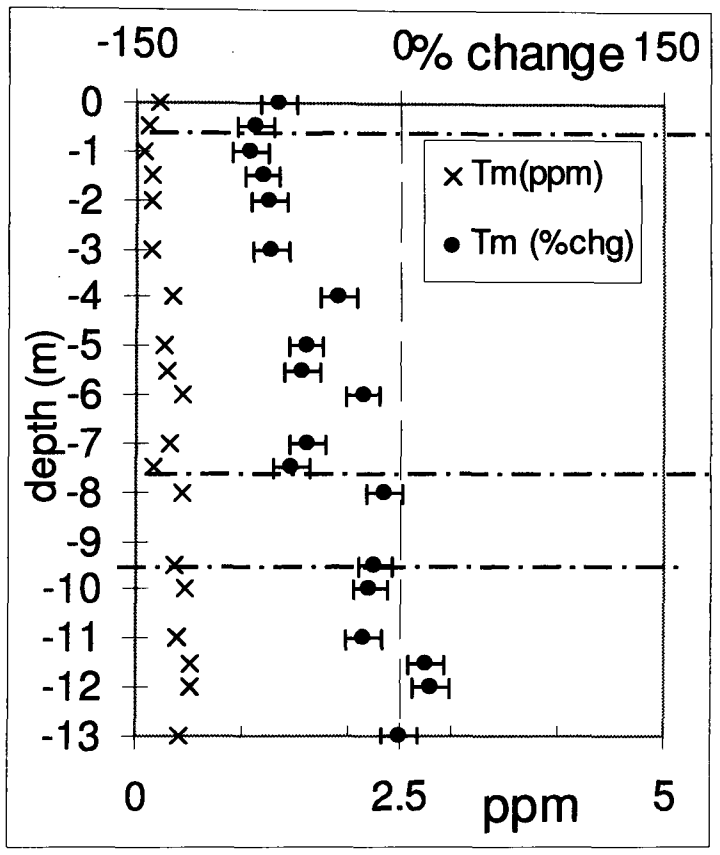

Figure 5.6.Cheras REE percentage change with respect to Zr of the parent rock (sample CA-21 at 13m depth) (**k**): Er, (**l**): Tm

(m)

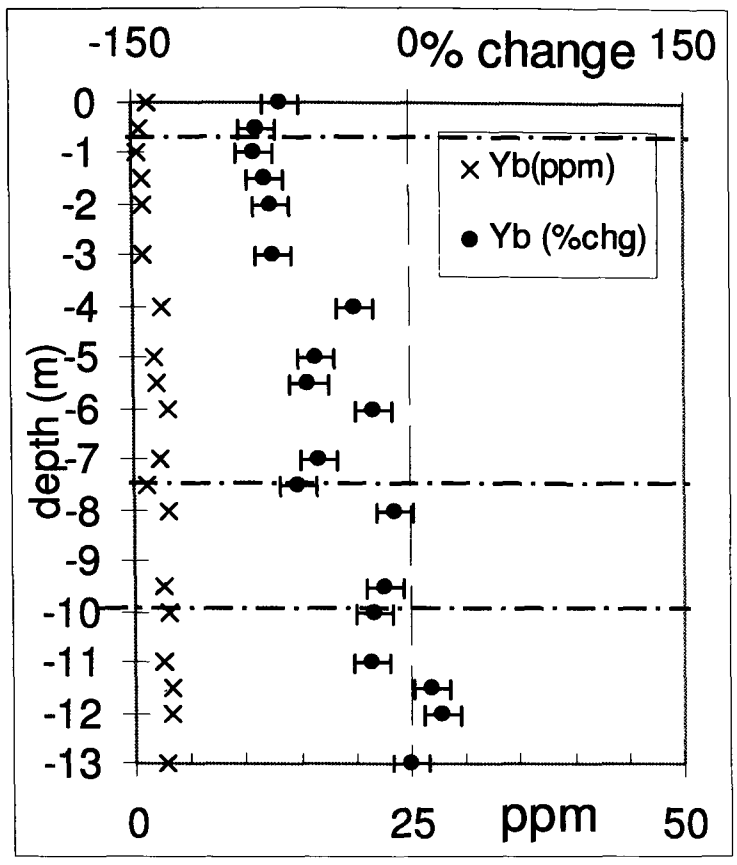

(n)

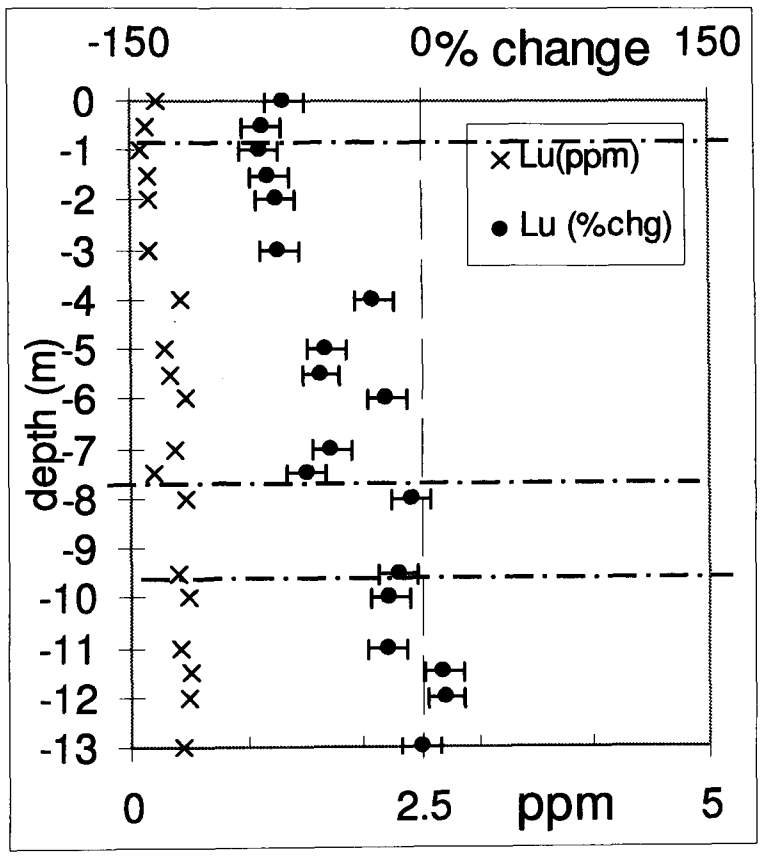

Figure 5.6.Cheras REE percentage change with respect to Zr of the parent rock (sample CA-21 at 13m depth) **(m)**: Yb, **(n)**: Lu

5.3.2 Mobility of REE relative to Zr in Rawang

The concentration of the REE in Rawang is given in Table 5.2 and plotted in Figure 5.7. For the REE in Rawang, Zr is also used as the normalising element.

Percentage change of elements relative to Zr

Generally, all RE elements shows negative percentage change or mobile relative to Zr in the top soil and upper part of the saprolite zones. LREE shows positive percentage change or immobile relative to Zr in the lower saprolite zones while the HREE shows nnegative percentage change or mobile relative to Zr. However, all the RE elements shows positive percentage change (immobile relative to Zr) in the boundary zone.

Zone	Depth bgl, (m)	sample name	La (ppm)	Ce (ppm)	Pr (ppm)	Nd (ppm)	Sm (ppm	Eu (ppm)	Gd (ppm)	Tb (ppm)	Dy (ppm)	Ho (ppm)	Er (ppm)	Tm (ppm)	Yb (ppm)	Lu (ppm)
Top soil (~1m depth)	0.0	RA-1	20.12	42.05	4.33	14.00	2.57	0.25	1.68	0.26	1.22	0.18	0.45	0.07	0.42	0.06
	5.0	RA-2	25.14	58.15	5.50	18.25	3.63	0.36	2.60	0.41	2.00	0.30	0.74	0.11	0.68	0.10
	8.0	RA-3	37.94	101.22	8.68	28.31	5.31	0.57	3.63	0.57	2.75	0.40	0.98	0.15	0.92	0.13
	10.0	RA-4	17.51	59.95	4.31	15.00	3.40	0.35	2.93	0.50	2.62	0.41	1.10	0.18	1.12	0.15
	13.0	RA-5	23.48	50.52	5.40	18.17	3.61	0.43	2.55	0.40	2.16	0.34	0.89	0.14	0.90	0.13
	15.0	RA-6	37.49	85.94	8.88	30.08	5.17	0.52	3.27	0.47	2.16	0.30	0.71	0.10	0.62	0.09
	17.0	RA-7	56.32	91.80	12.34	40.05	7.54	0.79	5.37	0.81	3.94	0.61	1.53	0.22	1.27	0.18
Saprolite	19.0	RA-8	58.42	104.03	13.56	45.82	8.12	0.88	5.48	0.80	3.85	0.58	1.39	0.20	1.15	0.16
	20.0	RA-9	51.92	121.95	12.27	42.54	7.82	0.83	5.29	0.78	3.82	0.60	1.51	0.22	1.32	0.19
	21.5	RA-10	67.88	112.28	15.25	51.29	9.08	0.92	5.92	0.86	4.11	0.64	1.59	0.24	1.42	0.20
	23.0	RA-11	73.72	129.63	17.41	61.40	11.48	1.20	8.06	1.19	5.92	0.95	2.50	0.38	2.29	0.32
	24.5	RA-12	84.26	1,623.78	23.14	89.88	16.38	1.90	12.72	1.97	9.61	1.80	5.15	0.81	4.87	0.70
	26.0	RA-13	39.86	35.89	11.80	47.31	9.64	1.18	7.83	1.14	6.46	1.25	3.65	0.59	3.45	0.49
	27.50	RA-14	128.01	95.23	32.03	121.86	23.42	3.21	20.16	2.94	16.58	3.30	9.62	1.51	8.95	1.29
Weathering boundary	28.50	RA-15	36.55	77.67	9.92	38.57	8.13	1.04	7.53	1.24	7.46	1.47	4.32	0.68	4.13	0.59
	28.52	RA-16	17.16	35.32	4.77	18.76	4.21	0.88	4.27	0.73	4.65	0.96	2.88	0.47	2.98	0.41
Unweathered granite	28.54	RA-17	16.27	38.53	5.10	20.21	4.51	1.07	4.35	0.75	4.56	0.91	2.71	0.43	2.66	0.37
	29.0	RA-18	30.20	69.73	8.37	31.87	6.63	0.84	5.82	0.96	5.64	1.09	3.17	0.51	3.00	0.43
	29.5	RA-19	31.29	65.05	8.23	30.74	6.25	0.90	5.12	0.78	4.30	0.76	2.11	0.32	1.87	0.27
	30.0	RA-20	37.50	82.62	9.67	35.88	7.19	0.88	5.95	0.92	4.93	0.90	2.46	0.37	2.17	0.31

Table 5.2. REE content in samples at different depth below ground level (bgl) in Rawang.

(a)

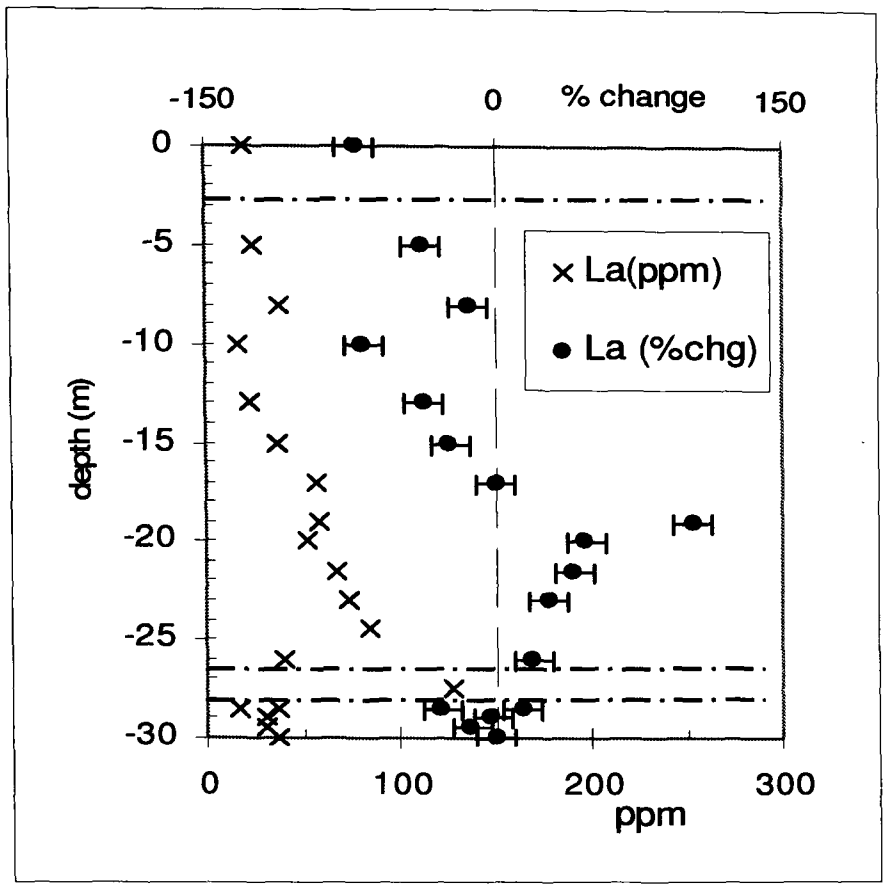

(b)

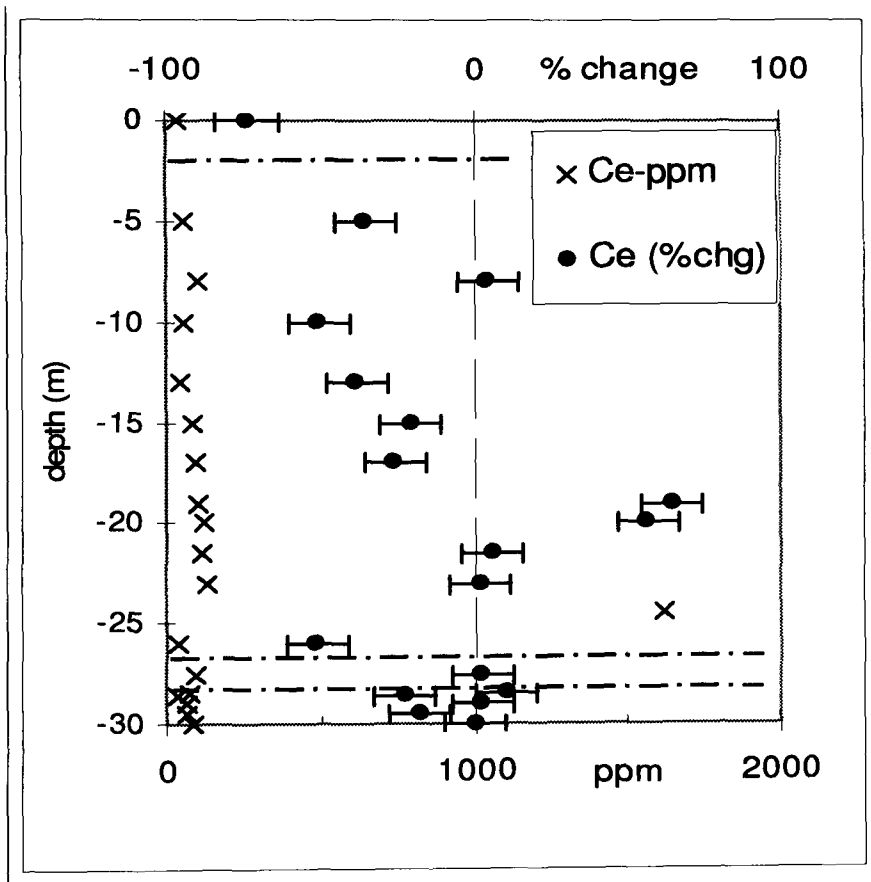

Figure 5.7.Rawang LREE percentage change with respect to Zr of the parent rock (sample RA-20 at 30m depth) **(a)**: La, **(b)**: Ce. The points were plotted at 10% error.

(c)

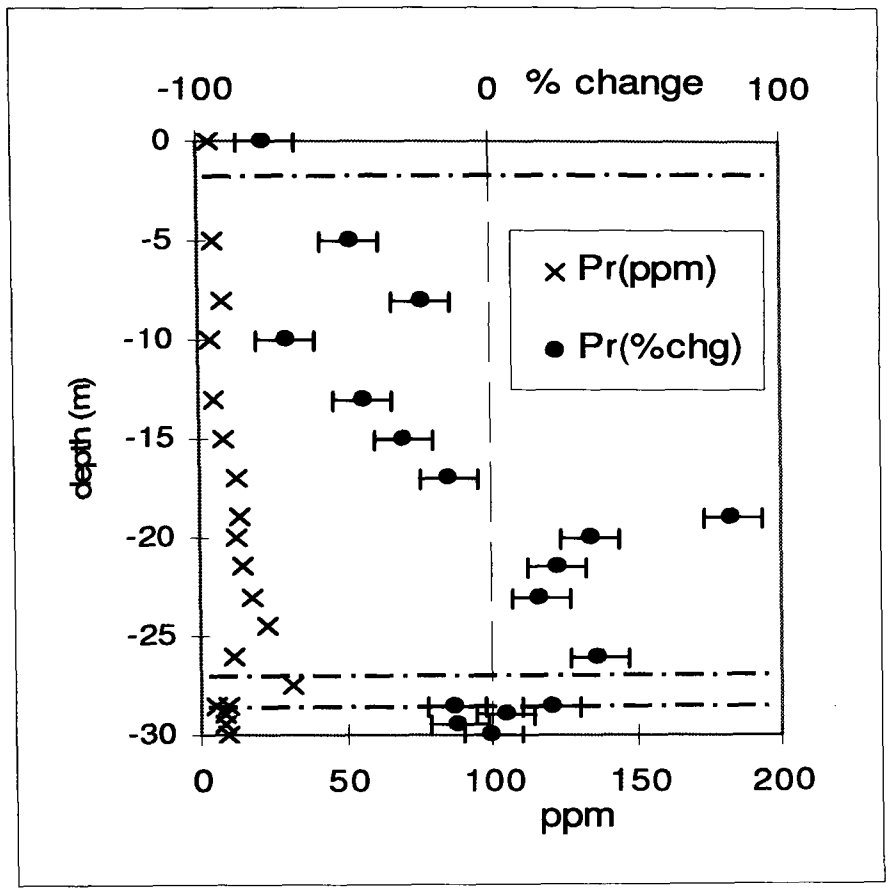

(d)

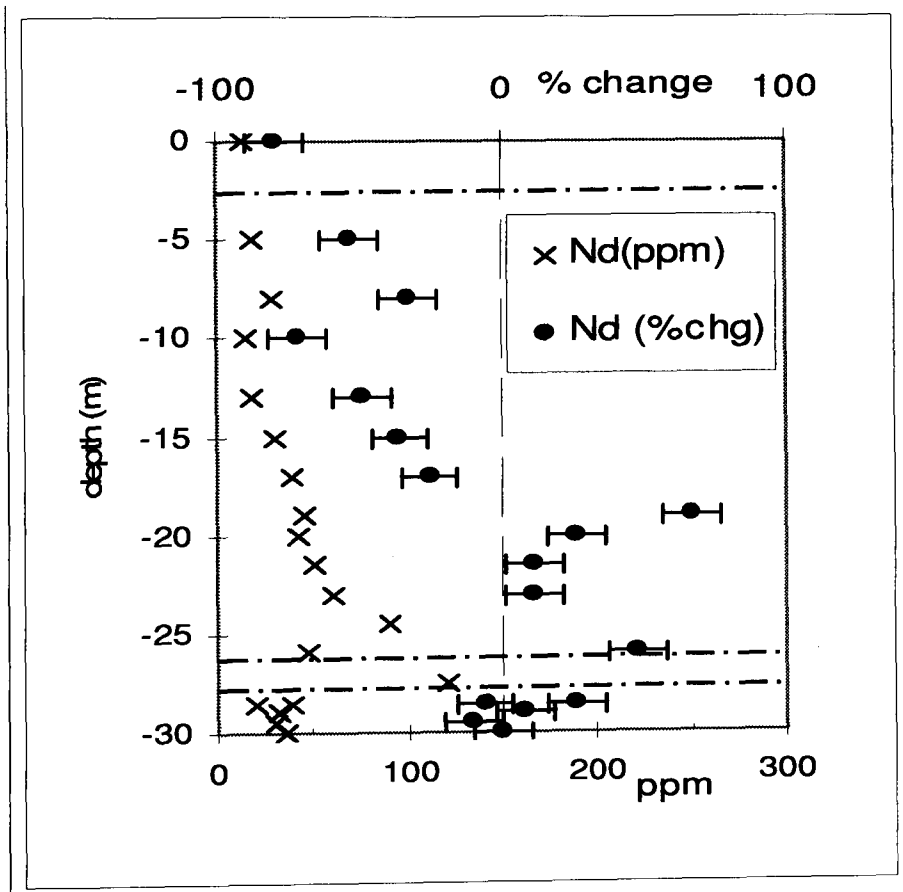

Figure 5.7.Rawang REE percentage change with respect to Zr of the parent rock (sample RA-20 at 30m depth) (**c**): Pr, (**d**): Nd

(e)

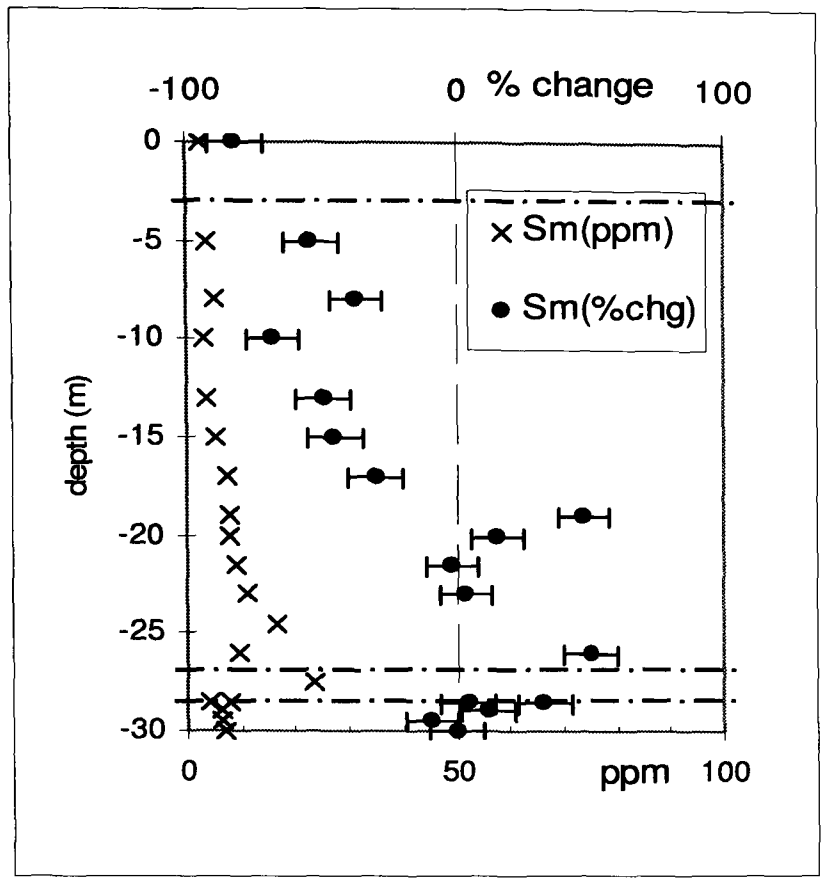

(f)

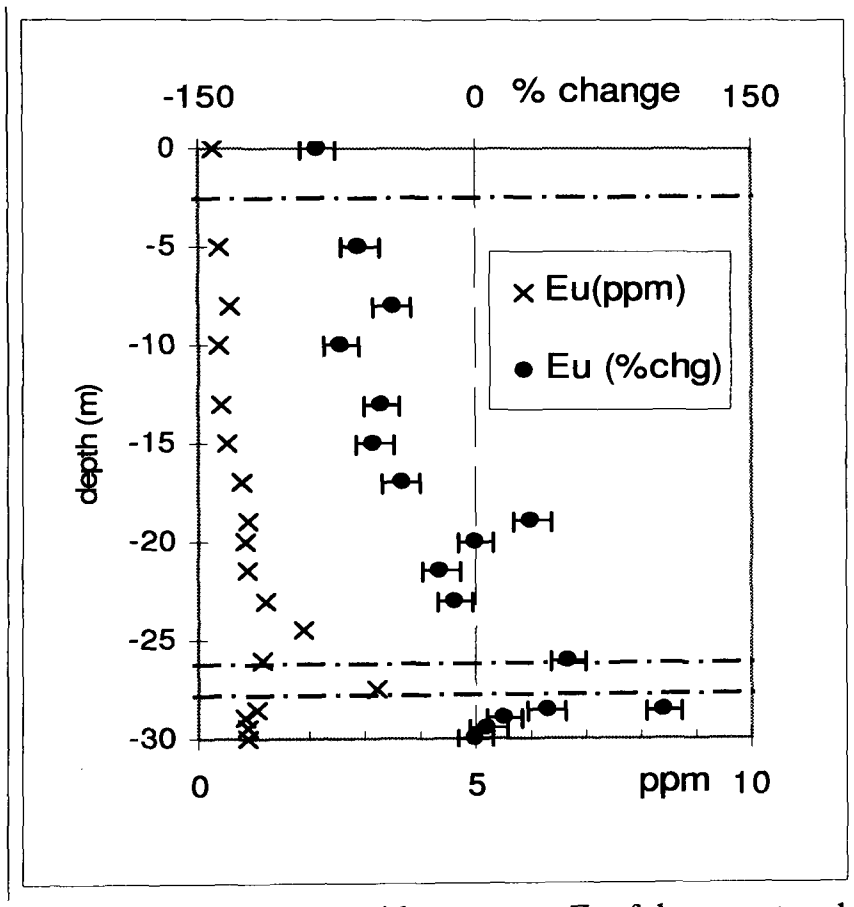

Figure 5.7.Rawang REE percentage change with respect to Zr of the parent rock (sample RA-20 at 30m depth) **(e)**: Sm, **(f)**: Eu

(g)

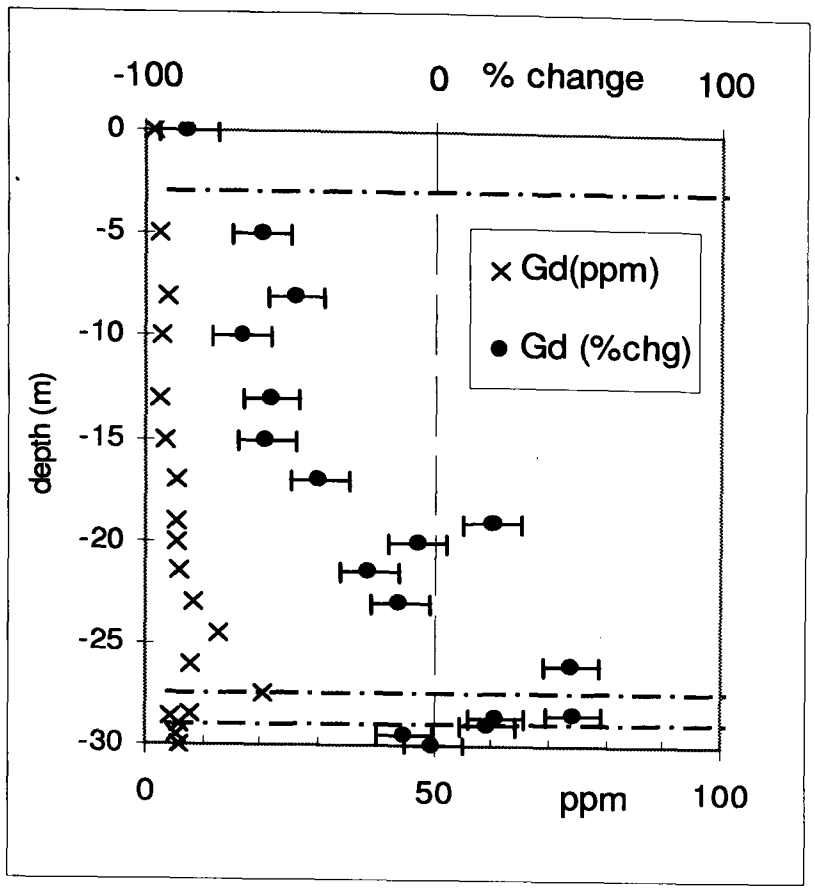

(h)

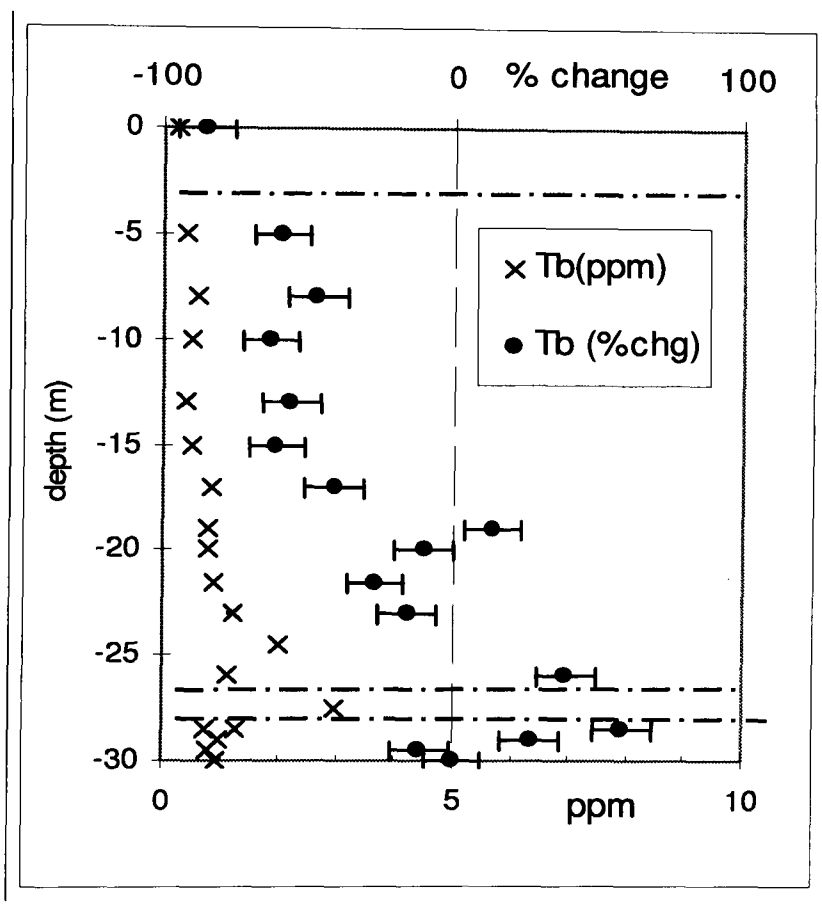

Figure 5.7.Rawang REE percentage change with respect to Zr of the parent rock (sample RA-20 at 30m depth) (**g**): Gd, (**h**): Tb

(i)

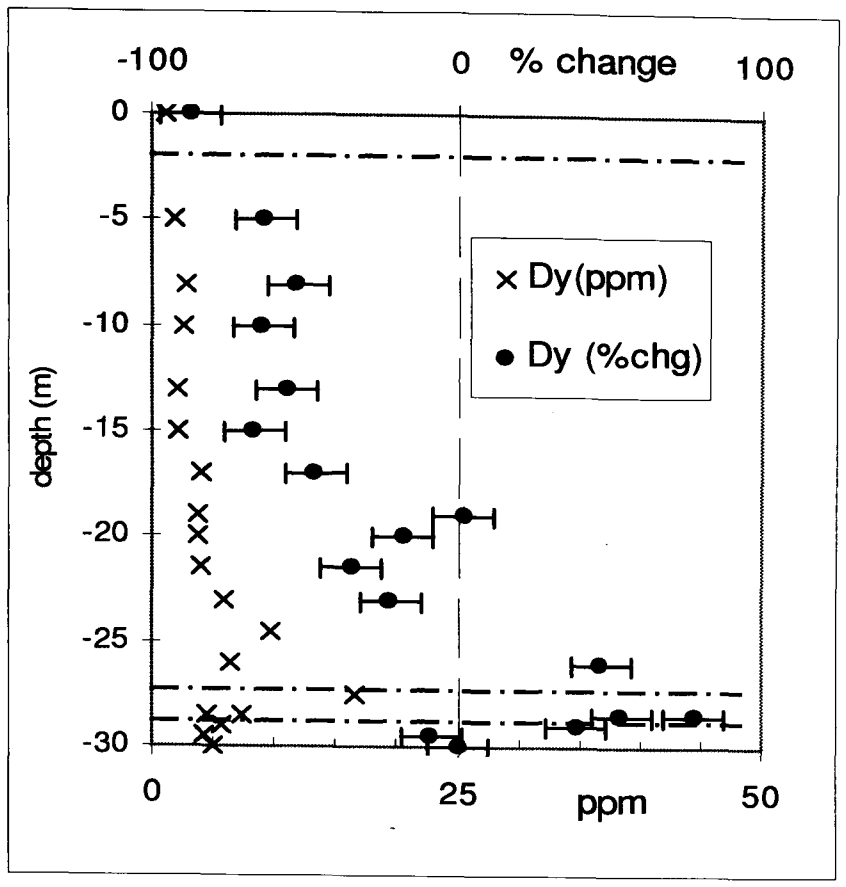

(j)

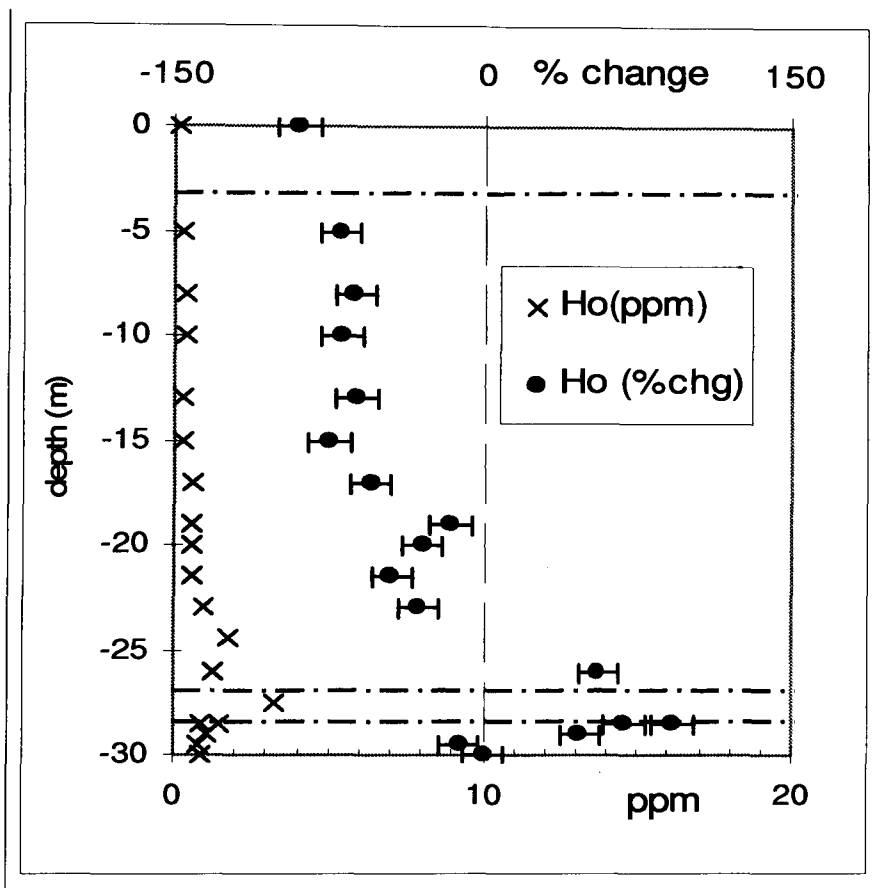

Figure 5.7.Rawang REE percentage change with respect to Zr of the parent rock (sample RA-20 at 30m depth) (**i**): Dy, (**j**): Ho

(k)

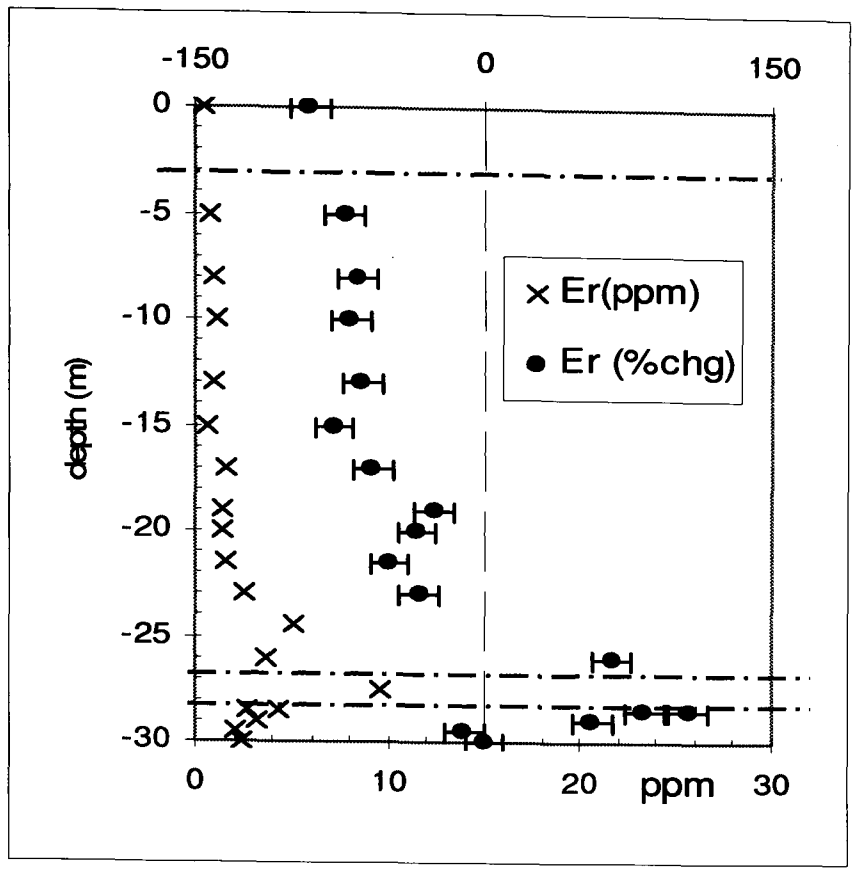

(l)

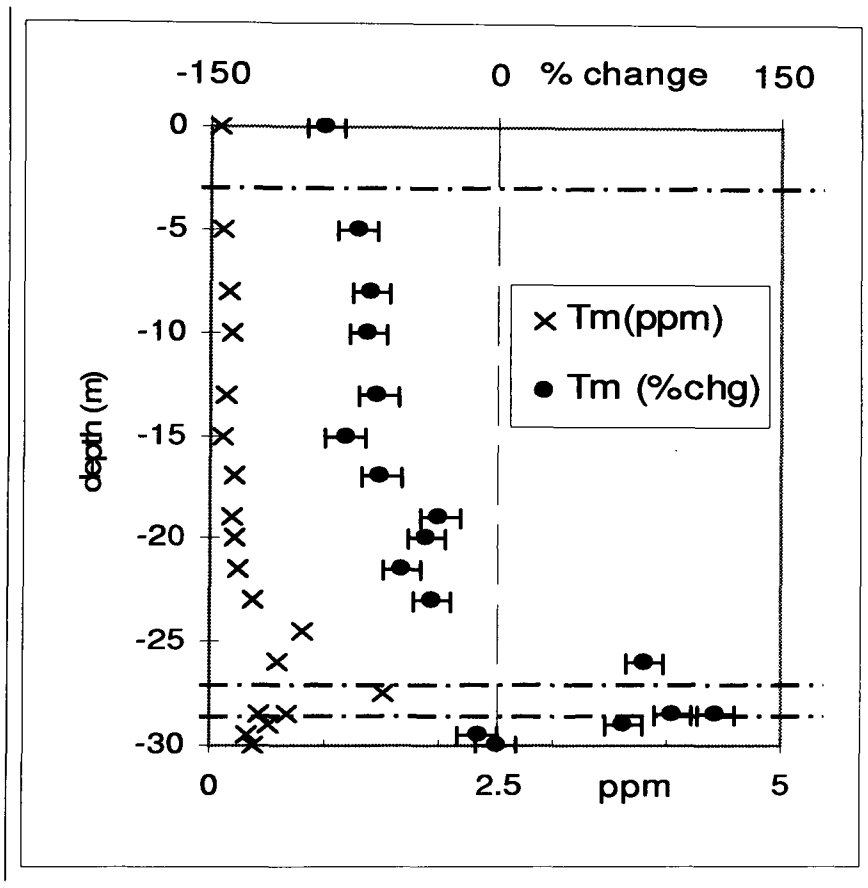

Figure 5.7.Rawang REE percentage change with respect to Zr of the parent rock (sample RA-20 at 30m depth) (**k**): Er, (**l**): Tm

(m)

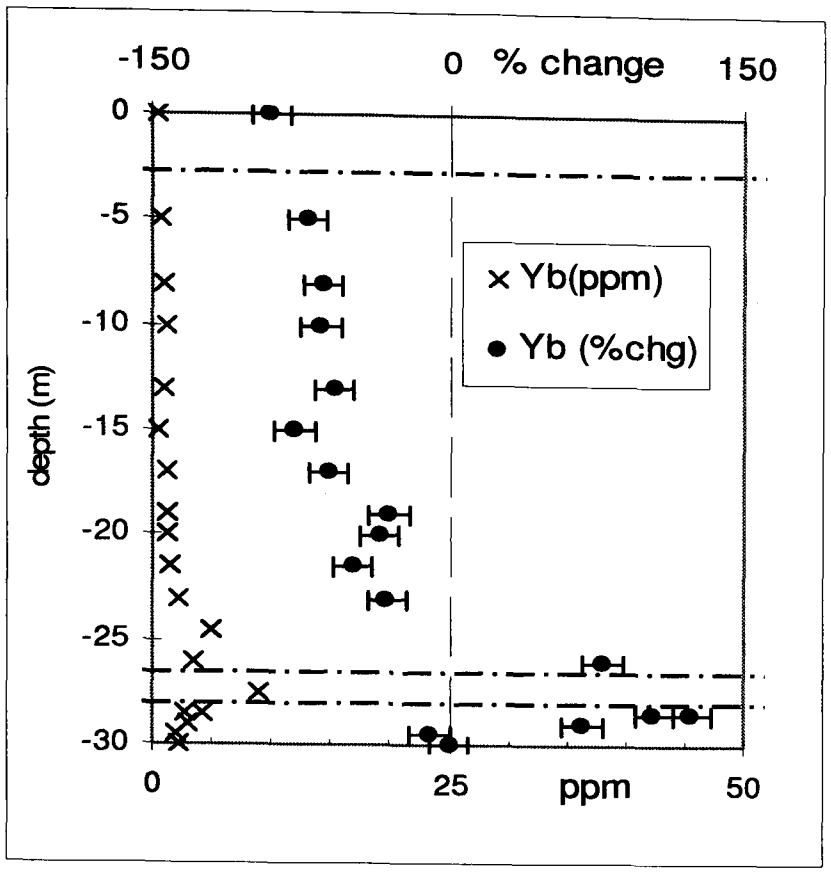

(n)

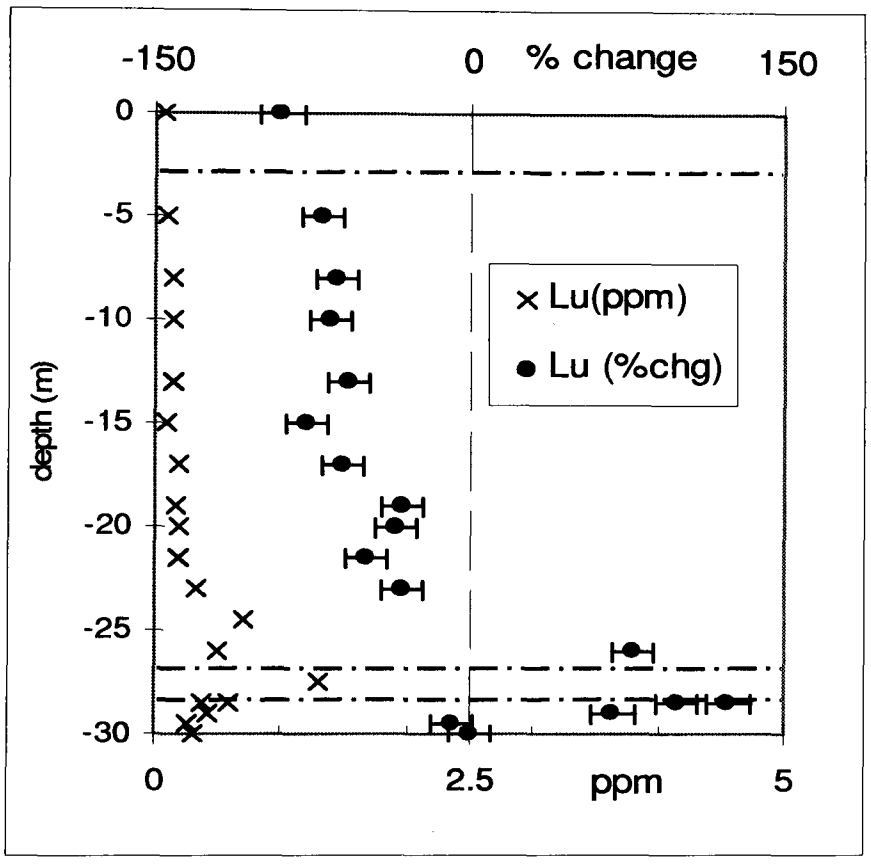

Figure 5.7.Rawang REE percentage change with respect to Zr of the parent rock (sample RA-20 at 30m depth) **(m)**: Yb **(n):** Lu

5.4 Discussion

Mobility of major and trace elements relative to Zr

Mobilities of major elements in the Cheras and Rawang granites are identical (Table 5.3). Both in Cheras and Rawang granites, the mobile elements are SiO_2, Na_2O, K_2O, CaO, P_2O_5, and MgO and the immobile elements Al_2O_3, Fe_2O_3 and TiO_2. The mobility of SiO_2, Na_2O, K_2O and CaO correspond to the dissolution of feldspar in the weathering process which starts in the weathering boundary zone. The immobile Al_2O_3 can be correlated to the formation of clay minerals. Fe_2O_3 accumulates in the upper part of the saprolite and is due to the oxidation of the iron containing minerals. The immobility of TiO_2 is related to the stabilities of the mineral anatase. Mobile trace elements in both Cheras and Rawang granites are Ba, Sr, and Rb (Table 5.9), which are all contained in feldspars. Sr and Rb are retained in K-feldspar until K-feldspar breaks down. The negative percentage change which indicates that Sr and Rb are mobile in the saprolte zone (Figure 5.8). Similarly, Sr is mobile as plagioclase dissolves (Figure 5.9).

Major elements			Trace elements			Rare Earth elements					
element	Cheras granite	Rawang granite	element	Cheras granite	Rawang granite		Cheras granite		Rawang granite		
							Top soil and sap.	Wea. bound	Top soil, upper sap	Lower sap.	Wea. bound
SiO_2	Neg.	Neg.	Ba	Neg.	Neg.	La	Neg.	+ ve	Neg.	+ ve	+ ve
Al_2O_3	+ ve	+ ve	Nb	+ ve	-	Ce	Neg.	+ ve	Neg.	+ ve	+ ve
Fe_2O_5	+ ve	+ ve	Zr	reference element		Pr	Neg.	+ ve	Neg.	+ ve	+ ve
MgO	Neg.	Neg.	Y	-	Neg.	Nd	Neg.	+ ve	Neg.	+ ve	+ ve
CaO	Neg.	Neg.	Sr	Neg.	Neg.	Sm	Neg.	+ ve	Neg.	+ ve	+ ve
Na_2O	Neg.	Neg.	Rb	Neg.	Neg.	Eu	Neg.	Neg.	Neg.	Neg.	+ ve
K_2O	Neg.	Neg.				Gd	Neg.	Neg.	Neg.	Neg.	+ ve
TiO_2	+ ve	+ ve				Tb	Neg.	Neg.	Neg.	Neg.	+ ve
P_2O_5	Neg.	Neg.				Dy	Neg.	Neg.	Neg.	Neg.	+ ve
						Ho	Neg.	Neg.	Neg.	Neg.	+ ve
						Er	Neg.	Neg.	Neg.	Neg.	+ ve
						Tm	Neg.	Neg.	Neg.	Neg.	+ ve
						Yb	Neg.	Neg.	Neg.	Neg.	+ ve
						Lu	Neg.	Neg.	Neg.	Neg.	+ ve

Table 5.3. Summary of the mobility of elements relative to Zr studied. 'neg' refers to negative percentage change (mobile relative to Zr), '+ve': positive percentage change (immobile relative to Zr) and '-': uncertain.

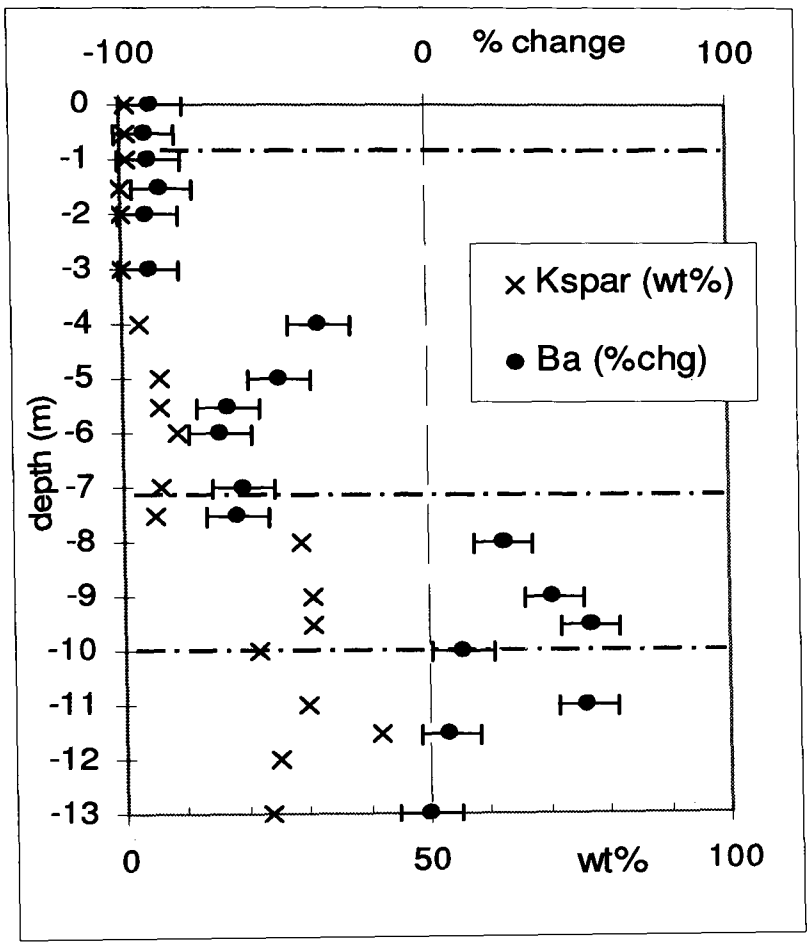

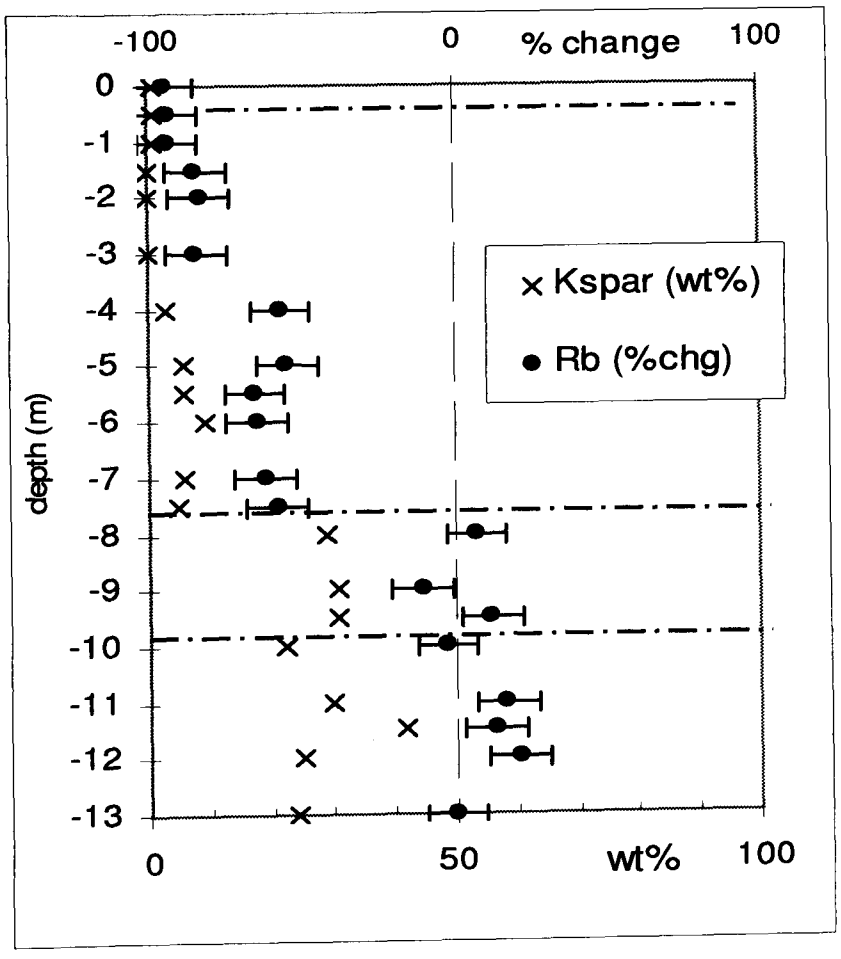

Figure 5.8. The relations between Ba and Rb with K-feldspars.

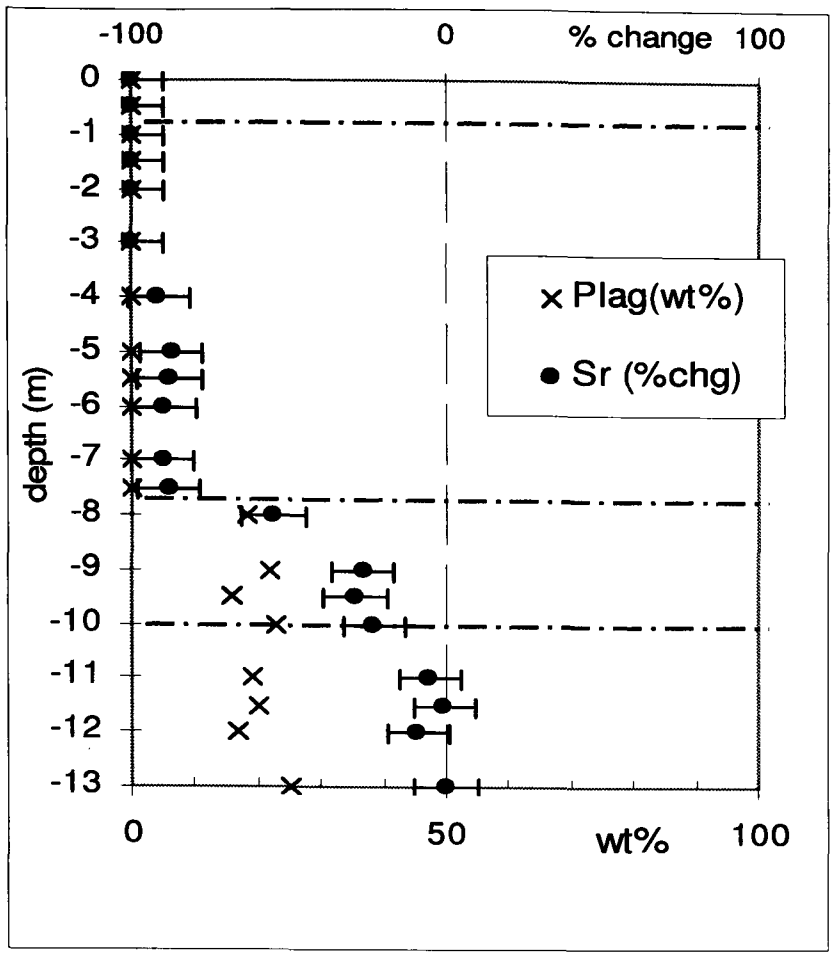

Figure 5.9. The relation between Sr and plagioclase.

Mobility of Rare Earth elements relative to Zr

There are differences in the REE behaviour between Cheras and Rawang. The absolute content of the REE in Cheras declines below the fresh rock level in the upper part of the saprolite layer. As Zr increases upwards behaving as a relative immobile residual element, it is not surprising that the relative concentration of REE in Cheras generally declines with height. There is no obvious systematic change in the weathering zone. There is a possible significant reversal in the depletion trend from 4-6m depth in the LREE. In the Rawang profiles, in all REEs there is a clear rise to above fresh-rock concentration in the REE content at the top of the weathering boundary zone and base of the saprolite before the levels decline with height to below the level on fresh rock, these same trends are enhanced because Zr is roughly constant in the weathering boundary zone before rising slowly thereafter.

The simplest explanation is that the REEs are migrating downwards in some form and accumulating at the base of the saprolite/top of the weathering boundary zone but not being lost to the system as a whole. They are thus mobile relative to

zirconium but not necessarily changing in their relationship at different heights. It is not clear whether this mobility is in the form of insoluble particulates moving physically downwards until arrested at the relatively impermeable granite or as REEs moving in solution before being adsorbed into some stable mineral substrate. It is also not clear why Cheras should differ from Rawang unless the Cheras profile, being shorter and by reference younger has not yet reached equilibrium.

5.5 Conclusion

The relative mobility study of the Cheras and Rawang granites show generally, for both granites, the same elements are mobile and immobile. This is obvious for the major elements. Few trace elements do not show an obvious mobility trend. There are obviously some differences in the REE behaviour between Cheras and Rawang.

6. DISCUSSION

6.1 Introduction

In this section, dissolution of feldspar is discussed by emphasizing its significance to the designing of a cut slope. It begins with the research aim and brief summary of the methodology used to achieve the aim before going into the review of basic slope design calculations. The writer will then relate the parameters used in the basic design calculations to the findings of this study.

6.2 Research aim and methodology to achieve the aim

The main aim of this research is to examine the properties and conditions of feldspars at different weathering depth in the tropical area, Malaysia. The understanding of these properties will give an insight on the weathering mechanism of feldspars in deep profiles.

In this study, two locations were selected. One was in Cheras (referred to as Cheras granite) and the other was in Rawang (referred to as Rawang granite). Cheras granite is a cut slope with a maximum profile thickness of 13m and Rawang granite is 30m, with the top 15m samples representing a cut slope and the lower 15m samples were taken from a borehole. Samples were analysed for their mineralogical content (QXRPD and optical microscopy), major and trace element contents (XRF), REE (ICP-MS) and feldspar grain characteristics (SEM and electron probe). From the QXRPD analyses of the unweathered granites, Cheras granite contains 40 to 67wt% feldspar while Rawang granite contains 48 to 66 wt% (Table 6.1). Majority of the minerals in both granites are quartz and feldspars. Feldspars weather significantly (while quartz is basically not affected by the weathering processes) making the weathering granites is represented by the weathering of feldspars.

Based on the changes in properties like mineralogical content, chemical content and the physical appearance, four zones were demarcated (from the bottom): unweathered granite, weathering boundary, saprolite and the top soil zones.

Next page: **Table 6.1** Summary of the similarities and differences between Cheras and Rawang granites. The term 'Nil' is used when the observation is qualitative (from SEM) and '0' is used for quantitative measurements (from QXRPD analyses).

	Cheras granite	Rawang granite
Top soil zone		
Thickness	0.5m	1m
Feldspar exsolution lamellae	No feldspar grains found	No feldspar grains found
Plagioclase (wt %) (QXRPD)	0	0
K-feldspar (wt %) (QXRPD)	1	0
Kaolinite (wt %) (QXRPD)	26 to 36	23 to 35
Halloysite (SEM)	Nil	Nil
Smectite (SEM)	Nil	Nil
Gibbsite (QXRPD)	6 to 8	4 to 25
Saprolite zone		
Thickness	7m	26.5m
Feldspar exsolution lamellae	no feldspar grains found	No feldspar grains found
Plagioclase (wt %) (QXRPD)	0	0
K-feldspar (wt %) (QXRPD)	1 to 9	0 to 9
Kaolinite (wt %) (QXRPD)	17 to 47	12 to 93
Halloysite (SEM)	present (lower part of saprolite)	present (lower part of saprolite)
Smectite (SEM)	Nil	Nil
Gibbsite (QXRPD)	0 to 22	0 to 40
Weathering boundary zone		
Thickness	2.5m	1.0m
Feldspar exsolution lamellae	albite is still present in lamellae	Albite is completely dissolved
Plagioclase (wt %) (QXRPD)	16 to 23	17 to 25
K-feldspar (wt %) (QXRPD)	22 to 31	27 to 35
Kaolinite (wt %) (QXRPD)	2 to 5	1 to 2
Halloysite (SEM)	present	present
Smectite (SEM)	Nil	present
Gibbsite (QXRPD)	0	0
Unweathered granite zone		
Petrology	S-type (more Al, SiO_2)	I-type (less Al, More CaO)
Feldspar exsolution lamellae	could not be seen because of weathering	
Plagioclase (wt %) (QXRPD)	17 to 25	24 to 28
K-feldspar (wt %) (QXRPD)	23 to 42	24 to 38
Kaolinite (wt %) (QXRPD)	1 to 2	0 to 1
Halloysite (SEM)	Nil	Nil
Smectite (SEM)	Nil	Nil
Gibbsite (QXRPD)	0	0

6.3 Review of basic slope design calculations

The basic principle in designing a stable slope is to obtain a 'Factor of safety', (FS) greater than 1. FS is defined as the ratio of resistive force over driving force (Equation 6.1). When the resistive force is greater, the slope will stay standing but when the driving force is greater, the slope will fall.

FS = (Resistive force/ Driving force) (Equation 6.1)

When taking moment about O, the driving force will be the weight of 'soil' mass per unit length (W), multiply by the horizontal distance, d to the centre O (Figure 6.1). For engineering purposes, the British Standard Institution (2004) define 'soil' as mineral 'material' that results from the 'weathering' of rock and 'material' is defined as substance that can be used to form product(s) for construction works while 'weathering' is change in colour or texture or composition. There are several schemes of soil classification in engineering terms, among them are: based on grain size (British Standard Institution, 1990c, Table 6.2), based on size, visual identification, origin, structure and color (British Standard Institution, 1981), gradation of the grains like well graded or poorly graded, and the laboratory criteria like C_u values (Unified Soil Classification System). 'Soil mass per unit length' means the density of the soil (kNm^{-3}) multiply by the cross-sectional area of the slope (m). The resistive force will be the 'undrained shear strength' (C_u) multiplied by 'length of failure arc' (L_a), the outcome being multiplied by the radius r. (Equation 6.3). The FS will then be given by Equation 6.4. The definition of 'undrained shear strength' will be discussed shortly.

Name	clay	silt	sand	gravel	cobbles	boulders
Grain size (mm)	<0.002	0.002 to 0.06	0.06 to 2	2 to 60	60 to 200	200 to 600

Table 6.2. Soil classification based on the grain size (British Standard Institution, 1990)

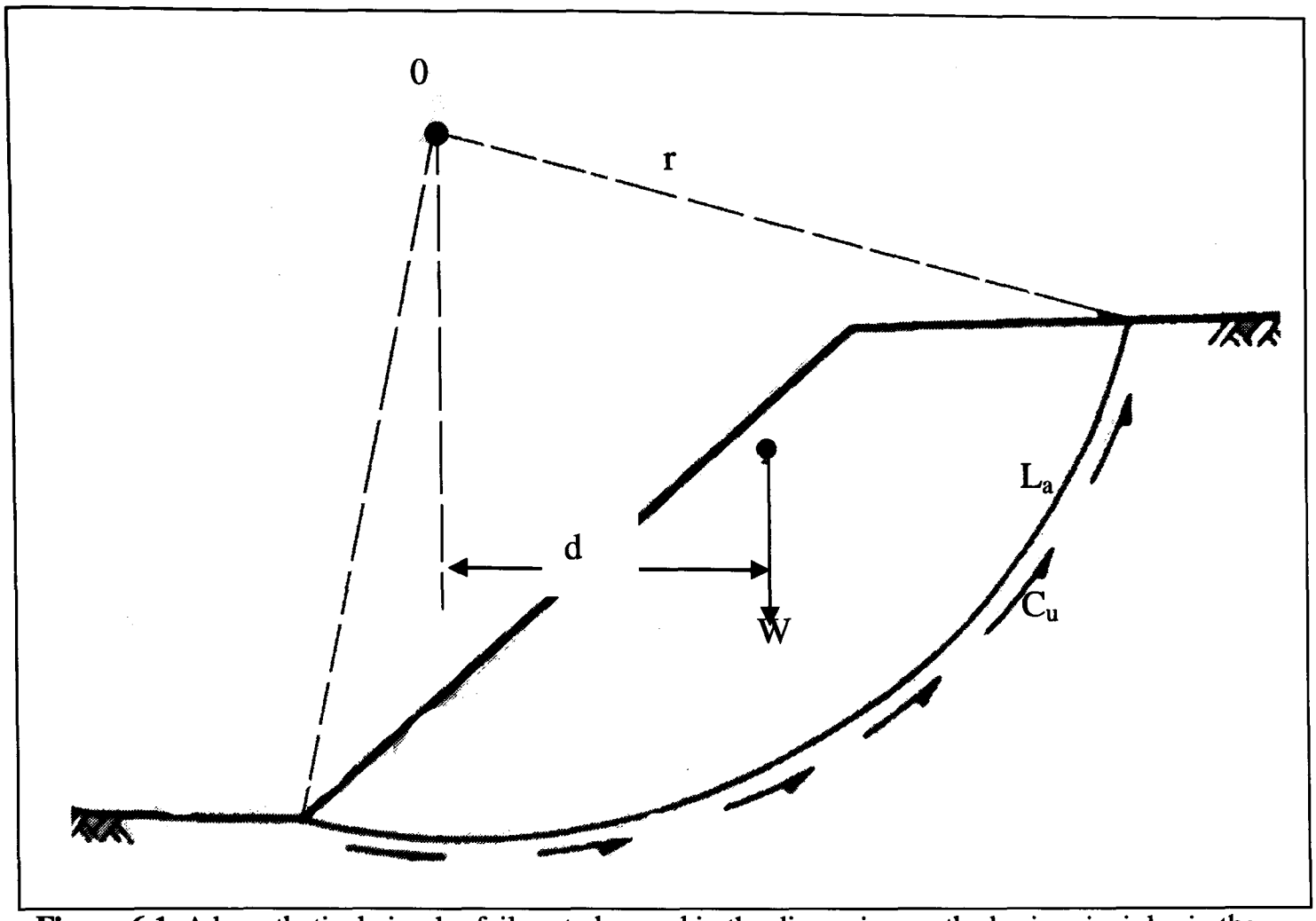

Figure 6.1. A hypothetical circular failure to be used in the discussion on the basic principles in the calculation of slope stability (Craig, 1997).

Driving force = W (kN/m) x d (m) (Equation 6.2)

Resisting force = $\{C_u$ (kN/m2) x L_a(m)$\}$ x r(m) (Equation 6.3)

Factor of safety, FS = $C_u L_a r/Wd$ (Equation 6.4)

A factor of safety, FS less than 1 represents a 'failed' slope or a slope that has already collapsed. FS equals 1 representing a just standing slope i.e. on the verge of failure while FS more than 1 represents a stable slope. As a normal practice in Malaysia, a slope is normally designed to have a FS between 1.3 to 1.5 (depending on factors like annual rainfall, rural or urban areas, for road cuts or housing developments etc.) The larger the factor of safety, the more stable the slope is. When the slope angle is small, the distance, d will increase and therefore FS increase. Other additional measures like retaining walls or soil nailing will increase the resistive force and therefore will also increase the FS. However, the larger the FS, the higher is the cost of making the slope stable. The main objective of the slope designers is to optimize the stability of the slope at a minimum cost.

Now, the writer will focus on the parameters that are related to this study.

Cohesion of soil depends on the 'clayey' property of the soil. The word clayey here means the cohesiveness of the grains. Cohesiveness is related to the grain size: the smaller the grain size, the more cohesive it gets. The atomic structures also influence the cohesiveness of the grains (Craig, 1997). For sand, c equals zero, meaning no cohesion at all. The apparent cohesion is not used in the calculation but, an 'effective cohesion' is. 'Effective stress' (σ') is the 'total stress' (σ) together with 'pore water pressure' (u) where total stress is stress applied onto the soil particles, effective stress is the reactive force acting within the soil particles and the pore water pressure is the force applied by the water in the pores (Equation 6.5, Figure 6.2). Pore water pressure (u) is the 'static water pressure' (u_s) together with the 'excess water pressure' (u_e) (Equation 6.6). Under a 'drained condition' where water flows out of the system, the excess water pressure, u_e equals zero.

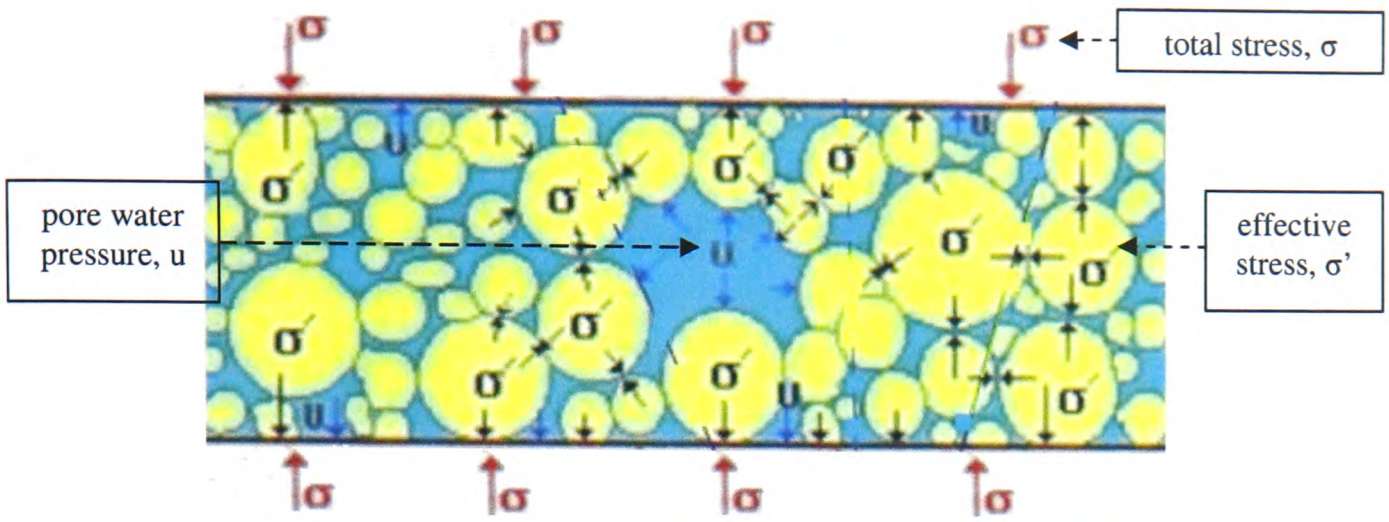

Figure 6.2. 'Soil skeleton diagram' showing the total stress, effective stress and pore water pressure acting on particles

$$\sigma' = \sigma + u \qquad \text{(Equation 6.5)}$$

(effective stress = total stress - pore water pressure)

$$u = u_s + u_e \qquad \text{(Equation 6.6)}$$

(pore water pressure = static water pressure + excess water pressure)

Shear strength of a soil at a point on a particular plane can be expressed as a linear function related to the normal stress (similar to total stress) and when looked at in relation to the pore water pressure, the parameters are in terms of effective stress (Equation 6.7). All these parameters can be obtained from laboratory tests on the samples (British Standard Institution, 1990b). Under an 'undrained condition' (C_u), there is no dissipation of water from the system and therefore this C_u is the effective cohesion, c'.

$$\tau' = c' + \sigma' \tan \varphi' \qquad \text{(Equation 6.7)}$$

where τ' is shear strength

c' is effective cohesion

σ' is shear stress

φ' is angle of shearing resistance

σ' is calculated from the stress applied on sample in the laboratory test while c' and φ' are calculated from the behavior of the sample to the stress applied.

The other parameter of our concern is the length (and shape) of the slope failure (L_a in Equation 6.4). The length and shape will naturally depend on the types of 'material' the failure zone encountered. To consider the different length and shapes of the failure line or surface in the FS calculation (Equation 6.4), methods like (a) dividing the failed mass of soil into small strips (or slices) and doing the calculations on each slice and (b) finite elements where the failed soil mass is assumed to be made up of small elements containing nodes and these nodes are connected to the adjacent nodes. The movement of these nodes is taken into account in the calculation.

The other important parameter for this study is the weight of soil mass per unit length (W), which is soil density multiplied by cross sectional area of the slope. The density depends on soil grain size and is therefore related to the degree of weathering.

The discussion above is assuming the slope has already failed but the objective of the calculations is to study 'slope stability' not 'slope failure'. To solve this problem, different combinations of the possible failure of the slope to be designed are considered and the non of the possible failures should be having a FS of less than that been agreed on (normally, 1.30) and the 'stable' slope chosen to be built should not exceed the agreed FS (normally 1.5). The FS of the 'stable' slopes normally are controlled by the financial constraints.

The summary of the relation between the parameters in the slope design calculations and the mineral grain characters is tabulated in Table 6.3

Parameters in Equation 6.4	Relation to the mineral grains
C_u (undrained shear strength)	• stresses on mineral grains • cohesion of the soil grains • Pore water pressure within the system
L_a (length of failure arc)	• Mineral type • Weathering zones
W (soil mass per unit length)	• Density depends on mineral type

Table 6.3. Summary of the parameters involved in the calculation of the slope FS and their relation to this study.

6.4 Dissolution of feldspars

From this study, it is observed that the feldspars dissolve faster than other minerals. When K-feldspar dissolves, the dissolution of the exsolution lamella will make the K-feldspar grains as a mass with a network of empty holes (Figure 6.3). If the empty spaces are filled with water, the system will be under an 'undrained condition' where excess pore water pressure will not be zero (Equation 6.6). However, if water does not fill the empty spaces due to the water surface tension, the 'pillars' in the K-feldspar will be very fragile and will easily collapse. This 'pore collapse' situation will be discussed in section 6.5.

Next 2 pages: **Figure 6.3** The sequence of dissolution K-feldspar grains. (a) grain (in Cheras) in the lower part of the weathering boundary zone showing the beginning of the dissolution of the exsolution lamellae. (b) Upper part of the weathering boundary zone (in Cheras) showing the disappearance of the albite in the exsolution lamellae (c) Resin casts of etched dislocations network containing tubular formed before exsolution lamellae have been dissolved (Lee, Hodson and Parsons, 1998) (d) collapsed of the 'pillars', shows the breakdown of feldspar grains lamellae (Lee, Hodson and Parsons, 1998). The presence of empty spaces will influence the pore water pressure and fragile character of the 'pillar' will affect the shear strength.

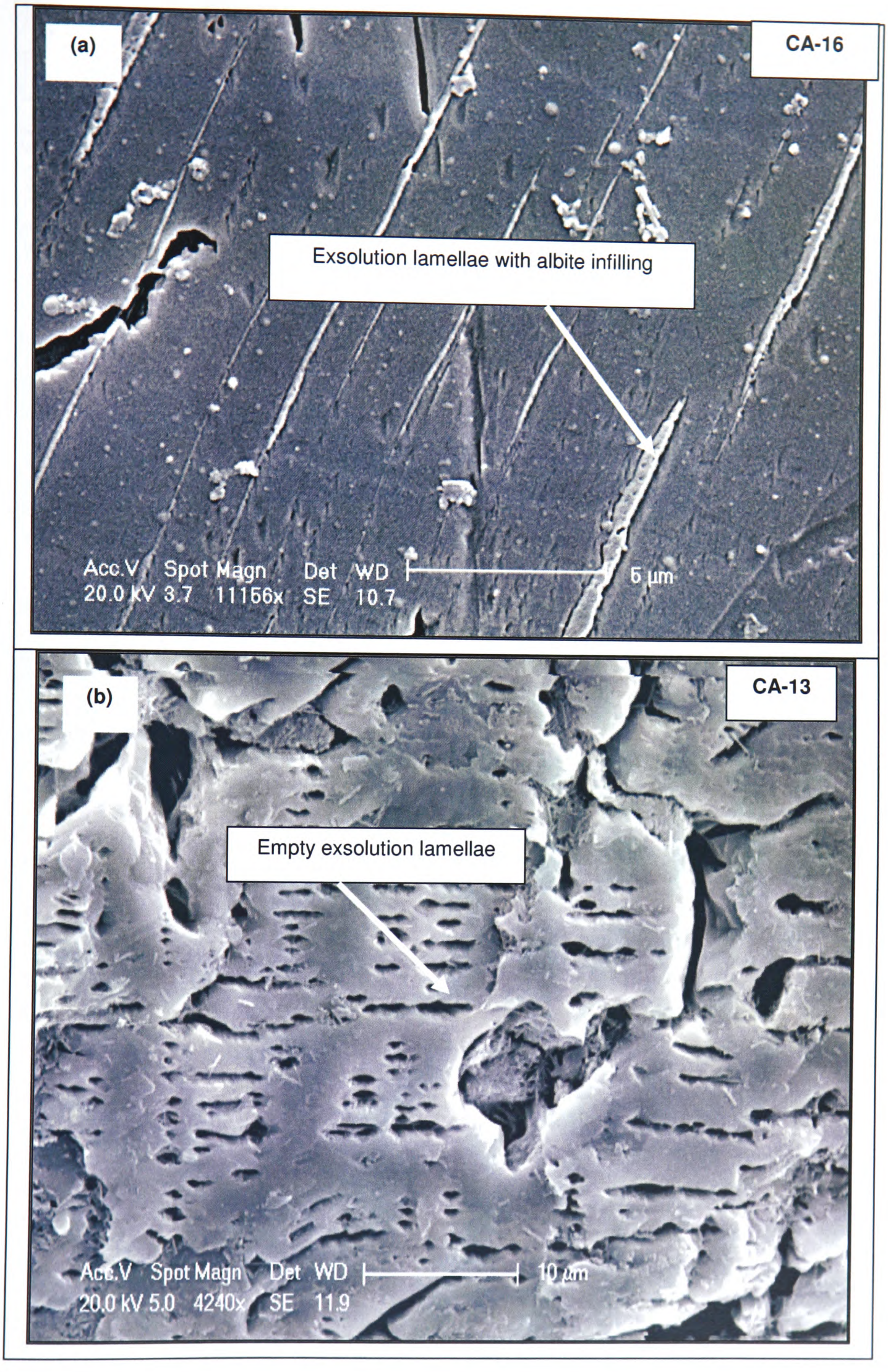
(a)
CA-16
Exsolution lamellae with albite infilling
Acc.V Spot Magn Det WD
20.0 kV 3.7 11156x SE 10.7
5 µm
(b)
CA-13
Empty exsolution lamellae
Acc.V Spot Magn Det WD
20.0 kV 5.0 4240x SE 11.9
10 µm

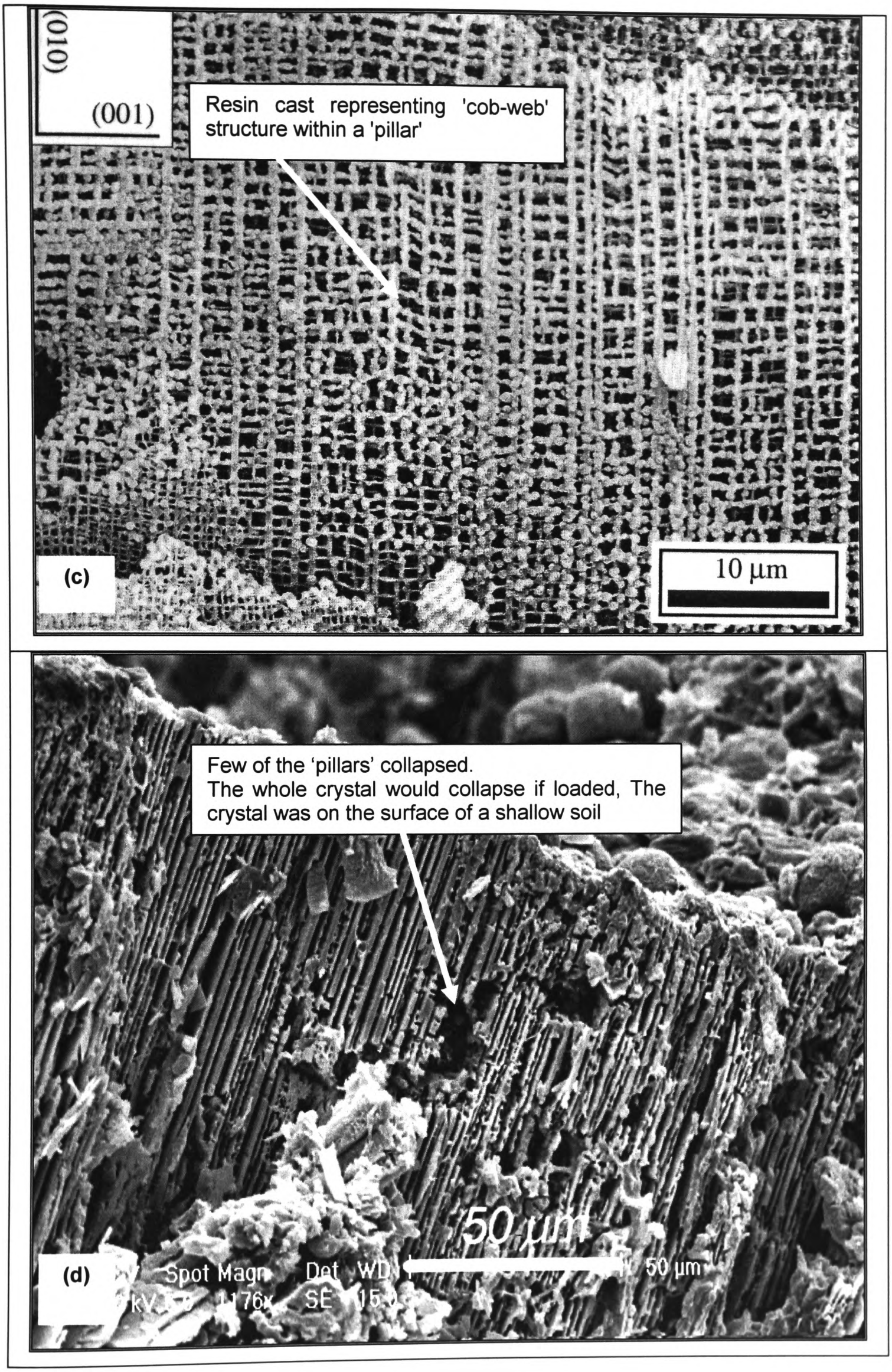
(010)
(001)
Resin cast representing 'cob-web' structure within a 'pillar'
(c)
10 µm
Few of the 'pillars' collapsed.
The whole crystal would collapse if loaded, The crystal was on the surface of a shallow soil
50 µm
(d)
Spot Magn
Det
WD
kV
1176x
SE
50 µm

Below water table soil can be considered as saturated. In coarse-grained soils, water will drain from the pores and air will therefore be present in the soil between the ground surface and the water table (Craig, 1997). In fine grained soils, surface tension effects can cause capillary water to rise above the water table. The writer suspects that the porosity of the zone containing a substantial amount of weathered K-feldspar would increase substantially only when the feldspar grains collapsed (defined as 'pore collapsed' and will be discussed further). The writer believes that the individual 'tubes' will not create any effect to the pore water pressure due to surface tension of water. However, when the grain collapses the missing albite sheets will create substantial voids. This will create a sudden decrease in the total stress (Figure 6.2) and assuming there is no change in pore water pressure (if the tubes are assumed to be empty) there will be sudden decrease in the shear strength (Equation 6.5). This will in turn decrease the value of C_u suddenly and the FS will be reduced (Equation 6.4). Lesser FS means that the chances of the slope will fail increase. This slope failure calculation is referring to a slope within a saprolite zone and only Cheras granite has some K-feldspar grains in the saprolite zone. Unfortunately, the reduction in C_u could not be proven mathematically as the relevant parameters like the undrained shear strength of the Cheras granite saprolite samples could not be obtained due to the sampling methods. Sampling for the strength tests should conform to the standards like those provided by the British Standard Institutions. Sampling of saprolites from the Rawang granites conform to these standards but unfortunately, no feldspar grains were present in the Rawang saprolite (Chapter 4).

At the saprolite-rock interface, other parameters will complicate the mechanics of a slope failure. For example, the formation of the failure arc, L_a. Almost always, the failure will follow a 'sliding surface' as there is a huge difference in density and compressive strength of the two zones. As the arc could not be related to a 'typical circular arc', different methods of calculations will have to be used. The differences in density and compressive strengths will also give rise to two different C_u values and W values. Further studies have to be conducted to look into these issues.

6.5 Pore collapse

Tsai et al (2007) studied a porphyritic andesite powder passing 0.37mm sieve mesh (therefore containing clay size and the smaller silt size grains, Table 6.2) under the action of different H_2SO_4 concentrations (0.1 N–4.0 N) at temperature of 90 °C and dosage of 10 g (andesite)/100 mL (water) for 0.5 h. on a stirrer/hot plate. The samples were then measured for the surface area and volume (Figure 6.4). Tsai et al (2007) concluded that the acid treatment significantly etched into the surface structure in the clay mineral, leaving a porous structure possessing large BET surface areas. The increasing trend in surface areas and volume reached a plateau while the acid concentration was increased from 2.5 N to 3.5 N. Thereafter, the pore properties were observed to decrease gradually at larger H_2SO_4 concentration whereby Tsai et al. inferred that it was due to the collapse or destruction of many pores. In the present study, the writer did not measure the surface area and pore volume of the feldspar grains but the writer would like to highlight the occurrence of 'pore collapse' which caused a sudden decrease in surface area and pore volume. These will in turn influence the value of C_u used in the calculation of FS (Equation 6.4). The writer believes that the 'pore-collapse' situation should be looked into further with a parallel research on the lamella present and the strength parameters.

Next page: **Figure 6.4**. Plots of the BET, external and micropore surface areas of the samples and table of the total pore volume and micropore volume (assessed by converting the amount of nitrogen gas adsorbed to the volume (cm3/g at STP) of liquid adsorbate using the single point adsorption and t-plot methods, respectively. (Tsai et al. 2007)

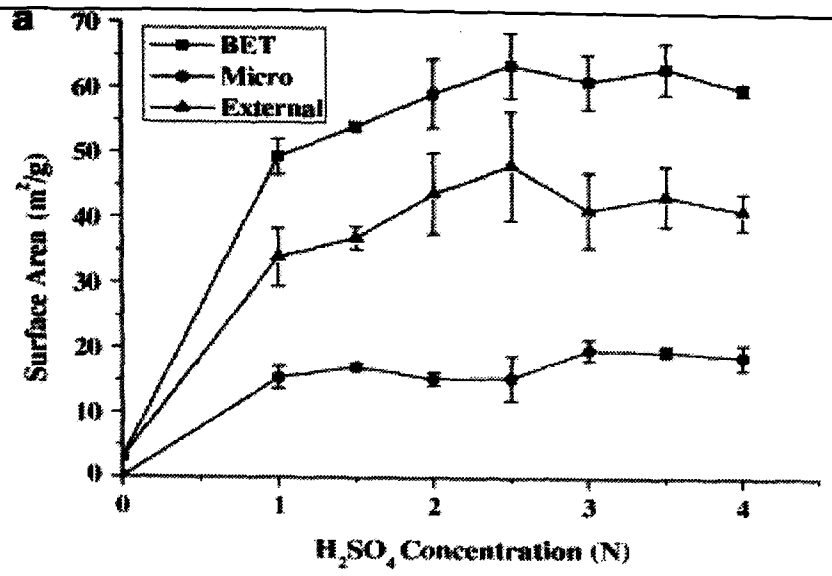

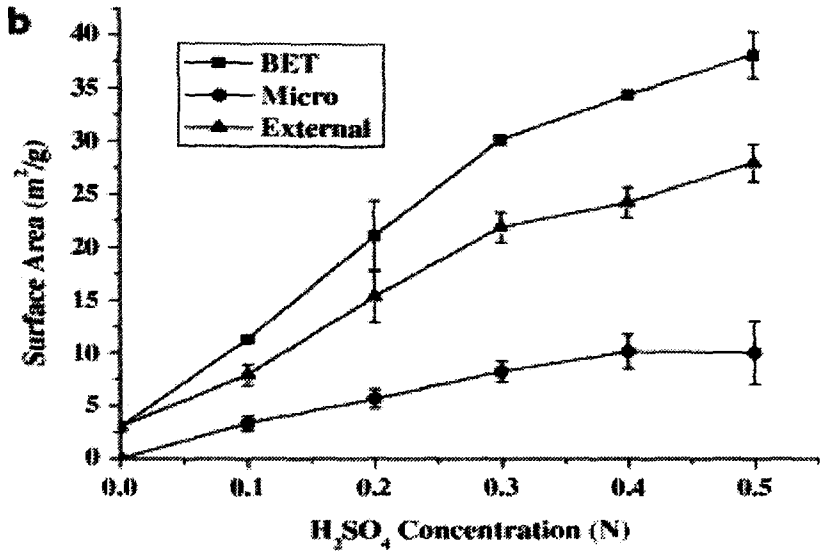

Acid Conc. N	Total pore volume (cm^3/g)	micropore volume (cm^3/g) Calculated from plot
Untreated	0.0107 ± 0.0004	0.0018 ± 0.0004
0.1	0.0173 ± 0.0005	0.0030 ± 0.0005
0.2	0.0228 ± 0.0030	0.0044 ± 0.0005
0.3	0.0269 ± 0.0007	0.0055 ± 0.0009
0.4	0.0312 ± 0.0034	0.0055 ± 0.0009
0.5	0.0352 ± 0.0025	0.0055 ± 0.0017
1.0	0.0413 ± 0.0002	0.0083 ± 0.0010
1.5	0.0453 ± 0.0024	0.0092 ± 0.0007
2.0	0.0479 ± 0.0033	0.0082 ± 0.0006
2.5	0.0537 ± 0.0034	0.0082 ± 0.0018
3.0	0.0476 ± 0.0054	0.0106 ± 0.0009
3.5	0.0490 ± 0.0047	0.0105 ± 0.0005
4.0	82 0.0462 ± 0.0017	0.0100 ± 0.0011

6.6 Formation of kaolinite

The dissolution of feldspar is related to the formation of kaolinite (Chapter 4). Instead of directly relating the engineering properties to the dissolution of feldspar, the writer intends to use an indirect approach. The writer will compare these engineering properties with the kaolinite content in the Rawang drill hole samples.

The drill hole samples from 15m depth (Figure 4.31) were sent to a commercial laboratory in Malaysia to conduct the index property, particle size distribution and strength tests (Table 6.4 and 6.5). These dataset are plotted in Figure 6.5.

		Index properties				[5]Particle size distribution test			
Depth (m)	Sample name	[1]MC (%)	[2]BD (mg/m^3)	[3]PD (mg/m^3)	[4]Porosity (%)	Gravel (wt %)	Sand (wt %)	Silt (wt %)	Clay (wt %)
15.0	RA-6	16	1.82	2.57	29	5	46	31	18
17.0	RA-7	14	1.47	2.62	44	16	49	26	9
19.0	RA-8	27	1.60	2.55	37	4	46	36	14
20.0	RA-9	31	1.79	2.54	30	3	35	51	11
21.5	RA-10	31	1.70	2.52	33	2	48	42	8
23.0	RA-11	29	1.74	2.56	32	3	38	51	8
24.5	RA-12	29	1.75	2.55	31	4	48	42	6
26.0	RA-13	34	1.69	2.58	34	5	42	47	6
27.5	RA-14	31	1.76	2.61	33	7	46	43	4
28.5	RA-15	Insufficient sample							

Table 6.4. Results of classification tests on samples from drill hole DH-5. The tests were conducted by a commercial laboratory in Malaysia as per standards stated below:

[1]MC (%), moisture content: amount of water expressed as a proportion by mass of the dry solid particles, (BS 1377:2, 1990)

[2]BD(mg/m^3), bulk density: mass per unit volume of the soil including any water it contains, BS 1377:2 (1990)

[3]PD, particle density= (mass of solid)/(volume of solid) (BS 1377:2, 1990)

[4]Porosity (%) = [1-(bulk density)/(particle density)]100 (BS 1377:2, 1990)

[5]Particle size distribution test: based on the grain size in Table 6.2. (BS 1377:2, 1990)

depth (m)	sample name	[1]UCS (N/mm2)	[2]Effective stress C' (kPa)	Phi' (0°)
17.0	RA-7	-	1	30
19.0	RA-8	-	12	32
28.5	RA-15	93.72		
29.5	RA-19	138.24		
30.0	RA-20	155.04		

Table 6.5. Results of strength tests done on samples taken from drill hole DH-5. The tests were conducted by a commercial laboratory in Malaysia as per standards stated below:

[1]UCS (Unconfined compressive strength): rock (of defined geometry) subjected to a compressive force until failure. UCS = Maximum force / Original cross-sectional area (mm2) (BS 7861:1, 2007)

[2]Effective stress: obtained by calculating the stress parameters from triaxial compression tests (BS 1377:8, 1990). C is the cohesion and Phi is the angle of shearing resistance of the soil.

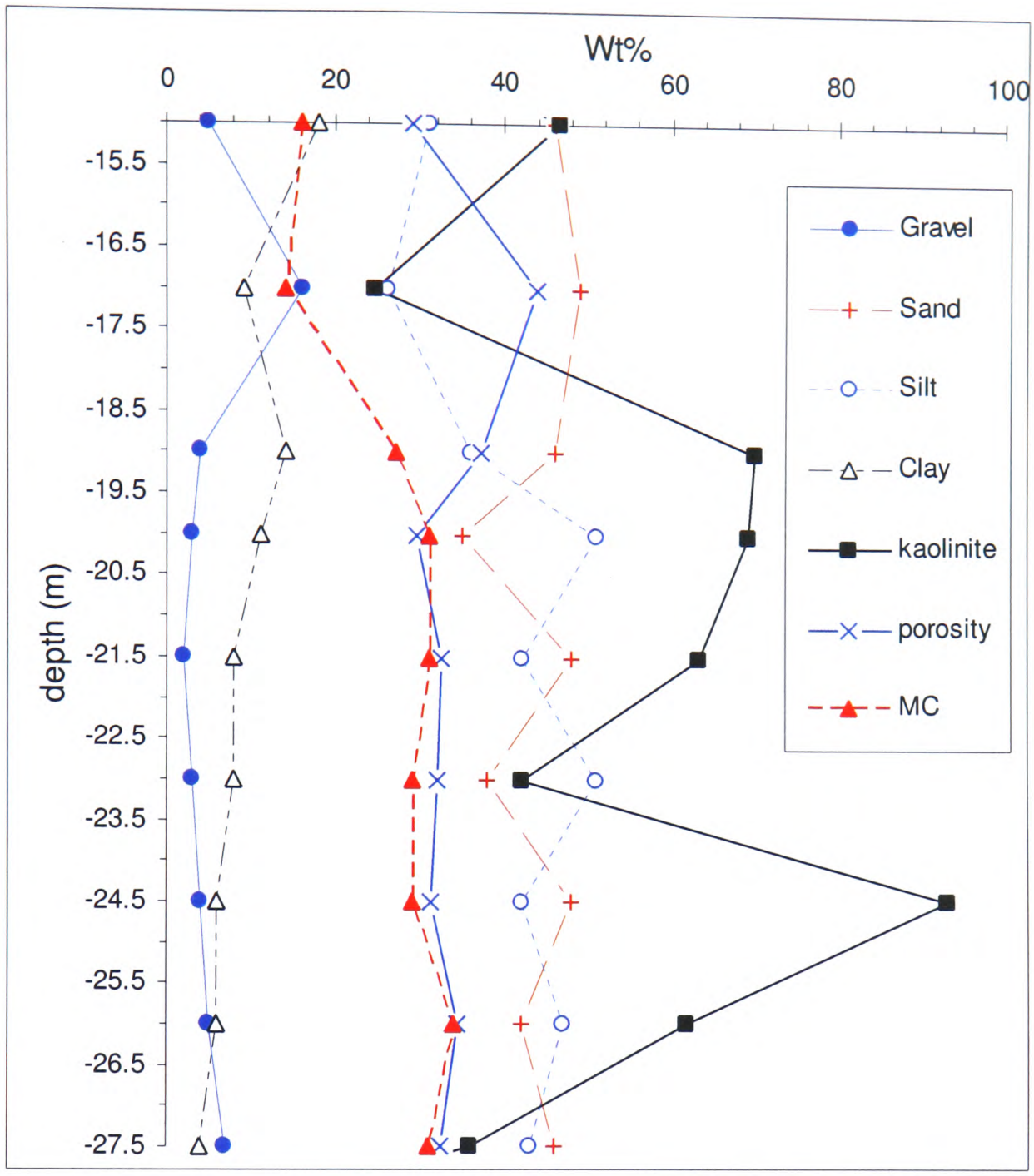

Figure 6.5. The plots of the classification tests conducted on the saprolite samples in Rawang granite as tabulated in Table 6.4. The kaolinite content is obtained from the QXRPD analysis as discussed in Chapter 4.

The kaolinite content (from QXRPD) conforms to the clay content obtained from the particle size distribution test (the solid black square for XQRPD clay and blue hollow triangle for grain size clay in Figure 6.5). The porosity conforms closely with the gravel and sand content (red 'x' for porosity, blue 'x' for gravel and blue '+' for sand in Figure 6.5). However, silt does not closely follow the trend showed by any of the other parameters (silt is represented by hollow blue rhombus in Figure 6.5). The sample at 17m depth shows a very low kaolinite content and this corresponds to a low clay and silt content and high sand and gravel content. The kaolinite could

probably be easily leached away as the high sand and gravel content creates a very high porosity layer (44% porosity, Table 6.4). The moisture content further supports this argument as less moisture is retained in highly porous materials.

In the slope FS calculations (Equation 6.4), the undrained shear strength, C_u can be related to the clay content by equation 6.8 (Craig 1997).

$$C_u/\sigma'_v = 0.11 + 0.00371\ I_p \qquad \text{(Equation 6.8)}$$

Where:

σ'_v is the effective vertical stress (from shear strength tests, British Standard Institution, 1990b)

I_p is the plasticity index (Table 6.6)

Depth (m)	Sample name	[1]Atterberg limit		
		[2]LL (%)	[3]PL (%)	[4]PI (%)
15.0	RA-6	40	29	11
17.0	RA-7	[5]Not applicable		
19.0	RA-8	47	37	10
20.0	RA-9	42	31	11
21.5	RA-10	Not applicable		
23.0	RA-11	Not applicable		
24.5	RA-12	Not applicable		
26.0	RA-13	Not applicable		
27.5	RA-14	Not applicable		

Table 6.6. . Results of index tests on samples from drill hole DH-5. The tests were conducted by a commercial laboratory in Malaysia as per standards stated below:

[1]Atterberg limit: originally created by Atterberg to distinguish (numerically) between silt and clay. Comprise of LL and PL.

[2]LL (%): Liquid limit is the water content where a soil changes from liquid to plastic behavior. Soil (of specified amount and moisture content) is placed into a metal cup (Casagrande apparatus) and a groove is made down its center with a standardized tool. The cup is repeatedly dropped 10mm onto a hard rubber base until the groove is closed. The moisture content at which it takes 25 drops of the cup to cause the groove to close is defined as the liquid limit (BS 1997:2, 2007)

[3]PL (%): Plastic limit is the water content where soil starts to exhibit plastic behavior. A thread of soil is at its plastic limit when it is rolled to a diameter of 3 mm and crumbles (BS 1997:2, 2007)

[4]PI (%): Plasticity index is the size of the range of water contents where the soil exhibits plastic properties and is given by: (PI = LL-PL).

[5] Not applicable: when a thread of soil could not be rolled to a diameter of 3 mm without crumbling (refer to [3]PL) PL values could not be taken. It shows that the soil is 'clayey' (BS 1997:2, 2007)

The plasticity index (PI) could be measured only in samples at 15, 19 and 20m depths. This shows that even when a high wt% of kaolinite is present (as in samples at 21.5m, 24.4m and 26m depths, Figure 6.5), the PI is controlled by the sand and gravel content. The presence of kaolinite is not directly considered in the calculation of slopes.

In Chapter 4, the clay minerals halloysite and smectite were quantitatively detected (SEM study) from the weathering boundary zone to the lower part of the saprolite

zones (Figures 4.30 and 4.31) and were observed to be flattened under scanning electron microscope (for examples, Figures 4.22 and 4.23). Their occurrences are believed to be in between fracture surfaces of minerals (observed were on feldspar fracture surfaces). It has also been discussed that these clay minerals have layered atomic structures (example, Figure 4.29). These can induce sliding and dictate the type of sliding zone of a failed slope. In the brief review of slope design calculations, a circular failure was considered. Soil slope failures might occur as near circular, wedge and any other combinations of sliding zone. This is reflected in the 'length of failure arc', L_a (Figure 6.1). Normally, an engineer would consider all sorts of possible sliding surface and calculate the FS. The minimum FS would be the worst case and necessary precautions (like increase in the resisting force by constructing retaining walls and placing soil nails) to increase the FS of a certain slope could be constructed for particular soil types. It would be very helpful to know the distribution of the clay minerals in saprolites from various localities particularly where slope failures actually occurred, which is one of the factors that influence the 'length of failure arc', L_a.

6.7 Minerals and slope stability

In this section, the writer will show a probable relation between the slope stability and the mineral content, especially K-feldspar and kaolinite. However, only the slopes in Cheras will be discussed. The main reason is that in Cheras, the slopes were designed by geotechnical engineers to be stable based on the geotechnical engineering parameters (in equation 6.4) as it is adjacent to a housing development area (Figure 6.6a) while in Rawang, the cut slopes were built haphazardly.

As mentioned in section 6.3, a slope is stable when the driving force is small (Equation 6.2). The cheapest way to achieve this is to reduce the slope angle, which will reduce the value of d (equation 6.2) and will therefore increase the FS (Equation 6.4). However, a slope designer will try to make as steep a slope as possible because of financial constraints. A steeper slope will have lesser

'overburden' or materials above the slope, to be removed. Too gentle slope will also create other problems such as encroaching into other people's land.

The slopes angles were measured and plotted against the mineral content along the 4 zones in Cheras (Figure 6.6b). It is found that a 70 to 80° cut slope is made on the unweathered granite zone, 60° on the weathering boundary zone, 45° on the lower part of the saprolite zone, and 30° on the upper part of the saprolite zone and the 0.5m thick top soil zone. It is interesting to note that there are two slope angles in the saprolite zones. The 45° slope in the lower part of the saprolite corresponds to the presence of K-feldspar grains (in minor amount) and a substantial amount of kaolinite. This shows that the presence of these minerals, to some extent, contribute to the strength of the saprolite. However, the writer thinks that more studies should be conducted to confirm this relationship.

(a)

(b)

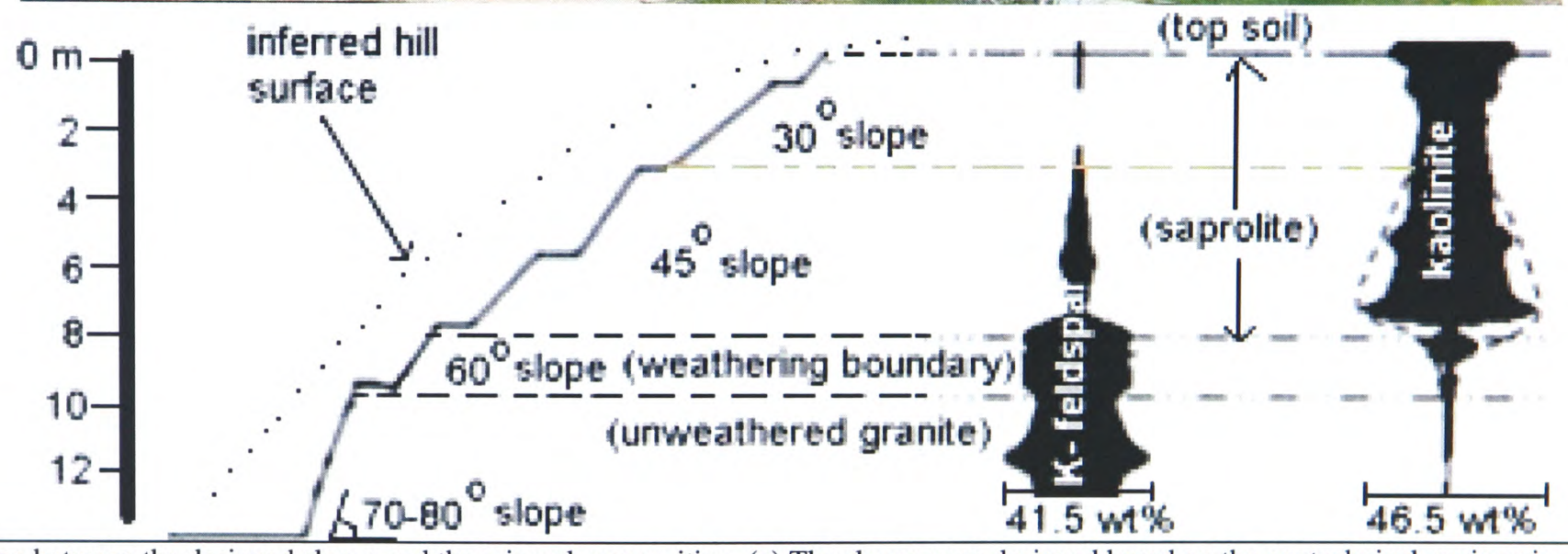

Figure 6.6. Relation between the designed slopes and the mineral composition. (a) The slopes were designed based on the geotechnical engineering strength properties by the engineers appointed by the housing developers adjacent to the hill. However, the writer could not have an access to the data used. (b) The slopes angles were measured and compared to the K-feldspar and kaolinite content.

7. CONCLUSION

The conclusions of this study can be split into three broad themes, those relating to the feldspar mineral dissolution, the element mobility and their significance to the design of cut slopes. To understand the properties of the mineral grains, especially feldspars, the profiles studied were subdivided into four different zones based on the characteristic of the minerals: unweathered granite, weathering boundary, saprolite and top soil.

Feldspar minerals in the unweathered granite zones 'feed' the solution medium with reactants for the chemical reactions to occur. The reactions occur in the weathering boundary zone, of variable thickness but nevertheless rather thin. The weathered granite will then form the saprolite zone where chemical reactions are at the minimal stage. Subsequently, the layer of top soil will develop with the presence of organic materials. First, plagioclase dissolves and during the dissolution of K feldspar, the chemical reactions also dissolved the albite exsolution lamella first and then mechanical weathering occurs within the mineral grains. Clay minerals are formed as feldspar dissolves.

In terms of major element mobility, K_2O, Na_2O and CaO which are basically K-feldspar and Na- and Ca- feldspar (plagioclase) are mobile, corresponding to the weathering of the feldspar minerals. The REE mobility relative to Zr shows some obvious differences between Cheras and Rawang.

The feldspar dissolution does impose a direct influence on the stability of slopes in the weathering boundary and saprolite zones. The occurance of 'pore collapse' due to the dissolution of the exsolution lamella has a direct relation to the pore water pressure, porosity of the 'soil', cohesiveness and effective stress on the mineral grains. The development of clay minerals relates directly to the slip zone with the layering characteristics of the clay atomic structures.

The slope angle slopes made in the Cheras saprolites ranges from 45° to 30° to avoid failure at the minimum cost. The different angles were based on the geotechnical strength the particular slope. From this study, it was found that the feldspar content in Rawang is absent right after the weathering boundary. However, the kaolinite content is very high in the saprolite in the drill-hole samples compared to the cut slope samples. We also know that the Rawang granite is more weathered compared to the Cheras granite. The writer believes that if we were to compare based only on these parameters (mineral content and degree of weathering), a stable Rawang slope could only be build with a slope angle a lot less than 30°.

References

Ahmad, A.R., Yusoff,I., and Ghani, A.A. (2002) Geochemical characteristics of granitic rocks from Boundary Range batholith, Peninsular Malaysia. *Geological Society of Malaysia Annual Conference*. Geological Society of Malaysia, Kelantan, Malaysia.

Asano, Y., Ohte, N., and Uchida, T. (2004) Sources of weathering-derived solutes in two granitic catchments with contrasting forest growth. *Hydrological Processes*, **18**, 651-66.

Berner, R.A. (1978) Rate control of Mineral Dissolution under earth Surface Conditions. *American Journal of Science*, **278**, 1235-52.

Berner, R.A., and Holdren, G.R. (1979) Mechanism of feldspar weathering - ll. Observationsof feldspars from soils. *Geochimica et Cosmochimica Acta*, **43**, 1173-86.

Berner, R.A., and Holdren, G.R. (1977) Mechanism of feldspar weathering: Some observational evidence. *Geology*, **5**, 369-72.

Best, M.G. (2003) Igneous and metamorphic petrology. Blackwell Science Ltd.

Blum, A.E. (1994) Feldspars in weathering. In Feldspars and their reactions. In I. Parsons, Ed. *Feldspars and their reactions. NATO ASI Ser. C421*, p. 595-630. Kluwer Academic Publ.

Bluth, G.J.S., and Kump, L.R. (1994) Lithologic and climatologic controls of river chemistry. *Geochimica et Cosmochimic Acta*, **58**, 2341-59.

Boulet, R., Lucas Y., Fritsch E., and Paquet H. (1997) Geochemical Processes in Tropical Landscapes: Role of the Soil Covers. In Paquet, H. and Clauer, H. (eds) Soils and Sediments, Mineralogy and Chemistry. In H.a.C. Paquet, H., Ed. *Soils and Sediments, Mineralogy and Chemistry.*, p. 67-96. Springer-Verlag Berlin Heidelberg.

Bowen, N.L., and Tuttle, O.F. (1950) The system $NaAlSi_3O_8$-$KalSi_3O_8$-H_2O. *The Journal of Geology*, **58**, 489-511.

Brady, P.V., and Walther,J.V. (1989) Controls on silicate dissolution rates in neutral and basic pH solutions at 25°C. *Geochimica et Cosmochimica Acta*, **53**, 2823-30.

British Standard Institution. (1981) Code of practice for site investigations, BS 5930. BSI London.

-. **(1990a)** Methods of test for soil for civil engineering purposes, BS 1377:1, General requirements and sample preparations. BSI London.

-. **(1990b)** Methods of test for soils for civil engineering purposes, BS 1377:8, shear strength tests (effective stress). BSI London.

-. **(1990c)** Methods of tests for civil engineering purposes. BS 1377:2, Classification Tests. BSI, London.

-. **(1990d)** Methods of tests for civil engineering purposes. BS 1377:6, In-situ tests. BSI, London.

-. **(2004)** Building and civil engineering-Vocabulary, BS 6100:1. BSI London.

Brown, W.L., and Parsons, I. (1989) Alkali feldspars: Ordering rates, phase transformations and behaviour diagrams for igneous rocks. *Mineralogical Magazine*, **53**, 25-42.

-. **(1994)** Feldspars in igneous rocks. In I. Parsons, Ed. *Feldspars and their reactions*, p. 449-99. Kluwer Academic Publ.

Carpenter, M.A. (1994) Subsolidus phase relations of the plagioclase feldspar solid solution. In I. Parsons, Ed. *Feldspars and their reactions (NATO ASI Series C 421)*, p. 221-69. Kluwer Academic Publishers, Dordrecht.

Cerny, P., Chapman, R., Ferreira, K., and Smeds, S.-A. (2004) Geochemistry of oxide minerals of Nb, Ta, Sn, and Sb in the Varutrask granitic pegmatite, Sweden: The case of an "anomalous" columbite-tantalite trend. *American Mineralogist*, **89**, 505-18.

Chappell, B.E., and White, A.J.R. (2001) Two contrasting granite types: 25 years later. *Australian Journal of Earth Sciences*, **48**, 489-99.

Chappell, B.W., and White, A.J.R. (1974) Two contrasting granite types. *Pacific Geology*, **8**, 173-4.

Compton, J.S., White,R.A.,and Smith,M. (2003) Rare earth element behavior in soils and salt pan sediments of a semi-arid granitic terrain in the Western Cape, South Africa. *Chemical Geology*, **201**, 239-55.

Craig, R.F. (1997) Soil mechanics. 485 p. E & FN Spon, London.

Deer, W.A., Howie, R.A., and Zussman, J. (1992) An introduction to the rock forming minerals. 696 p. Longman Scientific & Technical.

Dixon, J.B. (1989). Kaolin and Serpentine Group Minerals. In: *Minerals in Soil Environments* (Ed J.B. Dixon, and Weed,S.B.), SSSA Book Series No. 1, pp. 467-519. Soil Science Society of America.

Drever, J.I. (1994) The effect of land plants on weathering rates of silicate minerals. *Geochimica et Cosmochimic Acta*, **54**, 2325-32.

-. (1997) The geochemistry of natural waters: surface and groundwater environments. Prentice-Hall International Limited, NJ.

Elkins, L.T., and Grove, T.L. (1990) Ternary feldspar experiments and thermodynamic models. *American Mineralogist*, **75**, 544-59.

Fitton, J.G., and Godard,M. (2004) Origin and evolution of magmas on the Ontong Java Plateau. In J.G. Fitton, Mahoney, J.J., Wallace, P.J., and Saunders, A.D., Ed. *Origin and Evolution of the Ontong Java Plateau*, **229**, p. 151-78. Geological Society Special Publications.

Fitton, J.G., Saunders, A.D. Larsen, L.M., Hardarson, B.S., and Norry, M.J. (1998) Volcanic rocks from the southeast Greenland margin at 63°N: composition, petrogenesis and mantle sources. *Proceedings of the Ocean Drilling Program, Scientific Results*, **152**, 331-50.

Fitz Gerald, J., Parsons, I., and Cayzer, N. (2006) Nanotunnels and pull-aparts: Defects of exsolution lamellae in alkali feldspars. *American Mineralogist*, **91**, 772-83.

Fookes, P.G. (1997) Tropical residual soils, Geological Society Professional Handbooks. 1-184 p. The Geological Society, London.

Geological Survey of Malaysia. (1985) Geological Map of Peninsula Malaysia, scale: 1:750,000. Director of Geological Survey of Malaysia.

Ghani, A.A. (2000) The Western Belt granite of Peninsular Malaysia: some emergent problems on granite classification and its implication. *Geosciences Journal*, **4**, 283-93.

-. (2002) Geochemistry of biotite from Kuala Lumpur granite. *Malaysian Journal of Science*, **21**, 159-64.

Gobbett, D.J., and Hutchison, C.S. (1972) Geology of the Malay Peninsula. 215-30 p. Wiley-Interscience, London.

Goldsmith, J.R., and Newton, R.C. (1974) An experimental determination of the alkali feldspar solvus. In W.S. MacKenzie, and Zussman, J., Ed. *The feldspar*. Manchester University Press, New York.

Govindaraju, K. (1994) Compilation of working values and sample description for 383 geostandards. *Geostandards Newsletter*, **18**, 1-158.

Harnois, L. (1988) The 'CIW' index: A new chemical index of weathering. *Sedimentary Geology*, **55**, 319-22.

Helgeson, H.C., Murphy,W.M., and Aagard,P. (1984) Thermodynamic and kinetic constraints on reaction rates among minerals and aqueous solutions. II. Rate constants, effective surface area, and the hydrolysis of feldspar. *Geochimica et Cosmochimica Acta*, **48**, 2405-32.

Hellmann, R., Eggleston C.M., Hochella M.F., and Crerar D.A. (1990) The formation of leached layers on albite surfaces during dissolution under hydrothermal conditions. *Geochimica et Cosmochimica Acta*, **54**, 1267-81.

Hellmann, R., Penisson J.M., Hervig R.L., Thomassin J.H. and Abrioux M.F. (2003) An EFTEM/HRTEM high resolution study of the near surface of labradorite feldspar altered at acid pH: evidence for interfacial dissolution-reprecitation. *Phys Chem Minerals.*, **30**, 192-7.

Hillier, S. (1999) Use of an air brush to spray dry samples for X-ray powder diffraction. *Clay Minerals*, **34**, 127-35.

-. (2003) Quantitative analysis of clay and other minerals in sandstone by x-ray powder diffraction (XRPD). *Inst. Assoc. Sedimentol. Spec. Publ.*, **34**, 213-51.

Hodson, M.E., Lee, M.R, and Parsons, I. (1997) Origins of the surface roughness of unweathered alkali feldspar grains. *Geochimica et Cosmochimica Acta*, **61**, 3885-96.

Jochum, K.P., Seufert, H.M., and Thirlwall, M.F. (1990) High-sensitivity Nb analysis by spark-source mass spectrometry (SSMS) and calibration of XRF Nb and Zr. *Chemical Geology*, **81**, 1-16.

Kronberg, B.I., Nesbitt,H.W., and Fyfe,W.S. (1987) Mobilities of alkalis, alkaline earths and halogens during weathering. *Chemical Geology*, **60**, 41-9.

Langmuir, D. (1997) Aqueous environmental geochemistry. Prentice-Hall Inc., New Jersey.

Lasaga, A.C., and Blum, A.E. (1986) Surface chemistry, etch pits and mineral-water reactions. *Geochimica et Cosmochimic Acta*, **50**, 2363-79.

Lee, M.R., and Parsons, I. (1995a) Microtextural controls of weathering of perthitic alkali feldspars. *Geochimica et Cosmochimica Acta*, **59**, 4465-88.

-. (1997) Compositional and microtextural zoning in alkali feldspars from the Shap granite and its geochemical implications. *Journal of the Geolocical Society, London*, **154**, 183-8.

Lee, M.R., Hodson M.E., and Parsons, I. (1998) The role of intragranular microtextures and microstructures in chemical and mechanical weathering: Direct comparisons of experimentally and naturally weathered alkali feldspars. *Geochimica et Cosmochimica Acta*, **62**, 2771-88.

Lee, M.R., Waldron, K.A., and Parsons, I. (1995b) Exsolution and alteration microtextures in alkali feldspar phenocrysts from the Shap granite. *Mineralogical Magazine*, **59**, 63-78.

Morse, S.A. (1970) Alkali felspar with water at 5kb pressure. *Journal of Petrology*, **11**, 221-53.

Muir, I.J., and Nesbitt, H.W. (1992) Controls on differential leaching of calcium and aluminium from labradorite in dilute electrolyte solutions. *Geochimica et Cosmochimica Acta*, **56**, 3979-85.

Nesbitt, H.W. (1979) Mobility and fractionation of rare earth elements during weathering of a granodiorite. *Nature*, **279**, 206-10.

Nesbitt, H.W., and Markovics, G. (1997) Weathering of granodiorite crust, long-term storage of elements in weathering profiles and petrogenesis of siliciclastic sediments. *Geochimica et Cosmochimica Acta*, **61**, 1653-70.

Nesbitt, H.W., Markovics,G., and Price,R.C. (1980) Chemical processes affecting alkalis and alkaline earths during continental weathering. *Geochimica et Cosmochimica Acta*, **44**, 1659-66.

Nesbitt, H.W., and Young, G.M. (1982) Early Proterozoic climates and plate motions inferred from major element chemistry of lutites. *Nature*, **299**, 715.

Norrish, K., and Hutton, J.T. (1969) An accurate X-ray spectrographic method for the analysis of a wide range of geological samples. *Geochimica et Cosmochimica Acta*, **33**, 431-53.

Oelkers, E.H., and Schott, J. (1995) Experimental study of anorthite dissolution and the relative mechanism of feldspar hydrolysis. *Geochimica et Cosmochimica Acta*, **59**, 5039-53.

Olive,V., Ellam, R.M. and Wilson, L.(2001). A Protocol for the Determination of the Rare Earth Elements at Picomole Level in Rocks by ICP-MS: Results on Geological Reference Materials USGS PCC-1 and DTS-1. *Geostandards and Geoanalytical Research*, **25**: 219-228.

Paces, T. (1973) Steady-state kinetics and equilibrium between ground water and granitic rock. *Geochimica et Cosmochimic Acta*, **37**, 2641-63.

-. **(1983)** Rate constants of dissolution derived from the measurements of mass balance in hydrological catchments*1. *Geochimica et Cosmochimic Acta*, **47**, 855-1863.

Panahi, A., Young, G.M., and Rainbird, R.H. (2000) Behavior of major and trace elements (including REE) during Paleoproterozoic pedogenesis and diagenetic alteration of an Archean granite near Ville Marie, Québec, Canada. *Geochimica et Cosmochimica Acta*, **64**, 2199-220.

Parsons, I. (1984) Feldspar and the thermal history of igneous rocks. In W.L. Brown, Ed. *Feldspar and feldspathoids: structure, properties and occurrences.*, **137**, p. 317-71. NATO ASI series C, Reidel Publishing Company.

Parsons, I., and Lee, M. (2005) Minerals are not just chemical compounds. *The Canadian Mineralogist*, **43**, 2005.

Parsons, I., Thompson, P., Lee, M.R., and Cayzer, N. (2005) Alkali Feldspar Microtextures as Provenance Indicators in Siliciclastic Rocks and Their Role in Feldspar Dissolution During Transport and Diagenesis. *JOURNAL OF SEDIMENTARY RESEARCH*, **75**, 921-42.

Pedro, G. (1997) Clay miinerals in Weathered Rock Materials and in Soils. In H.a.C. Paquet, H., Ed. *Soils and Sediments, Mineralogy and Chemistry*, p. 1-18. Springer-Verlag Berlin Heidelberg.

Putnis, A. (1992) Introduction to Mineral Sciences. 457 p. Cambridge University Press.

Ribbe, P.H. (1983) Feldspar Mineralogy, Reviews in mineralogy, **Vol.2**, p. 362. Mineralogy of America, Washington DC.

Schwartz, M.O., Rajah, S.S., Askury A.K., Putthapiban P., and Djaswadi S. (1995) The Southeast Asian Tin Belt. *Earth-Science Reviews*, **38**, 95-293.

Singh, M., Sharma,M., and Tobschall,H.J. (2005) Weathering of the Ganga alluvial plain, northern India: implications from fluvial geochemistry of the Gomati River. *Applied Geochemistry*, **20**, 1-21.

Skoda, R., and Novák, M. (2007) Y,REE,Nb,Ta,Ti-oxide (AB2O6) minerals from REL-REE euxenite-subtype pegmatites of the Trebíc Pluton, Czech Republic; substitutions and fractionation trends. *Lithos*, **95**, 43.

Smith, J.V., and Brown, W.L. (1988) Feldspar Minerals (Vol. 1 Crystal Structure, Physical, Chemical, and Microtextural Properties). 828 p. Springer-Verlag, Berlin Heidelberg New York London Paris Tokyo.

Smith, P., and Parsons, I. (1974) The alkali-feldspar solvus at 1 Kilobar water-vapour pressure. *Mineralogical Magazine*, **39**, 747-67.

Stumm, W., and Morgan, J.J. (1996) Aquatic Chemistry-Chemical Equilbra and Rates in Natural Waters. John Wiley and Sons Inc, New York.

Taunton, A.E., Welch, S.A., and Banfield, J.F. (2000) Geomicrobiological controls on light rare earth element, Y and Ba distributions during granite weathering and soil formation. *Journal of Alloys and Compounds.*, **303-304**, 30-6.

Tsai, W.-T., Su, T.-Y., Hsu, H.-C., Lin, K.-Y., Lin, C.-M., and Tai, T.-H. (2007) Preparation of mesoporous solids by acid treatment of a porphyritic andesite (wheat-rice-stone). *Microporous and Mesoporous Materials*, **102**, 196.

Velbel, M.A. (1989) Effect of chemical affinity on feldspar hydrolysis rates in two natural weathering systems. *Chemical Geology*, **78**, 245-53.

Viers, J., and Wasserburg, G.J. (2004) Behavior of Sm and Nd in a lateritic soil profile. *Geochimica et Cosmochimic Acta*, **68**, 2043-54.

Voicu, G., and Bardoux, M. (2002) Geochemical behaviour under tropical weathering of the Barama-Mazaruni Greenstone Belt at Omai gold mine, Guina Shield. *Applied Geochemistry*, **17**, 321-36.

Waldron, K., Lee, M.R., and Parsons I. (1994) The microstructures of perthitic alkali feldspars revealed by hydrofloric acid etching. *Contrib. Mineral Petrol 116: 360-364*, **116**, 360-4.

Walker, F.D.L., Lee, M.R., and Parsons, I. (1995) Micropores amd micropermeable texture in alkali feldspars: geochemical and geophysical implications. *Mineralogical Magazine*, **59**, 505-34.

Welton, J.E. (1984) SEM petrology atlas. 237 p. American Association of Petroleum Geologists, Tulsa, Okla.

Wen, S., and Nekvasil, H. (1994) SOLVCALC: an interactive graphics program package for calculating the ternary feldspar solvus and for two-feldspar geothermometry. *Comput. Geosci.*, **20**, 1025-40.

White, A.F. (1995) Chemical weathering rates of Silicate Minerals in soils. In A.F. White, and Brantley, S.L., Ed. *Chemical Weathering Rates of Silicate Minerals. Reviews in Mineralogy.*, **31**, p. 407-61. Mineralogical Society of America, Washington, D.C.

Wilson, M.J. (1975) Chemical Weathering of Some Primary Rock-Forming Minerals. *Soil Science*, **119**, 349-55.

-. **(2004)** Weathering of the primary rock-forming minerals: processes, products and rates. *Clay Minerals*, **39**, 233-66.

Wollast, R. (1967) Kinetics of the alteration of K-feldspar in buffered solutions at low temperature. *Geochimica et Cosmochimic Acta*, **31**, 635-48.

Woods, B.J., and Walther,J.V. (1983) Rates of hydrothermal reactions. *Science*, **222**, 413-5.

Worden, R., Walker, F., Parsons, I., and Brown, W. (1990) Developemnt of microporosity, diffusion channels and deuteric coarsening in perthitic alkali feldspars. *Contributions to Mineralogy and Petrology*, **104**, 507-15.

Appendices

Appendix A1:-standards used

Element	Crystal	Standard
Na	Thallium acid phthalate (TAP)	Jadeite
Si	TAP	Wollastonite
K	Penterythritol (PET)	Orthoclase
Ca	Lithium fluoride (LiF)	Wollastonite
Mg	TAP	Periclase
Al	TAP	Corundum
Fe	PET	Fe metal
Ti	LiF	Rutile
Ba	PET	Baryte

Table A1.1 The diffracting crystals and standards used for each of the elements analysed for in the electron microbe analyses.

Appendix B1-Electron probe results.

Sample name	SiO_2	TiO_2	Al_2O_3	MgO	CaO	MnO	FeO	BaO	Na_2O	K_2O	Total
Cheras-K feldspar											
CA21_kfs1_core1	63.86	-	18.52	0.01	-	0.01	-	0.03	0.90	15.92	99.25
CA21_kfs1_core2	64.08	-	18.48	-	0.01	-	0.01	-	0.74	15.93	99.25
CA21_kfs2_core1	63.83	-	18.52	-	0.01	-	0.02	0.01	0.86	15.96	99.22
CA21_kfs2_core2	63.56	-	18.47	-	-	-	0.05	-	0.54	16.20	98.82
CA22_kfs4_core1	64.40	0.01	18.53	-	0.01	-	0.04	0.01	1.24	15.25	99.50
CA22_kfs4_core2	63.73	-	18.48	-	-	0.01	-	0.01	1.01	15.47	98.71
CA22_kfs4_rim1	63.59	-	18.63	-	-	-	0.01	0.04	0.48	16.14	98.90
CA22_kfs4_interm1	63.98	-	18.60	-	-	0.01	-	0.02	0.95	15.72	99.29
CA22_kfs4_interm2	63.54	-	18.43	-	-	-	0.04	-	0.52	16.05	98.58
CA22_kfs4_rim2	64.20	-	18.60	-	0.02	0.01	0.02	0.03	1.17	15.49	99.54
CA22_kfs1_core1	63.29	-	18.37	-	-	0.01	0.01	-	0.47	16.01	98.16
CA22_kfs1_interm1	63.38	-	18.21	0.01	0.02	-	0.01	-	0.74	15.61	97.98
CA22_kfs1_rim1	63.90	-	18.56	-	-	-	0.04	-	0.80	15.83	99.14
CA22_kfs3_core1	63.66	-	18.38	-	0.03	0.01	-	-	1.10	15.45	98.63
CA22_kfs3_core2	63.94	-	18.57	-	0.01	0.01	0.02	-	0.93	15.59	99.07
Rawang-K feldspar											
RA19_kfs1_core1	64.21	-	18.68	0.01	0.05	-	-	-	2.28	13.91	99.15
RA19_kfs1_core2	63.89	-	18.43	-	0.04	-	-	0.03	1.04	15.38	98.82
RA19_kfs adj plag2 rim1	63.83	-	18.35	-	-	0.01	0.01	0.173	0.30	16.31	98.97
RA20_kfs1_core1	64.23	0.01	18.52	0.01	0.06	0.01	0.02	0.38	2.01	13.78	99.03
RA20_kfs1_core2	64.42	-	18.57	-	0.06	-	0.06	-	2.35	13.69	99.15
RA20_kfs1_core2b	64.45	0.01	18.54	0.01	0.06	-	-	0.01	2.39	13.54	99.00
RA20_kfs3_core1	63.93	-	18.48	-	0.09	-	0.01	0.25	1.53	14.69	99.00
RA20_kfs3_core2	63.81	0.03	18.55	0.01	0.04	-	0.04	0.44	1.94	13.89	98.74
RB13_kfs1_core1	63.90	0.01	18.71	-	0.05	-	-	-	1.78	14.42	98.88
RB13_kfs1_core2	64.29	-	18.61	-	0.03	0.01	0.01	0.01	1.33	15.08	99.37
RB13_kfs2_rim1	64.38	-	18.51	-	0.05	0.01	-	0.02	1.71	14.54	99.23
RB13_kfs2_int1	63.60	-	18.47	-	0.05	0.02	-	0.34	1.36	15.14	98.99
RB13_kfs2_int2	63.53	0.01	18.52	-	0.04	-	0.04	0.22	0.85	15.62	98.83
RB13_kfs2_core1	63.89	-	18.75	-	0.08	0.01	-	0.59	2.29	13.61	99.23
RB14_kfs1_core1	63.86	-	18.50	-	0.02	0.01	0.03	0.22	1.20	15.39	99.23
RB14_kfs1_core2	63.99	-	18.56	-	0.03	-	0.01	0.12	0.86	15.72	99.30
RB14_kfs3_core1	64.18	0.01	18.55	-	0.12	-	0.04	0.07	2.28	13.67	98.92
RB14_kfs3_core2	64.60	-	18.44	-	0.09	-	0.03	0.05	2.21	13.78	99.19

Table B1.1. Results of electron microprobe analyses (oxide wt%) on K-feldspar (kfs).

Sample name	SiO_2	TiO_2	Al_2O_3	MgO	CaO	MnO	FeO	BaO	Na_2O	K_2O	Total
Cheras-plagioclase											
CA21_plag1_core2	67.24	-	20.58	-	1.09	0.01	-	-	11.44	0.10	100.47
CA21_plag1_core1	66.63	-	21.10	0.01	1.44	0.03	-	0.01	11.10	0.12	100.43
CA21_plag1_core2	67.24	-	20.58	-	1.09	0.01	-	-	11.44	0.10	100.47
CA21_plag2_core1	67.09	-	20.99	-	1.51	-	0.02	0.01	11.15	0.05	100.83
CA21_plag2_core2	66.99	-	20.79	-	1.30	0.01	-	-	11.26	0.12	100.48
CA22_plag1_rim1	67.65	-	20.54	-	0.99	0.01	0.03	0.02	11.38	0.10	100.71
CA22_plag1_core1	67.19	-	20.68	-	1.31	0.01	0.01	-	11.45	0.06	100.72
CA22_plag1_core2	67.94	-	20.55	-	0.57	0.02	0.01	-	11.54	0.05	100.68
CA22_plag1_rim2	68.08	-	20.36	-	0.71	-	-	-	11.47	0.15	100.76
CA22_plag2_rim1	67.19	-	20.73	-	1.19	-	0.02	-	11.36	0.08	100.56
CA22_plag2_rim2	65.77	0.01	21.90	-	2.65	-	-	-	10.57	0.15	101.05
CA22_plag2_interm1	64.37	-	22.51	-	3.35	0.02	0.02	0.03	10.07	0.13	100.49
CA22_plag2_core1	62.93	-	22.67	-	3.81	-	0.06	0.01	9.87	0.08	99.43
CA22_plag3_rim1	65.42	0.01	21.46	-	2.06	0.01	-	-	10.82	0.08	99.86
CA22_plag3_core1	64.23	-	22.75	-	3.57	-	0.04	0.03	9.83	0.07	100.52
CA22_lamella1	68.21	-	19.59	-	0.05	0.01	-	0.02	11.16	1.30	100.34
Rawang-plagioclase											
RA19_plag1_rim1	62.58	-	23.46	-	4.53	0.01	-	0.00	9.24	0.34	100.16
RA19_plag1_rim2	62.04	-	23.57	0.01	4.75	-	-	0.04	9.11	0.32	99.84
RA19_plag1_int1	57.22	-	26.94	-	8.77	0.01	-	-	6.66	0.22	99.82
RA19_plag1_int2	55.85	0.01	28.04	-	9.96	-	0.04	0.07	6.04	0.21	100.23
RA19_plag1_core1	55.67	0.02	28.21	0.01	10.46	-	0.06	-	5.87	0.26	100.56
RA19_plag2_rim1	63.27	-	21.40	0.43	1.78	0.02	0.23	0.02	8.86	0.17	96.18
RA19_plag2_int1	57.05	0.02	27.45	-	9.09	0.03	0.04	0.05	6.65	0.18	100.55
RA19_plag2_rim2	68.56	-	19.96	-	0.36	-	-	-	11.67	0.09	100.64
RA19_plag2_int2	65.72	-	21.54	-	2.29	0.01	0.03	0.02	10.41	0.31	100.34
RA19_plag2_int3	63.35	-	23.27	-	4.24	0.02	0.03	0.01	9.30	0.37	100.60
RA19_plag2_int4	56.19	0.02	27.83	0.01	9.80	0.01	0.02	0.07	6.32	0.19	100.46
RA19_plag2_core1	54.38	0.03	28.76	0.01	10.92	-	0.02	0.02	5.59	0.15	99.87
RA19_plag2_core2	62.62	-	23.43	-	4.66	0.01	0.03	0.02	9.20	0.18	100.15
RA20_plag1_core1	55.61	0.01	28.21	0.01	10.49	0.03	-	0.07	5.86	0.24	100.54
RA20_plag1_rim1	64.68	-	21.83	-	2.59	-	0.01	-	10.47	0.07	99.66
RA20_plag1_interm1	62.97	-	23.44	-	4.56	0.01	0.01	-	9.55	0.11	100.63
RA20_plag1_interm2	56.99	0.01	27.17	-	9.36	0.01	-	0.01	6.60	0.17	100.32
RA20_plag1_dark1	62.35	-	23.64	-	4.99	0.01	-	-	9.10	0.15	100.25
RA20_plag2_core1	55.28	0.02	28.03	-	10.26	-	0.02	-	5.98	0.18	99.78
RA20_plag2_interm1	58.88	-	26.09	-	7.74	0.03	0.01	-	7.41	0.24	100.41
RA20_plag2_rim1	65.75	-	21.29	-	1.92	0.02	-	-	10.70	0.09	99.77

Table B1.2a Results of electron microprobe analyses (oxide wt%) on plagioclase (plags) in Rawang unweathered granite zone samples from drillhole RA.

Sample name	SiO_2	TiO_2	Al_2O_3	MgO	CaO	MnO	FeO	BaO	Na_2O	K_2O	Total
RB13_plag1_rim1	61.92	0.01	24.01	-	5.07	-	-	-	8.39	0.19	99.59
RB13_plag1_int1	58.07	0.01	26.78	-	8.40	-	0.03	0.04	7.01	0.19	100.52
RB13_plag1_int2	57.02	0.01	27.29	0.01	8.90	0.04	0.04	0.04	6.55	0.23	100.13
RB13_plag1_core1	57.12	0.03	27.40	-	9.35	-	0.03	0.06	6.47	0.26	100.72
RB13_plag2_rim1	69.86	-	19.18	-	0.68	-	0.01	0.04	11.16	0.09	101.02
RB13_plag2_rim2	58.74	-	20.88	-	3.96	-	0.01	-	8.86	0.04	92.49
RB13_plag2_int1	58.40	-	26.15	-	7.88	0.03	-	0.02	7.38	0.21	100.08
RB13_plag2_int2	62.66	-	23.50	-	4.67	-	0.01	0.01	9.22	0.25	100.34
RB13_plag2_int3	55.93	0.01	28.23	-	10.21	0.02	0.01	0.01	5.99	0.13	100.54
RB13_plag2_core1	55.32	-	28.48	0.01	10.34	0.03	0.03	0.03	5.87	0.15	100.26
RB13_plag2_core2	59.05	-	25.86	0.01	7.44	0.03	0.02	-	7.70	0.11	100.21
RB14_plag1_rim1	62.37	-	23.87	-	5.03	0.01	0.06	-	8.93	0.36	100.62
RB14_plag1_rim2	61.43	-	23.93	-	5.20	0.01	0.04	-	8.92	0.26	99.80
RB14_plag1_int1	56.97		27.16	-	8.92	-	0.01	0.03	6.63	0.24	99.97
RB14_plag1_int2	60.26	0.01	25.46	-	6.79	0.02	-	-	7.79	0.34	100.68
RB14_plag1_int3	55.73	-	28.28	-	10.22	0.02	0.02	-	5.84	0.28	100.39
RB14_plag1_core1	56.18	0.01	27.58	-	9.80	0.01	-	0.03	6.14	0.20	99.95
RB14_plag2_rim1	67.24	-	21.14	-	1.62	0.00	0.02	-	10.94	0.15	101.11
RB14_plag2_rim2	62.35	-	23.73	-	4.97	0.01	-	-	9.03	0.26	100.35
RB14_plag2_int1	56.13	-	28.08	-	10.13	-	0.04	0.03	6.04	0.19	100.65
RB14_plag2_int2	56.34	0.01	27.83	-	9.67	0.01	-	-	6.09	0.19	100.14
RB14_plag2_core1	55.79	0.03	28.30	-	10.02	-	0.04	0.01	5.90	0.21	100.30
RB14_plag2_core2	52.65	0.02	32.64	0.01	9.44	0.01	0.07	0.03	5.60	0.18	100.65
RB14_plag2_core3	39.42	0.05	33.27	0.06	24.62	0.10	0.81	0.04	0.01	-	98.38

Table B1.2b Results of electron microprobe analyses (oxide wt%) on plagioclase (plags) in Rawang unweathered granite zone samples from drillhole RB, about 1m adjacent of drillhole RA.

Sample name	SiO_2	TiO_2	$Al2O_3$	Cr_2O_3	MgO	CaO	MnO	FeO	BaO	Na_2O	K_2O	F	Cl	Total	O=F , Cl	Total
CA21_musc-1c1	45.86	0.56	35.47	0.03	0.84	-	0.10	2.00	0.02	0.22	10.66	0.48	-	96.24	0.20	96.04
CA21_musc-1bc1	46.18	0.66	33.71	0.01	1.15	0.03	0.12	2.71	-	0.29	10.52	0.49	0.01	95.89	0.21	95.68
CA21_musc-2a	45.75	0.40	35.42	-	0.84	0.08	0.07	1.89	0.02	0.34	10.28	0.35	-	95.45	0.15	95.30
CA21_musc-2b	45.84	0.55	34.64	-	1.04	0.02	0.10	2.51	-	0.27	10.69	0.57	-	96.23	0.24	95.99
CA22_musc-1	45.94	0.87	33.90	0.02	1.02	0.01	0.17	3.17	0.05	0.13	10.93	0.45	-	96.66	0.19	96.47
CA22_musc-3a	45.85	0.46	35.01	0.01	0.90	0.01	0.08	2.35	-	0.24	10.79	0.42	-	96.12	0.18	95.95
CA22_musc-3b	46.18	0.49	34.21	0.03	1.12	0.01	0.14	2.79	-	0.21	11.07	0.64	-	96.89	0.27	96.62

Table B1.3 Results of electron microprobe analyses (oxide wt%) on muscovite grains in Cheras unweathered granite zone.

Sample name	SiO_2	TiO_2	$Al2O_3$	Cr_2O_3	MgO	CaO	MnO	FeO	BaO	Na_2O	K_2O	F	Cl	Total	O=F , Cl	Total
CA22_biot-1	32.28	1.39	19.29	0.01	3.62	0.04	0.91	27.01	0.03	0.01	6.60	0.23	0.10	91.50	0.12	91.38
CA22_biot-1b	26.59	0.70	20.44		4.11	0.10	1.42	33.76	0.01	0.00	2.06	0.01	0.03	89.23	0.01	89.22
RA19_biot-1	35.61	3.90	16.11	0.01	9.14	-	0.31	20.79	0.03	0.20	9.55	0.59	0.08	96.32	0.27	96.05
RA19_biot-1b	35.40	3.90	16.28	0.04	9.36	-	0.32	20.42	-	0.16	9.38	0.82	0.07	96.16	0.36	95.80
RA19_biot-2	34.91	4.36	15.94	0.03	8.57	-	0.34	21.09	0.26	0.22	9.23	0.60	0.07	95.62	0.27	95.36
RA19_biot-2b	35.33	4.58	16.13	0.05	8.69	0.00	0.31	20.77	0.09	0.19	9.37	0.56	0.06	96.12	0.25	95.87
RA20_biot-1a	35.71	4.72	15.60	0.07	8.88	-	0.25	20.76	0.11	0.25	9.43	0.55	0.08	96.42	0.25	96.17
RA20_biot-1b	35.34	4.74	15.62	0.08	8.84	0.05	0.34	21.13	0.22	0.15	9.39	0.72	0.07	96.69	0.32	96.37
RA20_biot-2a	35.19	3.90	16.49	0.02	9.13	0.01	0.32	21.05	-	0.17	9.45	0.80	0.06	96.59	0.35	96.23
RA20_biot-2b	35.78	4.23	16.11	0.06	9.06	0.01	0.31	21.11	0.10	0.09	9.66	0.56	0.08	97.15	0.25	96.90
RB13_biot-1	35.91	4.23	15.95	0.04	9.11	0.04	0.35	21.06	0.15	0.23	9.46	0.77	0.08	97.37	0.34	97.03
RB13_biot-1b	36.13	4.12	16.39	0.07	9.11	0.01	0.29	20.81	0.08	0.22	9.52	0.72	0.09	97.58	0.32	97.26
RB14_biot-1	34.98	4.27	16.13	0.12	9.21	-	0.30	21.45	0.13	0.10	9.20	0.43	0.08	96.39	0.20	96.19
RB14_biot-1b	35.99	5.47	15.36	0.12	8.60	-	0.29	20.67	0.21	0.22	9.46	0.62	0.09	97.10	0.28	96.82
RB14_biot-2	36.06	4.74	16.48	0.01	8.97	0.03	0.28	20.46	0.17	0.21	9.49	0.61	0.09	97.59	0.27	97.32
RB14_biot-2b	36.27	4.56	15.82	0.04	9.30	0.04	0.34	20.33	0.02	0.24	9.22	0.80	0.10	97.07	0.36	96.71
RB14_biot-2rim1	25.21	0.05	20.20	0.02	12.84	0.03	0.57	28.88	-	0.01	0.02	-	0.01	87.85	-	87.85
RB14_biot-2rim2	24.87	0.07	20.38	-	12.77	0.06	0.51	28.91	0.01	0.02	-	0.12	-	87.71	0.05	87.66

Table B1.4 Results of electron microprobe analyses (oxide wt%) on biotite grains in the Cheras (CA) and Rawang (RA and RB) unweathered granite zone.

Sample name	SiO_2	TiO_2	$Al2O_3$	Cr_2O_3	MgO	CaO	MnO	FeO	BaO	Na_2O	K_2O	F	Cl	Total	O=F , Cl	Total
CA21_chl-1a	23.39	0.11	21.50	-	4.84	0.01	1.47	37.33	-	0.01	0.02	0.12	0.01	88.81	0.05	88.76
CA21_chl- 1b	23.99	0.09	20.73	-	5.38	0.01	1.48	36.75	0.01	0.02	0.03	0.21	-	88.70	0.09	88.61
CA21_chl-3a	23.01	0.12	21.73	0.01	4.43	0.01	1.66	37.92	-	0.01	-	-	-	88.89	-	88.89
CA21_chl-3b	23.33	0.12	21.50	0.05	4.51	0.01	1.73	37.83	0.07	-	0.01	-	0.01	89.16	-	89.16
CA22_chl-1	23.22	0.14	21.01	0.01	4.20	0.06	1.64	38.13	-	-	0.05	-	-	88.46	-	88.45
CA22_chl-1b	22.98	0.12	21.36	-	4.41	0.05	1.99	38.53	-	-	0.02	-	0.01	89.48	-	89.48
RA19_chl-1	25.10	0.02	20.39	-	12.27	0.02	0.51	29.84	0.01	-	-	0.02	-	88.19	0.01	88.18
RA19_chl-1b	25.50	0.06	19.90	0.04	12.53	0.06	0.53	30.16	-	-	0.01	-	-	88.80	-	88.80
RA19_chl-2	25.79	0.06	21.11	0.01	12.04	0.10	0.42	28.52	-	0.01	0.02	-	-	88.09	-	88.09
RA19_chl-2b	25.95	0.07	20.36	-	12.46	0.06	0.43	29.04	0.02	-	-	0.07	0.02	88.49	0.03	88.45
RA20_chl-1a	25.31	0.10	19.85	0.07	12.44	0.09	0.48	30.39	-	-	0.17	0.04	0.01	88.95	0.02	88.94
RA20_chl-1b	25.23	0.06	19.87	0.04	12.66	0.04	0.51	29.73	-	-	0.01	-	-	88.15	-	88.15
RA20_chl-2a	24.82	0.12	21.59	0.06	11.88	0.03	0.52	30.26	-	-	0.01	0.03	0.00	89.33	0.01	89.32
RA20_chl-2b	25.75	0.09	20.04	0.06	13.25	0.01	0.51	29.06	-	0.01	0.07	0.11	0.01	88.96	0.05	88.91
RB13_chl-1	26.22	0.21	18.94	0.02	13.03	0.03	0.39	29.57	-	0.00	0.06	0.05	-	88.53	0.02	88.50
RB13_chl-1b	25.67	0.16	19.84	0.03	13.19	0.02	0.50	28.70	-	0.01	0.02	0.23	0.01	88.35	0.10	88.25
RB14_chl-1a	25.39	0.09	20.83	0.03	12.81	-	0.48	28.74	-	-	0.10	0.07	0.01	88.54	0.03	88.51
RB14_chl-1b	25.51	0.11	20.80	-	13.07	0.07	0.49	28.60	-	-	0.12	0.08	0.00	88.85	0.04	88.82
6R-14_chl-1c	25.37	1.24	20.31	0.01	12.38	1.12	0.57	27.77	-	-	0.02	0.14	0.01	88.93	0.06	88.87
RB14_chl-2a	25.67	0.06	20.62	0.02	13.07	0.02	0.51	28.45	-	0.01	0.02	0.05	-	88.50	0.02	88.48
RB14_chl-2b	25.21	0.09	20.45	0.05	12.48	0.05	0.48	29.55	-	0.01	0.03	-	0.01	88.42	0.00	88.41

Table B1.5 Results of electron microprobe analyses (oxide wt%) on chlorite in the Cheras (CA) and Rawang (RA and RB) unweathered granite zone.

Appendix B2-calculations (from electron probe results)

oxide (wt%)

Sample name	SiO_2	TiO_2	Al_2O_3	MgO	CaO	MnO	FeO	BaO	Na_2O	K_2O	Total
CA21_plag1_core1	66.63	-	21.10	0.01	1.44	0.03	-	0.01	11.10	0.12	100.43
CA21_plag1_core2	67.24	-	20.58	-	1.09	0.01	-	-	11.44	0.10	100.47
CA21_plag2_core1	67.09	-	20.99	-	1.51	-	0.02	0.01	11.15	0.05	100.83
CA21_plag2_core2	66.99	-	20.79	-	1.30	0.01	-	-	11.26	0.12	100.48

Cations, with respect to 24oxygen (using method proposed by Dear, Howie, and Zussman, 1992)

Sample name	Si	Ti	Al	Mg	Ca	Mn	Fe	Ba	Na	K
CA21_plag1_core1	8.74	-	3.26	-	0.20	-	-	-	2.82	0.02
CA21_plag1_core2	8.81	-	3.18	-	0.15	-	-	-	2.91	0.02
CA21_plag2_core1	8.76	-	3.23	-	0.21	-	-	-	2.82	0.01
CA21_plag2_core2	8.78	-	3.21	-	0.18	-	-	-	2.86	0.02

Cations, with respect to 32oxygen; Or = 100xK/(Ca+Na+K); Ab=100xNa/(Ca+Na+K); An=100xCa/(Ca+Na+K)

Sample name	Si	Ti	Al	Mg	Ca	Mn	Fe	Ba	Na	K	Or	Ab	An	Total
CA21_plag1_core1	11.7	-	4.3	-	0.3	-	-	-	3.8	0.01	**0.7**	**92.7**	**6.7**	100.0
CA21_plag1_core2	11.7	-	4.2	-	0.2	-	-	-	3.9	0.01	**0.6**	**94.5**	**5.0**	100.0
CA21_plag2_core1	11.7	-	4.3	-	0.3	-	-	-	3.8	0.01	**0.3**	**92.8**	**6.9**	100.0
CA21_plag2_core2	11.7	-	4.3	-	0.2	-	-	-	3.8	0.01	**0.7**	**93.4**	**5.9**	100.0

Cations, with respect to 8oxygen

Sample name	Si	Ti	Al	Mg	Ca	Mn	Fe	Ba	Na	K	Chemical formula
CA21_plag1_core1	2.9	-	1.4	-	0.1	-	-	-	1.3	0.01	$Na_{1.3}Ca_{0.1}Al_{1.4}Si_{2.9}O_8K_{0.01}$
CA21_plag1_core2	2.9	-	1.4	-	0.1	-	-	-	1.3	0.01	$Na_{1.3}Ca_{0.1}Al_{1.4}Si_{2.9}O_8K_{0.01}$
CA21_plag2_core1	2.9	-	1.4	-	0.1	-	-	-	1.3	0.01	$Na_{1.3}Ca_{0.1}Al_{1.4}Si_{2.9}O_8K_{0.01}$
CA21_plag2_core2	2.9	-	1.4	-	0.1	-	-	-	1.3	0.01	$Na_{1.3}Ca_{0.1}Al_{1.4}Si_{2.9}O_8K_{0.01}$

oxide (wt%)

Sample name	SiO_2	TiO_2	Al_2O_3	MgO	CaO	MnO	FeO	BaO	Na_2O	K_2O	Total
CA21_kfs1_core1	63.86	-	18.52	0.01	-	0.01	-	0.03	0.90	15.92	99.25
CA21_kfs1_core2	64.08	-	18.48	-	0.01	-	0.01	-	0.74	15.93	99.25
CA21_kfs2_core1	63.83	-	18.52	-	0.01	-	0.02	0.01	0.86	15.96	99.22
CA21_kfs2_core2	63.56	-	18.47	-	-	-	0.05	-	0.54	16.20	98.82

Cations, with respect to 24oxygen (using method proposed by Dear, Howie, and Zussman, 1992)

Sample name	Si	Ti	Al	Mg	Ca	Mn	Fe	Ba	Na	K
CA21_kfs1_core1	8.94	-	3.06	-	-	-	-	-	0.24	2.84
CA21_kfs1_core2	8.96	-	3.04	-	-	-	-	-	0.20	2.84
CA21_kfs2_core1	8.94	-	3.06	-	-	-	-	-	0.23	2.85
CA21_kfs2_core2	8.94	-	3.06	-	-	-	0.01	-	0.15	2.91

Cations, with respect to 32oxygen; Or = 100xK/(Ca+Na+K); Ab=100xNa/(Ca+Na+K); An=100xCa/(Ca+Na+K)

Sample name	Si	Ti	Al	Mg	Ca	Mn	Fe	Ba	Na	K	Or	Ab	An	Total
CA21_kfs1_core1	11.9	-	4.1	-	-	0.0	-	-	0.3	3.8	**92.1**	**7.9**	-	100.0
CA21_kfs1_core2	11.9	-	4.1	-	-	-	-	-	0.3	3.8	**93.3**	**6.6**	**0.1**	100.0
CA21_kfs2_core1	11.9	-	4.1	-	-	-	-	-	0.3	3.8	**92.4**	**7.6**	**0.1**	100.0
CA21_kfs2_core2	11.9	-	4.1	-	-	-	-	-	0.2	3.9	**95.2**	**4.8**	-	100.0

Cations, with respect to 8oxygen

Sample name	Si	Ti	Al	Mg	Ca	Mn	Fe	Ba	Na	K	Chemical formula
CA21_kfs1_core1	3.0	-	1.4	-	-	-	-	-	0.1	1.3	$Na_{0.1}Al_{1.4}Si_{3.0}O_8K_{1.3}$
CA21_kfs1_core2	3.0	-	1.4	-	-	-	-	-	0.1	1.3	$Na_{0.1}Al_{1.4}Si_{3.0}O_8K_{1.3}$
CA21_kfs2_core1	3.0	-	1.4	-	-	-	-	-	0.1	1.3	$Na_{0.1}Al_{1.4}Si_{3.0}O_8K_{1.3}$
CA21_kfs2_core2	3.0	-	1.4	-	-	-	-	-	0.1	1.3	$Na_{0.1}Al_{1.4}Si_{3.0}O_8K_{1.3}$

Table B2.1 Calculation for feldspar end members and chemical formula from electron probe results (sample CA21)

Appendix B3-electron beam on some of the minerals

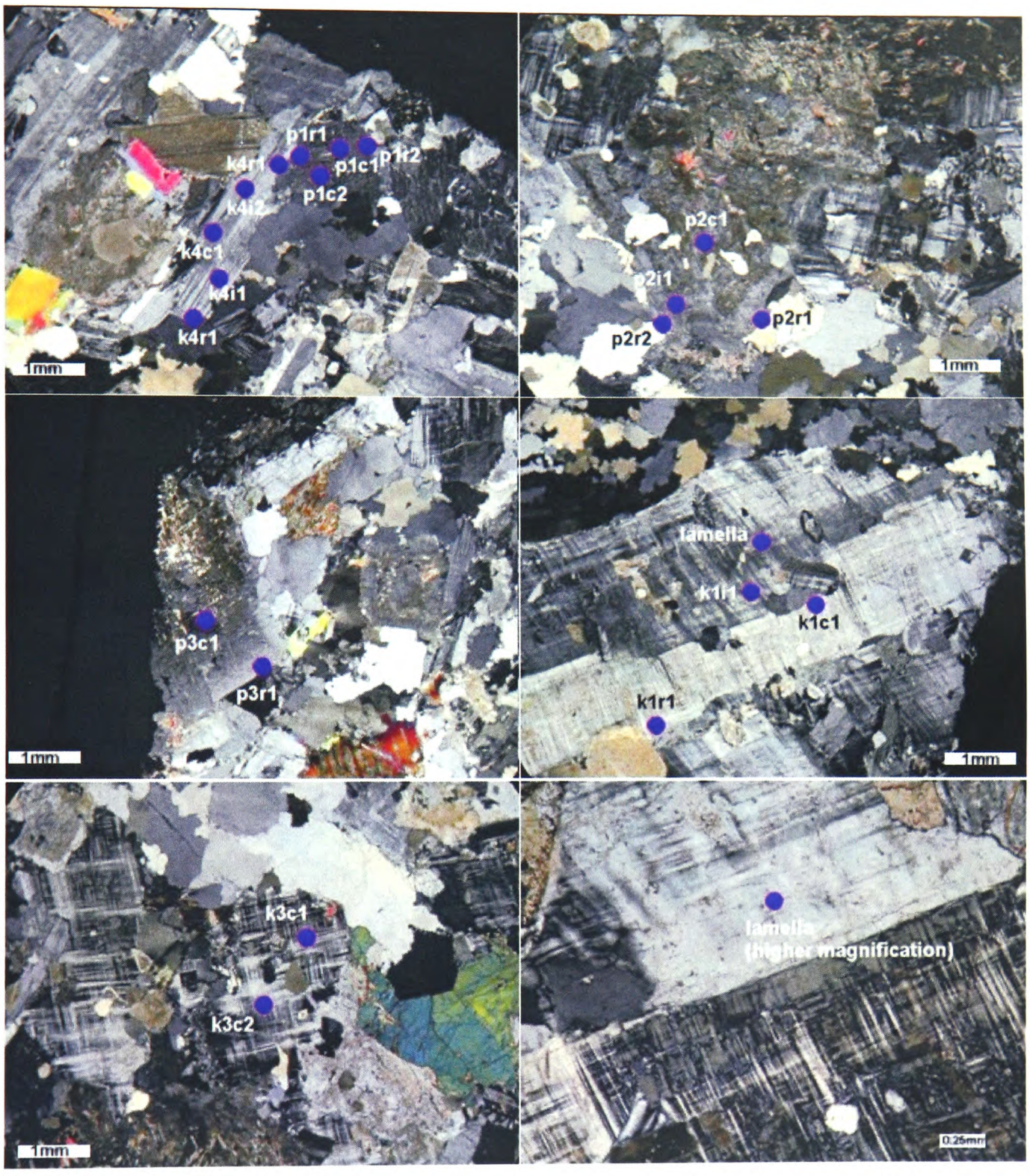

Plate B3.1: Analyses done using a defocused beam (50μm) on individual plagioclase and K-feldspar (Cheras CA22 samples).

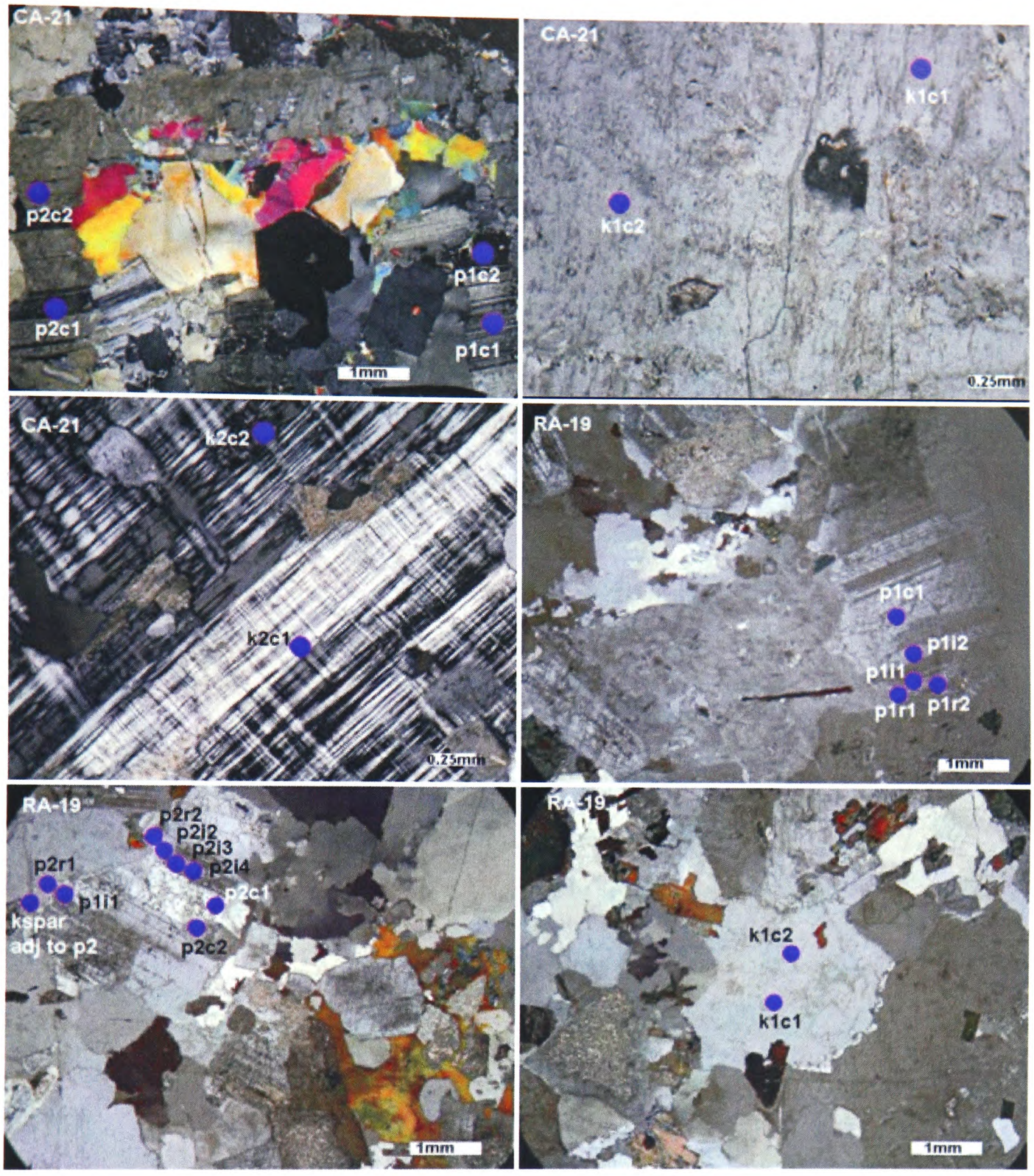

Plate B3.2: Analyses done using a defocused beam (50μm) on individual plagioclase and K-feldspar (Samples Cheras CA21 and Rawang RA19).

Appendix C1-Norm calculations

(programme written by Hollecher, K., Geology Department, Union University, Schenectady, NY, 12308)

CA18- norm4

Norm Calculation Program
Sample Number: CA18

Program run: 08/12/2008

HELP

	Rock Analysis	
SiO2	76.24	%
TiO2	0.10	%
Al2O3	12.88	%
Fe2O3	1.02	%
FeO		%
MnO	0.04	%
MgO	0.19	%
CaO	0.30	%
Na2O	2.46	%
K2O	6.20	%
P2O5	0.05	%
CO2		%
SO3		%
S		%
F		%
Cl		%
Sr	19	ppm
Ba	80	ppm
Ni		ppm
Cr		ppm
Zr	66	ppm
Total	99.48	

Normalization Factors	
Total=100%? Y/N	n
Fe3+/(Total Iron)	0.3
Total Fe as FeO	0.92
Desired Fe2O3	0.31
Desired FeO	0.64
Weight corr. factor	1.000

Zero values not shown

Norm calculation checks:
Norm seems OK

Normalized Analysis
76.24
0.10
12.88
0.31
0.64
0.04
0.19
0.30
2.46
6.20
0.05
0.01
0.01
99.43

Normative Minerals	Weight % Norm	Volume % Norm
Quartz	36.98	37.11
Plagioclase	21.98	22.24
Orthoclase	36.71	38.13
Nepheline		
Leucite		
Kalsilite		
Corundum	1.68	1.12
Diopside		
Hypersthene	1.30	0.95
Wollastonite		
Olivine		
Larnite		
Acmite		
K2SiO3		
Na2SiO3		
Rutile		
Ilmenite	0.19	0.11
Magnetite	0.45	0.23
Hematite		
Apatite	0.12	0.10
Zircon	0.01	0.01
Perovskite		
Chromite		
Sphene		
Pyrite		
Halite		
Fluorite		
Anhydrite		
Na2SO4		
Calcite		
Na2CO3		
Total	99.42	100.00

Fe3+/(Total Fe) in rock	30.4	30.4
Mg/(Mg+Total Fe) in rock	26.9	26.9
Mg/(Mg+Fe2+) in rock	34.6	34.6
Mg/(Mg+Fe2+) in silicates	42.9	42.9
Ca/(Ca+Na) in rock	6.3	6.3
Ca/(Ca+Na) in plagioclase	5.0	5.0
Differentiation Index	95.7	97.5
Calculated density, g/cc	2.64	2.64
Calculated liquid density, g/cc	2.35	2.35
Calculated viscosity, dry, Pas	1.17	1.17
Calculated viscosity, wet, Pas	0.79	0.79
Estimated liquidus temp., °C	725	725
Estimated H2O content, wt. %	4.67	4.67

This program was written by Kurt Hollocher, Geology Department, Union College, Schenectady, NY, 12308, hollochk@union.edu

Norm Calculation Program

Sample Number: CA18

Program run: 08/12/2008

HELP

	Rock Analysis	
SiO2	76.24	%
TiO2	0.10	%
Al2O3	12.88	%
Fe2O3	1.02	%
FeO		%
MnO	0.04	%
MgO	0.19	%
CaO	0.30	%
Na2O	2.46	%
K2O	6.20	%
P2O5	0.05	%
CO2		%
SO3		%
S		%
F		%
Cl		%
Sr	19	ppm
Ba	80	ppm
Ni		ppm
Cr		ppm
Zr	66	ppm
Total	99.48	

Normalization Factors	
Total=100%? Y/N	n
Fe3+/(Total Iron)	0.3
Total Fe as FeO	0.92
Desired Fe2O3	0.31
Desired FeO	0.64
Weight corr. factor	1.000

Zero values not shown

Norm calculation checks:
Norm seems OK

Normalized Analysis
76.24
0.10
12.88
0.31
0.64
0.04
0.19
0.30
2.46
6.20
0.05
0.01
0.01
99.43

Normative Minerals	Weight % Norm	Volume % Norm
Quartz	36.98	37.11
Plagioclase	21.98	22.24
Orthoclase	36.71	38.13
Nepheline		
Leucite		
Kalsilite		
Corundum	1.68	1.12
Diopside		
Hypersthene	1.30	0.95
Wollastonite		
Olivine		
Larnite		
Acmite		
K2SiO3		
Na2SiO3		
Rutile		
Ilmenite	0.19	0.11
Magnetite	0.45	0.23
Hematite		
Apatite	0.12	0.10
Zircon	0.01	0.01
Perovskite		
Chromite		
Sphene		
Pyrite		
Halite		
Fluorite		
Anhydrite		
Na2SO4		
Calcite		
Na2CO3		
Total	99.42	100.00

Fe3+/(Total Fe) in rock	30.4	30.4
Mg/(Mg+Total Fe) in rock	26.9	26.9
Mg/(Mg+Fe2+) in rock	34.6	34.6
Mg/(Mg+Fe2+) in silicates	42.9	42.9
Ca/(Ca+Na) in rock	6.3	6.3
Ca/(Ca+Na) in plagioclase	5.0	5.0
Differentiation Index	95.7	97.5
Calculated density, g/cc	2.64	2.64
Calculated liquid density, g/cc	2.35	2.35
Calculated viscosity, dry, Pas	1.17	1.17
Calculated viscosity, wet, Pas	0.79	0.79
Estimated liquidus temp., °C	725	725
Estimated H2O content, wt. %	4.67	4.67

This program was written by Kurt Hollocher, Geology Department, Union College, Schenectady, NY, 12308, hollochk@union.edu

Norm Calculation Program

Sample Number: CA19

Program run: 08/12/2008

HELP

	Rock Analysis	
SiO2	76.01	%
TiO2	0.12	%
Al2O3	12.63	%
Fe2O3	1.09	%
FeO		%
MnO	0.04	%
MgO	0.23	%
CaO	0.38	%
Na2O	2.62	%
K2O	5.31	%
P2O5	0.06	%
CO2		%
SO3		%
S		%
F		%
Cl		%
Sr	18	ppm
Ba	52	ppm
Ni		ppm
Cr		ppm
Zr	61	ppm
Total	98.49	

Normalization Factors	
Total=100%? Y/N	n
Fe3+/(Total Iron)	0.3
Total Fe as FeO	0.98
Desired Fe2O3	0.33
Desired FeO	0.69
Weight corr. factor	1.000

Zero values not shown

Norm calculation checks:
Norm seems OK

Normalized Analysis
76.01
0.12
12.63
0.33
0.69
0.04
0.23
0.38
2.62
5.31
0.06
0.01
0.01
98.44

Normative Minerals	Weight % Norm	Volume % Norm
Quartz	39.01	39.68
Plagioclase	23.66	24.27
Orthoclase	31.45	33.12
Nepheline		
Leucite		
Kalsilite		
Corundum	2.01	1.36
Diopside		
Hypersthene	1.44	1.08
Wollastonite		
Olivine		
Larnite		
Acmite		
K2SiO3		
Na2SiO3		
Rutile		
Ilmenite	0.23	0.13
Magnetite	0.48	0.25
Hematite		
Apatite	0.14	0.12
Zircon	0.01	0.01
Perovskite		
Chromite		
Sphene		
Pyrite		
Halite		
Fluorite		
Anhydrite		
Na2SO4		
Calcite		
Na2CO3		
Total	98.43	100.02

Fe3+/(Total Fe) in rock	30.1	30.1
Mg/(Mg+Total Fe) in rock	29.3	29.3
Mg/(Mg+Fe2+) in rock	37.3	37.3
Mg/(Mg+Fe2+) in silicates	46.4	46.4
Ca/(Ca+Na) in rock	7.4	7.4
Ca/(Ca+Na) in plagioclase	6.0	6.0
Differentiation Index	94.1	97.1
Calculated density, g/cc	2.65	2.65
Calculated liquid density, g/cc	2.35	2.35
Calculated viscosity, dry, Pas	1.21	1.21
Calculated viscosity, wet, Pas	0.80	0.80
Estimated liquidus temp., °C	715	715
Estimated H2O content, wt. %	4.79	4.79

This program was written by Kurt Hollocher, Geology Department, Union College, Schenectady, NY, 12308, hollochk@union.edu

CA20- norm4

Norm Calculation Program
Sample Number: CA20

Program run: 08/12/2008

HELP

	Rock Analysis	
SiO2	77.02	%
TiO2	0.09	%
Al2O3	12.52	%
Fe2O3	0.93	%
FeO		%
MnO	0.02	%
MgO	0.15	%
CaO	0.27	%
Na2O	2.55	%
K2O	5.59	%
P2O5	0.06	%
CO2		%
SO3		%
S		%
F		%
Cl		%
Sr	16	ppm
Ba	106	ppm
Ni		ppm
Cr		ppm
Zr	58	ppm
Total	99.20	

Normalization Factors	
Total=100%? Y/N	n
Fe3+/(Total Iron)	0.3
Total Fe as FeO	0.84
Desired Fe2O3	0.28
Desired FeO	0.59
Weight corr. factor	1.000

Zero values not shown

Norm calculation checks:
Norm seems OK

Normalized Analysis
77.02
0.09
12.52
0.28
0.59
0.02
0.15
0.27
2.55
5.59
0.06
0.01
0.01
99.16

Normative Minerals	Weight % Norm	Volume % Norm
Quartz	39.77	40.06
Plagioclase	22.52	22.90
Orthoclase	33.11	34.52
Nepheline		
Leucite		
Kalsilite		
Corundum	1.91	1.28
Diopside		
Hypersthene	1.11	0.81
Wollastonite		
Olivine		
Larnite		
Acmite		
K2SiO3		
Na2SiO3		
Rutile		
Ilmenite	0.17	0.10
Magnetite	0.41	0.21
Hematite		
Apatite	0.14	0.12
Zircon	0.01	0.01
Perovskite		
Chromite		
Sphene		
Pyrite		
Halite		
Fluorite		
Anhydrite		
Na2SO4		
Calcite		
Na2CO3		
Total	99.15	100.01

Fe3+/(Total Fe) in rock	29.9	29.9
Mg/(Mg+Total Fe) in rock	24.1	24.1
Mg/(Mg+Fe2+) in rock	31.2	31.2
Mg/(Mg+Fe2+) in silicates	39.9	39.9
Ca/(Ca+Na) in rock	5.5	5.5
Ca/(Ca+Na) in plagioclase	4.0	4.0
Differentiation Index	95.4	97.5
Calculated density, g/cc	2.65	2.65
Calculated liquid density, g/cc	2.35	2.35
Calculated viscosity, dry, Pas	1.23	1.23
Calculated viscosity, wet, Pas	0.81	0.81
Estimated liquidus temp., °C	706	706
Estimated H2O content, wt. %	4.88	4.88

This program was written by Kurt Hollocher, Geology Department, Union College, Schenectady, NY, 12308, hollochk@union.edu

CA21- norm4

Norm Calculation Program
Sample Number: CA21

Program run: 08/12/2008

HELP

	Rock Analysis	
SiO2	77.33	%
TiO2	0.11	%
Al2O3	12.40	%
Fe2O3	0.97	%
FeO		%
MnO	0.03	%
MgO	0.12	%
CaO	0.47	%
Na2O	3.57	%
K2O	4.53	%
P2O5	0.06	%
CO2		%
SO3		%
S		%
F		%
Cl		%
Sr	17	ppm
Ba	46	ppm
Ni		ppm
Cr		ppm
Zr	58	ppm
Total	99.59	

Normalization Factors	
Total=100%? Y/N	n
Fe3+/(Total Iron)	0.3
Total Fe as FeO	0.87
Desired Fe2O3	0.29
Desired FeO	0.61
Weight corr. factor	1.000

Zero values not shown

Norm calculation checks:
Norm seems OK

Normalized Analysis
77.33
0.11
12.40
0.29
0.61
0.03
0.12
0.47
3.57
4.53
0.06
0.01
0.01
99.54

Normative Minerals	Weight % Norm	Volume % Norm
Quartz	37.81	37.88
Plagioclase	32.15	32.47
Orthoclase	26.84	27.84
Nepheline		
Leucite		
Kalsilite		
Corundum	0.90	0.60
Diopside		
Hypersthene	1.05	0.76
Wollastonite		
Olivine		
Larnite		
Acmite		
K2SiO3		
Na2SiO3		
Rutile		
Ilmenite	0.21	0.12
Magnetite	0.42	0.21
Hematite		
Apatite	0.14	0.12
Zircon	0.01	0.01
Perovskite		
Chromite		
Sphene		
Pyrite		
Halite		
Fluorite		
Anhydrite		
Na2SO4		
Calcite		
Na2CO3		
Total	99.53	100.01

Fe3+/(Total Fe) in rock	30.0	30.0
Mg/(Mg+Total Fe) in rock	19.7	19.7
Mg/(Mg+Fe2+) in rock	26.0	26.0
Mg/(Mg+Fe2+) in silicates	34.2	34.2
Ca/(Ca+Na) in rock	6.8	6.8
Ca/(Ca+Na) in plagioclase	5.7	5.7
Differentiation Index	96.8	98.2
Calculated density, g/cc	2.64	2.64
Calculated liquid density, g/cc	2.35	2.35
Calculated viscosity, dry, Pas	1.21	1.21
Calculated viscosity, wet, Pas	0.80	0.80
Estimated liquidus temp., °C	706	706
Estimated H2O content, wt. %	4.88	4.88

This program was written by Kurt Hollocher, Geology Department, Union College, Schenectady, NY, 12308, hollochk@union.edu

Norm Calculation Program

Sample Number: CA22

Program run: 08/12/2008

HELP

	Rock Analysis	
SiO2	72.73	%
TiO2	0.12	%
Al2O3	15.11	%
Fe2O3	0.95	%
FeO		%
MnO	0.03	%
MgO	0.17	%
CaO	0.47	%
Na2O	2.90	%
K2O	7.05	%
P2O5	0.06	%
CO2		%
SO3		%
S		%
F		%
Cl		%
Sr	35	ppm
Ba	288	ppm
Ni		ppm
Cr		ppm
Zr	58	ppm
Total	99.59	

Normalization Factors	
Total=100%? Y/N	n
Fe3+/(Total Iron)	0.3
Total Fe as FeO	0.85
Desired Fe2O3	0.29
Desired FeO	0.60
Weight corr. factor	1.000

Zero values not shown

Norm calculation checks:
Norm seems OK

Normalized Analysis
72.73
0.12
15.11
0.29
0.60
0.03
0.17
0.47
2.90
7.05
0.06
0.03
0.01
99.57

Normative Minerals	Weight % Norm	Volume % Norm
Quartz	27.31	27.32
Plagioclase	26.48	26.70
Orthoclase	41.88	43.38
Nepheline		
Leucite		
Kalsilite		
Corundum	1.96	1.30
Diopside		
Hypersthene	1.14	0.83
Wollastonite		
Olivine		
Larnite		
Acmite		
K2SiO3		
Na2SiO3		
Rutile		
Ilmenite	0.23	0.13
Magnetite	0.42	0.21
Hematite		
Apatite	0.14	0.12
Zircon	0.01	0.01
Perovskite		
Chromite		
Sphene		
Pyrite		
Halite		
Fluorite		
Anhydrite		
Na2SO4		
Calcite		
Na2CO3		
Total	99.57	100.00

Fe3+/(Total Fe) in rock	30.3	30.3
Mg/(Mg+Total Fe) in rock	26.0	26.0
Mg/(Mg+Fe2+) in rock	33.6	33.6
Mg/(Mg+Fe2+) in silicates	43.6	43.6
Ca/(Ca+Na) in rock	8.2	8.2
Ca/(Ca+Na) in plagioclase	6.9	6.9
Differentiation Index	95.7	97.4
Calculated density, g/cc	2.64	2.64
Calculated liquid density, g/cc	2.36	2.36
Calculated viscosity, dry, Pas	1.00	1.00
Calculated viscosity, wet, Pas	0.73	0.73
Estimated liquidus temp., °C	791	791
Estimated H2O content, wt. %	3.93	3.93

This program was written by Kurt Hollocher, Geology Department, Union College, Schenectady, NY, 12308, hollochk@union.edu

Norm Calculation Program Program run: 08/12/2008 HELP

Sample Number: RA-16-did not analyse for trace E

	Rock Analysis	
SiO2	67.27	%
TiO2	0.40	%
Al2O3	15.76	%
Fe2O3	2.24	%
FeO		%
MnO	0.03	%
MgO	0.73	%
CaO	1.31	%
Na2O	2.83	%
K2O	6.59	%
P2O5	0.13	%
CO2		%
SO3		%
S		%
F		%
Cl		%
Sr		ppm
Ba		ppm
Ni		ppm
Cr		ppm
Zr		ppm
Total	97.29	

Normalization Factors	
Total=100%? Y/N	n
Fe3+/(Total Iron)	0.3
Total Fe as FeO	2.02
Desired Fe2O3	0.67
Desired FeO	1.41
Weight corr. factor	1.000

Zero values not shown

Norm calculation checks:
Norm seems OK

Normalized Analysis
67.27
0.40
15.76
0.67
1.41
0.03
0.73
1.31
2.83
6.59
0.13
97.13

Normative Minerals	Weight % Norm	Volume % Norm
Quartz	21.41	22.24
Plagioclase	29.60	30.79
Orthoclase	38.94	41.88
Nepheline		
Leucite		
Kalsilite		
Corundum	1.90	1.31
Diopside		
Hypersthene	3.25	2.56
Wollastonite		
Olivine		
Larnite		
Acmite		
K2SiO3		
Na2SiO3		
Rutile		
Ilmenite	0.76	0.44
Magnetite	0.97	0.51
Hematite		
Apatite	0.30	0.26
Zircon		
Perovskite		
Chromite		
Sphene		
Pyrite		
Halite		
Fluorite		
Anhydrite		
Na2SO4		
Calcite		
Na2CO3		
Total	97.13	99.99

Fe3+/(Total Fe) in rock	30.0	30.0
Mg/(Mg+Total Fe) in rock	39.3	39.3
Mg/(Mg+Fe2+) in rock	48.0	48.0
Mg/(Mg+Fe2+) in silicates	62.5	62.5
Ca/(Ca+Na) in rock	20.4	20.4
Ca/(Ca+Na) in plagioclase	18.2	18.2
Differentiation Index	90.0	94.9
Calculated density, g/cc	2.67	2.67
Calculated liquid density, g/cc	2.40	2.40
Calculated viscosity, dry, Pas	0.82	0.82
Calculated viscosity, wet, Pas	0.64	0.64
Estimated liquidus temp., °C	861	861
Estimated H2O content, wt. %	3.15	3.15

This program was written by Kurt Hollocher, Geology Department, Union College, Schenectady, NY, 12308, hollochk@union.edu

RA17- norm4

Norm Calculation Program

Sample Number: RA-17

Program run: 08/12/2008

HELP

	Rock Analysis	
SiO2	70.09	%
TiO2	0.37	%
Al2O3	15.85	%
Fe2O3	1.93	%
FeO		%
MnO	0.03	%
MgO	0.64	%
CaO	1.42	%
Na2O	2.87	%
K2O	7.41	%
P2O5	0.12	%
CO2		%
SO3		%
S		%
F		%
Cl		%
Sr	115	ppm
Ba	1060	ppm
Ni		ppm
Cr		ppm
Zr	103	ppm
Total	100.73	

Normalization Factors	
Total=100%? Y/N	n
Fe3+/(Total Iron)	0.3
Total Fe as FeO	1.74
Desired Fe2O3	0.58
Desired FeO	1.22
Weight corr. factor	1.000

Zero values not shown

Norm calculation checks:
Norm seems OK

Normalized Analysis
70.09
0.37
15.85
0.58
1.22
0.03
0.64
1.42
2.87
7.41
0.12
0.01
0.12
0.01
100.74

Normative Minerals	Weight % Norm	Volume % Norm
Quartz	20.24	20.10
Plagioclase	30.57	30.39
Orthoclase	44.66	45.91
Nepheline		
Leucite		
Kalsilite		
Corundum	0.64	0.43
Diopside		
Hypersthene	2.80	2.12
Wollastonite		
Olivine		
Larnite		
Acmite		
K2SiO3		
Na2SiO3		
Rutile		
Ilmenite	0.70	0.39
Magnetite	0.84	0.43
Hematite		
Apatite	0.28	0.23
Zircon	0.01	0.01
Perovskite		
Chromite		
Sphene		
Pyrite		
Halite		
Fluorite		
Anhydrite		
Na2SO4		
Calcite		
Na2CO3		
Total	100.74	100.01

Fe3+/(Total Fe) in rock	30.0	30.0
Mg/(Mg+Total Fe) in rock	39.6	39.6
Mg/(Mg+Fe2+) in rock	48.3	48.3
Mg/(Mg+Fe2+) in silicates	63.5	63.5
Ca/(Ca+Na) in rock	21.5	21.5
Ca/(Ca+Na) in plagioclase	19.6	19.6
Differentiation Index	95.5	96.4
Calculated density, g/cc	2.65	2.65
Calculated liquid density, g/cc	2.39	2.39
Calculated viscosity, dry, Pas	0.83	0.83
Calculated viscosity, wet, Pas	0.65	0.65
Estimated liquidus temp., °C	855	855
Estimated H2O content, wt. %	3.23	3.23

This program was written by Kurt Hollocher, Geology Department, Union College, Schenectady, NY, 12308, hollochk@union.edu

RA18- norm4

Norm Calculation Program

Sample Number: RA-18

Program run: 08/12/2008

HELP

	Rock Analysis	
SiO2	71.74	%
TiO2	0.51	%
Al2O3	14.48	%
Fe2O3	2.72	%
FeO		%
MnO	0.05	%
MgO	0.96	%
CaO	2.00	%
Na2O	2.87	%
K2O	5.05	%
P2O5	0.15	%
CO2		%
SO3		%
S		%
F		%
Cl		%
Sr	87	ppm
Ba	432	ppm
Ni		ppm
Cr		ppm
Zr	141	ppm
Total	100.53	

Normalization Factors	
Total=100%? Y/N	n
Fe3+/(Total Iron)	0.3
Total Fe as FeO	2.45
Desired Fe2O3	0.82
Desired FeO	1.71
Weight corr. factor	1.000

Zero values not shown

Norm calculation checks:
Norm seems OK

Normalized Analysis
71.74
0.51
14.48
0.82
1.71
0.05
0.96
2.00
2.87
5.05
0.15
0.01
0.05
0.02
100.42

Normative Minerals	Weight % Norm	Volume % Norm
Quartz	29.38	29.67
Plagioclase	33.25	33.50
Orthoclase	30.21	31.58
Nepheline		
Leucite		
Kalsilite		
Corundum	0.94	0.63
Diopside		
Hypersthene	4.10	3.16
Wollastonite		
Olivine		
Larnite		
Acmite		
K2SiO3		
Na2SiO3		
Rutile		
Ilmenite	0.97	0.55
Magnetite	1.19	0.61
Hematite		
Apatite	0.35	0.29
Zircon	0.03	0.02
Perovskite		
Chromite		
Sphene		
Pyrite		
Halite		
Fluorite		
Anhydrite		
Na2SO4		
Calcite		
Na2CO3		
Total	100.42	100.01

Fe3+/(Total Fe) in rock	30.1	30.1
Mg/(Mg+Total Fe) in rock	41.1	41.1
Mg/(Mg+Fe2+) in rock	50.0	50.0
Mg/(Mg+Fe2+) in silicates	64.7	64.7
Ca/(Ca+Na) in rock	27.8	27.8
Ca/(Ca+Na) in plagioclase	25.8	25.8
Differentiation Index	92.8	94.8
Calculated density, g/cc	2.69	2.69
Calculated liquid density, g/cc	2.41	2.41
Calculated viscosity, dry, Pas	0.90	0.90
Calculated viscosity, wet, Pas	0.68	0.68
Estimated liquidus temp., °C	821	821
Estimated H2O content, wt. %	3.60	3.60

This program was written by Kurt Hollocher, Geology Department, Union College, Schenectady, NY, 12308, hollochk@union.edu

RA19- norm4

Norm Calculation Program
Sample Number: RA-19

Program run: 08/12/2008

HELP

	Rock Analysis	
SiO2	67.15	%
TiO2	0.51	%
Al2O3	13.58	%
Fe2O3	2.79	%
FeO		%
MnO	0.05	%
MgO	1.03	%
CaO	1.84	%
Na2O	2.57	%
K2O	5.16	%
P2O5	0.15	%
CO2		%
SO3		%
S		%
F		%
Cl		%
Sr	96	ppm
Ba	719	ppm
Ni		ppm
Cr		ppm
Zr	165	ppm
Total	94.83	

Normalization Factors	
Total=100%? Y/N	n
Fe3+/(Total Iron)	0.3
Total Fe as FeO	2.51
Desired Fe2O3	0.84
Desired FeO	1.76
Weight corr. factor	1.000

Zero values not shown

Norm calculation checks:
Norm seems OK

Normalized Analysis
67.15
0.51
13.58
0.84
1.76
0.05
1.03
1.84
2.57
5.16
0.15
0.01
0.08
0.02
94.75

Normative Minerals	Weight % Norm	Volume % Norm
Quartz	26.18	28.02
Plagioclase	29.92	31.95
Orthoclase	31.07	34.43
Nepheline		
Leucite		
Kalsilite		
Corundum	0.66	0.47
Diopside		
Hypersthene	4.35	3.56
Wollastonite		
Olivine		
Larnite		
Acmite		
K2SiO3		
Na2SiO3		
Rutile		
Ilmenite	0.97	0.58
Magnetite	1.22	0.66
Hematite		
Apatite	0.35	0.31
Zircon	0.03	0.02
Perovskite		
Chromite		
Sphene		
Pyrite		
Halite		
Fluorite		
Anhydrite		
Na2SO4		
Calcite		
Na2CO3		
Total	94.75	100.00

Fe3+/(Total Fe) in rock	30.0	30.0
Mg/(Mg+Total Fe) in rock	42.2	42.2
Mg/(Mg+Fe2+) in rock	51.1	51.1
Mg/(Mg+Fe2+) in silicates	65.3	65.3
Ca/(Ca+Na) in rock	28.3	28.3
Ca/(Ca+Na) in plagioclase	26.2	26.2
Differentiation Index	87.2	94.4
Calculated density, g/cc	2.69	2.69
Calculated liquid density, g/cc	2.41	2.41
Calculated viscosity, dry, Pas	0.87	0.87
Calculated viscosity, wet, Pas	0.67	0.67
Estimated liquidus temp., °C	831	831
Estimated H2O content, wt. %	3.49	3.49

This program was written by Kurt Hollocher, Geology Department, Union College, Schenectady, NY, 12308, hollochk@union.edu

RA20- norm4

Norm Calculation Program
Sample Number: RA-20

Program run: 08/12/2008

HELP

	Rock Analysis	
SiO2	69.59	%
TiO2	0.60	%
Al2O3	14.13	%
Fe2O3	3.25	%
FeO		%
MnO	0.05	%
MgO	1.19	%
CaO	1.88	%
Na2O	2.60	%
K2O	5.59	%
P2O5	0.18	%
CO2		%
SO3		%
S		%
F		%
Cl		%
Sr	86	ppm
Ba	572	ppm
Ni		ppm
Cr		ppm
Zr	172	ppm
Total	99.06	

Normalization Factors	
Total=100%? Y/N	n
Fe3+/(Total Iron)	0.3
Total Fe as FeO	2.92
Desired Fe2O3	0.98
Desired FeO	2.05
Weight corr. factor	1.000

Zero values not shown

Norm calculation checks:
Norm seems OK

Normalized Analysis
69.59
0.60
14.13
0.98
2.05
0.05
1.19
1.88
2.60
5.59
0.18
0.01
0.06
0.02
98.93

Normative Minerals	Weight % Norm	Volume % Norm
Quartz	26.53	27.26
Plagioclase	30.18	30.93
Orthoclase	33.47	35.60
Nepheline		
Leucite		
Kalsilite		
Corundum	0.73	0.50
Diopside		
Hypersthene	5.02	3.94
Wollastonite		
Olivine		
Larnite		
Acmite		
K2SiO3		
Na2SiO3		
Rutile		
Ilmenite	1.14	0.65
Magnetite	1.42	0.74
Hematite		
Apatite	0.42	0.35
Zircon	0.03	0.02
Perovskite		
Chromite		
Sphene		
Pyrite		
Halite		
Fluorite		
Anhydrite		
Na2SO4		
Calcite		
Na2CO3		
Total	98.94	99.99

Fe3+/(Total Fe) in rock	30.1	30.1
Mg/(Mg+Total Fe) in rock	42.0	42.0
Mg/(Mg+Fe2+) in rock	50.9	50.9
Mg/(Mg+Fe2+) in silicates	65.4	65.4
Ca/(Ca+Na) in rock	28.5	28.5
Ca/(Ca+Na) in plagioclase	25.9	25.9
Differentiation Index	90.2	93.8
Calculated density, g/cc	2.69	2.69
Calculated liquid density, g/cc	2.42	2.42
Calculated viscosity, dry, Pas	0.85	0.85
Calculated viscosity, wet, Pas	0.65	0.65
Estimated liquidus temp., °C	841	841
Estimated H2O content, wt. %	3.38	3.38

This program was written by Kurt Hollocher, Geology Department, Union College, Schenectady, NY, 12308, hollochk@union.edu